HAL
archives-ouvertes.fr

Conditioning of surfaces in particle accelerators

Valentine Petit

▶ **To cite this version:**

Valentine Petit. Conditioning of surfaces in particle accelerators. High Energy Physics - Experiment [hep-ex]. Institut Supérieur de l'Aéronautique et de l'Espace, 2020. English. tel-02919120

HAL Id: tel-02919120
https://hal.archives-ouvertes.fr/tel-02919120

Submitted on 21 Aug 2020

HAL is a multi-disciplinary open access archive for the deposit and dissemination of scientific research documents, whether they are published or not. The documents may come from teaching and research institutions in France or abroad, or from public or private research centers.

L'archive ouverte pluridisciplinaire **HAL**, est destinée au dépôt et à la diffusion de documents scientifiques de niveau recherche, publiés ou non, émanant des établissements d'enseignement et de recherche français ou étrangers, des laboratoires publics ou privés.

Université Fédérale
Toulouse Midi-Pyrénées

ONERA
THE FRENCH AEROSPACE LAB

THÈSE

En vue de l'obtention du
DOCTORAT DE L'UNIVERSITÉ DE TOULOUSE

Délivré par l'Institut Supérieur de l'Aéronautique et de l'Espace

---

Présentée et soutenue par

Valentine PETIT

Le 17 janvier 2020

Conditioning of Surfaces in Particle Accelerators

Ecole doctorale : **GEET - Génie Electrique Electronique et Télécommunications : du système au nanosystème**

Spécialité : **Ingénierie des Plasmas**

Unité de recherche :
ISAE-ONERA OLIMPES Optronique, Laser, Imagerie Physique et Environnement Spatial

Thèse dirigée par
Thierry PAULMIER et Mohamed BELHAJ

Encadrée au CERN par
Mauro TABORELLI

Jury

M. Pedro FERNANDES TAVARES, Rapporteur
Mme Anouk GALTAYRIES, Rapporteure
M. Omar JBARA, Examinateur
M. Julien HILLAIRET, Examinateur
M. Mauro TABORELLI, Examinateur
M. Thierry PAULMIER, Directeur de thèse

CERN-THESIS-2019-358
17/01/2020

Université Fédérale
Toulouse Midi-Pyrénées

ONERA
THE FRENCH AEROSPACE LAB

THÈSE

En vue de l'obtention du
DOCTORAT DE L'UNIVERSITÉ DE TOULOUSE

Délivré par l'Institut Supérieur de l'Aéronautique et de l'Espace

---

Présentée et soutenue par

Valentine PETIT

Le 17 janvier 2020

Conditionnement des surfaces dans les accélérateurs de particules

---

Ecole doctorale : **GEET - Génie Electrique Electronique et Télécommunications : du système au nanosystème**

Spécialité : **Ingénierie des Plasmas**

Unité de recherche :
ISAE-ONERA OLIMPES Optronique, Laser, Imagerie Physique et Environnement Spatial

Thèse dirigée par
Thierry PAULMIER et Mohamed BELHAJ

Encadrée au CERN par
Mauro TABORELLI

Jury

M. Pedro FERNANDES TAVARES, Rapporteur
Mme Anouk GALTAYRIES, Rapporteure
M. Omar JBARA, Examinateur
M. Julien HILLAIRET, Examinateur
M. Mauro TABORELLI, Examinateur
M. Thierry PAULMIER, Directeur de thèse

CERN-THESIS-2019-358
17/01/2020

I hope you can accept Nature as She is - absurd.
— Richard P. Feynman, 1985

Abstract

The electron cloud developing in the vacuum chambers of the LHC during the proton beam operation is responsible for heat load on the cryogenic system of the superconducting magnets. The observed heat load exhibits a strong dispersion between the different LHC arcs, although identical by design. Some of them are currently close to the limit of the cryoplant capacity. Under the effect of the cloud itself, conditioning of the copper surface of the LHC beam pipes is expected, decreasing thus the secondary electron yield of the surface and leading to a decrease of the cloud intensity down to operation-compatible levels. Such a process seems therefore to be hindered in some parts of the LHC ring. This work aims to understand the copper conditioning processes occurring in the LHC, to unravel the origin of the heat load dispersion observed along the ring. Copper conditioning mechanisms were studied in the laboratory at room temperature by mimicking the electron cloud by an electron gun. The fundamental role of carbon, among the surface chemical components, in the reduction of the secondary electron yield during conditioning was evidenced. Studying the deconditioning, occurring while exposing a conditioned surface to air (necessary step to extract beam pipes from the LHC) allowed establishing a procedure to limit the erasing of the *in-situ* conditioning state of such components before the analysis of their surface in the laboratory. The surface of beam pipes extracted from a low heat load magnet were found to have similar characteristics as the ones conditioned in the laboratory. However, beam pipes extracted from a high heat load magnet exhibit cupric oxide CuO and a very low amount of surface carbon. It is demonstrated that these modifications are induced by the LHC operation and lead to a slower conditioning of these surfaces. Therefore, these modifications are currently the best candidate to explain the heat load dispersion observed in the LHC.

Keywords: Conditioning, secondary electrons, surface, copper, carbon, LHC

Résumé

Le nuage d'électrons se développant dans les chambres à vide du LHC lors de l'opération des faisceaux de protons engendre une charge thermique sur le système cryogénique de ses aimants supraconducteurs. La valeur de cette charge thermique présente une forte dispersion entre les différents arcs du LHC, pourtant identiques par design, dont certains sont actuellement proches de la limite de la capacité cryogénique. Sous l'effet du nuage d'électrons, le conditionnement de la surface de cuivre des chambres à vide du LHC a lieu, réduisant son rendement d'électrons secondaires. Un tel processus est supposé décroitre l'activité du nuage vers un niveau acceptable pour l'opération du LHC et semble donc localement mis en défaut. Ce travail a analysé les phénomènes de conditionnement du cuivre ayant lieu dans le LHC afin d'expliquer les différences d'activités du nuage électronique observées dans l'accélérateur. L'étude des mécanismes de conditionnement du cuivre en laboratoire, à température ambiante, en remplaçant le nuage par un canon à électrons, a mis en évidence le rôle crucial du carbone dans la décroissance du rendement d'électrons secondaires. L'étude du déconditionnement, ayant lieu à la remise à l'air d'une surface irradiée (étape nécessaire à l'extraction de tubes faisceau du LHC) a permis d'établir une procédure limitant l'effacement de l'état de conditionnement *in-situ* de ces composants en vue de l'analyse de leur surface en laboratoire. Des analyses réalisées sur des tubes faisceau extraits d'un aimant à faible charge thermique montrent que ces surfaces présentent des caractéristiques similaires à celles conditionnées en laboratoire. En revanche, les tubes faisceau extraits d'un aimant à forte charge thermique présentent du CuO ainsi qu'un taux de carbone surfacique extrêmement faible. Il est prouvé que ces modifications résultent de l'opération du LHC et conduisent à un conditionnement altéré de ces surfaces. Ces modifications sont actuellement le meilleur candidat pour expliquer l'origine des différences de charge thermique observées dans le LHC.

Mots clés : Conditionnement, électrons secondaires, surface, cuivre, carbone, LHC

Acknowledgements

The present work results from a fruitful collaboration with people who contributed to make this period a unique experience. I now would like to acknowledge them.

First of all, I would like to thank my CERN supervisor, Mauro Taborelli. I am eminently grateful for all your support and trust during this work. Your patience, while countless time sharing your knowledge with me and your daily guidance onto the right path were solid anchors which allowed me to safely progress every day towards my objectives. I also appreciated to always find your door open whenever needed, to clear up my fears in the hardest times and to discuss any of my ideas.

I then deeply thank Paolo Chiggiato for stirring in me the taste of perfection, for the motivation and advices you transmitted me through our PhD meetings and for your trust over these years.

I am glad to have been part of your team and to have shared this experience with both of you, thank you!

Then, I wish to thank Mohamed Belhaj and Thierry Paulmier for accepting me as their PhD student at ONERA and for their supervision during this work. I am also grateful to Pedro Fernandes Tavares, Anouk Galtayries, Omar Jbara and Julien Hillairet for accepting to review my work.

I then warmly acknowledge the marvellous CERN surface analysis team: Holger, for guiding me in the laboratories from my very first steps at CERN, Danilo, for his priceless positive mood, availability and Python skills and Marcel, for his expertise on the dark mysteries of surface science.

This work could not have been possible without the help of many other colleagues and teams. I am thus grateful to the surface treatment team, Pierre, Florent and Louise for dealing with my always-urgent requests, to my beloved chemists Colette and Benoit, to the serial beam screen cutters Paul and Hendrik, to Gianni for his explanations of the electron cloud phenomenon and the time spent together challenging our brains on the puzzling LHC heat load pattern, and to Anité and Elisa for their support on microscope observations. I also wish to thank all the members of the LHC Beam-Induced Heat Loads Task Force for the fantastic work achieved together.

Beyond the scientific aspects, these years have been enriched by several encounters which provided me daily energy and made my everyday life at CERN a great experience. Therefore, I wish to give my thanks to Colette and Benoit for listening and supporting me during the periods of doubts, to Thibaut for his peculiar thoughts on the life as a PhD student and on human social interactions, to Katia, Lucie and Stéphanie for our friendship built over these years and to Christian, Pierre and Lucie for sharing hours of training on the paths, on a bicycle and in a swimming pool. Another thank goes to Wil, Pedro, Alban, Fabio, Daria, Guillaume, Tony, Delphine, David, Elena, Anne-Marie, Jean-Pierre and the open-space crew for all the coffee breaks, the advices and daily discussions during these three years.

Enfin, mes dernières pensées vont à ma famille, Serge, Catherine, Gwénaëlle, Mathieu et Erwann, pour leur soutien inconditionel et sans faille depuis les premiers jours. Tout cela n'aurait été possible sans vous, je vous en remercie profondément !

Contents

List of acronyms

EDX: Energy-Dispersive X-ray Spectroscopy

ESD: Electron Stimulated Desorption

EYETS: Extended Year-End Technical Stop

HL-LHC: High-Luminosity Large Hadron Collider

IP: Interaction Point

LHC: Large Hadron Collider

LS: Long Shut-down

LSS: Long Straight Section

PE: Polyethylene

PIM: Plug-In Module

PS: Proton Synchrotron

RF: Radio Frequency

SEM: Scanning Electron Microscope

SEY: Secondary Electron Yield

SPS: Super Proton Synchrotron

UHV: Ultra-High Vacuum

XPS: X-Ray Photoelectron Spectroscopy

YETS: Year-End Technical Stop

Introduction

The Large Hadron Collider (LHC) at CERN is the world's largest particle accelerator, which successfully achieved to produce and investigate collisions between protons and between ions at an unprecedented high energy and rate. In the beam vacuum chambers of the LHC, an electron cloud develops during operation with proton beams at nominal parameters and is responsible for a heat load on the cryogenic system of the superconducting magnets. The observed heat load currently presents a wide scattering between the different arcs of the machine in spite of their identical design. Some of these arcs are close to the limit of the cryogenic cooling capacity, and the available margin is expected to shrink in the High-Luminosity era where the LHC will routinely operate with higher beam intensity.

Under the electron cloud effect, the conditioning of the copper surface of the LHC beam screens is expected, i.e. the secondary electron yield of their surface decreases and, as a consequence, so does the electron cloud density. Such a process is expected to lower the electron cloud-associated heat load down to a level which is compatible with operation at nominal LHC parameters and even with the future High-Luminosity LHC beam characteristics. The wide scattering mentioned above indicates that this conditioning is actually hindered in some parts of the accelerator.

This work investigates the copper conditioning and deconditionning mechanisms occurring in the LHC, with the objective of unravelling the scattering of electron cloud activity observed along the ring.

A laboratory study, where the electron bombardment is carried out at room temperature by an electron flood gun, is performed to disentangle the role of the different chemical components of an air exposed copper surface in its conditioning. The mechanisms of copper deconditioning occurring when an irradiated surface is exposed to air (necessary step for the extraction of beam vacuum pipes from the LHC) are investigated. A specific procedure is derived, aiming at limiting at most the loss of memory of the *in-situ* conditioning state of the LHC extracted vacuum components in view of their surface analysis in the laboratory.

In a second phase, secondary electron yield measurements and surface chemical analyses are performed on the beam screens extracted from a low and a high heat load LHC dipole. An interpretation of these analyses is given, aiming at explaining the difference of heat load observed along the LHC.

An extended French summary of this work can be found at the end of this manuscript.

Chapter 1

Context of the study

1.1 CERN accelerator complex

The European Organization for Nuclear Research (CERN) founded in 1954 and located at the Franco-Swiss border, is currently the world's largest particle physics laboratory. It aims at the exploration of the Universe laws, in particular the so-called Standard Model [1, 2] which encapsulates the elementary particles and three of the four fundamental forces acting on them, as well as at the investigation of further fundamental questions such as the existence of dark matter and the origin of dark energy [1].

1.1.1 General layout

At CERN, such research is performed through the thorough analysis of collisions between highly energetic particles. For this purpose, the Organization developed and exploits an accelerator complex which produces and gradually increases the energy of proton beams before injecting them into the largest particle accelerator ever built, the Large Hadron Collider (LHC). In this gigantic and highly complex machine, two proton beams are brought into frontal collisions at an unprecedented energy and rate, as required to obtain statistical evidence of phenomena in a reasonable amount of time. A schematic of the CERN main accelerator chain in 2017 is displayed in Fig. 1.1, together with other accelerators and experimental areas of the complex.

1.1.2 The Large Hadron Collider

The LHC is a 26.7 km circumference twin ring collider, designed to bring two high intensity proton beams into collisions at 14 TeV at the center of mass. The accelerator was built between 1998 and 2008 and is installed in a 100 m deep tunnel, previously hosting the Large Electron Positron collider (LEP) [4, 5]. The first proton beam to perform a full turn of the machine was recorded the 10^{th} of September 2008. Nine days later, a faulty interconnection between two superconducting magnets failed, leading to the violent release of overpressured helium directly into the tunnel, damaging magnets over hundreds of meters and polluting several kilometres of vacuum beam pipes with debris of the explosion [4, 6]. After a year of repair and consolidation works, the LHC

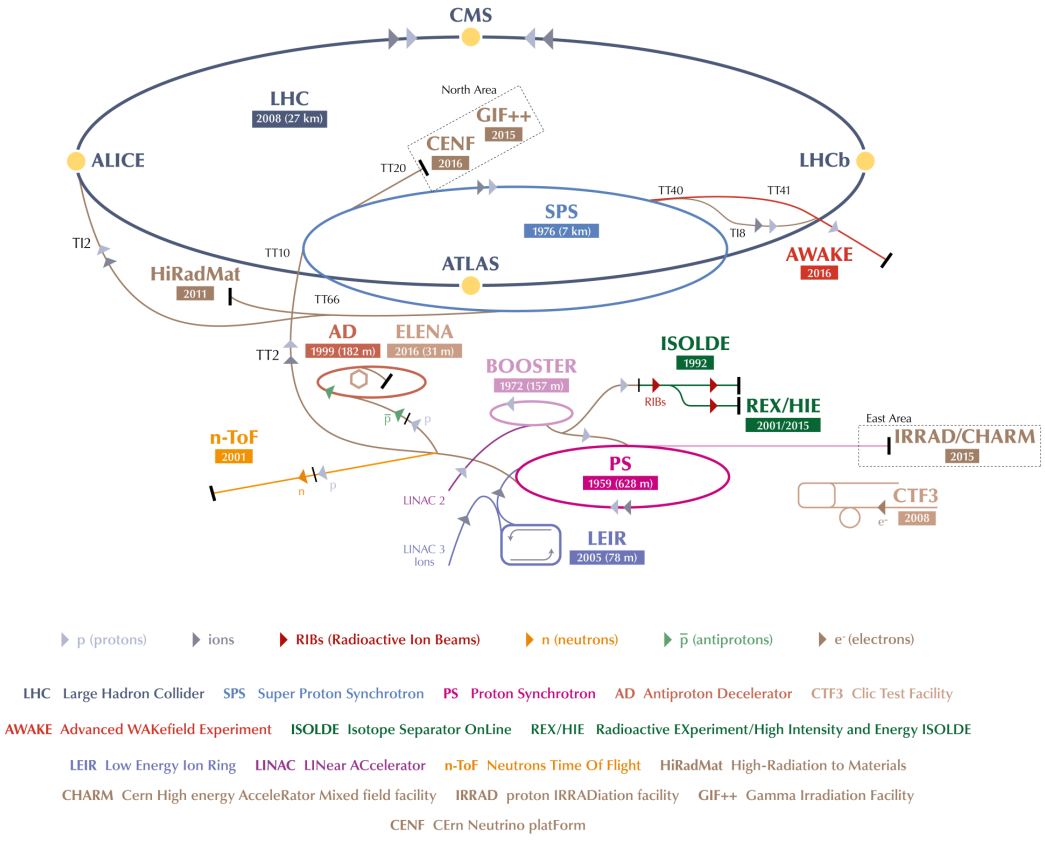

Figure 1.1: The CERN accelerator complex in 2017 [3]. The proton beam is created from hydrogen atoms and first accelerated into the linear accelerator LINAC2 (being replaced by LINAC4 in Run 3). The beam is then transferred to the Proton Synchrotron Booster (PSB) which injects it into the Proton Synchrotron (PS). It reaches next the Super Proton Synchrotron (SPS) which finally distributes it to the LHC. The complex also hosts other accelerators and experiments such as the Antiproton Decelerator (AD) or the Isotope Separator Online (ISOLDE). The dates correspond to the year of first operation of each machine.

was back to operation by the end of 2009.

The LHC operation schedule alternates between 3-year-long Runs, namely periods dedicated to physics where data from the collisions are accumulated, and Long Shutdown (LS) periods of 2 years devoted to major maintenance and upgrade works. A timeline of the LHC schedule with the major achievements of each period is given in Fig 1.2. During Run periods, the machine is typically colliding protons from April to October, while November is usually dedicated to ion collisions. From December to February, the machine is stopped for a Year End Technical Stop (YETS) in order to perform yearly maintenance work. During winter 2016-2017, an extended YETS (EYETS) occured, to let more time to perform some specific works.

In 2027, as a result of several upgrade phases, the LHC will enter in its High-Luminosity era (HL-LHC), increasing its designed luminosity by a factor of 5 [7]. More details about the HL-LHC project are given in Section 1.1.2.3.

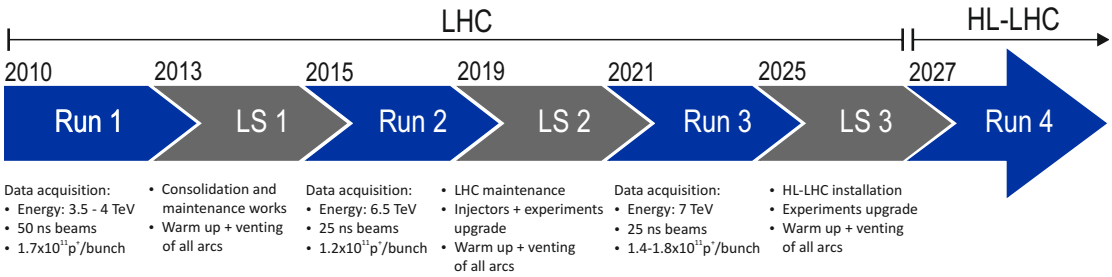

Figure 1.2: Timeline of the LHC from the first year of data acquisition to its upgrade to its High Luminosity configuration. The main achievements and keys points of each period are given.

1.1.2.1 Machine layout

The LHC ring is an alternation of 2.8-km-long cryogenic arcs and 600-m-long room temperature Long Straight Sections (LSS). A global schematic layout of the accelerator is given in Fig. 1.3. Beam 1 (blue), is injected in LSS 2 and circulates clockwise while beam 2 (red) is injected in LSS 8 and travels counter-clockwise. Each of the two proton beams is running along the ring into its own separate vacuum chamber, the vacuum pipes of the two beams only merging in the interaction points (IP) to allow the beams to collide.

Four straight sections host experimental areas where particle detectors, namely ATLAS, CMS, ALICE and LHCb in IP 1, 2, 5 and 8 respectively, collect the debris of beam collisions. The other LSSs host the Radio-Frequency (RF) accelerating cavities (LSS 4), the collimation systems (LSS 3 and 7) and the extraction lines to the LHC dump (LSS 6).

In the arcs, the beam orbits are curved by a total of 1232 superconducting dipoles cooled by superfluid helium at 1.9 K. Each LHC arc is divided into 23 cells forming a classical FODO lattice, i.e. an alternation of focussing and defocussing quadrupoles [8]. Each cell is split into two 53.45-m-long half-cells, composed of 3 dipoles (main bends) and 1 quadrupole. A schematic of a LHC arc half-cell is given in Fig. 1.4, with the corresponding dimensions. In the arcs, the space constraint led to the design of twin bore magnets, where the two beam vacuum pipes and their respective magnet coil are embedded in a single cryostat, 0.91 m in diameter [2, 9].

1.1.2.2 LHC beam parameters

The performance of a collider is closely related to the production rate R of a given physics event [10]:

$$R = L.\sigma_{event} \tag{1.1}$$

where σ_{event} [cm^2] is the event cross-section and L [cm^{-2}s^{-1}] is the machine luminosity, describing the efficiency of the collider in producing collision events.

For two beams colliding head-on and presenting identical Gaussian beam distribu-

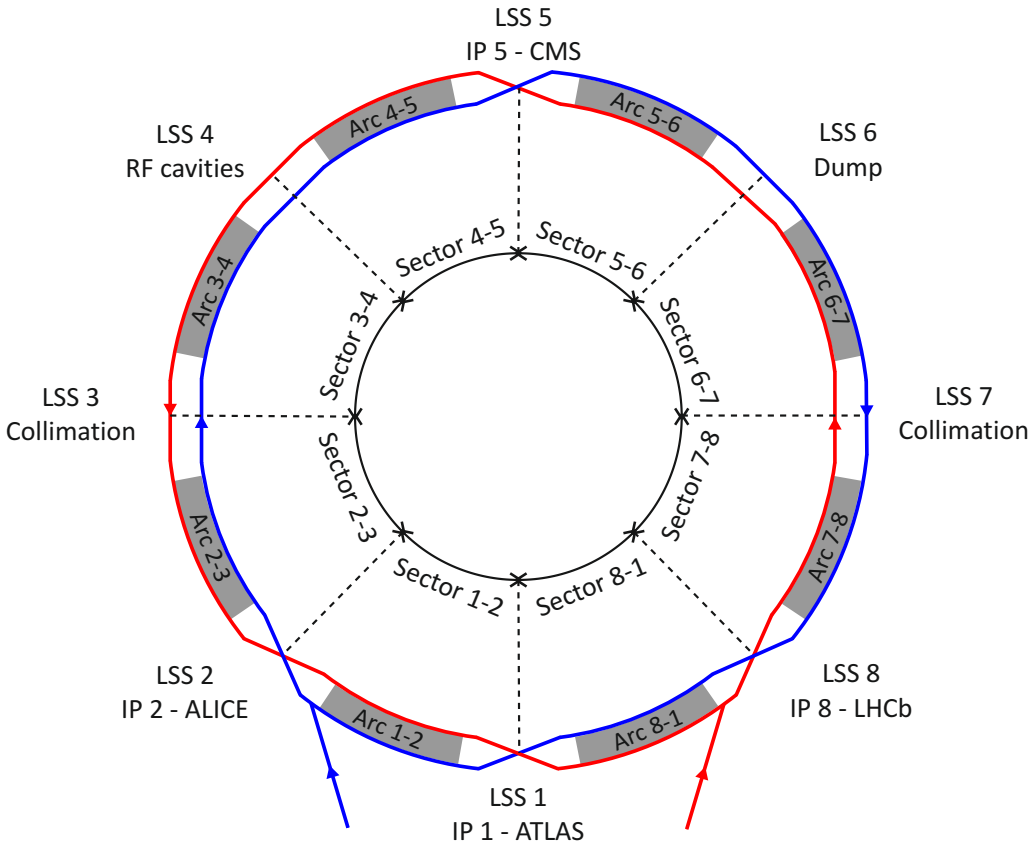

Figure 1.3: Schematic layout of the LHC

tions, the luminosity is expressed as [10]:

$$L = \frac{N_1 N_2 n_b f}{4\pi\sigma_x\sigma_y} \tag{1.2}$$

where N_1 and N_2 are the bunch populations of the two beams, n_b is the number of bunches per beam, f is the revolution frequency and σ_x and σ_y the horizontal and vertical root mean square (r.m.s.) bunch sizes.

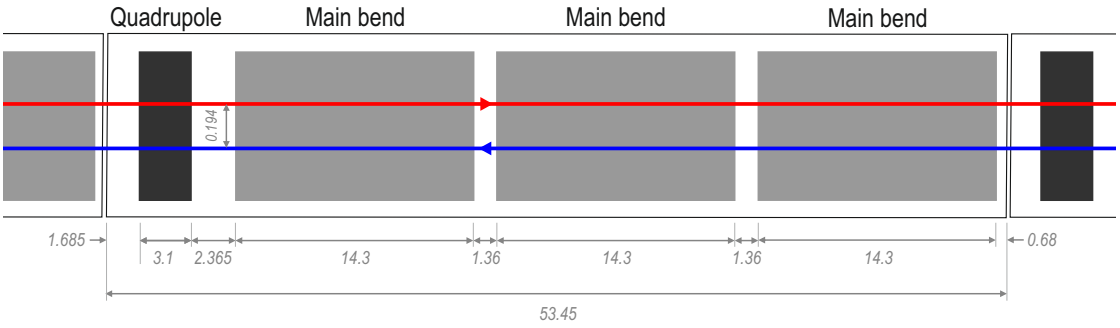

Figure 1.4: Schematic layout of a LHC arc half-cell with two circulating beams. The dimensions are given in meters.

Table 1.1: Main nominal parameters of the LHC machine and beams [9]

		Injection	Collision
Proton energy	[GeV]	450	7000
Relativistic Gamma		479.6	7461
Number of protons per bunch		1.15×10^{11}	
Number of bunches		2808	
Bunch spacing	[ns]	25	
Circulating beam current	[A]	0.584	
Stored energy per beam	[MJ]	23.3	362
Field of main bends	[T]	0.535	8.33
Bending radius of main bends	[m]	2803.95	
RMS bunch length	[cm]	11.24	7.55
RMS beam size at IP 1 and 5	μm	375.2	16.7
RMS beam size at IP 2 and 8	μm	279.6	70.9
RMS beam size in arcs	[mm]	1.19	0.3
Peak luminosity at IP 1 and 5	[$\mathrm{cm}^{-2}\mathrm{sec}^{-1}$]		1.0×10^{34}
Synchrotron radiation power per ring	[W]	6.15×10^{-2}	3.6×10^{3}
Synchrotron radiation power in main bends	[W/m/beam]	0.0	0.206
Critical photon energy	[eV]	0.01	44.14

The luminosity is therefore determined by the machine and beam parameters and can be increased by increasing the bunch intensity and/or decreasing the bunch size.

The main nominal parameters of the LHC beam are summarized in Table 1.1. A nominal LHC beam consists of 2808 bunches of 1.15×10^{11} protons each and spaced by 25 ns. The time structure of the LHC beam results from its production scheme in the injectors and is driven by the necessity of having gaps between groups of protons to ramp the intensity in the kicker magnets used to deflect the beam during injection into accelerators. A train consists of a variable number of batches (2 or 4, spaced by 225 ns), each containing 72 bunches. A complete LHC beam is then obtained from the accumulation of 11 trains spaced by 925 ns provided by the SPS.

At top energy, the r.m.s. transverse beam size in the LHC arcs is 300 µm and is locally shrunk by the optics down to 16.7 µm at IP 1 and 5.

Due to the bending of its trajectory by the main dipoles in the arc, the proton beam emits synchrotron radiation. The characteristics of the radiation are related to the machine and beam parameters. The spectrum of emitted photons is characterised by its critical energy, which by definition splits the total emitted power into two equal parts and is given by [11]:

$$E_c = 3\frac{\hbar c \gamma^3}{2\rho} \tag{1.3}$$

where $\hbar$ is the Dirac constant, ρ the bending radius of the LHC arc dipoles and γ the relativistic factor. In the LHC case, the critical energy is equal to 44.14 eV [9], which results in extreme ultraviolet radiation. The associated emitted power is 0.206 W/m/ring in the main bends, and has to be dissipated by the cryogenic system.

Table 1.2: Main nominal parameters of the HL-LHC machine and beams (proton collisions, 25 ns standard beam) [7]

Proton energy in collisions	[TeV]	7
Number of protons per bunch		2.2×10^{11}
Number of bunches		2748
Circulating beam current	[A]	1.09
Levelled luminosity at IP 1 and 5	[$cm^{-2}sec^{-1}$]	5.32×10^{34}
Synchrotron radiation power in main bends	[W/m/beam]	0.66

1.1.2.3 High-Luminosity upgrade

Based on the fact that keeping operating the LHC with nominal parameters after Run 3 would result in a marginal statistical gain in terms of accumulated data and because the full exploitation of the LHC physics potential was the first priority of the CERN council when adopting the European Strategy for Particle Physics in 2006 [7], CERN set up the High Luminosity LHC (HL-LHC) project in 2010. This LHC upgrade aims at increasing the LHC instantaneous and integrated designed luminosities by a factor of 5 and 10 respectively as well as extending the LHC operability by 10 years. To provide beams with the required characteristics to the HL-LHC machine and cope with the increased amount of collisions produced in the interaction points, two main upgrade projects come along with the HL-LHC one, namely the LHC Injector Upgrade (LIU) project and an upgrade of the LHC experiments. To design such an upgrade, the HL-LHC project must deal with the constraints imposed by the present LHC configuration i.e. missing free space for inserting new devices, limited flexibility of the cryogenic system and overcome the current luminosity limitations such as radiation-induced damages or inability of components to accommodate higher intensity beams. The HL-LHC upgrade relies on new cutting-edge technologies such as the 11 T superconducting magnets and new cavities, the so-called crab cavities, for optimizing the number of collisions at the interaction points. In order to avoid the saturation of the experimental detectors by a too high number of events per bunch crossing in the interaction points, the luminosity is adjusted to a constant value of 5.32×10^{34} $cm^{-2}sec^{-1}$ over the fill (so-called luminosity levelling). A summary of the main nominal beam and machine parameters for HL-LHC as a proton collider is given in Table 1.2.

1.2 Electron cloud in accelerators

Electron multipacting is a resonant phenomenon resulting from the emission of electrons from surfaces submitted to an oscillating electric field in vacuum [12]. If the synchronism condition is satisfied between emitted electrons and electric field, an avalanche multiplication of electrons can occur, leading to an exponential increase of the electron density in the device [12]. Such a phenomenon is responsible for several adverse effects such as RF component heating, degradation of resonant RF cavities performance or breakdowns leading to component failure or puncture [12]. Electron multipacting is found to occur

in diverse fields including nuclear fusion systems [13], communication satellites [14] or particle accelerators [15]. The latter case, for which this phenomenon is referred to as electron cloud, is discussed in details in the following sections.

1.2.1 Electron cloud mechanisms and history

The first observations of electron cloud related effects in accelerators were made in the mid-60's when beam instabilities were reported at BINP [16]. Later, pressure rises were observed in the CERN's Intersecting Storage Rings (ISR) with the passage of high intensity bunched proton beams [17]. Since then, many signs of the presence of an electron cloud have been reported in different accelerators world-wide, with sometimes dramatic consequences on the machine operations: at RHIC in the USA [18], at KEKB [19] and SuperKEKB [20] in Japan or in the CERN accelerator complex, including in the LHC [21].

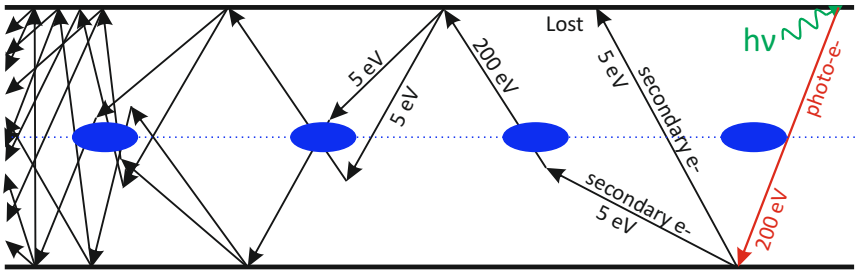

Figure 1.5: Electron cloud build-up mechanisms. Synchrotron radiation impinging on the beam pipe surface (green) stimulates the emission of a photoelectron (red) which gets accelerated by the passing bunch (blue). At its collision with the chamber walls, the surface emits secondary electrons which may in turn be accelerated or get lost. Schematics adapted from [22].

The build-up of an electron cloud in an accelerator beam pipe originates from a cascade phenomenon involving 3 steps, as schematically described in Fig. 1.5:

- **Primary electron generation**

The production of primary electrons inside the beam vacuum chamber results from two mechanisms. Collisions between the residual gas and the proton bunches lead to ionization of gas molecules and emission of electrons. The ionization rate depends on the gas density, the particle flux and the ionization cross section of the gas molecule at the beam energy [23]. In addition, primary electrons are generated by photoelectric effect at the chamber walls, triggered by the impinging synchrotron radiation. The threshold energy required for an incident photon to extract an electron from a material is equal to the work function of the material. The work function of typical technical materials used in the vacuum system of particle accelerators (e.g. copper or stainless steel) is usually between 4 and 5 eV [24]. From the LHC machine and beam parameters (see Table 1.1), the critical energy of the synchrotron radiation emitted by the beam becomes

sufficiently high to enable photo-emission when the protons reach an energy of about 2-3 TeV [23], i.e. during the energy ramp. Because of its ultra-relativistic beam, the LHC is the first proton accelerator where the beam emits significant amount of synchrotron radiation, leading to a non-negligible amount of photoelectrons emitted in the vacuum chamber [25]. Another key quantity of the photo-emission process and thus in the seeding of the primary electrons in the beam pipe is the so-called photoelectron yield of the wall surface which quantifies the number of emitted electrons per incident photon.

- **Primary electron acceleration**

The above-mentioned mechanisms alone are usually not sufficient to produce a significant amount of electrons in the beam vacuum pipe. However, in accelerators operating with closely spaced bunches, the primary electrons generated by the passage of a given bunch may survive in the vacuum chamber until the passage of the following bunch. Each primary electron will then receive a kick induced by the beam potential, whose effect depends on the initial position of the primary electron, the bunch population and distribution [26]. If electrons are far away from the beam, which is the case for photoelectrons assuming a large chamber diameter with respect to the transverse beam dimensions, their interaction with the beam will result in an increase of their transverse momentum by an amount depending on the radial position of the electrons, therefore leading to a global increase of the mean energy of the primary electrons [23].

- **Secondary electron emission**

After acceleration by the beam, primary electrons impinge on the chamber walls with an energy eventually high enough to excite secondary electron emission from the vacuum pipe surface. The number of secondary electrons emitted per incident primary electron defines the Secondary Electron Yield (SEY) of the wall material. The SEY of a surface depends on several parameters such as the surface composition, morphology and history as well as on the energy and angle of incidence of primary electrons [27–33] as it will be discussed in Section 1.3. The SEY of the vacuum chamber walls is a crucial parameter for the development of the electron cloud since it governs the multiplication of primary electrons inside the beam pipe. In a first approximation, for a given primary electron energy, a surface with an SEY below unity will behave as an electron absorber, while it will be an electron multiplier for an SEY above 1. Typical materials encountered in the vacuum system of accelerators have a maximum SEY at machine installation equal or greater than 2 [28,34,35], leading then to an exponential multiplications of the electrons inside the vacuum pipe.

According to these mechanisms, the electron cloud is observed only in machines operating with positively charged beams and became a critical issue with the trend of continuously increasing the beam intensity.

Multiple parameters influence the occurrence and the intensity of the electron cloud such as the presence of a magnetic field, the geometry of the beam vacuum chamber and the secondary electron yield of its inner surface as well as the beam parameters (bunch

intensity, number of bunches...) [36–38]. Among them, the bunch spacing is particularly important, since with closer bunches, the probability of having electrons generated by the bunch N surviving until the passage of the bunch N+1 is greater. Indeed, the time required by an electron of 10 eV to cross a chamber of 5 cm in diameter is about 25 ns. The multipacting process is therefore enhanced.

1.2.2 Impact of electron cloud on accelerator performance and mitigation techniques

Several detrimental effects arise from the presence of an electron cloud in the beam pipe. The interaction between the cloud and the beam itself can lead to single bunch [39] and coupled-bunch [40] instabilities resulting from the coupling of the head to the tail of a single bunch and of the head to the tail of the bunch train, respectively. These instabilities can result in beam emittance growth [22, 23, 39], namely an increase of the beam size, eventually causing beam losses, and translating into a reduction of the luminosity of the machine. In addition, electron bombardment of the inner surface of the vacuum pipe is responsible for pressure increase driven by electron stimulated desorption (ESD) of adsorbed species [18,38,41]. Finally, in the case of machines including cryogenic parts such as the LHC, the power deposited onto the vacuum pipe by electron bombardment has to be dissipated by the cryogenic system, which has a limited capacity [9].

Consequently, various counter-measures have been developed to limit the occurrence of the electron cloud in accelerators. A relevant strategy consists in reducing the number of electrons emitted from the chamber walls by adding clearing (positively biased) electrodes in the beam chamber [42] or reducing the SEY of its inner surface. The latest solution is achieved either by coating the beam pipe surface with a low SEY material such as graphitic carbon or Non-Evaporable Getter (NEG) [43,44] or by roughening the surface, for instance by laser engineering [45]. Another approach relies on the confinement of the emitted electrons to the pipe surface by a magnetic field to prevent them from gaining enough energy from the beam to trigger multipacting [46]. Finally, one can also profit from a spontaneous decrease of the cloud intensity with the operation time of the accelerator. This phenomenon, known as beam conditioning or beam scrubbing, relies on the modification of the beam pipe surface driven by its irradiation by electrons from the cloud itself, as it will be extensively described in this work.

The strategy chosen for the LHC is a combination of several of the above mentioned possibilities. In the room temperature parts of the machine, the beam pipe inner surface is coated with NEG alloy (Ti-Zr-V) [9,44,47] which provides both a large and distributed pumping speed as well as a secondary electron yield below the multipacting threshold of the considered areas [9,48]. However, to behave as a getter pump, the NEG film needs to be activated to dissolve the native oxide layer into the bulk and expose a pure metallic surface to the volume to be pumped. This step requires the *in-situ* heating of the NEG, and thus of the beam pipe itself, for 24 hours at 180 °C [44]. In the cryogenic parts of the LHC such a bake-out is not possible because the vacuum pipe is tightly surrounded by the magnet coils and embedded in the cryostat. Therefore, basing on numerous studies on the conditioning of copper (material of the inner surface of the beam pipe in the

arcs) [49, 50] the mitigation of the detrimental effects of the cloud in the arcs relies on the beam conditioning of the inner surface of the pipe [9].

1.2.3 Electron cloud in the LHC injectors

Observations in the CERN accelerator complex [21, 51] revealed the presence of an electron cloud in both the Proton Synchrotron (PS) and the Super Proton Synchrotron (SPS).

In the PS operating with LHC beams, the beam structure only allows the build-up of an electron cloud in the last part of the cycle, when the bunch length is shortened in view of the beam transfer to the SPS [36, 51]. Indeed, the presence of a cloud was revealed in 2001 as both transverse instabilities and baseline drift in the pick-up signals were observed [52].

In the SPS, pressure rises together with beam instabilities leading to beam losses already occurred in 1999 in the presence of LHC-type beams [53, 54]. Scrubbing runs appeared to be efficient in mitigating the electron cloud, leading to currently unperturbed operation with 25 ns LHC beams [21,51]. However, dedicated studies showed that higher intensity beams, such as the ones required for HL-LHC era, are still strongly suffering from electron cloud effects [55]. In parallel, efforts were put to identify the critical parts of the machine in terms of electron cloud build-up to define a mitigation strategy [21]. It was finally decided to rely both on coating the inner surface of the critical parts with amorphous carbon (low SEY) films and on scrubbing of the rest of the machine for the HL-LHC era [56]. *In-situ* amorphous carbon coatings have already been successfully implemented [57] and a stepwise deployment will continue up to LS3 included.

Both the PS and the SPS are hosting several electron cloud measurements and characterisation devices such as strip monitors allowing for transversally resolved electron cloud observations [37], *in-situ* SEY measurement set-up [38] or cryogenic test bench [58, 59]. For the current understanding of the electron cloud phenomenon in the CERN's accelerator complex and in the frame of the HL-LHC and LIU projects, these tools are of primary importance as they allow for better understanding of the electron cloud mechanisms and dependencies [37], validation of mitigation techniques [43, 45] in particular in cold conditions, for LHC applications [60, 61].

1.2.4 Electron cloud observations and simulations in the LHC

1.2.4.1 LHC vacuum system in the arcs

LHC beam vacuum requirements are driven by beam lifetime and by minimisation of background noise for the experiments [9]. The lifetime associated with vacuum, i.e. related to the loss of protons by scattering on the residual gas, is set to 100 h corresponding to a hydrogen pressure of 6.7×10^{-10} mbar at 5 K. In addition, constraints of beam stability set the limits for longitudinal and transverse impedance, therefore adding further constraints on the choice of the materials of the vacuum system walls [9].

In the room temperature field-free regions, the vacuum system consists in 7-m-long OFS copper chambers with an inner Ti-Zr-V NEG coating which provides a large and

distributed pumping speed as well as a low secondary electron yield [9, 44, 48].

In the cold regions, mainly constituted by the arcs, additional constraints originate from the cryogenic environment. The beam vacuum system is indeed embedded in the superconducting coil, inside the cryostat filled with liquid helium at 1.9 K. Several sources of beam-induced heat load on the supercritical helium circuit have been identified (values for nominal machine parameters) [9]:

- Beam emitted synchrotron radiation (0.2 W/m/beam)
- Energy loss by nuclear scattering on the residual gas (30 mW/m/beam)
- Image currents (impedance) (0.2 W/m/beam)
- Electron cloud (deposited power depends in particular on the SEY of the beam pipe surface)

Dissipating the associated powers at 1.9 K would require a considerable cooling capacity. Therefore, to held the cryogenic budget in reasonable value, a beam screen operating at 5-20 K is inserted into the 1.9 K cold bore [62] to intercept the beam-induced heat loads. A schematic of the resulting design is given in Fig. 1.6.

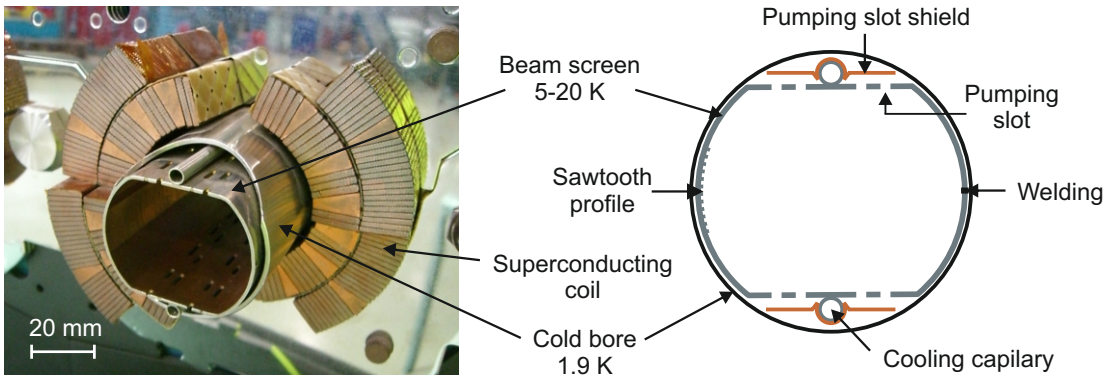

Figure 1.6: LHC vacuum system for one beam in a LHC arc dipole: view of one beam pipe in a LHC cryo-dipole (left) and corresponding schematic (right).

Each beam is circulating in its own vacuum pipe from one arc extremity to the other. For each beam, the austenitic steel cold bore (inner diameter: 50 mm) is located in the center of the corresponding superconducting magnet coil, in direct contact with the 1.9 K helium bath. The inner surface of the cold bore is therefore an extremely efficient cryo-pump, providing the pumping capacity necessary to fulfil the beam lifetime requirements [63].

The racetrack-shape beam screen, 36.8 mm and 46.4 mm of vertical and horizontal apertures respectively, is inserted into the cold bore. A low resistivity of the inner beam screen wall, required to limit heat load associated with circulating image currents, is achieved by colaminating a 75 µm thick OFE copper sheet (inner beam screen surface) onto a 1 mm thick stainless steel plate specially developed to fit the magnetic constraints.

A sawtooth structure, rolled onto the external (with respect to beam orbit) copper side of the beam screen, absorbs the synchrotron radiation at normal incidence, therefore limiting the amount of reflected photons. Pumping slots, permitting to gas molecules desorbed from the inner surface of the beam screen to get condensed onto the cold bore, are then punched into the top and bottom sides of the screen. The resulting beam screen transparency of 4% [47] allows to efficiently screen the cold bore from particle bombardment which would induce large gas desorption and drive a pressure instability, while taking profit from its massive pumping capacity. The final racetrack shape is obtained by rolling and closing the 2-layer sheet by a longitudinal welding. Two capillaries laser-welded on top and bottom of the pipe carry the liquid helium for the active cooling of the beam screen.

Finally, copper beryllium shields clipped on the beam screen helium capillaries intercept any electrons from the cloud escaping through the pumping slots, preventing them to deposit heat load onto the cold bore or desorb the accumulated gas.

The 15.6 m long cold bore - beam screen assemblies of each arc dipole (5.8 to 7 m in the case of quadrupole) are connected to the neighbouring ones through the so-called Plug-In Modules (PIM), designed to guaranty the electrical conductivity and to compensate for contraction and expansion of adjacent beam pipes during thermal cycles of the machine [9].

In addition to a specific design, the LHC beam vacuum quality in the arcs relies on a particular commissioning and operation scenario. The pump-down of the machine, first by Roots pumps from atmosphere to 10^{-1} mbar, then by turbo pumping groups including primary oil pumps, allows to reach a pressure in the 10^{-4} mbar after several weeks of pumping. At that level, the cool-down of the cryostat starts, but no liquid helium is flown in the beam screen capillaries. The active cool-down of the beam screen only starts when the cold bore is at about 20 K [9]. This precise scheme ensures that most of the gas species are mainly condensed onto the cold bore, therefore minimising the gas coverage of the beam screen copper surface. However, even with these precautions, beam scrubbing, namely beam screen surface conditioning induced by the beam itself, is required to meet the beam vacuum requirements [9].

1.2.4.2 LHC observations

Analytical studies and simulations performed in the late 90's led to the conclusion that the LHC will suffer from electron cloud effects [15, 64]. In particular, the expected electron density inside the beam pipe, resulting from electron multipacting, was shown to be high enough to trigger beam instabilities [15], and to be a concern in terms of pressure rise through electron stimulated desorption and heat load on the cryogenic system [15, 64]. Following these studies, a crash program was launched at CERN in 1997 to deeper investigate the electron cloud effect in the LHC and develop mitigation techniques [65].

As expected, the first signs of the presence of an electron cloud in the LHC appeared in 2010 when pressure rises were observed in the common vacuum chambers close to the Interaction Regions, while operating beams with bunch spacing of 150 ns [66]. Later

in the year, the presence of the cloud was observed through emittance growth and beam losses at 75 and 50 ns bunch spacing [66]. In addition, heat load exceeding the estimations for synchrotron radiation and impedance contributions alone was measured with 50 ns beams. Owing on the scrubbing accumulated along Run 1 and on optimization of machine parameters, the LHC could operate with 75 ns and later with 50 ns beams without suffering electron cloud effects [67, 68], but effects on the beam remain visible at 25 ns [68].

Because of the full LHC machine venting during LS1, leading to a reset of the conditioning state of the beam screens, electron cloud became again visible with 50 ns beams at the resuming of operation for Run 2 in 2015 [69]. The situation improved during the dedicated scrubbing run, mainly performed with 25 ns beams, but large beam screen temperature transients with a risk of loosing the cryo-conditions were limiting the intensity ramp-up [69]. Further scrubbing and machine parameters tuning were required to finally inject 2244 bunches with 1.2×10^{11} protons/bunch at 25 ns by the end of the year, while staying within the limits of the cooling capacity [69]. At that time, a strong scattering was observed in the average heat load between the different sectors [69].

Since 2016, effects of the cloud on the beam itself do not prevent stable beam operations, but slow beam degradation is visible along the fill, mainly through beam losses and emittance blow-up [70]. In parallel, pressure rises are still observed during the beam energy ramp-up [71], but do not impact beam operation: a good beam vacuum quality is currently achieved in the different parts of the machine thanks to accumulated beam scrubbing [47, 71].

The main electron cloud related concern remains thus the heat load deposited on the cryogenic system through the electron bombardment of the beam screen. Indeed, despite the upgrade of the cryogenic control system to cope with the large heat load transients present during beam injection, energy ramp and beam dump and eventually leading to loss of cryo-conditions [72], the average heat load of some LHC arcs is very close to the limit of the design cooling capacity [70]. Although, since 2016, the maximum intensity which is possible to inject into the LHC is limited by other factors than the electron cloud [73, 74], the LHC beam induced heat load presents some specificities with respect to its value, its spacial distribution and its evolution over time which are of concern for the achievable LHC and HL-LHC performance. The key characteristics of the LHC beam-induced heat load are given here below. A more detailed description of the heat loads on the LHC arc beam screens during Run 2 is given in Ref. [75].

- **Spatial distribution**

The measurement of the thermodynamic properties of liquid helium at the inlet and outlet of the beam screen cooling circuit for each LHC arc half-cell allows to infer the total deposited heat load in each half-cell. A picture of the LHC heat load situation in 2018 is given in Fig.1.7 which shows the normalized heat load distribution over the 46 half-cells of each of the 8 arcs, for injection (450 GeV) and top energy (6.5 TeV). From these measurements, it appears that the heat load is inhomogeneous along the ring at different scales.

Indeed, even if the 8 arcs are identical by design, the machine appears to be split into two parts: arcs 34, 45, 56 and 67 have an average heat load of about 1.2×10^{-13} Watt/half-cell/proton against around 2×10^{-13} Watt/half-cell/proton for arcs 12, 23, 78 and 81 at 6.5 TeV. For all arcs, the heat load is significantly higher than the estimated values for impedance and synchrotron radiation contributions alone. In addition, the spread of the heat load distribution over the half-cells of a given arc is much wider for the high heat load arcs than for the low heat load ones, both at injection and top energy.

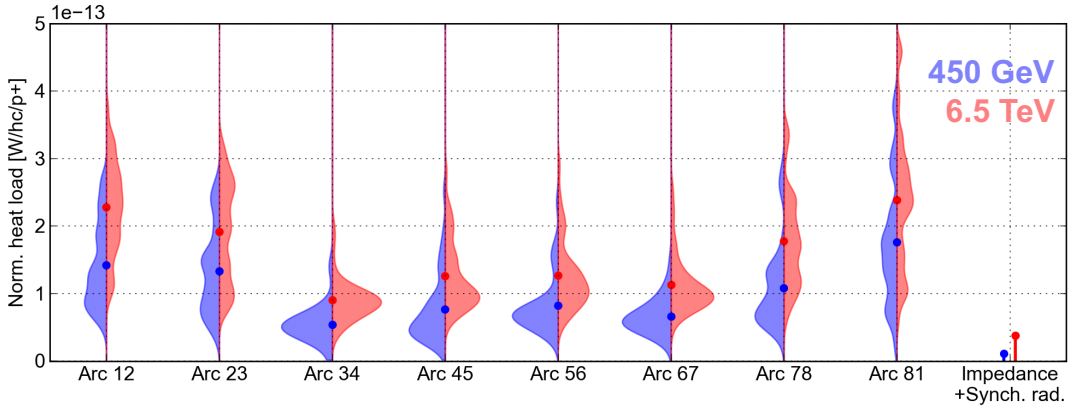

Figure 1.7: Measured heat load in the LHC in 2018 (fill 6674, 25 ns, 2556 bunches/ beam, 2 beams) [76]. For each arc of the machine, the average normalized heat load distribution in Watt/half-cell/proton over the 46 half-cells is plotted at injection (450 GeV) and top energy (6.5 TeV). The average heat load of the arcs is given by the coloured dots. The heat load associated with impedance and synchrotron radiation is given for comparison.

The spacial resolution of the LHC heat load is usually limited to the scale of the half-cell, since sensors are only located at the beam screen helium circuit inlet and outlet of each half-cell. However, 4 half-cells, located in arc 12 and 45, have been instrumented, i.e. additional temperature sensors were added on the beam screens in the interconnection between magnets. Therefore, for these particular places, the heat load can be inferred for each aperture of each magnet of the half-cell. The heat load values for the 4 instrumented half-cells are given in Fig. 1.8. Within a half-cell, the heat load difference between magnets can be as high as a factor 10, and the total heat load of a given magnet is not always equally shared by the two beam apertures.

The spatial distribution of the heat load in the LHC is thus exhibiting strong inhomogeneities along the ring: between arcs, between half-cells, between magnets and between the two beam apertures.

- **History of the heat load distribution**

Fig. 1.9 shows the evolution of the average heat load per arc during a fill in 2012 (end of Run 1, test period with 25 ns beams) and a similar one during Run 2 in 2018. As expected from machine design, the heat load curves are overlapping for all arcs in 2012, witnessing a very uniform heat load distribution over the machine. In 2018, low heat load arcs (arcs 34, 45, 56 and 67) are found at the same level as before LS1, while

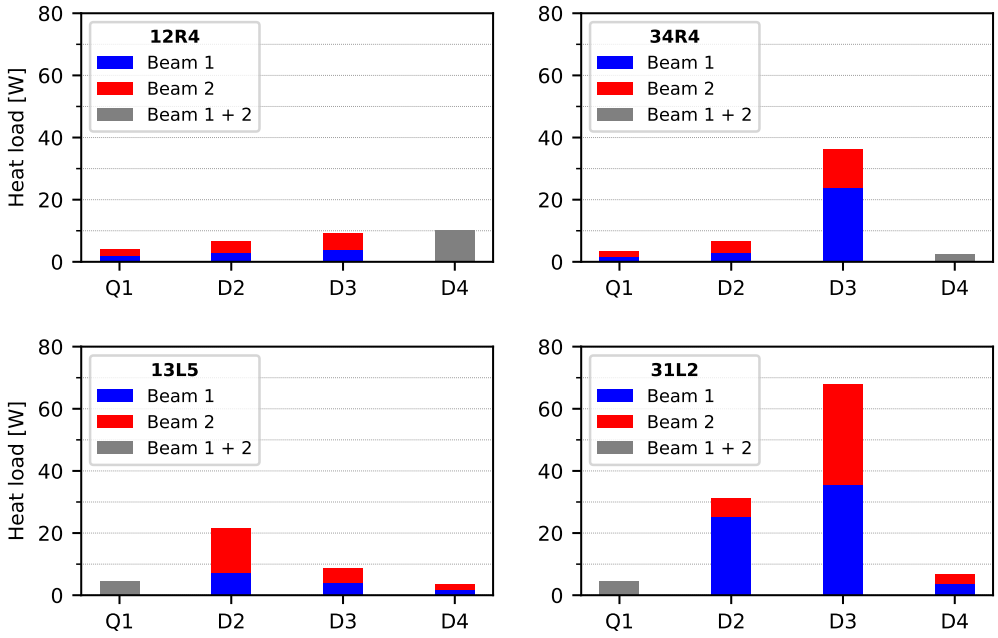

Figure 1.8: Measured heat load in the four LHC instrumented half-cells: half-cells 12R4, 34R4 and 13L5 in arc 45 and 31L2 in arc 12. For each magnet (dipole D and quadrupole Q), the heat load associated with beam 1 and beam 2 is given in blue and red respectively. When the distinction between the two beams is not possible due to the position of the sensors, the total heat load of the magnet is given in grey. Courtesy of B. Bradu.

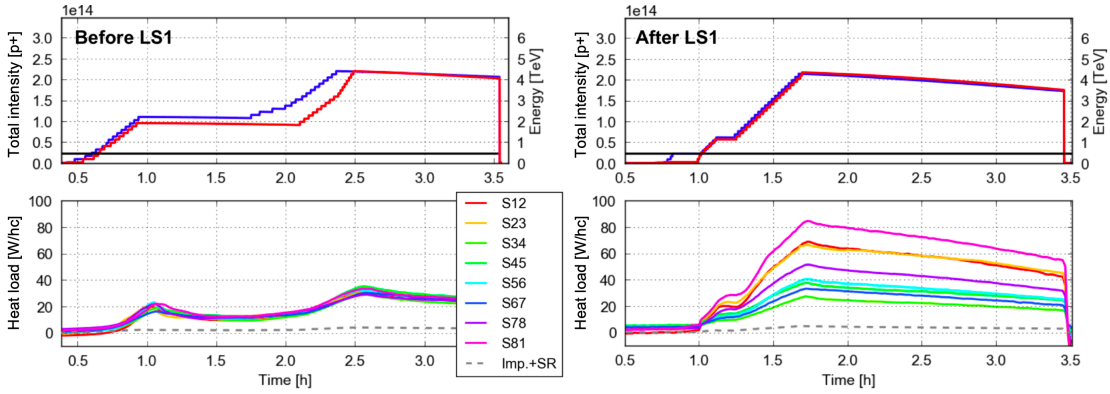

Figure 1.9: Beam intensities and energy (top) and average heat load per arc (bottom) for a fill at the end of Run 1 in 2012 (left) and during Run 2 in 2018 (right) [70]. The two fills have similar characteristics, in particular 25 ns beams of same intensity.

the heat load of arcs 12, 23, 78 and 81 increased up to a factor of 3. Such a dispersion was already observed at the resuming of operations in 2015 [69], thus suggesting it to be a consequence of LS1.

- **Conditioning effect**

The evolution of the average normalized heat load per arc during Run 2 is shown in Fig. 1.10. A clear conditioning effect, visible through the decrease of the measured heat load, is observed over time or fill number for 2015 and 2016, and mainly saturates for

the rest of the Run. The different sectors clearly saturate at different heat load levels. Even after years of accumulated scrubbing dose, conditioning does not have any impact on the heat load dispersion between arcs: the spread between the different parts of the machine remains constant over Run 2. The deconditioning of arc 12 due to its venting during EYETS 2016-2017 is clearly visible as its associated heat load at the begining of 2017 is significantly higher than at the end of 2016. Its reconditioning when resuming operations in 2017 is efficient, but the sector reaches the same high heat load saturation value as before its venting.

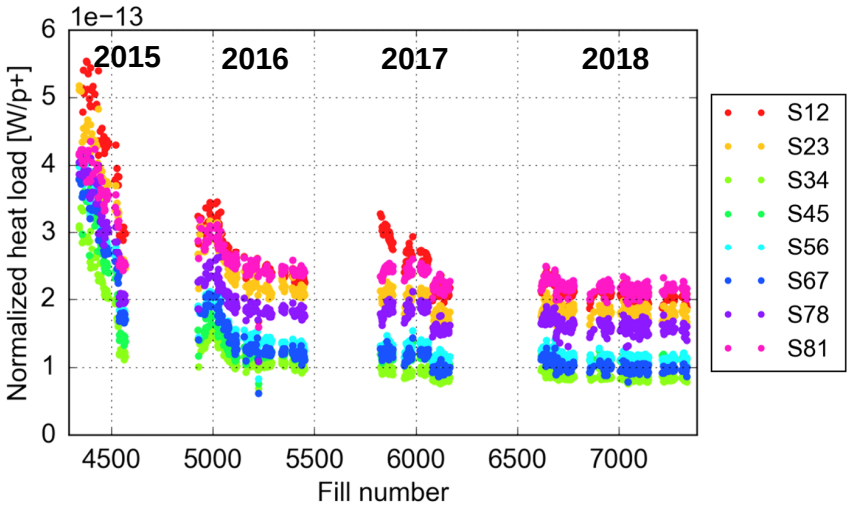

Figure 1.10: Evolution of the average normalized heat load per arc in the LHC during Run 2 [70].

1.2.4.3 Electron cloud simulations for the LHC

Electron cloud simulation studies for the LHC started at CERN in 1997, as a consequence of analytical studies foreseeing the development of a cloud inside the LHC [15, 22]. Simulations are currently performed using the 2D PyECLOUD code, which simulates the electron cloud in a thin slice located at a given position along the accelerator [36, 77]. To limit the computational load, electrons are grouped in macro-particles (MP) whose dynamics is simulated by the code in several phases for each time step.

First, seeds are generated in the beam pipe as a results of residual gas ionization and photoemission induced by the passing bunch slice. Then, the fields associated with both the beam and the cloud and acting on the MP are computed, and the motion of each MP (position and momenta) is deduced accordingly. Finally, at each impact of a MP with the pipe wall, secondary electrons are generated according to a model for energy and angular distribution. A detailed description of the modelling and simulation of electron cloud build-up with PyECLOUD can be found in Ref. [36].

In the following, the main properties of the electron cloud developing in the LHC arcs are given, as obtained by PyECLOUD simulations. A complete study of the electron cloud phenomenon in the CERN accelerator complex is available in Ref. [36].

- **Multipacting threshold**

The evolution of the normalized heat load as a function of the maximum SEY of the beam screen surface is given in Fig. 1.11 for LHC arc dipole and quadrupole. For the two magnets, the heat load evolution clearly exhibits a SEY threshold (about 1.05 for the quadrupole and 1.25 for the dipole for a bunch population of 1.1×10^{11} protons/bunch). When the SEY of each magnet is above the respective threshold, and taking into account the length of each element of the half-cell, the dipoles are the main contributors to the total half-cell heat load.

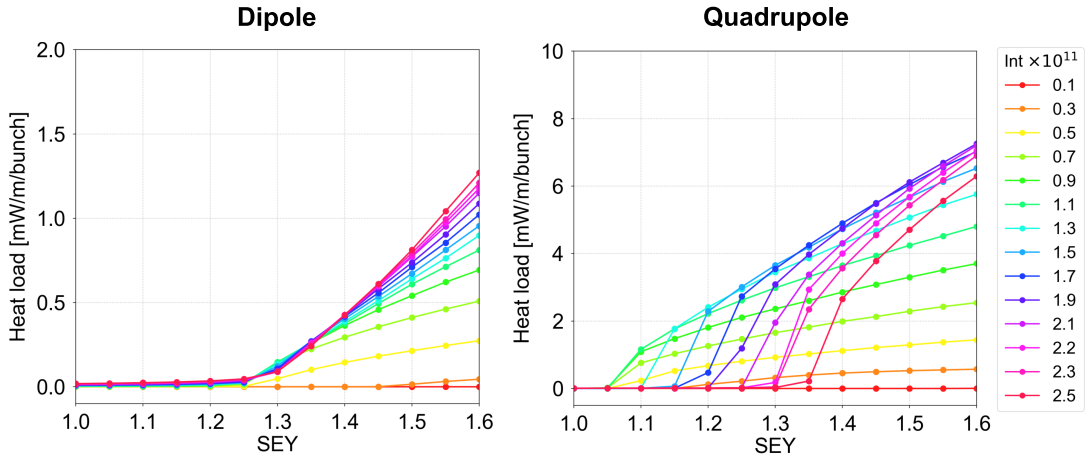

Figure 1.11: Evolution of the normalized heat load as a function of the maximum SEY of the beam pipe surface for LHC arc dipole (left) and quadrupole (right) for different bunch intensities [78]. Simulations for 25 ns bunch spacing and 7 TeV.

- **Electron cloud density distribution**

The electron cloud density distributions simulated for a field-free region, a LHC arc dipole and a LHC arc quadrupole are shown in Fig. 1.12. From these snapshots, it is evident that the presence of a magnetic field and its type both play a major role in the density distribution.

In an LHC dipole field (0.54 T at injection, 8.33 T at 7 TeV [9]), the Larmor radius of a 20 eV electron decreases from 28 µm at injection to about 2 µm at top energy. Therefore, electrons generated on the bent (welding and sawtooth) sides of the beam screen are almost not accelerated by the beam potential, but are immediately deflected and hit the pipe wall again, without energy gain. Therefore, these electrons do not contribute to multipacting, leading to a low electron density close to the bent beam screen sides (Fig. 1.12 (center)). In addition, the electrons the closest to the beam, i.e. emitted in a central stripe (around x = 0 mm in the case of Fig. 1.12 (center)) receive the highest kick, which eventually increases their energy in a range where the secondary electron yield of the beam screen surface is already less than its maximum (see Section 1.3.1 and Fig. 1.16). Multipacting efficiency is therefore not maximum. However, for electrons emitted further away from the beam, the energy gained may

correspond to the one where the SEY is maximum, leading thus to a strong electron multipacting and a high electron density. The confinement of the electron cloud in two stripes separated by a depleted central region is thus the result of the combined effects of the beam field, the magnet field and the energy dependence of the SEY. Because of the increased kick provided by the beam to the electrons, the size of the depleted zone increases when increasing the bunch intensity, as shown in Fig. 1.13. Accordingly, the electron bombarded beam screen regions change over a physics fill duration, as a result of beam intensity decrease driven by proton losses in collisions. In Fig. 1.13, the effect of synchrotron radiation inducing photoemission is clearly visible as the scrubbing current at | x | >15 mm (i.e. on the bent sides, see Fig. 1.12) is significantly higher at 7 TeV.

Confinement of the electrons by the magnetic field is also observed inside an LHC arc quadrupole (Fig.1.12 (right)).

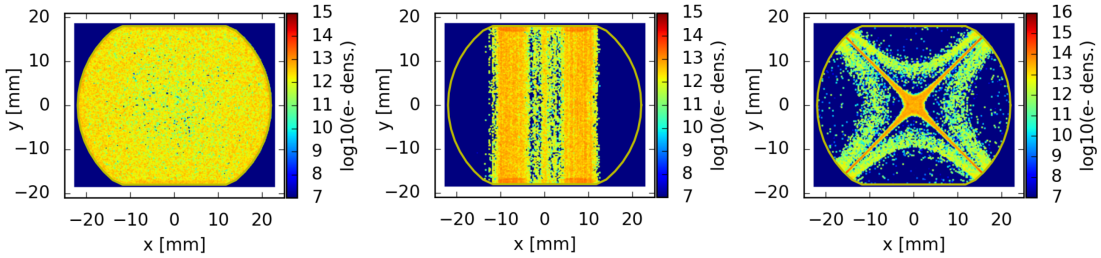

Figure 1.12: Electron cloud density distributions in a field-free region (left), a dipole (center) and in a quadrupole (right) in a LHC arc half-cell [79].

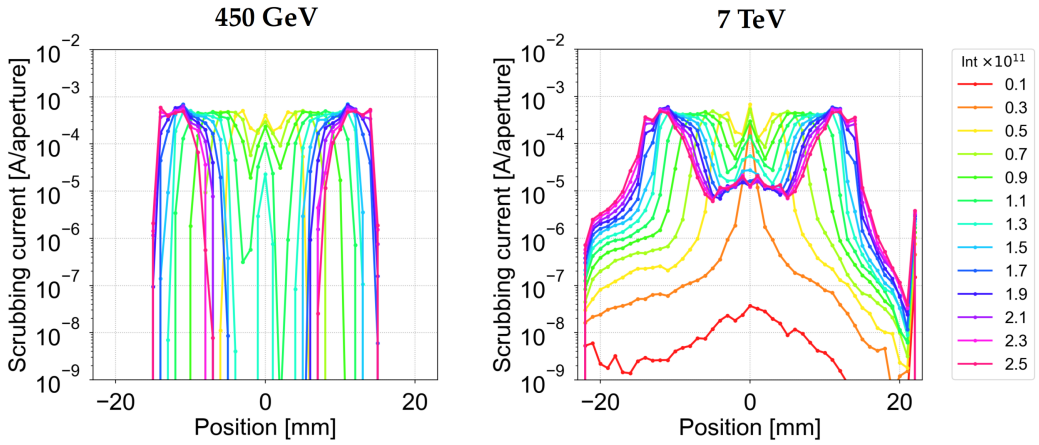

Figure 1.13: Transverse distribution of the electron scrubbing current (with E >20 eV) in an arc dipole, for injection and top energy and different bunch intensities [78]. Simulations for 25 ns bunch spacing and SEY = 1.5. The x axes correspond to the one in Fig. 1.12.

- **Energy spectrum of the electrons**

The normalized energy spectrum of the electrons impacting the beam screen walls exhibits two components, as shown in Fig. 1.14 for a dipole at 7 TeV. The low energy

peak, which constitutes the main population, corresponds to electrons reaching the wall without having been accelerated by a proton bunch. The higher energy bump, whose position depends on the bunch intensity, is related to electrons actually accelerated by the beam and contributing to multipacting [36]. The knowledge of the energy spectrum of the electrons at their impact with the beam screen wall is a key for the understanding of the machine conditioning, since it is known that conditioning effect is energy dependent [31] (see Section 1.3.2).

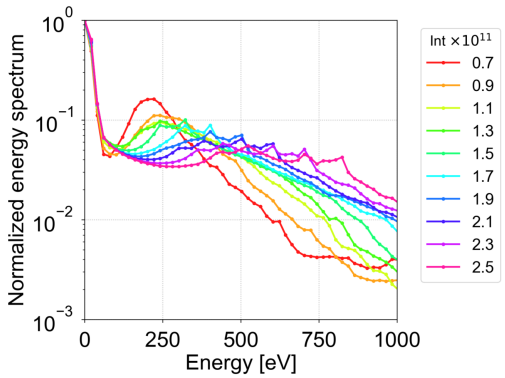

Figure 1.14: Normalized energy spectrum of electrons impacting the beam pipe in a LHC arc dipole magnet, for different bunch intensities [78]. Simulations for 25 ns bunch spacing, 7 TeV.

1.2.4.4 Consequences and CERN's action plan in view of HL-LHC

During its High-Luminosity era, the LHC machine will be operating with higher intensity beams. Consequently, the dynamic heat loads associated with impedance and synchrotron radiation will significanly increase [7]. According to dedicated machine development studies and simulations of the electron cloud induced heat load, the electron cloud contribution to heat load of the high luminosity beams is expected to only mildly increase [78, 80]. However, since the cryo-capacity will not be increased during the HL-LHC upgrade, the margins available for coping with the electron cloud will be drastically reduced after subtraction of the impedance and synchrotron radiation contributions from the cryo-capacity [70, 80]. In particular, for the high heat load sectors, these margins are expected to be insufficient to survive the intensity increase [70, 80].

Since the current picture of the LHC beam induced heat load is not understood and is expected to be a major limitation for the operation of the HL-LHC machine in terms of cryogenics, CERN set up an inter-departmental task force at the end of 2017 to investigate the origin of the observed heat loads in the LHC [81].

In addition of confirming the change of heat load situation consecutively to LS1, other origins of the heat load beyond the electron cloud were considered: heating by electromagnetic coupling (impedance), beam losses, ion bombardment or radiation [70]. All of these hypotheses, except a heating induced by electron cloud effect, could be discarded by studying the dependence of the heat load on beam parameters and on the beam loss monitor recordings [70, 82]. The possibility of a cryogenic measurement artefact was also considered. The possible errors were carefully evaluated and when possible

the cryogenic equipments were re-calibrated [82], confirming the initial observations. The electron cloud is thus currently considered as the most probable responsible for the observed heat load.

Under this hypothesis, the observed heat load dispersion translates into strong dispersion in terms of electron cloud activity along the LHC ring. Therefore, efforts were dedicated to the identification of the source of this scattering. Available information about the production, cleaning, testing and installation of the vacuum components (e.g. production batch of the raw material, installation sequence etc.) as well as the sequence and the nature of the works performed in the different parts of the accelerator during LS1 were gathered. However, no correlation could be found between the history of a given location of the ring and its associated heat load [82].

In parallel, the hypothesis of a beam screen surface modification hindering its proper conditioning and leading to a high electron cloud activity was proposed. This hypothesis was tested by laboratory experiments, and when the opportunity arose, by direct surface analysis of LHC extracted beam screens. The present work will report on those aspects.

Finally, the task force proposed the implementation of additional diagnostic tools, as the cryogenic monitoring of additional half-cells at single magnet resolution, improved sector cryogenic monitoring and a campaign of electron cloud density measurement by microwave transmission [83–85]. The deployment of these additional tools started during the LS2.

1.3 Surface science and electron cloud

As for the LHC, several other accelerators and devices rely on conditioning to safely operate with respect to electron multipacting effect [9,18,86–88]. In the frame of electron cloud issues in particle accelerators, the behaviour of technical surfaces under electron bombardment, in particular the evolution of their secondary electron emission properties, has been extensively studied [31, 33, 35, 89–96], to predict, understand and control the operation of the machines.

This part describes the key points of secondary electron emission and of the current understanding of the conditioning phenomenon, both applied to the case of particle accelerators.

1.3.1 Secondary electron emission

Bombardment of a solid by an electron flux triggers a cascade of phenomena at its surface, eventually leading to the emission of secondary electrons. The different varieties of interaction between primary electrons and the target result in several types of emitted electrons, which may be distinguished by acquiring their energy distribution [97].

The energy spectrum of sputter-cleaned copper under 97 eV electron irradiation is given in Fig. 1.15. In the conventional approach, the main part of the distribution consists of low energy electrons, emitted through interactions between incident electrons and electrons from the material itself. These electrons are referred to as *true secondary* electrons. The peak located at the same energy as the incident electrons corresponds

to elastically reflected electrons, i.e. primary electrons reflected without energy loss. Between the two main peaks are found inelastically reflected electrons, namely backscattered primary electrons having suffered energy loss. When the energy of the incident electron decreases, the different contributions tend to overlap and a clear distinction between the different mechanisms is no longer possible [98].

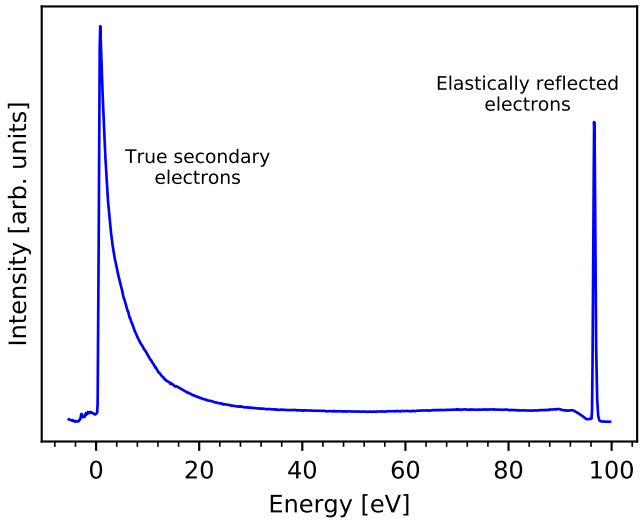

Figure 1.15: Energy distribution of electrons emitted from a sputter-cleaned copper sample under bombardment by 97 eV electrons at 50° incidence angle.

In the case of electron cloud, all the electrons emitted by a solid upon primary irradiation will contribute to the cloud regardless their production mechanism. Therefore, in this work, all emitted electrons are gathered under the term *secondary* electrons:

$$I_{sec} = I_{true\,sec} + I_{reflected} \tag{1.4}$$

Accordingly, we define the secondary electron yield δ at a primary energy E as the total number of emitted electrons per incident one:

$$\delta(E) = \frac{I_{sec}(E)}{I_{prim}(E)} \tag{1.5}$$

A secondary electron yield curve acquired on cuprous oxide Cu_2O is given in Fig. 1.16. The curve clearly exhibits an energy dependence of the yield and can be described by 4 parameters:

- the maximum secondary electron yield δ_{max}
- the energy E_{max} at which δ_{max} occurs
- the crossover energies E_I (resp. E_{II}) defined as the energy below (resp. above) which the SEY is less than unity

The phenomenological theory on secondary electron emission proposed by Salow and Bruining and later developed by Dekker, Dionne and others [99–102] describes the

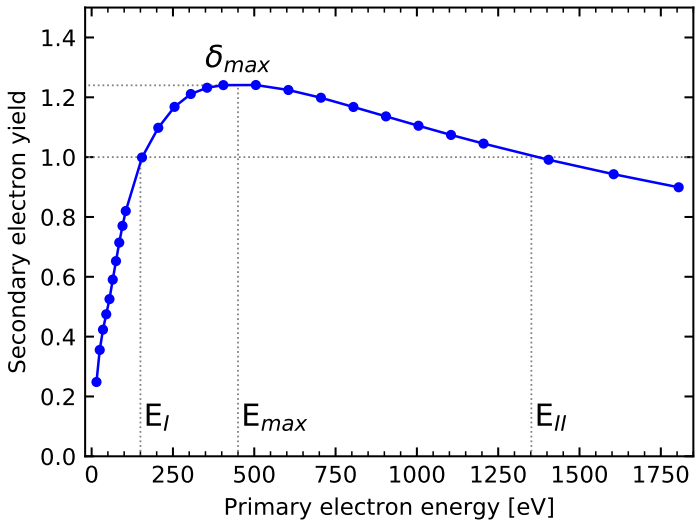

Figure 1.16: Secondary electron yield of cuprous oxide Cu_2O between 10 and 1800 eV of primary energy.

emission phenomenon as the results of three steps: production of the secondary electrons within the material, their transport to the surface and their escape from the surface. In this description, the value of δ as well as the different above-mentioned parameters are related to bulk material and surface properties such as surface barrier potential, material density and conductivity [102]. The escape depth of the secondaries is closely related to both their elastic and inelastic mean free paths, the latter in turn depends on the channels for electron energy loss. In the case of conductors, an efficient way of energy dissipation is through electron-electron interactions. In the case of insulators, this possibility is restrained due to the presence of a band gap, leading to a larger inelastic mean free path [102] and thus a greater escape depth of the secondaries. This explains in particular why insulators tend to have greater yields than metals [102, 103]. Finally, an electron has to overcome the vacuum barrier to be effectively released from the solid. In the case of a metal, this barrier is called the work function, and is typically about 3-5 eV. For semi-conductors and insulators, this barrier corresponds to the sum of the band gap and electron affinity. The latter is usually around unity, while the gap can vary between 1 and 10 eV [102].

This three step model also allows to explain the SEY curve shape. Starting from low energy, an increase of the primary energy translates into more energy available for producing secondaries, and therefore an increasing SEY. However, rising the energy also increases the penetration depth of the primaries, which end up exciting secondaries at a depth where they can no longer escape the solid. A decreasing yield is thus observed above a primary energy E_{max} which depends on the balance between the penetration and escape depths of primaries and secondaries, respectively.

The mean escape depth of secondaries has been evaluated to 0.5-1.5 nm for metals [104]. Therefore, secondary electron emission is a very surface sensitive process. This is confirmed by the observed increased yield while varying the angle of incidence of primary electrons onto the surface from normal to grazing [99]. Accordingly, the SEY of

a material does not only depend on the bulk material itself, but is strongly influenced by its surface state. The presence of adsorbed atoms/layers or surface oxidation is indeed known to modify the yield of the bare material through a modification of the escape probability of the secondaries or of the reflection coefficient for instance [27, 29, 99, 105].

Finally, the surface structure is also observed to play an important role on the secondary electron yield. Indeed, when a secondary electron escapes from a smooth surface, it is directly released into vacuum. For a rough surface, the leaving secondary electron may encounter obstacles and be recollected by the surrounding walls, therefore reducing the effective SEY [99].

In the case of particle accelerator beam pipes, as the secondary electron yield of a material depends also on its surface properties, it may significantly be affected by the material history such as manufacturing and cleaning steps, storage conditions or bombardment by particles such as electrons, as discussed in the next section.

1.3.2 Conditioning by electron irradiation

During the production and installation of the vacuum parts of an accelerator, the inner surface of the beam pipes is exposed to air. Even though the pipes are carefully cleaned before installation to ensure their (ultra-high) vacuum (UHV) compatibility, the resulting surface consists in a layered structure including oxides, hydroxides, carbonaceous species and other adsorbates on top of the bulk material [106–108]. Many of these chemical components are known to increase the secondary electron yield of the bulk material [27, 29, 34, 105] and some are desorbed under electron irradiation [89, 94, 109], leading thus to a high electron cloud activity and pressure rises during machine operation.

Fortunately, electron bombardment of the inner surface of the beam pipes is also responsible for an advantageous effect called conditioning and which results in the vanishing of the detrimental effects of the cloud itself. Therefore, as a potential remedy against the adverse effects of electron multipacting, conditioning of surfaces by electron bombardment has been extensively studied in the laboratory in the last decades, in particular in the context of electron cloud effect in accelerator [31, 33, 35, 89–96].

Several characteristic surface modifications have been observed to occur during electron irradiation. First, the secondary electron yield of several materials used in accelerators is found to decrease under electron bombardment [31, 89, 96, 110, 111]. Typical conditioning curves, i.e. evolution of the maxiumum SEY with respect to electron irradiation dose, of air exposed LHC beam screen samples are given in Fig. 1.17 from Ref. [31] for different energies of bombarding electrons. For impinging energies above 200 eV, it is seen that the maximum SEY of the sample decreases from an initial value around 2.1 down to an ultimate SEY (maximum SEY at the saturation of the decrease) of about 1.1. The saturation of the SEY decrease is obtained for doses higher than 5 x 10^{-3} C/mm^2. SEY decrease has also been observed during conditioning of stainless steel, TiN coating on aluminium, and other metals [89, 96, 111–113], even though the initial and ultimate SEY differ depending on the material. In the frame of electron cloud issues in the LHC, conditioning of copper at cryogenic temperature has also been performed [47, 50, 114] showing a similar SEY decrease as at room temperature.

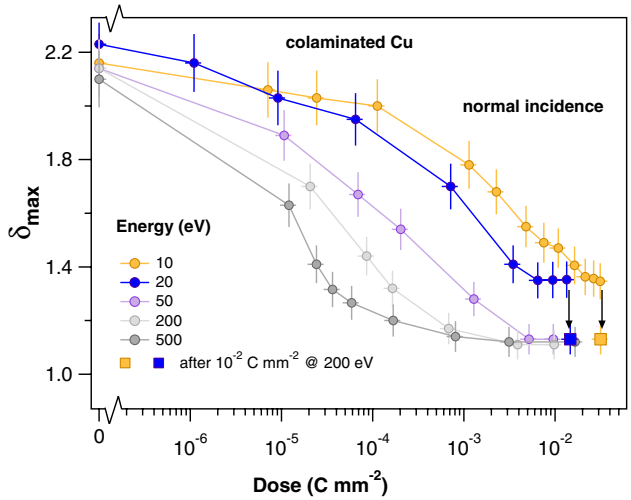

Figure 1.17: Evolution of the maximum SEY δ_{max} of LHC beam screen copper samples as a function of the electron irradiation dose, for different energies of the bombarding electrons, from Ref. [31].

In the particular case of copper, which is the main material of interest in this work, several chemical surface modifications have been observed which may be responsible for the corresponding SEY decrease.

Surface cleaning by electron stimulated desorption has been reported by several studies [94, 109], and is visible through the at least partial removal of some surface contaminants such as carbon containing species and oxidation products of copper [31, 89]. It is known that such chemical compounds tend to increase the SEY of the bare copper surface [27, 29, 105]. Therefore, part of the SEY decrease occurring during electron bombardment can be ascribed to the removal of these products. However, this cleaning process is believed to be dominant only for low irradiation dose, since the released gas quantity from the surface is observed to progress much more slowly for high irradiation doses than at the beginning of conditioning [94]. In addition, neither the native copper oxide Cu_2O nor a pure metallic copper surface exhibit a maximum SEY as low as the one observed after the conditioning of air exposed copper [28, 29, 33, 115]. Accordingly, surface cleaning alone cannot be held responsible for the full SEY decrease observed during conditioning.

Indeed, carbon graphitization, i.e. transformation of the chemical environment of carbon from sp^3 to sp^2 (graphite-like) hybridization state, is also observed during electron irradiation [31, 33, 89, 95]. The secondary electron yield of highly oriented pyrolytic graphite (HOPG, purely sp^2 carbon) has been measured to be as low as 1.05 [31]. The modification of the adventitious carbon layer into a more graphitic one has thus been proposed as an explanation to the low SEY obtained for a fully conditioned air exposed copper surface [31]. Furthermore, it has been shown that the higher ultimate SEY obtained for conditioning at energy below 20 eV (Fig. 1.17) is due to the incomplete graphitization of the carbon layer [31]. These results suggest an energy threshold for this chemical transformation leading to an energy dependence of the scrubbing efficiency.

Moreover, some authors reported carbon layer growth on the surface of electron

irradiated copper [33, 89, 90, 95]. Different hypothesis have been proposed concerning the origin and the mechanisms of such a phenomenon, including surface and bulk diffusion [89, 95], electron stimulated adsorption of carbon-containing gas molecules [33] and deposition of molecular fragments produced in the electron gun used for conditioning [90]. However, the origin of this additional carbon layer is not yet fully understood, even though found to be necessary by some authors to decrease the SEY of air exposed copper to the observed values [89].

Finally, several *in-situ* experiments involving samples directly exposed to beams confirmed the SEY decrease of several materials, including copper, under electron bombardment in accelerator environment [91–93, 116, 117]. However, only few studies report on the associated surface chemical modifications. For aluminium and TiN coating [92], surface carbon amount was observed to decrease. On an other hand, surface analysis performed on stainless steel beam chambers after their extraction from the CERN SPS and air exposure clearly evidenced the carbon nature of the black stripe visible in the pipes [118]. These results suggest disparities of electron cloud induced surface modifications depending either on the material and/or the environment.

In the case of the LHC, no SEY measurement neither surface analysis set-ups are available *in-situ*. Therefore, no quantitative assessment of the current or of the evolution of the *in-situ* surface state during machine operation can be done. The machine state with respect to electron cloud is thus only inferred from heat load and pressure measurements as well as from the cloud effects on the beams.

1.4 Aim and strategy of the study

Under the hypothesis of electron cloud being at the origin of the abnormal LHC beam induced heat load, the vacuum system of the LHC arcs is far from reaching the expected ultimate SEY value. Such a behaviour would potentially limit the performance of the High Luminosity upgrade of the machine. Accordingly, efforts are currently being made to understand the origin of this unexpected heat load pattern, as a first step in solving this critical issue. In this context, the objective of this work is to provide a better understanding of the electron conditioning related phenomena occurring in a machine such as the LHC under the electron cloud effect.

Understanding the behaviour of the LHC beam screen when exposed to the cloud requires first a better understanding of the copper conditioning mechanisms. Therefore, the role of the different chemical components of an air exposed copper surface in its conditioning process will be studied and disentangled. In particular, open questions about the role of carbon and its eventual growth as a necessary condition to obtain a low SEY will be addressed. Furthermore, the role of an eventual electron-induced modification of the copper oxide in the observed SEY decrease during irradiation is assessed. Since no *in-situ* surface characterisation techniques are available in the LHC, the copper conditioning mechanisms will be studied in the laboratory, where the the electron bombardment of the samples surface is obtained using an electron flood gun. Surface chemistry modifications will be monitored by X-ray Photoelectron Spectroscopy

(XPS).

The second consequence of the absence of *in-situ* surface characterisation set-up is that analysing the surface state of vacuum components exposed to the electron cloud during machine operation is possible only when components are extracted from the ring, e.g. for maintenance purpose. Such events are rare and they require the venting of the corresponding part of the accelerator. The impact of air exposure on a conditioned surface thus needs to be assessed, to determine the limit of the accessible information when analysing a conditioned surface after venting and to define an optimized procedure for preserving at most its *in-situ* conditioning state. Consequently, the deconditioning kinetics and how it is influenced by the storage conditions, as well as the induced surface modifications and the impact of deconditioning on eventual *in-situ* SEY contrasts will be studied.

In parallel, in the frame of the task force on beam-induced heat loads, the possibility of the LHC beam screen surface having been modified or contaminated in parts of the machine, in a way that would prevent its proper conditioning, was proposed and assessed. Several surface modifications have been applied to beam screen samples and their conditioning has been performed in the laboratory.

Finally, the opportunity of analysing vacuum components exposed to the electron cloud in the LHC occurred both during the EYETS 2016-2017 and the Long Shutdown 2 (2019-2020). Beam screens extracted from a low and a high heat load cryo-dipole will be analysed with the aim of detecting any difference of surface state which could explain the heat load discrepancy. The characteristic features of beam exposed surfaces will be compared with the ones of surfaces conditioned in the laboratory, in order to gain understanding in the mechanisms of *in-situ* conditioning.

According to the developed axes of research, the present manuscript is divided as follows. Chapter 2 describes the experimental details of the study. Chapter 3 gives the findings of the laboratory study: copper conditioning and deconditioning mechanisms and effect of surface modification on the beam screen conditioning. Chapter 4 is dedicated to the analysis of components exposed to the electron cloud in the LHC. Finally, Chapter 5 provides a critical discussion on the presented results, including possible origins for the LHC heat load picture, and limitations of the laboratory experiments to mimic conditioning phenomenon for machines such as the LHC.

Chapter 2

Experiments and methods

This chapter provides the basic concepts of the techniques used for the surface characterisation in this work: X-ray Photoelectron Spectroscopy (XPS), SEY and work function measurements. Then, a specific description of the experimental set-ups available in the laboratory is given, as well as details on the preparation, conditioning and storage procedures of the samples.

2.1 Surface characterisation

2.1.1 X-Ray photoelectron spectroscopy[1]

A surface exposed to X-rays emits photoelectrons by photoelectric effect. As a result of the deexcitation of the ionized atom, Auger electrons may also be released from the surface. Both processes are illustrated in Fig. 2.1. The kinetic energy E_k of the emitted photoelectrons is given by [120]:

$$E_k = h\nu - E_b - \phi_s \tag{2.1}$$

where $h\nu$ is the energy of the impinging photons, E_b is the binding energy of the atomic orbital hosting the photoelectron and ϕ_s the spectrometer work function.

Measuring the kinetic energy of the emitted electrons allows thus to evaluate their binding energy. In the case of XPS, the high energy of the X-ray photons enables to extract electrons from core levels. Each element has its own set of binding energies [120]. Furthermore, difference in the chemical bond of the atom, e.g. pure metal versus oxide, may lead to variation of the binding energy of its electrons due to the effect of the partial charge of the valence shells induced by the chemical bond which influences the energy of the core level. In parallel, while incident photons can penetrate over micrometers in the material, only electrons emitted within tens of angstroms below the solid surface can effectively leave the solid [120]. Consequently, XPS is a surface-sensitive technique used both for identifying the elements present in the near-surface region, and determining their chemical state [120]. It must be pointed out that XPS cannot directly detect hydrogen [121].

[1] A comprehensive textbook on the XPS technique is available in Ref. [119]

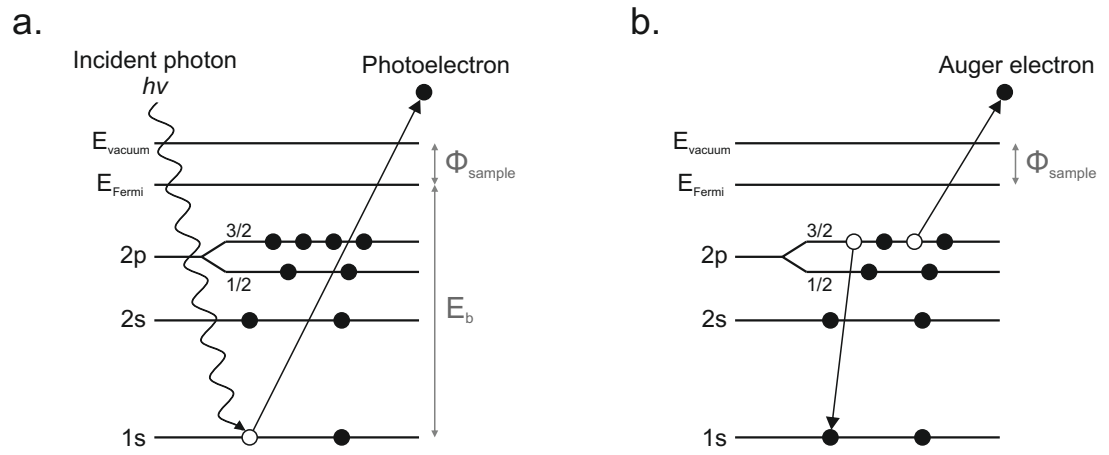

Figure 2.1: (a) XPS photoemission process: an incident photon excites a core electron having a binding energy E_b, leading to its ejection from the material. (b) Auger electron emission process: to relax the generated ion, an outer electron fills in the inner vacancy and a Auger electron is emitted with the energy excess.

For each analysis, a full energy spectrum is acquired for identification of the constituent elements and additional sweeps are then performed in narrower energy regions to obtain high energy-resolution spectra. In the following, the spectra are displayed after subtraction of a linear background for the Cu 2p lines, of a flat background taken around 281 eV for the C 1s lines (for comparison of the high energy tail as in Ref. [122]) and of a Shirley background [119] for the other lines. Spectra displayed in the following in normalized intensity were obtained after the background subtraction and normalization of the signal to its maximum intensity.

The relative concentration, in atomic percent, of an element x is obtained from the area below its corresponding line I_x after background subtraction (for the computation, a linear background was applied for the Cu 2p line, and a Shirley background was applied for all the other lines) weighted by the respective sensitivity factor S_x and normalized over all the detected elements i [120]:

$$C_x = \frac{I_x/S_x}{\sum_i I_i/S_i} \times 100 \tag{2.2}$$

In this study, the XPS energy scale is calibrated using the Au $4f_{7/2}$ (84.0 eV) and the Cu $2p_{3/2}$ (932.7 eV) lines. The analysed area is about 8 mm^2.

2.1.2 Secondary electron yield measurements

Two different measurement principles are used at CERN for the acquisition of the SEY and both are schematized in Fig. 2.2, where the values given for the bias voltages are the one actually used in the laboratory.

In the collector system (Fig. 2.2 (a)), the primary electrons I_p impinge on a negatively biased sample (V_{sa} = -18 V). The emitted secondary electrons I_{sec} are thus repelled and are collected by a positively biased collector (V_{col} = +45 V). I_{sec} and the sample-to-ground current I_{sa} are acquired simultaneously and for each primary energy E. The

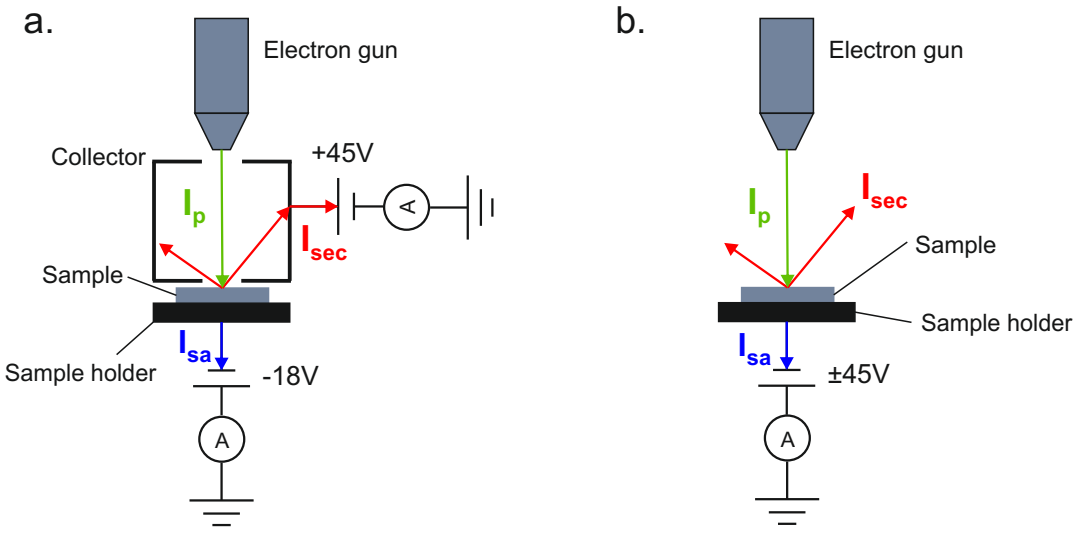

Figure 2.2: SEY measurement principle for (a) the collector system and (b) the sample bias method. The currents are chosen as being positive when electrons travel in the direction of the arrows.

Kirchhoff's law gives the primary current:

$$I_p = I_{sec} + I_{sa} \tag{2.3}$$

Injecting Eq. 2.3 in Eq. 1.5 gives the SEY:

$$\delta(E) = \frac{I_{sec}(E)}{I_{sec}(E) + I_{sa}(E)} \tag{2.4}$$

From the error calculation detailed in Appendix A, the error on the SEY induced by the sample and collector currents reading is evaluated to at most 0.01. Experimentally, it is verified that measuring twice in a row the SEY in the exact same location of a sample gives an SEY variation of ~ 0.01, which is therefore considered as the precision of the measurement.

The sample bias method (Fig. 2.2 (b)) is a two-step SEY measurement. First, the primary current I_p is acquired for each primary energy E either with a Faraday cup, or in the present case, by applying a positive sample bias ($V_{sa} = +45$ V) and thus trapping the secondaries. The sample polarity is then switched to a negative value ($V_{sa} = -45$ V) and I_{sa} is acquired while shooting with the electron gun on the sample with the same energy settings as during I_p acquisition. The energy settings of the electron gun are determined to have the desired landing electron energy when measuring I_{sa} with the negative sample bias. Deducing I_{sec} from Eq. 2.3 and injecting it into Eq. 1.5, the SEY for the sample bias method is obtained by:

$$\delta(E) = 1 - \frac{I_{sa}(E)}{I_p(E)} \tag{2.5}$$

From the error calculation detailed in Appendix A, the error on the SEY induced by the sample currents reading is below 0.01. Experimentally, it is verified that measuring

twice in a row the SEY in the exact same location of a sample gives an SEY variation of ~ 0.01, which is thus considered as the precision of the measurement. In addition, measuring the primary current by positively biasing the sample induces an error on the absolute value of the SEY, since elastically reflected electrons can escape from the surface even with the positive sample bias, leading to an underestimate of I_p. This impacts differently the SEY depending whether δ is below or above unity (see Appendix A). However, a comparison on sputter-cleaned copper between literature curves where measurements were performed with a Faraday cup [28] and curves presented in Section 3.2.2 shows that this error is negligible on the entire energy range.

All SEY measurements are performed at normal incidence, coherently with the fact that electrons from the cloud mainly impinge with small incidence angles with respect to the normal of the beam pipe surface in the dipole and field-free sections [123]. The primary current was kept low enough to limit the sample conditioning during the SEY measurement i.e. the dose associated with a full SEY measurement is about 10^{-7} C/mm^2. The SEY measurements were performed before XPS analysis, to prevent any conditioning effect by X-rays on the measured yield. For each sample state (as received, conditioned, etc.) the SEY was acquired in three different locations of the sample, to assess its homogeneity. In general the uncertainty on the SEY value is dominated by the scattering between the different locations, which is beyond the precision of the measurements. The beam spot on the sample surface is typically 1-2 mm in diameter.

2.1.3 Work-function measurements

The sample work function ϕ is extracted from the low energy part (below 10 eV) of the SEY curve obtained with the sample bias method (see Section 2.1.2). This method has already been applied in the past and a detailed description of it can be found in Ref. [124]. This method is correct when the beam is impinging normally to the surface. The value of the work function was chosen as being at the inflexion point of the SEY drop corresponding to the transition from fully backscattered ($\delta_{max} = 1$) to partly absorbed beam ($\delta_{max} < 1$). This procedure is in principle exact for a Gaussian beam energy profile and a sharp step function as a surface barrier. The accuracy of this method is experimentally estimated to be ± 0.1 eV. A sputter-cleaned gold sample ($\phi = 5.3$ eV [24]) was used for the calibration of the energy scale of the SEY curves acquired with the sample bias method.

2.2 Laboratory experimental setups

Two experimental systems equipped for XPS analysis and SEY measurements and shown in Fig. 2.3 are available for this work.

The 'PHI' system consists of two separated baked UHV chambers, linked through a transfer line. The first chamber (base pressure 5×10^{-9} mbar) is equipped for XPS analysis at 45° emission angle with a non-monochromatic Mg Kα source ($h\nu = 1253.6$ eV). The second chamber (base pressure: 5×10^{-10} mbar) hosts a set-up for SEY measurement with the collector method. An electron flood gun, whose dose and spatial

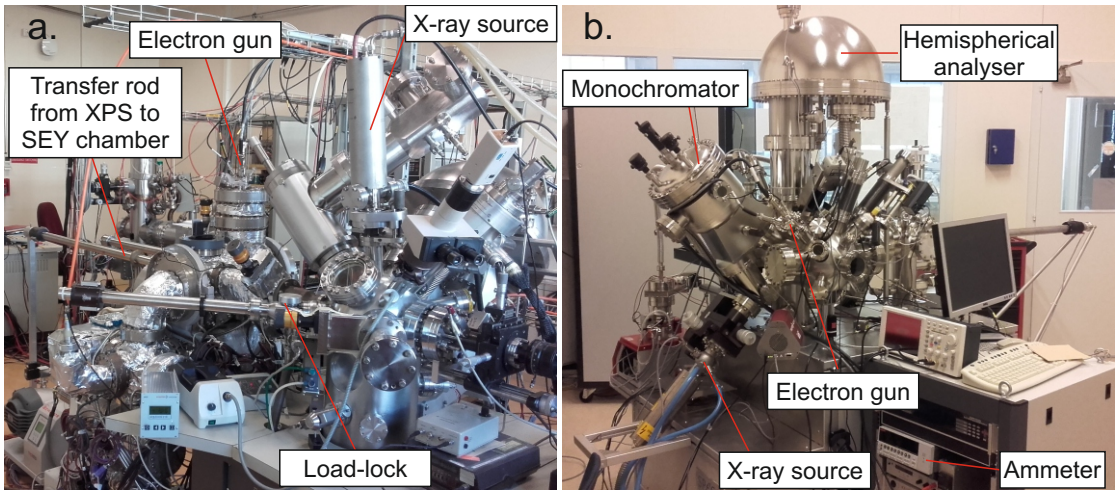

Figure 2.3: Experimental systems used in this work: (a) PHI system, (b) SPECS system

distribution of the delivered beam are characterised thanks to a Faraday cup, enables sample irradiation for the conditioning study. The samples are inserted in and extracted from the system through the XPS load-lock (nitrogen vented). They can be transferred from the XPS to SEY position under vacuum, with a transfer rod. However, because of the sample fixation method (the cylindrical sample holder is successively caught by two forks) it may rotate during the transfer. Furthermore, the presence of a collector above the sample prevents from having a direct view of the electron beam spot on the sample. Therefore, only an approximate match (few millimetres) can be done between the position of the spot analysed by XPS and the one where the SEY is measured.

The 'SPECS' system consists of a single baked UHV chamber (base pressure: 6×10^{-10} mbar) hosting both the XPS and SEY measurement set-ups. The sample is carried by a single manipulator, allowing for a precise positioning of the sample in the chamber. The SEY is measured with the sample bias method, the sample is thus directly visible during the measurement. A perfect match can therefore be achieved with this system between the SEY and XPS analysed spots. The system is equipped with a monochromatic Al Kα X-ray source ($h\nu$ = 1486.7 eV) and during XPS analysis, the photoelectrons are collected at normal emission. Due to the different irradiation source and set-up geometry, the analysed depth is slightly larger for the SPECS than for the PHI XPS system. An electron flood gun is mounted for conditioning and an Ar^+ ion gun is available for *in-situ* cleaning of the samples and XPS sputter depth profiling (erosion speed calibrated for Ta_2O_5). A load-lock pumped with a turbomolecular pump (base pressure: 2×10^{-8} mbar) is used for inserting and exposing samples to controlled atmospheres. In the latter case, the load-lock was flushed with the desired gas and repumped down just before the real sample exposure. This system is built in μ-metal, and therefore allows the measurement of the SEY down to landing energy of 0 eV as well as sample work-function measurement as described in Section 2.1.3.

2.3 Sample preparation

For the laboratory study (Chapter 3), copper samples were indifferently cut in a polycrystalline OFE copper sheet (1-2 mm thick) or in a beam screen (OFE copper colaminated on stainless steel) from the stock. In Chapter 4, samples are cut in beam screens extracted from the LHC, which have thus been exposed to the proton beam during LHC operation. The beam screen cleaning procedure before their installation in the LHC consists in a degreasing by immersion in a commercial alkaline detergent solution (NGL 17.40 from NGL cleaning Technology SA [125], 20 g/L), assisted with ultrasonic agitation. After the detergent bath, the beam screens were rinsed in tap water, followed by immersion in a continuously purified ultra-pure water bath. Finally, the beam screens were sprayed with ethanol to speed up the drying phase. A similar procedure was applied for the cleaning of the samples of this work, to stick at most to the real LHC beam screen surface. The pumping slot shields (copper beryllium alloy UNS C17200) were not only degreased, but also passivated by immersion in a chromic acid solution. The same treatment is applied for the pumping slot shield samples studied in the laboratory.

After cleaning, all the samples were wrapped in aluminium foil and stored in a polyethylene (PE) bag, in air. The storage time before the samples were actually used for experiments varies between 1 to 12 months. The sample state after cleaning and storage is referred to as 'as received' or 'air exposed'.

2.4 Conditioning

The energy distribution of the electron cloud in a LHC dipole obtained from simulations is dominated by slow electrons (E $<$ 30 eV), but exhibits a higher energy contribution varying from 200 to 500 eV (see Fig. 1.14). It was shown that slow electrons are not efficient in scrubbing, while above 50 eV of impinging energy, the ultimate SEY and dose required to reach it are independent of the scrubbing energy [31]. Therefore, an energy of 250 eV was chosen for the conditioning in this work. Conditioning was carried out at normal incidence angle. A current density of about 120 nA/mm^2 was used, ensuring no warm-up of the sample during irradiation, as confirmed thanks to a thermocouple fixed on the sample holder. During conditioning, the current was periodically monitored by applying a bias of +20 V on the sample, and was observed to be stable over the time scale of a full conditioning process, i.e. about 24 hours. When not monitoring the current, the sample was grounded. Before a conditioning, the flood gun was degassed overnight. At the start of a sample conditioning, the pressure in the UHV chamber typically raises in the low 10^{-8} mbar range when powering the flood gun.

2.5 Sample ageing and storage

For the deconditioning study (Section 3.3), samples were stored in specific atmospheres, in particular into a desiccator. It consists in a closed glass container accommodating some silica gel used as a desiccant and therefore maintaining a dry atmosphere. As measured with an hygrometer, the air humidity in the desiccator raises up to about 20%

when opening it for inserting samples, and a humidity level lower than 10% is typically reached within less than one hour after closure. The samples were wrapped in aluminium foil before insertion in the desiccator, to allow stacking them. Other storage procedures include unbaked vacuum, saturated vapour pressure of water (sample hanging above water in a closed glass container) and cleaned closed stainless steel tube, in air.

Chapter 3

Study of copper conditioning and deconditioning mechanisms in the laboratory

After discussing the relevance of the laboratory experiment in investigating the conditioning mechanisms in the LHC, the mechanisms of copper conditioning are studied in the laboratory, at room temperature. In particular, the role of carbon among the chemical components of the surface is investigated. The mechanisms and the kinetics of deconditioning, occurring when a conditioned surface is exposed to air, are also investigated. A procedure for saving at most the conditioning state of the accelerator extracted components in view of their surface analysis is given, as well as a limit of the accessible information, when analysing such surfaces. Finally, in an attempt to explain the origin of the high heat load observed in some parts of the LHC, different possible surface states of the beam screen induced by operation or maintenance are investigated and their impact on conditioning is reported.

3.1 Relevance of the laboratory experiments for the LHC case

In the ideal case, the laboratory experiments should reproduce as much as possible the conditions of the LHC machine in operation. However, several striking differences appear between the laboratory and the LHC cases whose implications are discussed in the following.

The first major distinction between the laboratory and the LHC systems concerns the temperature, which in turn influences the experimental conditions through different channels. Several material properties such as conductivity or diffusion coefficients are temperature dependent and are therefore expected to be different between the laboratory and the LHC. In particular, native copper oxide Cu_2O is a semi-conductor, the conductivity of which thus decreases with decreasing temperature [126]. More generally, potential charging effects are expected to be more severe in the LHC case than in

the laboratory. At low temperature, diffusion is reduced so that atoms remain confined either in the bulk or in areas of the surface. In addition chemical reactions are slowed down or hindered. The physical surface-gas interaction is affected so that the sticking coefficients of most of the molecules, excepted hydrogen and helium for the LHC case, are close to one and sojourn times of adsorbed molecules are increased compared to room temperature [127]. The latter effect increases the probability of having chemical modifications induced by the cloud electrons on adsorbates. It is worse mentioning that the energy of the electrons from the cloud is large compared to the 26 meV associated with the thermal energy at 300 K. Therefore, primary electron-induced modifications, such as carbon graphitization which seems to have an energy threshold above 20 eV [31] and ESD, are not expected to be hindered by cold conditions, neither are expected differences of SEY values between cryogenic and ambient temperatures. Indeed, similar conditioning kinetics and SEY values were observed for conditioning at room temperature and 9 K, both on a laboratory set-up [47]. The gas composition in the cold beam screen environment and in a baked UHV analysis chamber is similar, in the sense that the main contribution is given by hydrogen [127], but in general with a lower total pressure (about 50-200 times lower in the LHC than in the laboratory). Upon beam operation, ESD will increase mainly the amounts of H_2, CO, CH_4 and CO_2 [94].

The second series of differences are due to the configuration of the beam screen surface in the cold bore compared to the sample in the surface analysis system, as described in the following. In the laboratory configuration (a small sample in a large vacuum chamber and a smaller sticking coefficient) a gas molecule which is desorbed from the sample via ESD during conditioning has a negligible probability of being readsorbed onto the sample surface. However, in the LHC case, where the full vacuum system is the 'sample' and where the sticking coefficient of the gas to the surface is about one, the probability of re-adsorption is very high before the gas molecule eventually escapes to the cold bore through the pumping slots. An other difference between laboratory and an LHC dipole or quadrupole is the presence of a magnetic field. A field up to several Tesla is not expected to influence the secondary electron generation cascade, since the mean free path of electrons in the relevant energy range is much smaller than the resulting Larmor radii and the trajectories are not significantly modified. Moreover, the Larmor radius of a 10 eV electron in a 8.3 T field is 1.3 μm, hence much larger than the Ra beam screen roughness [128]. The presence of the field trapping the electron trajectories produces the coexistence of regions irradiated with very different current densities (see Fig. 1.12 and 1.13), where the balance between ESD and adsorption of resulting residues can be very different. Moreover, the energy distribution of the electrons impinging on the beam screen wall exhibits a wide range, and is widely dominated by a low energy contribution (see Fig. 1.14) which are less efficient in scrubbing the surfaces [31].

In the laboratory, the electron beam is mono-energetic. This feature may have an impact on the kinetics and conditioning levels rather than creating conditioning mechanisms discrepancy between laboratory and LHC cases. Not only the current density but also the energy spectrum of the impinging electrons from the cloud depends on the azimuth. Indeed, in a dipole, the energy of the electrons impinging on the lateral sides of

the beam screen is lower, since the magnetic field prevents them from gaining significant energy from the beam. Their conditioning efficiency is therefore weaker. Finally, in the laboratory, the conditioning and electron emission processes are decoupled: a constant flux of electrons is provided by the gun all along the conditioning process. Conversely, in the LHC, both processes are coupled since electrons emitted by the beam screen will, after crossing the vacuum chamber, impinge on the walls and contribute to conditioning. Therefore, a conditioning-induced SEY decrease will decrease the cloud density, which in turn decreases the conditioning current. Consequently, the time needed for a full conditioning process in the laboratory cannot be directly translated into required time for a full machine scrubbing. Furthermore, once the scrubbing allowed to reach the electron cloud build-up SEY threshold, electron multipacting is no longer occuring and the SEY decrease is thus expected to stop.

The conclusions which can be extracted from the following investigations must consequently be balanced in the light of the above mentioned limitations.

3.2 Copper conditioning mechanisms

In this section, the mechanisms of copper conditioning are investigated and the role of the different surface components in the conditioning process is disentangled. Unless mentioned otherwise, the experiments presented in the following are performed on the SPECS system (SEY measured with the sample bias method, monochromatic Al Kα XPS source).

3.2.1 Conditioning of air exposed copper surface

The evolution of the secondary electron yield of an air exposed beam screen sample (detergent cleaned) during its irradiation at room temperature by 250 eV energy electrons is shown in Fig. 3.1. The secondary electron yield is observed to decrease over the full considered energy range. In particular, the maximum SEY, initially equal to 2 decreases down to 1.15 after a dose of 8×10^{-3} C/mm^2, as displayed in Fig. 3.2. For greater doses, the SEY decrease stops and the maximum SEY remains constant. Meanwhile, an increase of E_{max} (energy of the maximum SEY) occurs from 300 to 400 eV. In parallel, the shape of the low energy range SEY (Fig. 3.1 (bottom)) is strongly modified during the irradiation. For the as received state (dose = 1×10^{-7} C/mm^2), the curve sharply decreases down to 0.25 when the energy of the incident electrons overcomes the work function, then increases up to 0.6 where a plateau is reached. It finally increases again for energies greater than 15 eV. Under electron bombardment, the secondary electron yield just above the vacuum level decreases and the following SEY plateau is less and less visible. Finally, a significant increase of the sample work function is observed for doses between 1×10^{-4} and 6×10^{-4} C/mm^2 as witnessed by the shift of the SEY drop at the vacuum level (inset of Fig. 3.1 (bottom)).

XPS spectra acquired at the as received state show the presence of carbon from the airborne contamination, oxygen and copper as well as nitrogen and traces of usual

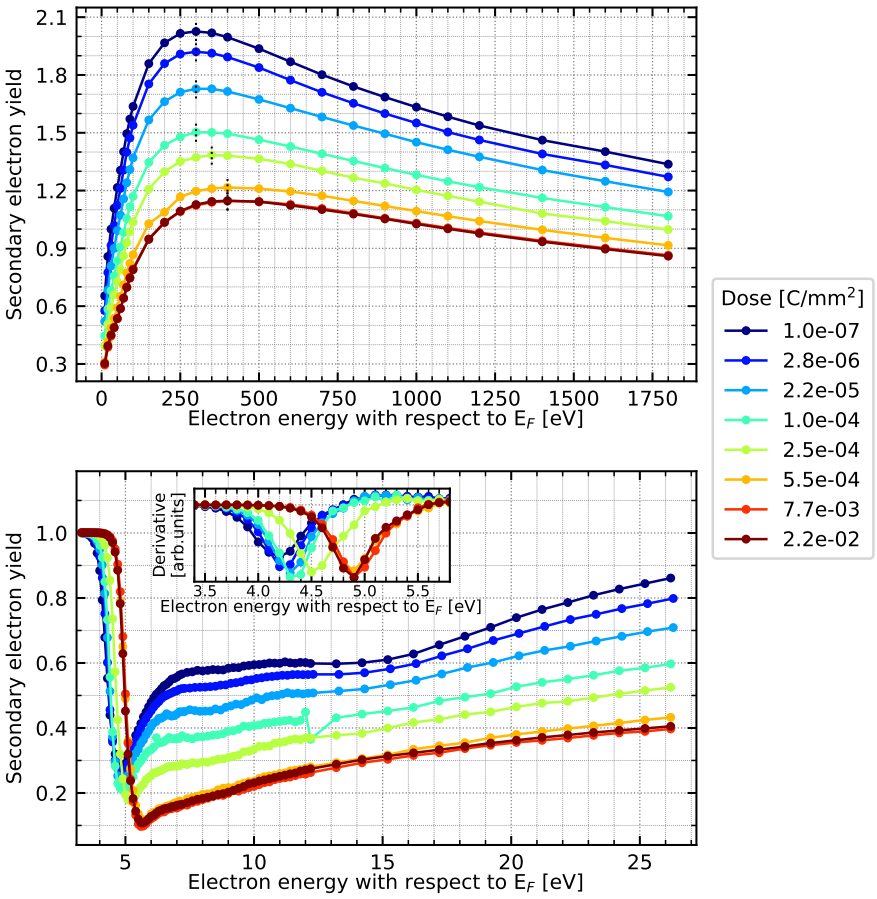

Figure 3.1: Secondary electron yield curves of an air exposed beam screen sample at different irradiation doses: for a primary electron energy between 10 and 1800 eV (top) and between 3 and 26 eV (bottom), inset: derivative of the SEY curves in the vacuum level region.

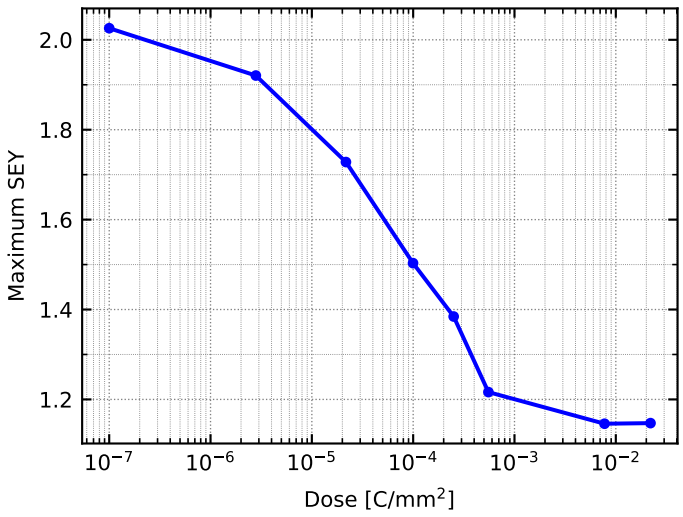

Figure 3.2: Evolution of the maximum SEY of an air exposed beam screen sample as a function of the irradiation dose.

Table 3.1: Surface atomic concentration of the different elements found on the surface of an air exposed beam screen sample, before and after full conditioning process.

Sample state	Atomic concentration [at.%]					
	C	O	Cu	N	Si	Cl
As received	23.4	43.6	28.5	0.7	2.3	1.6
Fully conditioned	14.6	21.6	58.1	1.6	2.5	1.6

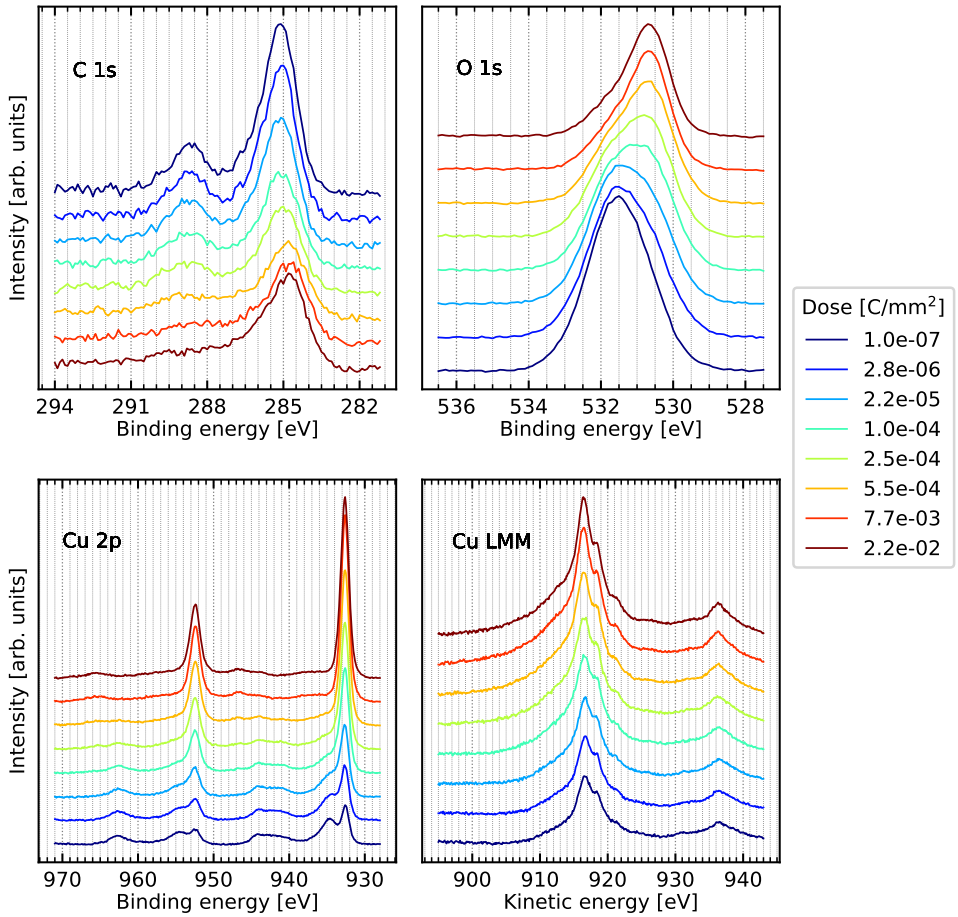

Figure 3.3: C 1s, O 1s, Cu 2p and Cu LMM lines of an air exposed beam screen sample at different irradiation doses (raw intensity, after background subtraction).

contaminants such as chlorine and silicon coming from the detergent cleaning. The atomic concentrations of these different elements are given in Table 3.1.

The C 1s, O 1s, Cu 2p and copper Auger lines acquired before and during conditioning are given in Fig. 3.3. In the as received state, the C 1s line exhibits a main peak at 285.1 eV ascribed to C-C bonds (sp^3 hybridization), and a secondary peak at 288.5 eV related to O-C=O groups [120]. The presence of C-O is highly probable and the respective contribution is expected around 286 eV [129]. A detailed C 1s peak fitting including the typical species for airborne carbon and applied to the particular case of copper conditioning can be found in Ref. [31] and is beyond the scope of the present

investigation. Indeed, as discussed below, the main message for this line is the shift of the main C 1s peak, which is well visible without fitting. For the other XPS lines a fitting procedure is presented here in order to identify once the various components. In the further sections and chapters, the fitting will not be repeated and the identification will be based on the detailed analysis of the lines of the present section. The Cu 2p line exhibits several contributions, visible in Fig. 3.3, and detailed in Fig. 3.4. The main one, located at 932.5 eV (Cu $2p_{3/2}$) corresponds both to metallic copper and cuprous oxide Cu_2O [120, 130]. This native oxide spontaneously grows on an air exposed copper surface and is reported in the literature to be about 1.5 nm thick [106, 107]. Another contribution is found at 934.7 eV and is ascribed to copper hydroxide $Cu(OH)_2$ [107,131], which is also expected to form during the air exposure of copper [106]. The presence of hydroxide, i.e. of Cu^{2+}, results in a satellite structure observed between 939 and 946 eV, whose shape is also pointing towards the presence of $Cu(OH)_2$ [130, 131]. In Fig. 3.4, the satellites are fitted only for the coherence of the shape of the high energy side of the Cu $2p_{3/2}$ peak and their fit does not have any physical meaning. The O 1s line contains three contributions (Fig. 3.3 and 3.4). The component at 531.6 eV is ascribed to hydroxide anions OH^-, as expected in the presence of $Cu(OH)_2$ [107, 132]. Furthermore, the presence of a contribution around 530.6 eV indicates the presence of Cu_2O [132]. The last contribution at 532.7 eV is ascribed to adsorbed hydrocarbons. Finally, the Cu $L_3M_{45}M_{45}$ Auger line (hereafter referred to as Cu LMM) shown in Fig. 3.3 exhibits the maximum at 916.6 eV (kinetic energy), as expected for Cu_2O [133], as well as a shoulder at 918.4 eV compatible with metallic copper [133]. All these observations are compatible with literature describing the air exposed copper surface as a bulk metallic copper covered by a Cu_2O layer and a thin topmost layer containing hydrocarbons, hydroxyl species and water [106, 107].

During the conditioning, all lines undergo transformations which result from surface chemistry modifications. In the first steps of irradiation, surface cleaning is observed through several channels. The disappearing of the bump at 288.5 eV on the C 1s line indicates the removal or conversion of the O-C=O groups, as also visible in the O 1s line of Fig. 3.4 where the hydrocarbons contribution disappears. The shift of the O 1s line towards 530.6 eV visible in Fig. 3.3 results from the decrease of the OH^- contribution as seen in Fig. 3.4. Such an observation is coherent with the disappearing of the contribution at 934.6 eV and of the satellite of the Cu 2p line and all witnesses the reduction of $Cu(OH)_2$ amount. The increase of the peak ascribed to Cu_2O with respect to the one corresponding to metallic Cu on the Cu LMM line (Fig. 3.3) suggests a conversion of copper hydroxide into Cu_2O under irradiation. Furthermore, the surface concentrations of carbon and oxygen are reduced resulting in an increasing copper concentration during irradiation, as shown in Fig. 3.5. In particular, the evolution of the copper amount shows two steps: it steeply increases for doses below 5.5×10^{-4} C/mm^2, and increases only marginally afterwards. The atomic percentages of Si and Cl remain constant over the full conditioning (see Table 3.1).

For a dose greater than 1×10^{-4} C/mm^2, the C 1s line starts shifting towards lower binding energies, as clearly visible in Fig. 3.6 where the lines are plotted in normalized

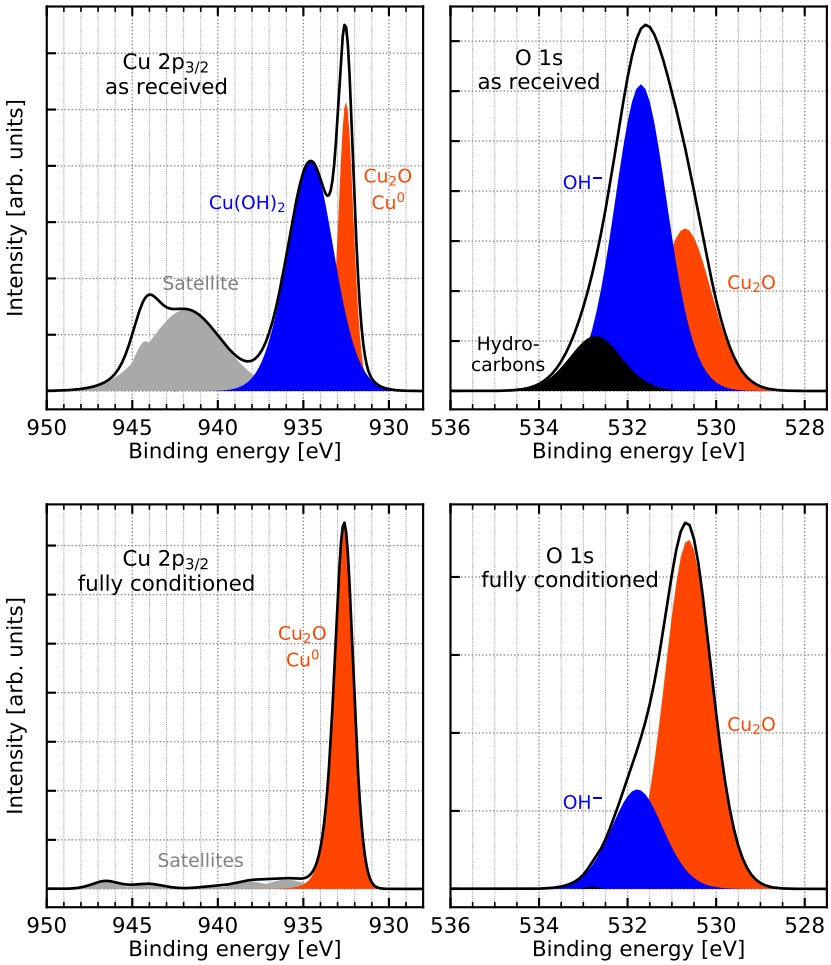

Figure 3.4: Evolution of the different components of the Cu 2p (left) and O 1s (right): as received state (top), after full conditioning (bottom).

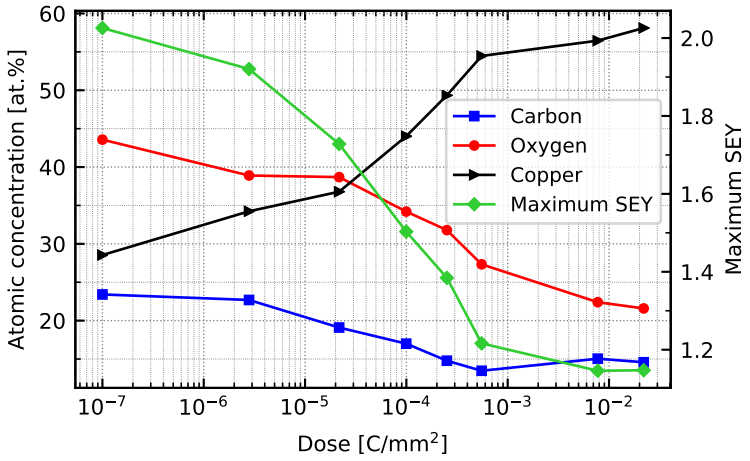

Figure 3.5: Evolution of the surface atomic concentration of carbon, oxygen and copper and of the maximum SEY during the conditioning of an air exposed beam screen sample.

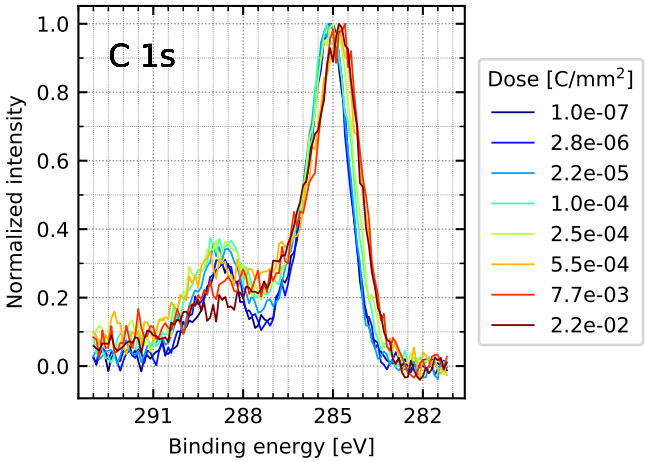

Figure 3.6: C 1s line of an air exposed beam screen sample for different irradiation doses (normalized intensity). A shift towards lower binding energy indicates an increase of graphitic character.

intensity. This shift results from the graphitization of the adventitious carbon layer i.e. its transformation into a more graphitic (sp^2) form [134], as already observed in previous studies [31, 33, 89, 95]. For a dose above 5.5×10^{-4} C/mm^2, the shift seems to saturate, resulting in a maximum of the intensity at 284.8 eV. However, the intensity of the high energy tail of the C 1s line (above 287 eV) keeps decreasing. Since the intensity at these energies is related to carbon linked to oxygen, the decrease of the C 1s tail is coherent with the decrease of oxygen amount observed in Fig. 3.5.

As a summary, a schematic of the surface chemical transformations during conditioning is shown in Fig. 3.7.

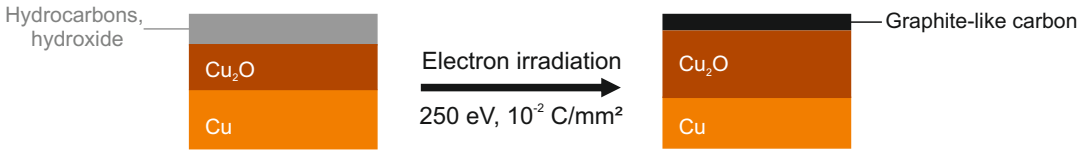

Figure 3.7: Surface chemical modifications during conditioning by 250 eV electrons up to a dose of 10^{-2} C/mm^2. The relative thickness of the different layers is not to the real scale and just indicates the trend.

Both hydroxide and adsorbed hydrocarbons are known to increase the SEY of chemically cleaned surfaces [27, 29, 105]. Therefore, part of the SEY reduction observed during irradiation can be ascribed to the electron stimulated desorption or conversion of the species. However, the SEY observed after the conditioning of the air exposed surface is lower than both the SEY of metallic copper and Cu_2O [28, 29, 124]. Surface cleaning alone is thus not responsible for the full SEY decrease. In parallel, a decrease of surface carbon content is observed during conditioning. Therefore, carbon growth stimulated by electron bombardment can neither be held responsible for the observed SEY decrease, contrary to the conclusions drawn in Ref. [89]. Graphitic carbon, for instance in amorphous carbon films form, has a maximum SEY around 1 [43]. Its presence could thus

help decreasing the SEY of the air exposed surface down to the value measured at the end of conditioning. Nonetheless, other processes such as oxide modification upon electron irradiation, could significantly contribute to the SEY decrease and must be considered.

3.2.2 Role of the different chemical components of the surface

To disentangle the role of each chemical component of the air exposed copper surface in its conditioning process, model surfaces were produced to isolate and condition separately each of the layers constituting the surface. Therefore, pure (sputter-cleaned) metallic copper, pure (carbon-free) Cu_2O and air exposed copper surfaces have been produced and conditioned. Their SEY evolution together with their induced surface modifications during conditioning are reported and compared. More details can be found in Ref. [135].

3.2.2.1 Experimental details

The samples used in the following experiments were 10 x 10 mm^2 pieces of OFE copper. As received samples were obtained either by pre-degreasing in hexane and dipping for 2 hours in an ultrasonic bath of ethanol or wet cleaning in the 17.40 detergent, as specified later for each sample. 'Sputter-cleaned' samples were produced by *in-situ* Ar^+ sputtering at 3 keV of the full sample surface until only traces of argon could be detected by XPS. Carbon-free oxidized surfaces were obtained by two different processes to obtain a thin and a thicker oxide layer. In the first process, sputter-cleaned samples were transferred to the load lock chamber, where they were vented to atmospheric pressure with a mixture of N_2 (80 mol%, purity 55) and O_2 (20 mol%, purity 60) for 45 minutes. These 'load lock' samples were then transferred back to the analysis chamber. In the second process, an as received sample (detergent-cleaned) was oxidized for 270 h to 120°C in air, changing its surface color to blue. This 'thick oxide' sample was then introduced in the UHV system, where it was shortly sputtered to remove carbon contamination. This sputtering step is not expected to modify the oxide stoichiometry [136], but the production of defects within the oxide layer cannot be excluded. The oxide thickness of the two kinds of oxide was measured by depth profiling in the XPS system and were found to be 1.9 and 55 nm (Ta_2O_5 equivalent) for the load lock and the thick oxide sample, respectively. These values are in agreement with expectations from literature [137–139].

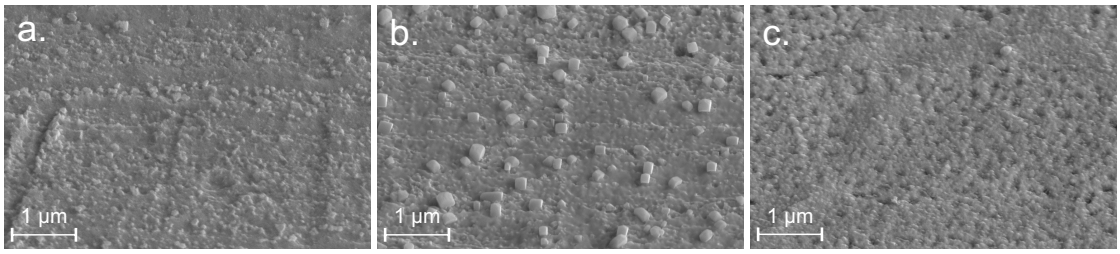

Figure 3.8: Scanning electron microscope images of (a) as received sample after hexane and ethanol cleaning, (b) load lock oxide sample after 1 day in air and (c) thick oxide sample. The pictures were taken with the electron beam impinging on the sample at 45 degrees with respect to the surface normal, to enhance contrast.

The surface morphology of these samples was observed by Scanning Electron Microscopy (SEM) and the corresponding images are given in Fig. 3.8, together with observations performed on an as received (hexane and ethanol cleaned) sample. The surface of the as received sample exhibits damages such as striae characteristic for a laminated material. Scattered cubic surface features of few hundredth of nanometres on the surface of the load lock sample are compatible with the cubic crystallographic structure of cuprous oxide. The surface of the thick oxide sample appears rougher and more porous than the two other samples, possibly as a result of the oxidation procedure.

Conditioning was carried out in the conditions described in Chapter 2 up to a dose of 10^{-2} C/mm^2 leading to full conditioning. The pressure typically increased from 6-7 x 10^{-10} mbar to about 2 x 10^{-9} mbar when starting the irradiation, except for the as received sample where the pressure increased from 1 x 10^{-9} mbar to 5 x 10^{-9} mbar. The pressure at the end of the conditioning before stopping the flood gun was 1 x 10^{-9} mbar for all the samples. Before each experiment, the flood gun was extensively degassed and the sample holder and sample stage were baked *in-situ* at 250°C for 12 hours to obtain the cleanest possible environment.

3.2.2.2 Conditioning of model surfaces

A summary of the surface atomic concentrations measured by XPS, electron emission parameters and work function is presented in Table 3.2 for all the samples and their corresponding states.

Table 3.2: Summary of analysed characteristics of all the samples in their different states: surface atomic concentrations of carbon, oxygen, nitrogen and copper determined by XPS, electron emission parameters (δ_{max} and E_{max}) and work function ϕ.

Sample name	Atomic concentration [at.%]					δ_{max}	E_{max} [eV]	ϕ [eV]
	C	O	N	Cu	Other			
As received	40.6	32.0	1.9	24.3	1.2[a]	2.00	300	4.8
As received + conditioned	36.8	12.5	2.7	45.3	2.7[a]	1.07	300-350	4.9
Sputter cleaned	-	-	-	99.3	0.7[b]	1.44	700	4.3
Sputter cleaned + conditioned	1.6	0.6	0.3	97.1	0.5[b]	1.32	600	4.7
Load lock sample	0.5	8.4	0.1	90.6	0.4[b]	1.26	500	4.8
Load lock + conditioned	1.7	7.2	0.7	89.8	0.6[b]	1.16	500	5.0
Thick oxide sample	0.2	15.3	-	83.3	1.3[c]	1.25	500	4.9
Thick oxide + conditioned	2.0	14.8	-	82.1	1.1[c]	1.18	400	5.2

[a] Cl and Ca
[b] Ar
[c] Si and Ar

- **Air exposed sample**

After years of air exposure followed by cleaning with hexane and ethanol, the surface of the as received sample exhibits an airborne contamination layer [106] containing carbon species up to 40.6 at.%, oxygen, nitrogen and traces of calcium and chlorine below 1 at.%. The core level spectra for carbon, oxygen and copper of the as received sample

are shown in Fig. 3.9. As for the as received beam screen sample presented in Section 3.2.1, a Cu_2O layer is identified by the position of the Cu LMM line at 916.4 eV [133], and is compatible with the Cu 2p component at 932.5 eV [130]. The presence of hydroxide is deduced from the Cu $2p_{3/2}$ line at 934.3 eV [107, 130], its associated satellite shape [130] and the position of the O 1s line at 531.5 eV [132]. From the decrease of the O 1s intensity in the XPS depth profile, the thickness of the oxide/hydroxide layer was measured to be 5.5 nm thick (equivalent Ta_2O_5). It is worth mentioning that the as received state of the current sample presents some differences with respect to the as received state of the beam screen sample of Section 3.2.1: different carbon content, slightly different C 1s line (position of the maximum, intensity of the peak at 288.5 eV), different Cu LMM lines (contribution from metallic copper not visible in the current sample suggesting a thicker airborne layer). These differences may result from the different cleaning procedure (detergent or hexane and ethanol) as well as from the storage time and conditions [107, 132, 140]. This confirms that 'as received' state is not a well defined chemical state, but the observed discrepancies are certainly also observed along the vacuum chambers of accelerators such as the LHC. In the following, we keep referring to the current air exposed OFE copper sample, since it was conditioned in the exact same conditions as for the sputter-cleaned and oxidized samples described below.

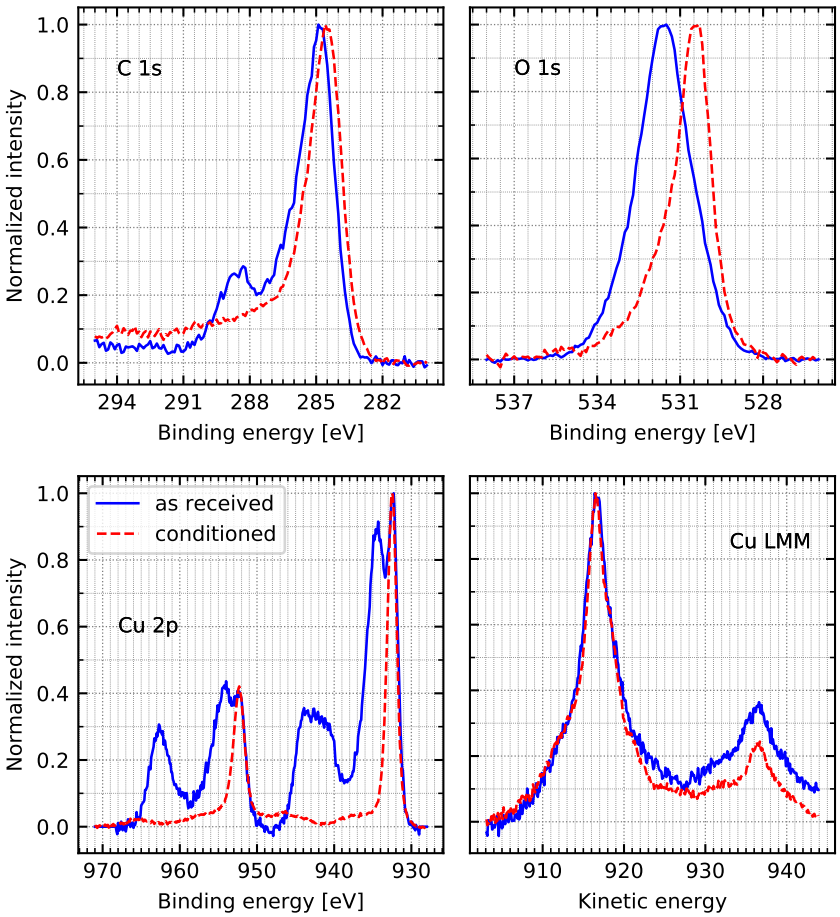

Figure 3.9: C 1s, O 1s, Cu 2p and Cu LMM lines of an as received OFE Cu sample, before and after a full conditioning process.

The as received SEY curves presented in Fig. 3.10 are similar to the one reported in Fig. 3.1 for a beam screen sample: δ_{max} yields at 2, at E_{max} = 300 eV. However, the work function is slightly higher (4.8 eV). After full conditioning, δ_{max} is decreased down to 1.07 (therefore, slightly lower than for the air exposed beam screen sample in Section 3.2.1) and E_{max} is about 300-350 eV. Apart from this point, a similar SEY curve is obtained for the present and for the previous beam screen sample. As for the air exposed beam screen sample of Section 3.2.1, surface cleaning and chemical modifications are observed through: the disappearance of the peak at 288.5 eV on the C 1s line, the vanishing of the copper hydroxide contribution in the Cu $2p_{3/2}$ peak together with the shift of the O 1s line to 530.3 eV (see Fig. 3.9). Furthermore, a decrease of the oxygen and carbon amounts are also observed (see Table 3.2). Finally, carbon graphitization occured as witnessed by the shift of the C 1s line towards lower binding energies.

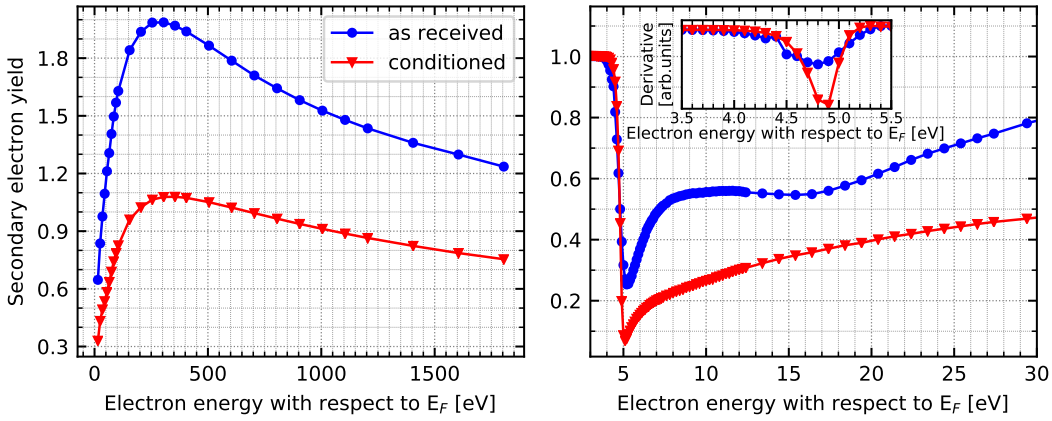

Figure 3.10: (left) SEY curves from 10 to 1800 eV of an as received OFE Cu sample, before and after full conditioning, (right) low energy SEY curves, inset: derivative of the SEY curves in the vacuum level region.

- **Sputter-cleaned samples**

XPS spectra acquired on a sputter-cleaned sample and shown in Fig. 3.11 exhibit Cu $2p_{3/2}$ and Cu LMM peaks at E_b = 932.6 eV and E_k = 918.7 eV respectively, as expected for the metallic copper state [106, 133]. Apart from argon (implanted during ion bombardment), no other element was detected.

The SEY curves for sputter-cleaned sample are given in Fig. 3.12. The maximum SEY of such samples was measured at δ_{max} = 1.44 for E_{max} = 700 eV. The values and the curve shape are consistent with literature [28, 33]. The work function was found to be between 4.2 and 4.4 eV among several samples (4.3 eV for the sample shown in Fig. 3.11 and Fig. 3.12) in agreement with Ref. [24]. The low energy part of the SEY curve presents some specific features: a step just above the vacuum level as well as two bumps at 18 eV and 26 eV are clearly visible. Some of these structures can be related to the band structure and plasmon energy of copper [141, 142] and are not discussed further here. After a conditioning dose of 10^{-2} C/mm^2, carbon and oxygen were detected to an amount of 1.6 at.% and 0.6 at.% respectively (see Table 3.2). These contaminants can be

related to the use of the flood gun. Indeed, the total pressure in the chamber increases up to 1.5 x 10^{-9} mbar when the flood gun is powered. Meanwhile, an increase of the peaks at m/q = 16 (CH_4), and m/q = 44 (CO_2) is observed in the residual gas analyser spectrum. The intensity of these peaks remains at least one order of magnitude below the dominant one at m/q=2 (H_2). Even though the signal to noise ratio of the C 1s peak is low, a clear shift to lower binding energy is distinguished in Fig. 3.11 (curves c. and a.), with respect to the carbon present at the as received state of the sample. No modification is observed neither on the Cu $2p_{3/2}$ nor on the Cu LMM spectra.

The variation of the secondary electron yield during conditioning is not the same at all primary energies. While a slight decrease is observed above E_p = 70 eV, with δ_{max} going down to 1.32 at E_{max} = 600 eV, the yield between 7 and 70 eV is increased by electron irradiation. The bumps present at 18 and 26 eV above Fermi level after sputtering are barely visible, and the reflectivity just above the vacuum level reaches almost zero. The work function is increased up to 4.7 eV.

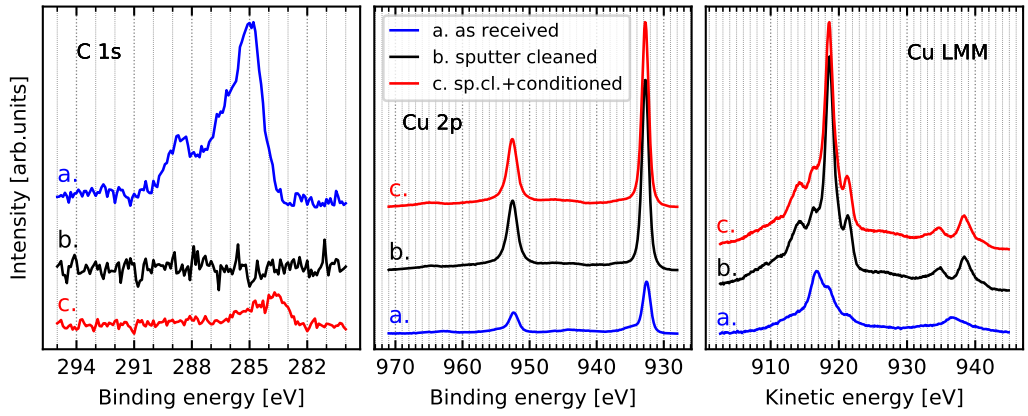

Figure 3.11: C 1s (left), Cu 2p (centre) and Cu LMM (right) lines of a sputter-cleaned sample, before and after conditioning. The as received state of the sputter-cleaned sample is shown for comparison.

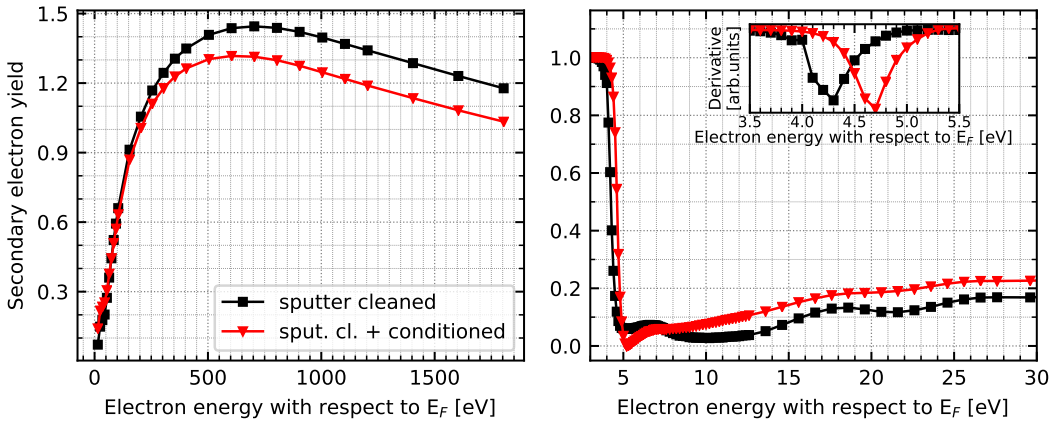

Figure 3.12: (left) SEY curves from 10 to 1800 eV of a sputter-cleaned sample, before and after conditioning, (right) low energy SEY curves, inset: derivative of the SEY curves in the vacuum level region.

- **Oxidized samples**

The Cu LMM lines for the two kinds of oxidized samples (load lock and thick oxide samples) are shown in Fig. 3.13. For the load lock sample the metallic copper peak at 918.6 eV is still the main contribution, while for the thick oxide sample the main component is at 916.6 eV (compatible with Cu_2O [133]) and the bulk copper component is no longer visible. After oxidation, the load lock sample exhibits traces of carbon (0.5 at.%) which are attributed to initial impurities in the oxidation gas bottle or contamination of the gas by the injection line. Traces of silicon up to 0.8 at.%, probably resulting from the detergent cleaning process, were found on the surface of the thick oxide sample.

The SEY curves for the two oxidized samples are shown in Fig. 3.14 together with the curves of sputter-cleaned sample, as a reference. Above 12 eV of energy, the SEY of the two oxidized samples is identical. Oxidation is responsible for a global decrease of the SEY above 250 eV with respect to the sputter-cleaned state. The maximum SEY, 1.26 and 1.25 for load lock and thick oxide samples respectively, is found at E_{max} = 500 eV. These values are in good agreement with previous studies [115]. For primary energies below 250 eV, the yield is increased by the oxidation process with respect to sputter-cleaned copper. For both oxidized samples, no structures are visible at 18 and 26 eV and the work function is very similar: ϕ = 4.8 – 4.9 eV (coherent with Ref. [143] i.e. higher than for the clean copper surface

After conditioning of the load lock sample, 1.7 at.% of carbon was detected on the sample surface, as for the conditioning of the sputter-cleaned copper sample (Table 3.2). The oxygen amount slightly decreased down to 7.2 at.%. For the thick oxide sample, 2.0 at.% of carbon was found after conditioning and oxygen content remained constant. During conditioning, the ratio of the Cu_2O to Cu component of the Cu LMM line of the load lock sample is slightly increased as visible in Fig. 3.13 (left). Fig. 3.13 (right) shows the C 1s lines of the load lock and thick oxide samples, after full conditioning, as well as the as received C 1s line of the load lock sample, as a reference. For both the load lock and the thick oxide samples, the conditioning induces a clear shift of the C 1s line with respect to airborne carbon contamination present at the as received state. No modification is observed for the other element lines.

The SEY of both oxidized samples decreases at high primary energies during conditioning. δ_{max} yields at 1.16 and 1.18 for load lock and thick oxide samples respectively, at E_{max} = 400 - 500 eV. For the load lock sample, the yield at low energies also decreases, the shape of the SEY curve remaining the same. However, for the thick oxide sample, the low energy SEY curves before and after conditioning are overlapping. For both samples, the work function increased during irradiation to reach 5.0-5.2 eV.

3.2.2.3 Discussion and conclusions on the copper conditioning mechanisms

- **Secondary electron yield**

The secondary electron yield of as received (air exposed) copper strongly decreases within the entire considered energy range during electron irradiation. For the presented

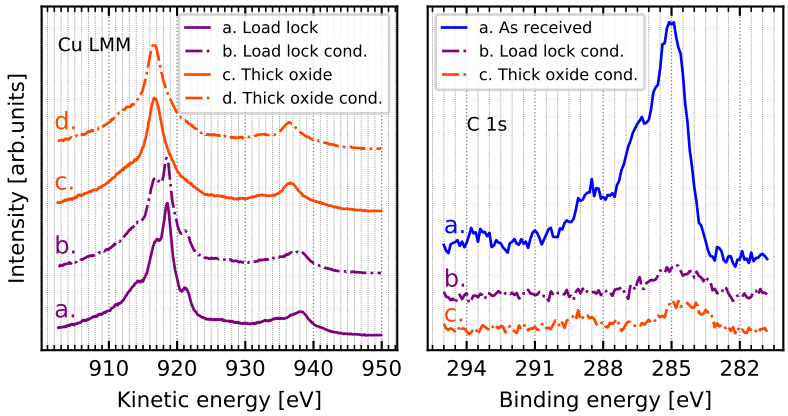

Figure 3.13: (left) Cu LMM lines of load lock and thick oxide samples, before and after conditioning, (right) C 1s lines of conditioned states for load lock and thick oxide samples. The C 1s line of the as received state of the load lock sample is given as a reference.

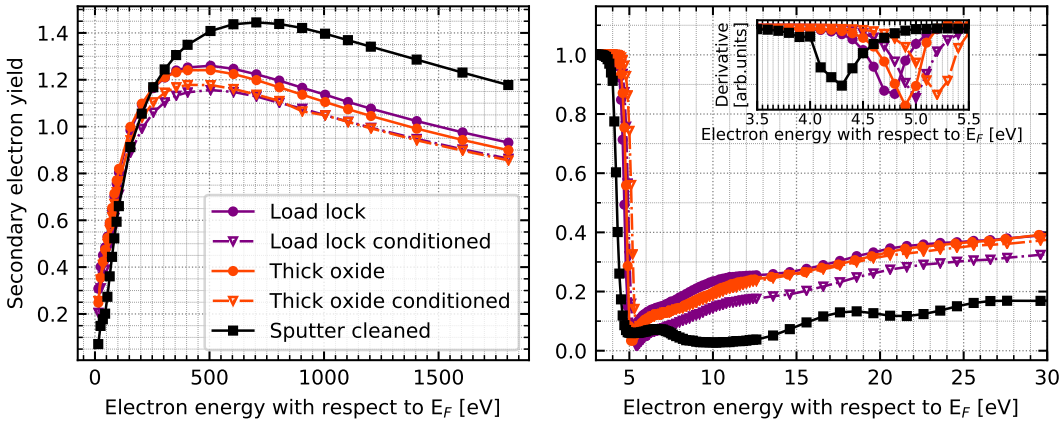

Figure 3.14: (left) SEY curves from 10 to 1800 eV of a load lock and thick oxide samples, before and after conditioning, (right) low energy SEY curves, inset: derivative of the SEY curves in the vacuum level region. The sputter-cleaned state is given for comparison.

OFE copper sample, the maximum SEY δ_{max} decreases from 2.00 to 1.07, E_{max} remaining constant around 300-350 eV. XPS analysis reveals the removal the $Cu(OH)_2$ surface layer and carboxyl adsorbates. Such modifications were also observed on another air exposed copper (beam screen) sample, presented in Section 3.2.1 and can be held responsible for part of the SEY reduction observed during irradiation.

The conditioning of a sputter-cleaned copper sample results in a δ_{max} decrease from 1.44 to 1.32, while E_{max} shifts from 700 to 600 eV. Only a small amount of carbon is observed on the surface after conditioning and the C 1s line position indicates that this carbon is more graphitic than the airborne carbon contamination [134]. Since no other surface modification is observed for this sample, the observed δ_{max} and E_{max} decrease during conditioning could be attributed to the appearance of graphitic carbon. The ultimate δ_{max} of the cleaned sample after conditioning remains still much higher than the one obtained for the conditioning of an air exposed sample. Therefore, the decrease of δ_{max} down to the value observed for a conditioned air exposed sample requires either

copper oxide and/or modification of adsorbed hydrocarbons to graphitic carbon. For the sputter-cleaned surface, in the low energy part of the curve (below 70 eV), the SEY is increased by both the conditioning process and the vacuum storage. This opposite trend in the SEY variation upon surface modification depending on primary energy was already observed [28] and was attributed to enhanced surface scattering of low energy incident electrons due to adsorbed molecules.

The effect of copper surface oxidation on the SEY is independent of the oxide thickness in the investigated range: the maximum SEY of the load lock and thick Cu_2O oxide samples is 1.26 and 1.25, respectively, and occurs at E_{max} = 500 eV. Since the oxide thickness of the load lock sample is very low compared to the scale of the copper surface roughness, the roughness is not expected to increase significantly during this oxidation process. Furthermore, the geometric configuration (aspect ratio and spacing) of the cubic structures observed on the surface of the load lock oxide will not influence the SEY of the sample [144]. Thus, the lower maximum SEY of the load lock oxide with respect to the sputter-cleaned sample is unambiguously ascribed to the chemical modification of the surface. From Fig. 3.8, the thick oxide sample appears rougher and more porous than the load lock oxide. In addition, its oxide layer is more than 25 times thicker. Both the thicker oxide layer and the rougher surface would tend to decrease the SEY of the thick oxide sample below the one of the load lock sample. However, both samples exhibit the same maximum SEY at the same incident energy. It is thus concluded that the maximum SEY measured on the thick oxide sample is not influenced by its apparently rougher surface, and that the maximum SEY of the surface does not depend on the oxide thickness above 2 nm (equivalent Ta_2O_5). As a further effect, the oxidation process increases the yield and strongly modifies the SEY curve shape below 250 eV. Full conditioning of oxidized samples reduces their yield down to δ_{max} = 1.16 and 1.18 for load lock and thick oxide sample, respectively. For both samples, this decrease can be attributed, as in the case of sputter-cleaned sample, to the small amount of graphitic carbon observed on the surface after conditioning. In all cases, the ultimate δ_{max} reached at the end of the conditioning remains higher than the one measured on a fully conditioned air-exposed copper sample. Therefore, the formation of graphitic carbon appears to be necessary to decrease δ_{max} down to the ultimate value observed on an as received sample.

The experiments show that oxidation decreases E_{max} with respect to sputter-cleaned copper (Table 3.2). However, for the as received sample, after conditioning, E_{max} is even lower, at 300-350 eV. This lower value cannot be explained by the oxide layer, which is in the thickness range between the load lock and the thick oxide samples, both giving higher E_{max}. Therefore, carbon seems to be also responsible for the low value of E_{max} observed on the as received sample. Indeed, thin films of graphitic-like carbon show an E_{max} around 300 eV [43].

- **Work function**

In common phenomenological models of secondary electron emission, both the surface barrier (work function) and the density of states play a role. It is generally expected

that an increase of work function results in a decrease of the maximum SEY. For both sputter-cleaned and oxidized surfaces, the work function was found to increase during electron irradiation while the maximum SEY decreases. Therefore, during conditioning, the evolution of both quantities is consistent with the expectations. The work function of load lock sample increases from 4.3 to 4.8 eV during oxidation and the one of thick oxide is found at 4.9 eV. The lower δ_{max} of oxidized samples with respect to sputter-cleaned copper could thus also be explained by the work function increase. However, since previous studies showed that the work function increase occurs in the first oxidation steps [143], while the SEY decrease is rather pronounced for higher oxidation times [29], the lower maximum SEY observed after oxidation cannot be only ascribed to the work function increase. Furthermore, in the case of as received copper, conditioning leads to the largest SEY decrease, but the work function remains unchanged (variation within the accuracy of the applied work function measurement method). This shows that the decrease of SEY cannot be explained only by the increase of work function and the contribution of the change in electronic density of states cannot be disentangled.

In conclusion, it is shown that none of the tested carbon-free surfaces conditions down to an ultimate δ_{max} as low as the one obtained after the conditioning of an air-exposed copper sample. Cuprous oxide Cu_2O is found to have a passive role in reducing the maximum electron yield of a pure bulk copper: Cu_2O has a lower δ_{max} than Cu, but no significant SEY decrease driven by oxide modification during irradiation is observed, i.e. the irradiation of Cu_2O alone is not enough to decrease its yield down to the values measured on an air exposed surface after conditioning. Carbon has an active role in reducing the maximum electron yield. Surface carbon amount of an air-exposed copper surface was found to slightly decrease during irradiation. Therefore, an increase of carbon coverage is not necessary to reduce the secondary electron yield to values close to 1. It is shown that it is the modification of the airborne carbon into a more graphitic form during electron irradiation at 250 eV that allows reducing the maximum electron yield of an air exposed copper surface down to values lower than for pure copper or Cu_2O. In this sense, the higher ultimate SEY observed after conditioning of the present air exposed copper sample with respect to the previously studied beam screen sample (Section 3.2.1) could be due to a different carbon amount ($\delta_{max} = 1.07$ with 36.8 at.% of carbon for the current copper sample against $\delta_{max} = 1.15$ with 14.6 at.% of carbon for the beam screen sample of Section 3.2.1).

3.3 Copper deconditioning mechanisms

The surface analysis of vacuum components extracted from the LHC during the EYETS 2016-2017 and presented in Section 4.1 evidenced the loss of their conditioning state, i.e. their deconditioning induced by air exposure. This phenomenon limits the possibility to reconstruct the original *in-situ* conditioning state of the machine in terms of SEY. Furthermore, it was observed that surfaces analysed at several weeks of interval were presenting significantly different deconditioning states, making their comparison irrele-

vant. Therefore, in view of further analyses to be performed on components extracted from the LHC during the LS2 (2019-2020), a study was performed, to investigate the deconditioning mechanisms, kinetics and impacts on the *in-situ* conditioning contrasts (e.g. persistence or not of possible *in-situ* SEY contrasts). As a result of this study and taking into account the constraints related to the machine environment and schedule, a optimized procedure is proposed for limiting the deconditioning of the accelerator extracted components, and a limit is assessed for the information which is accessible in the analysis of such surfaces.

The following experiments were performed on the PHI system on OFE copper samples. To study the deconditioning kinetics and mechanisms, samples were conditioned and the evolution of their SEY and surface chemistry were followed over storage time in a desiccator (see Section 2.5), which provides a reasonably reproducible atmosphere, in opposition to 'laboratory air'. In a second phase, the influence of the storage conditions is studied.

3.3.1 Storage in a desiccator

3.3.1.1 Kinetics

To evaluate the time scale related to the deconditioning occuring during air exposure, two OFE copper samples (detergent cleaned, followed by a 3-4 months storage in an aluminium foil in air) were fully conditioned and then stored in a desiccator, via a short (3 min) transfer through laboratory air. The SEY was measured after several storage times and the evolution of the maximum SEY over time is given in Fig. 3.15.

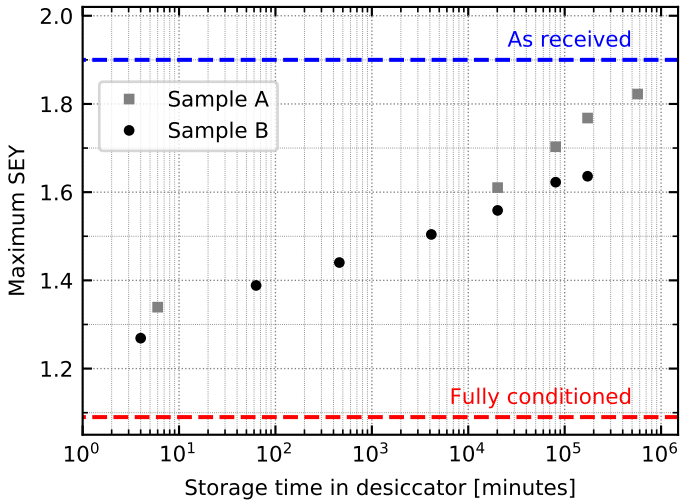

Figure 3.15: Evolution of the maximum SEY of two OFE copper samples stored in a desiccator after full conditioning.

For a storage time shorter than 2 weeks (2×10^4 minutes), the two samples exhibit the same behaviour: δ_{max} undergoes a fast increase in the first instants of storage and the increase then slows down. Indeed, in the first six minutes of air exposure, δ_{max} increases by about 0.25, and it then takes two more weeks to increase it again by the same amount.

For more than 2 weeks of storage, the SEY of sample A keeps increasing, while the one of sample B tends to saturate. However, after 4 months of storage ($\sim 2 \times 10^5$ min), the SEY of both samples is still significantly lower than for an as received sample, i.e. the memory effect of conditioning is still present after 4 months of storage in desiccator. The SEY curves of sample B, before and after full conditionning as well as during storage, are given in Fig. 3.16. As mentioned in Section 3.2, the energy of the maximum SEY E_{max} shifts to higher values during conditioning. E_{max} then immediately starts shifting back to lower energy during air exposure and recovers its as received value after only 8 hours of storage.

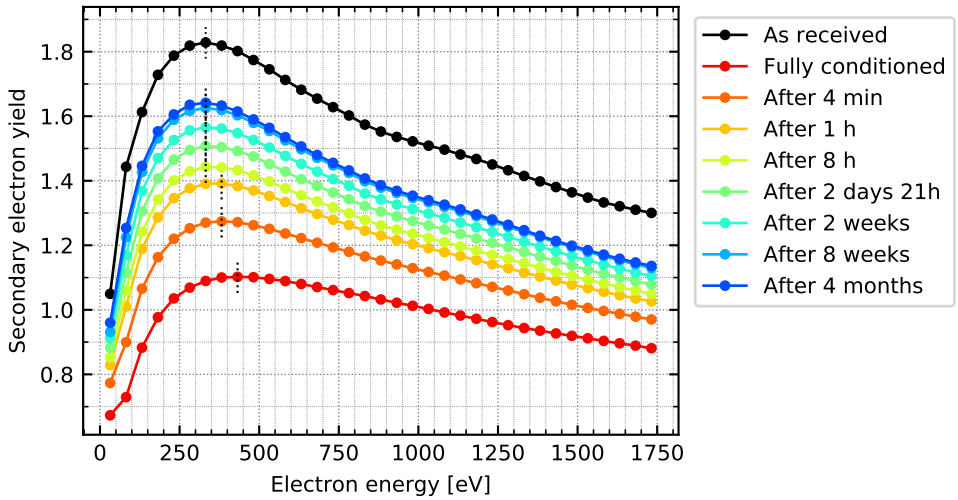

Figure 3.16: SEY curves of an OFE copper sample stored in a desiccator after full conditioning.

The minimum time required to disconnect an LHC magnet from its neighbours in the tunnel, transport it to the surface and extract its vacuum components involves an air exposure period of about 2 weeks. Furthermore, analysing the components may take several additional weeks. According to Fig. 3.15, a significant SEY increase will occur during the magnet extraction time and deconditioning may still significantly proceed during the following weeks of analyses. Therefore, if stored in a desiccator after extraction from the LHC, surfaces analysed immediately after extraction and several weeks later will not be directly comparable, due to deconditioning effects. Storage in desiccator thus helps preserving the conditioning state over several months but is not sufficient for an application to the analysis of LHC extracted components.

3.3.1.2 Deconditioning mechanisms

The study of copper conditioning process presented in Section 3.2 evidenced several characteristics of the conditioning mechanisms: decrease of the copper hydroxide and carbon contents and carbon graphitization. When an irradiated surface is exposed to air, one can thus expect the initial chemical state to be partially restored, in particular through adsorption. Consequently, the evolution of the surface chemistry was followed for the sample B presented in Fig. 3.15. The Cu 2p lines corresponding to the as received

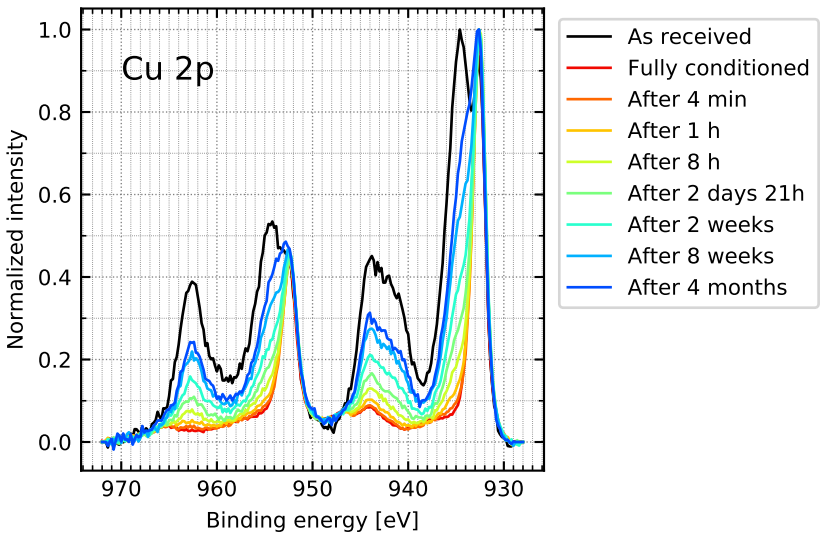

Figure 3.17: Cu 2p lines of an OFE copper sample stored in a desiccator for different times after full conditioning.

and conditioned states as well as after several storage times in desiccator are shown in Fig. 3.17.

It clearly appears from the shape and intensity of the satellite as well as from the intensity of the high energy shoulder of the Cu $2p_{3/2}$ line that the amount of $Cu(OH)_2$ increases during storage. However, after 4 months, it remains significantly lower than for the as received state of the sample.

The evolution of the maximum SEY, of the atomic carbon concentration and of the ratio of the intensity of the Cu 2p line at 934.4 eV to the intensity at 932.6 eV: $I_{Cu(OH)_2}/I_{Cu,Cu_2O}$ is shown in Fig. 3.18 for the sample B from Fig. 3.15. Both the carbon concentration and the amount of $Cu(OH)_2$ are found to increase during storage. Since both adsorbed hydrocarbons and copper hydroxide increase the yield of clean surfaces, their appearance on the surface contributes to its deconditioning. However, the kinetics for the two species is different. Indeed, immediately at the air exposure the carbon content significantly increases, while $I_{Cu(OH)_2}/I_{Cu,Cu_2O}$ remains constant. The SEY increase is therefore driven by carbon recontamination for storage time below 4 minutes. For times between 4 minutes and 8 hours, both the carbon amount and the hydroxide contribution increase. For storage times longer than 8 hours, the carbon concentration is stable and the SEY increase seems therefore only driven by hydroxide growth.

Carbon recontamination is also observed through the evolution of the C 1s line, as shown in Fig. 3.19. First, the peak at 288.5 eV (O-C=O) clearly reappears during storage. Furthermore, the C 1s line, which shifted to lower binding energies during full conditioning, shifts back towards its initial position, as expected for a recontamination by hydrocarbons (sp^3 hybridization). It should be mentioned here that the shift back most probably results from a globally less graphitic carbon overlayer due to the readsorption of

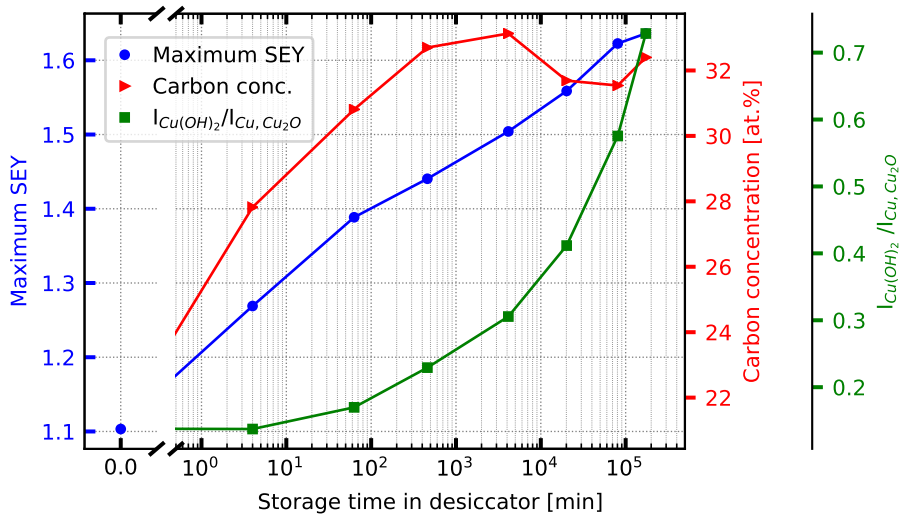

Figure 3.18: Evolution of the maximum SEY, of the atomic concentration of carbon and of the ratio $I_{Cu(OH)_2}/I_{Cu,Cu_2O}$ over storage time in desiccator. The time t=0 represents the fully conditioned state, and the data points of the three quantities overlap there.

sp^3 carbon, rather than from a conversion of the graphitic film into sp^3 carbon. Indeed, graphite is known to be chemically inert with respect to air exposure. After 4 months, the C 1s line position is at only 0.1 eV from its as received position, i.e. the shift back is mostly completed and the remaining difference with the as received state is of the order of the energy accuracy of the experimental set-up. Furthermore, since the as received state is unknown in the case of LHC extracted components (the as received position of the C 1s line may vary by few tenth of eV), determining whether the carbon was graphitized or not during LHC operation may not be possible.

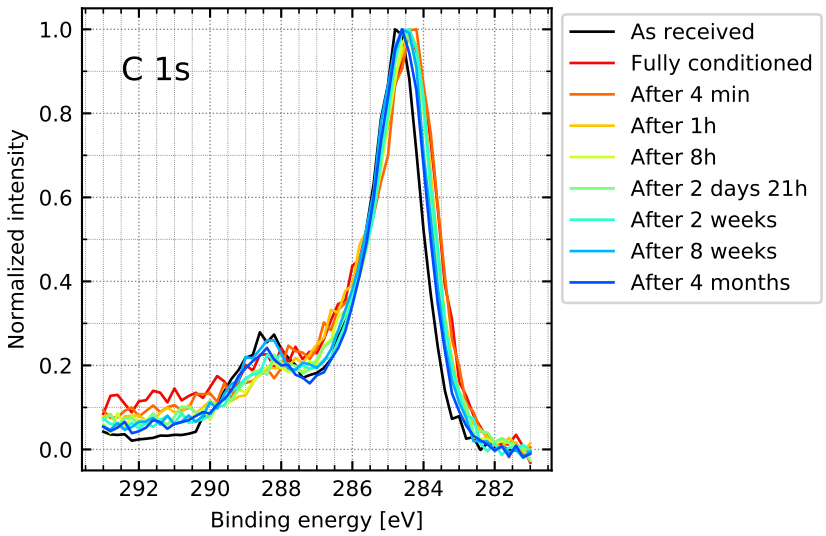

Figure 3.19: C 1s lines of an OFE copper sample stored in a desiccator for different times after full conditioning.

3.3.1.3 SEY contrasts

An essential question arising from the LHC heat load observations described in Section 1.2.4 concerns the *in-situ* value of the SEY in the different parts of the ring. More generally, understanding whether and for how long the possible presence of *in-situ* SEY differences (contrasts) persists after venting of the surfaces is a key point in the interpretation of the analyses performed on irradiated surfaces after air exposure. To evaluate this aspect, samples were conditioned down to different SEY by stopping the conditioning at different doses and were then stored in a desiccator. Their SEY was measured after 2 weeks, 8 weeks and 4 months of storage, as relevant time scales for the application. The results are presented in Fig. 3.20.

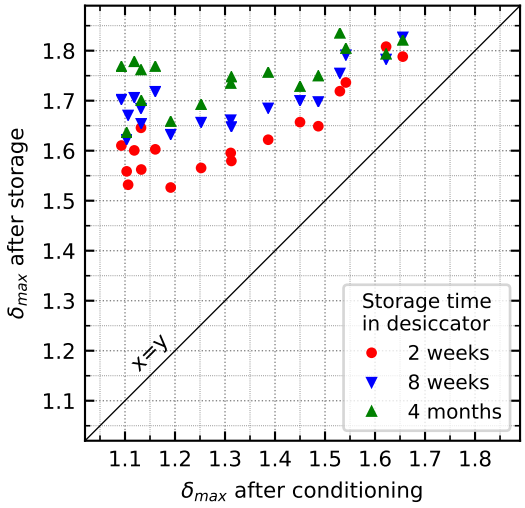

Figure 3.20: Maximum SEY after different storage times in desiccator of OFE copper samples conditioned to different SEY values.

After 2 weeks of storage, a clear trend is visible for the samples conditioned down to a δ_{max} between 1.2 and 1.7: the highest the δ_{max} after conditioning, the highest the δ_{max} after 2 weeks of storage. The SEY contrasts are thus preserved between these samples, which have a δ_{max} ranging from 1.55 to 1.8 after 2 weeks of storage. Meanwhile, samples conditioned down to a maximum SEY around 1.15 (fully conditioned samples) see their yield increasing up to 1.55 - 1.65, i.e. to the SEY level measured after storage on samples conditioned to a δ_{max} between 1.2 and 1.45. The yield increase is therefore larger for the fully conditioned samples, which may be explained by their cleaner and thus more reactive surface. This results in an equivalent δ_{max} after 2 weeks of storage of about 1.6 for all the samples initially conditioned to a δ_{max} between 1.1 and 1.45. The SEY contrast between those samples is thus lost after only 2 weeks in the desiccator. Furthermore, for a given δ_{max} after conditioning, the dispersion after storage in between the fully conditioned samples is larger than for the partially conditioned samples. This observation is coherent with Fig. 3.15 where the two fully conditioned samples exhibit different δ_{max} after weeks of storage. Such dispersion could be ascribed to higher $I_{Cu(OH)_2}/I_{Cu,Cu_2O}$ ratio and/or higher carbon recontamination.

After 8 weeks of storage, the δ_{max} globally increased. Based on the same reasoning as above, the limit of δ_{max} after conditioning below which the samples become equivalent in SEY after 8 weeks of storage is now shifted to 1.5. Finally, after 4 months of storage all the samples exhibit a δ_{max} between 1.65 and 1.85, without any correlation to the δ_{max} after conditioning.

These measurements clearly show that the contrasts between different SEY after conditioning vanish during storage in desiccator. Therefore, the analyses of surfaces exposed to the beams in the LHC should be performed as early as possible after their venting to preserve at most the possible contrasts. In any case, since the analyses cannot reasonably be performed after less than 2 weeks of air exposure (in conditions possibly worse than in a desiccator), all the *in-situ* SEY contrasts present below a δ_{max} of 1.45 are irremediably lost.

3.3.2 Influence of storage conditions

The mechanisms of copper deconditioning suggest that the preservation of the *in-situ* conditioning state requires a storage in clean and dry atmosphere to limit carbon re-contamination and hydroxide grow-up. Furthermore, it is shown that deconditioning keeps significantly progressing after 2 weeks of storage in a desiccator, suggesting that even in such storage conditions, surfaces analysed after different times of storage are not directly comparable. To investigate the best reasonable storage conditions applicable to the extraction of LHC components and as a confirmation of the mechanisms of copper deconditioning, OFE copper samples were stored in different controlled atmospheres after full conditioning in the laboratory. These atmospheres are:

- Unbaked vacuum (base pressure: 10^{-8} mbar) after a 1h-transfer in air
- Saturated vapour pressure of water (sample hanging above water in a closed glass container)
- Closed stainless steel tube in atmospheric pressure of laboratory air (cleaned with the CERN UHV cleaning procedure). This corresponds to the situation where the beam lines of the magnet to be extracted are cut and then closed with Viton-sealed covers, to allow for the magnet transport from the tunnel towards a surface facility where the vacuum components are extracted.
- Desiccator

The evolution of the maximum SEY of the different samples is given in Fig. 3.21 and the relation between their maximum SEY and their $I_{Cu(OH)_2}/I_{Cu,Cu_2O}$ ratio is given in Fig. 3.22. The storage in a closed stainless steel tube allows for an equivalent preservation of the SEY as a storage in desiccator (for storage in desiccator, a single sample was selected close to the average SEY value of all the fully conditioned samples presented in Fig. 3.20). Besides, these two samples exhibit similar evolution of the $Cu(OH)_2$ amount. As expected, the sample stored in saturated vapour pressure of water undergoes the fastest SEY increase. After only two weeks in humid atmosphere, the SEY is found at

the level of the as received state. This large and fast increase can be related to the rapid growth of $Cu(OH)_2$ as shown in Fig. 3.22 (triangles), where the $I_{Cu(OH)_2}/I_{Cu,Cu_2O}$ of this sample after only two weeks of storage overcomes the ones of the samples stored in a stainless steel tube or in a desiccator for four months. By opposition, a storage in vacuum is very efficient in limiting the SEY increase. The observed δ_{max} increase, about 0.3, corresponds actually well to the expected one for a 1 h air-exposure (see Fig. 3.15) which was the time for the transfer of the sample from the laboratory set-up to the storage vacuum chamber. A storage in vacuum seems therefore to considerably slow down, if not fully stop, the deconditioning process. In particular, it efficiently prevents from hydroxide grow-up, as shown in Fig. 3.22. It must be pointed out that such a storage was only performed for two weeks, for logistics reasons.

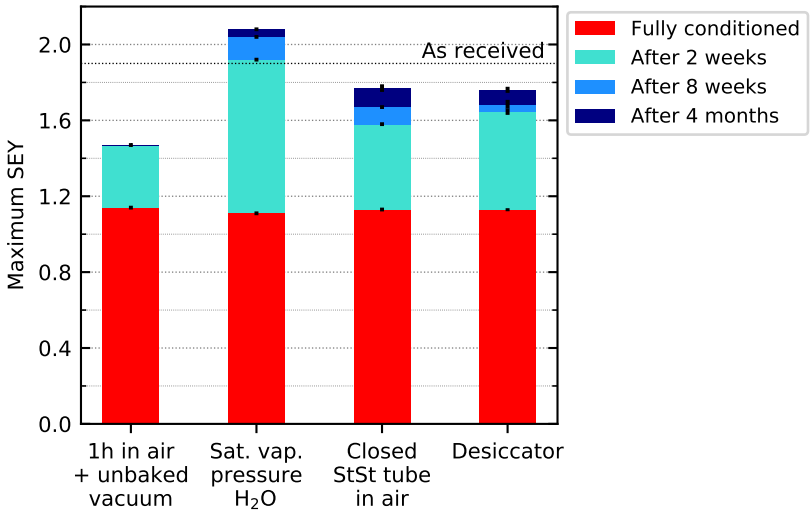

Figure 3.21: Evolution of the maximum SEY of fully conditioned OFE copper samples during their storage in different atmospheres (vacuum storage performed for only two weeks).

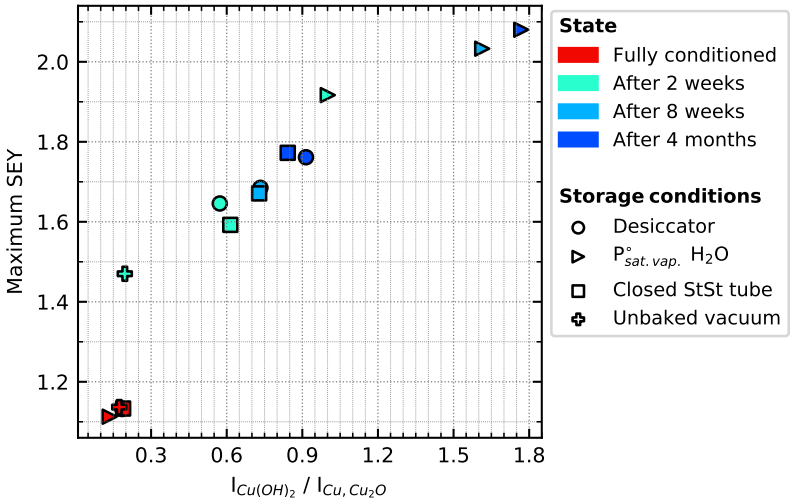

Figure 3.22: Maximum SEY with respect to the $I_{Cu(OH)_2}/I_{Cu,Cu_2O}$ ratio for the fully conditioned state and after 2 weeks, 8 weeks and 4 months of storage in different atmospheres.

3.3.3 Conclusions on the deconditioning mechanisms

The study of deconditioning mechanisms allowed to identify the surface and SEY modifications and their associated time scale. It evidenced the role of airborne carbon recontamination and hydroxide grow-up in the increase of the SEY during storage. It clearly shows that, since a reduction of the air exposure time below 2 weeks before analysing the surface of LHC extracted components is currently impossible, *in-situ* SEY contrasts below $\delta_{max} = 1.45$ will be irreversibly lost. It demonstrated that vacuum is a very efficient storage medium for limiting the SEY increase and surface chemistry degradation. This solution will therefore be implemented for the storage of components extracted during the LS2 (2019-2020) in view of their surface analysis in the laboratory (see Section 4.2).

However, a crucial limitation of this study lies in the different conditions between ideal laboratory experiment and practical (LHC extracted components) cases. Indeed, extracting 15.5 m-long vacuum components from an LHC magnet and preparing samples fitting into the laboratory set-up require steps such as sawing, drilling, etc. which are not included in the present laboratory study. Even though these different actions are performed with the highest care (e.g. UHV cleaning of the tools), the accelerator extracted surfaces are there exposed to scarcely controlled conditions (air humidity, dusts etc.) which can only further degrade and erase their *in-situ* conditioning state. Furthermore, this study compares the deconditioned with the as received state of the samples. In the case of LHC extracted components, such a comparison is not possible since the as received state of the component at installation was not characterised. Therefore, the persistence or not of the memory effect of conditioning, namely of an SEY and a hydroxide amount lower than for the as received state as well as a shift of the C 1s line, has to be assessed in absolute or by comparison with a reference as received sample, whose state may be slightly different from the initial one of the considered component. Consequently, the present study should not be used as a calibration tool for converting the 'after extraction' surface state to a corresponding *in-situ* state but rather as a guide giving the limit of accessible information when interpreting the analyses.

3.4 Copper reconditioning, influence of venting conditions

Until the EYETS 2016-2017 included, the venting procedure of the LHC started by breaking the beam vacuum with pure nitrogen. Afterwards, to check for any eventual beam pipe obstruction induced by components mechanically deformed during the warm-up (typically, the PIMs in the magnet interconnections), a polycarbonate ball equipped with an RF localization system, the so-called RF ball, was pushed into the two beam lines by filtered air from the tunnel. The first reactive gas to which the beam screen surface was exposed was therefore not a well defined atmosphere, e.g. in terms of humidity, and could have been different from one part of the machine to an other. Consequently, it was suggested to change the venting procedure, by breaking the beam vacuum with a mixture of N_2/O_2 (80%/20%) to better control and improve the reproducibility of the venting. The effect of such a venting on a conditioned surface was thus assessed in the laboratory, for validation of the procedure.

The experiments were carried out on the SPECS system. OFE copper samples were fully conditioned, then vented for about 60 hours with an atmospheric pressure mixture of N_2/O_2 (80 mol%/20 mol%, purity 55 and 60) or pure N_2 (purity 45) in the system load lock and reconditioned. In addition, after its second conditioning, the sample vented with N_2 was stored for 2 days in a desiccator. Before each sample venting, the load lock was flushed with the corresponding gas and repumped-down.

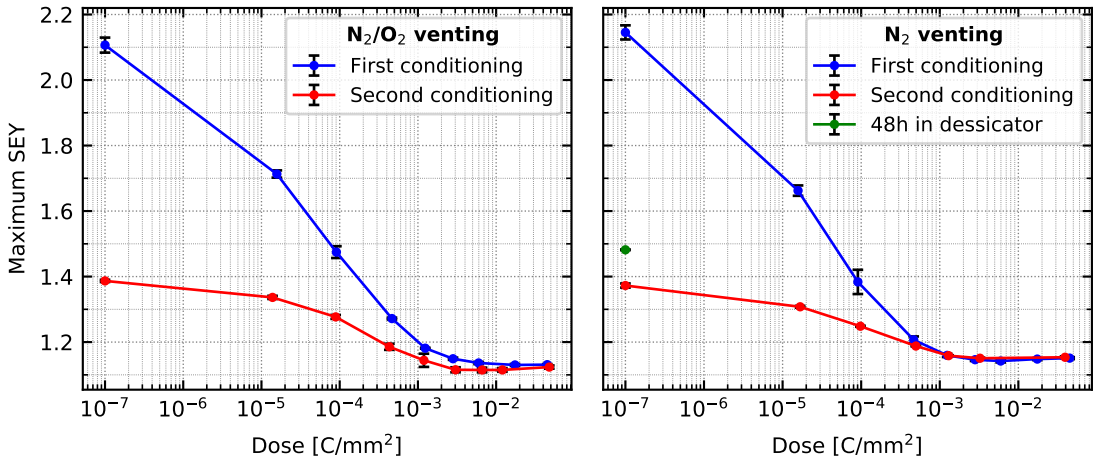

Figure 3.23: Evolution of the maximum SEY of air exposed OFE copper samples during conditioning and reconditioning after dry air (left) and nitrogen (right) venting. The error bars represent the δ_{max} dispersion over 3 locations of the samples.

The conditioning and reconditioning curves of the corresponding samples are given in Fig. 3.23. After venting with N_2/O_2, the maximum SEY increased by 0.25, proving again the efficiency of clean and dry atmosphere in preserving the conditioning state. The following reconditioning leads to the same ultimate SEY but is slightly faster: the dose required to reach the saturation of the SEY decrease is slightly lower than for the first conditioning. The deconditioning observed when venting with nitrogen is similar to N_2/O_2 venting. The ultimate SEY and the dose needed to reach it are identical to the ones of the first conditioning and to the ones for N_2/O_2 venting. These results show that the N_2/O_2 venting will not harm the beam screen conditionability. After N_2 venting and 2 days storage in desiccator, the sample shows a slightly higher SEY than for the two others cases, but the memory of the conditioning is still clearly present.

The C 1s, Cu 2p and O 1s lines of the different samples, after full conditioning and after venting/storage in the different atmospheres are shown in Fig. 3.24. For clarity reasons, only the lines for the first conditioning of the sample vented with N_2/O_2 are shown, since it was found to be identical for the two samples and after each of the two conditionings.

Even though a slight carbon recontamination was observed on the surface during the ventings with N_2/O_2 and N_2 (the atomic concentration increased by 2.5-4.5 at.%, which may result from initial gas impurities or gas contamination in the supply line), the C 1s lines after these ventings are both overlapping with the fully conditioned state. In particular, no shift back of the line is observed. The growth of a satellite on the Cu 2p

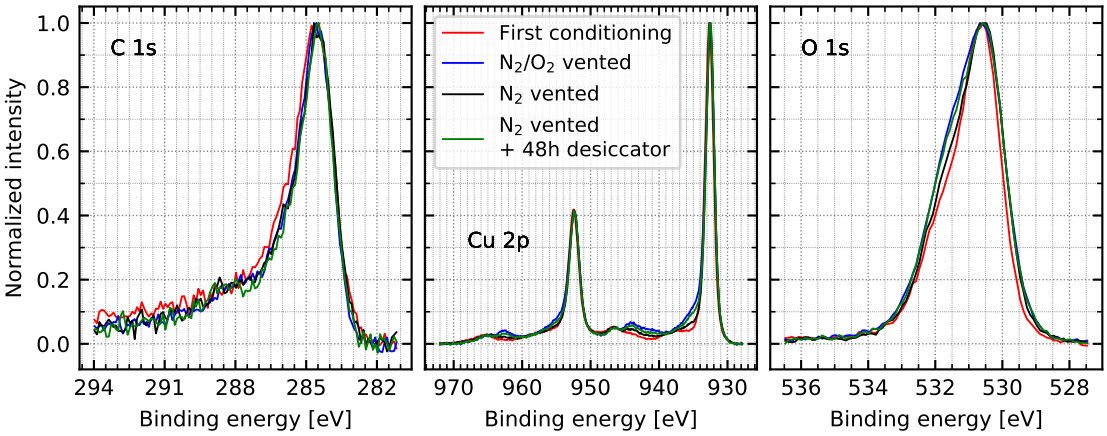

Figure 3.24: C 1s (left), Cu 2p (centre) and O 1s (right) lines of air exposed OFE copper samples after full conditioning and venting for 60 h in different atmospheres.

line, and of a high energy shoulder on the Cu $2p_{3/2}$ and on the O 1s line is compatible with the build-up of a copper hydroxide layer. According to the intensity of these different features, $Cu(OH)_2$ is more present on the surface vented with N_2/O_2 than on the one vented with nitrogen, but its presence remains marginal. Such a copper specie is not expected to form under these venting conditions [132]. However, the contamination of the gas in the supply line could be responsible for the observed surface modifications. In turn, the small SEY increase during venting, even with non-reactive gas such as nitrogen, is coherent with these surface modifications. After nitrogen venting and 2 days in the desiccator, the hydroxide amount is identical to the N_2/O_2 vented sample. However, the bump at 288.5 eV on the C 1s line starts reappearing and may be responsible for the slightly higher SEY observed with respect to the N_2/O_2 vented sample.

In conclusion, N_2/O_2 venting does not alter the conditionability of the surfaces in the laboratory conditions. Although it does not seem to improve the situation with respect to the procedure applied in the past either, the proposal of venting the LHC arcs with this gas mixture was adopted for the LS2 (2019-2020), as a more controlled and reproducible procedure.

3.5 Investigating the origin of the LHC heat load pattern by laboratory experiments

According to the heat load observations given in Ref. [69] clearly showing that the LHC heat load picture changed consecutively to LS1, two main hypotheses were made concerning the origin of this change. Both of them rely on a modification of the beam screen copper surface hindering its conditioning. A contamination of some beam screens induced by LS1-related activities, preventing then their proper conditioning during Run 2 is the first hypothesis. In the second scenario, we consider the possibility that the beam pipe surface was already modified before LS1, but conditioned as expected during

Run 1. Its venting during LS1 would have led to the build-up of a new product on the reactive surface, which would have hindered proper conditioning during Run 2. The possible sequences of events leading to an abnormal beam screen conditioning in Run 2 are given in Fig. 3.25 for the two scenarii.

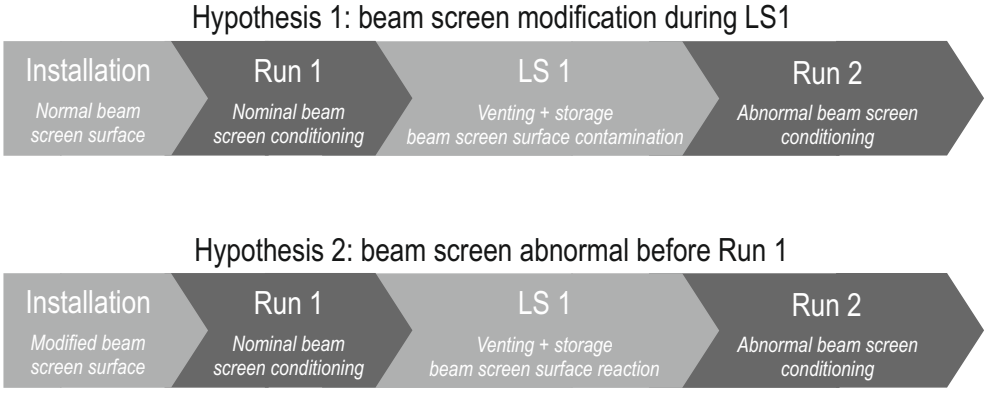

Figure 3.25: Sequence of events for the two scenarii leading to an abnormal beam screen conditioning during Run 2: hypothesis of a beam screen surface modification during LS1 (top), hypothesis of a beam screen surface presenting anomalies before Run 1 (bottom).

For each scenario, a list of possible events eventually leading to the modification of the beam screen surface was established and the effect of such modifications on the beam screen conditioning was qualitatively assessed. If not mentioned otherwise, the associated surface analyses and conditioning experiments were carried out on the PHI system (Mg Kα source and collector SEY system).

3.5.1 Hypothesis 1: beam screen surface modification during LS1

3.5.1.1 Possible events

Long Shutdowns (LS) are periods of maintenance and upgrade works where different activities are performed inside and around the beam pipes. The hypothesis of the beam screen surface being contaminated during LS1 activities was thus naturally proposed.

Typical LS activities involving the vacuum components start with the warm-up of the cryogenic parts of the machine, the beam pipe being in static vacuum. At that time, the sector valves (separating each arc from its neighbouring LSS) and the valves to the transfer lines are closed. Each beam pipe is then vented independently and at one arc extremity to atmospheric pressure with pure nitrogen. The RF ball (polycarbonate shell) is then pushed inside each beam pipe by compressed and filtered tunnel air. The air injected into the beam pipe may be different (e.g. in terms of humidity rate) from one part of the machine to the other due to different environmental conditions inside the tunnel along the ring. Visual inspections, involving the introduction of an endoscope in the beam pipes over several tens of meters were also performed. At the end of LS1, the vacuum system was re-pumped and cooled down according to the procedure described in Section 1.2.4.1.

From these different operations, several possible events leading to beam screen surface contamination were identified and an equivalent contamination was reproduced on beam screen samples to asses the effect of such contamination on the conditioning of the beam screen samples in the laboratory. A summary of possible events, their associated sample preparation in the laboratory as well as their main effect on the surface is given in Table 3.3. During the preparation of the samples, the modification of the surface was deliberately exaggerated, i.e. the surface was on purpose more damaged in the laboratory tests than it was possibly in the machine. In the hypothesis of a contamination of the beam screen during LS1, the surface being contaminated was already exposed to the beam during Run 1. To mimic this situation, the contamination tests were performed on parts of beam screens extracted from the LHC during the EYETS 2016-2017 (see Section 4.1), after about a year of storage in aluminium foil in air. The conditioning of the modified samples is compared with a reference, namely an EYETS-extracted LHC beam screen sample which did not undergo any further modification.

Table 3.3: Hypothesis of a modification of the beam screen surface during LS1: possible events leading to the beam screen surface modification, their associated sample preparation for laboratory conditioning and main effects on the surface.

Possible event	Sample preparation	Effect on the surface
RF ball scratching the beam screen	Scratched with RF ball	Visibly damaged (scratches) + carbon contaminated
Endoscope sheath scratching the beam screen	Scratched with endoscope sheath	Carbon contaminated
Beam screen in humid atmosphere during LS1	Stored for 2 weeks in saturated vapour pressure of water	Increased $Cu(OH)_2$ amount
Beam screen contamination by primary pump oil	Pump oil spread directly on the surface	Carbon contaminated
Beam screen contamination by Roots pump	4 days in a chamber pumped by Roots pump	Presence of fluorine (PTFE compatible)
Beam screen vented below dew point (water condensation)	Dipped in liquid nitrogen and exposed to ambient air	Similar to reference

3.5.1.2 Effects on the surface

Before contamination, the surface of the different samples used for the tests was typically exhibiting about 30 at.% of carbon, 38 at.% of oxygen, 26 at.% of copper, 5 at.% of nitrogen and traces of silicon. The maximum SEY of the samples was ranging from 1.65 to 1.85 at 300 - 350 eV. Depending on the treatment applied to the sample, different surfaces modifications were observed.

As a consequence of its storage in saturated vapour pressure of water, the copper hydroxide amount on the surface of the corresponding sample increased, leading to a maximum SEY increase from to 1.74 to 1.87 for this particular sample. For the samples scratched with the endoscope sheath, the RF ball and the one contaminated with pump

oil, the main surface modification detected by XPS is a large increase of the carbon amount, compatible with the carbonaceous nature of the contaminant component (see Fig. 3.26). In these three cases, the contamination results in a large maximum SEY increase and a shift of E_{max} to lower energies as visible in Fig. 3.27. In addition, for the sample scratched with the RF ball, a large SEY dispersion was observed over the surface, as expected from the visible inhomogeneous and damaged surface produced by the scratching. After a 4 day storage in a chamber evacuated by a Roots pump, 9 at.% of fluorine were found on the surface of the corresponding sample. The position of the F 1s peak at 688.4 eV is compatible with the presence of polytetrafluoroethylene (PTFE, Teflon) [120], typically found in the bearings of Roots pumps. The SEY of this sample was not significantly modified by this contamination. The sample dipped in liquid nitrogen did not show any SEY increase, neither surface modification.

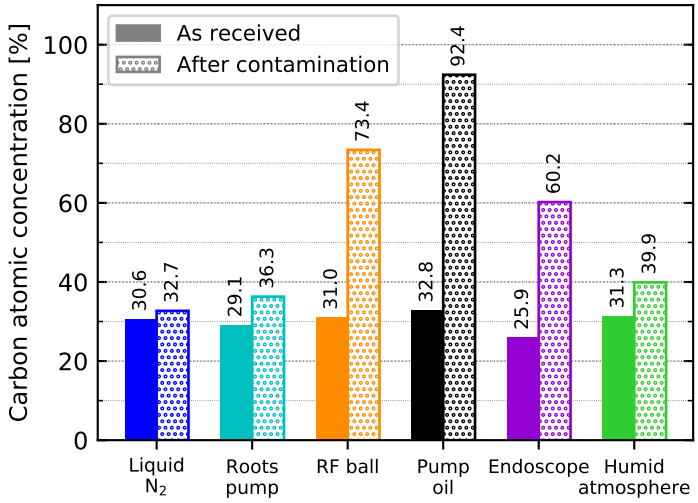

Figure 3.26: Carbon atomic concentration of the different samples of the contamination tests, before and after contamination.

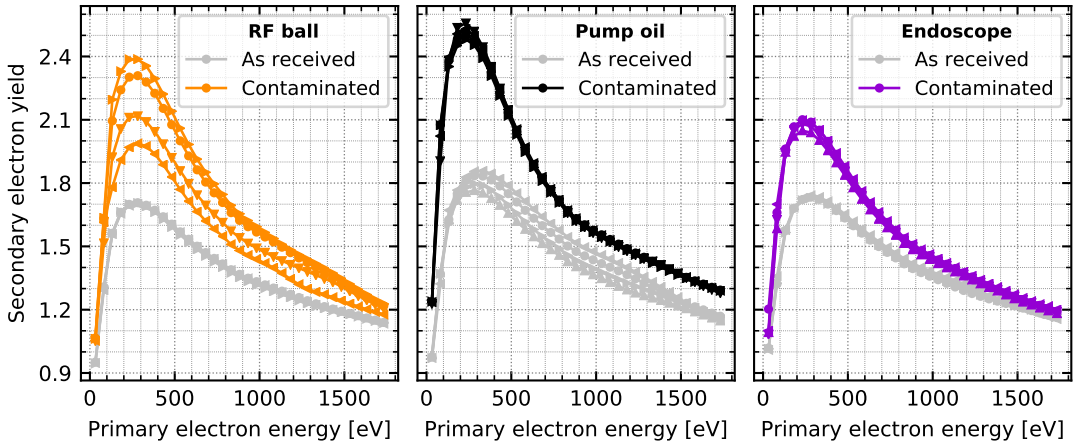

Figure 3.27: SEY curves before and after contamination of the samples scratched with RF ball (left) and endoscope (right) and contaminated with pump oil (center), for different locations on the surfaces.

3.5.1.3 Conditioning of modified surfaces

The conditioning curves of the different samples with a modified surface are shown in Fig. 3.28 together with the conditioning curve of a reference sample. Even though a large dispersion of average maximum SEY is observed just after contamination among the samples (points at a dose of 10^{-7} C/mm^2), a clear decrease of the maximum SEY is observed for all of them during irradiation at room temperature with electrons at 250 eV. In particular, for all but the pump oil sample, the decrease is observed to saturate in a maximum SEY range between 1.07 and 1.11 for a dose of about 5 x 10^{-3} C/mm^2. After irradiation with a dose of 10^{-2} C/mm^2, the ultimate maximum SEY value of 1.01 is reached for the pump oil sample. Thus, for all the samples, the conditioning is effective and the saturation dose and ultimate SEY are similar to the values observed for the reference sample. After a full conditioning process, each sample had a uniform SEY over its surface. It should be mentioned that during the conditioning, a change of the SEY curve shape, in contrast with the usual smooth behaviour, is observed for both the pump oil and the RF ball samples as seen in Fig. 3.29, where the curves exhibit a broken shape at a primary energy of about 100 eV. Indeed, during irradiation of insulating materials such as pump oil or polycarbonate from RF ball, the bombarded surface may charge positively or negatively due to the holes created by leaving electrons when the SEY is above unity or the accumulated electrons when the SEY is below unity, respectively. This leads to the appearance of a surface potential which, in addition to internal effects influencing the transport of the produced secondaries, results in a modified secondary electron yield curve [145]. In the present case, the maximum SEY, clearly expected to be above unity, is therefore underestimated since, in particular, the positive surface potential will reduce the number of electrons escaping into vacuum. However, since this effect disappears with the increasing dose, due to the modification of the insulating layer into a more conductive one, the ultimate maximum SEY obtained at the saturation dose remains valid.

Several surface modifications are observed during the conditioning of the modified samples. As expected from the conditioning study presented in Section 3.2, surface cleaning is observed for all samples through the disappearing of $Cu(OH)_2$ component on the Cu 2p line and the decrease of the oxygen amount on the surface together with an increase of the copper one. The amount of carbon only slightly decreased, even for the most carbon contaminated samples. The C 1s lines of all the samples after full conditioning are shown in Fig. 3.30. A comparison between before (not shown here) and after the full conditioning of each sample shows that the conditioning induced a graphitization of the surface carbon layer. In particular, the low energy side of the C 1s lines, dominated by the sp^2 component, is overlapping for all the samples. However, differences of intensity are visible in the high energy tail of these lines, suggesting that globally, the carbon layer remains different from one sample to another. No correlation between the height of this tail and the ultimate SEY of the corresponding sample could be found, in contrast with the case of amorphous carbon thin film coatings [122].

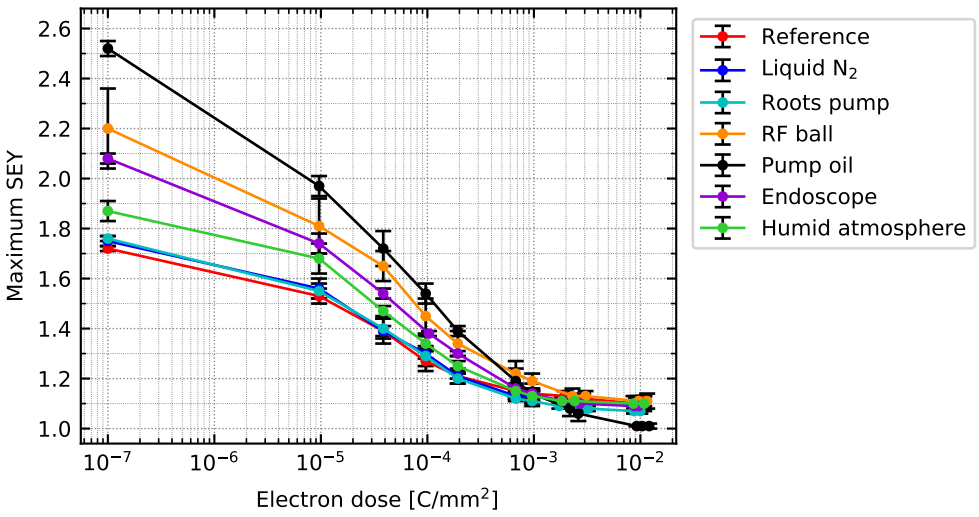

Figure 3.28: Conditioning curves of the beam screen samples after different surface modifications. The conditioning of a non-modified beam screen surface is shown as a reference. The error bars correspond to the standard deviation of the maximum SEY acquired in 4 different locations of the sample.

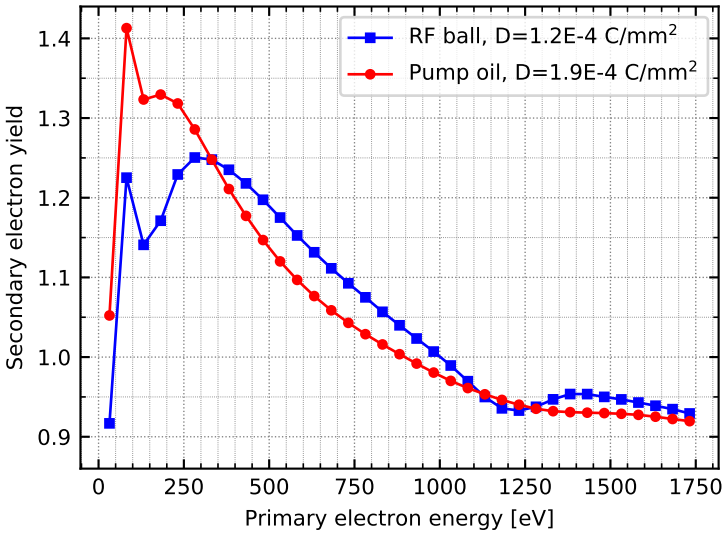

Figure 3.29: Examples of deformed SEY curves induced by a possible charging effect

3.5.2 Hypothesis 2: beam screen surface anomalies present before LS1

In this second scenario, we consider the following possible sequence of events. The surface of the beam screens was already abnormal before LS1, namely at their installation or consecutively to the accident and repair of 2008-2009. The first conditioning of these surfaces during Run 1 took place as expected from a nominal surface. However, because conditioning induces surface chemical modifications, including the break of chemical bonds, the conditioned surface is more reactive than an air exposed one. During the first venting of the conditioned abnormal beam screen surface, i.e. during LS1, the surface would have reacted and a new product would have built up on top of it. This

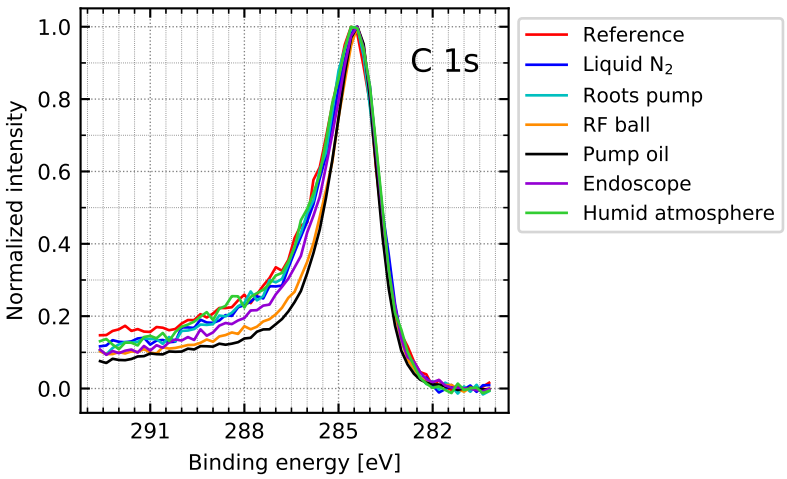

Figure 3.30: C 1s lines of the different modified samples after full conditioning.

new product would then have prevented the beam screen re-conditioning at its exposure to the electron cloud during Run 2.

3.5.2.1 Possible events

The most evident possible source of surface modification during beam screen preparation sequence is the cleaning step of the beam screens themselves. Indeed, the possibility of having detergent residues from the cleaning bath remaining onto the beam screen surface after cleaning should be considered. The effect of such an event on the conditioning and reconditioning of the beam screen was thus assessed in the laboratory.

In addition, many of the classical interventions required during a shut-down and mentioned in the previous scenario (Section 3.5.1) already occurred during machine installation and commissioning or consecutively to the accidental venting and damage of the beam pipe in 2008. Thus, the effect on a second conditioning of surfaces possibly contaminated by these interventions also needs to be assessed. It is worth mentioning that an eventual role of the contamination of the beam pipes induced by the accident itself (chips of multi-layer insulation blanket inside the beam pipes, soot [6]) in the current LHC heat load picture is discarded since the accident occurred in the arc 3-4 which is actually one of the lowest heat load arc (see Fig. 1.7 and 1.10).

Finally, inspections of spare beam screens from the stock, ready for insertion in LHC magnets, were also performed, looking for any possible anomalies.

3.5.2.2 Detergent contamination

To asses the effect of detergent solution remaining on the beam screen surface after rinsing, different samples were prepared by pouring cleaning solutions at 100%, 10% and 1% of the nominal detergent concentration used in the cleaning bath (see Section 2.3) on beam screen samples from the stock and letting the solution naturally drying in air. Here again, the amount of contaminant was deliberately exaggerated with respect to the

real case, to amplify any possible effect. The samples were then conditioned, nitrogen vented and exposed to air, and reconditioned.

After pouring the detergent solution and drying of the liquid, the samples surface was visibly darker. XPS analysis of these samples revealed the presence of sodium, potassium, phosphor and sulphur in addition to the expected carbon, oxygen and copper elements. The surface atomic concentrations of these elements for the different samples are given in Fig. 3.31 (left), together with values for a reference non-contaminated beam screen sample from the stock. The presence of these additional elements is compatible with the chemical formula of the detergent [125] and their amount coherently increases when increasing the concentration of the detergent solution poured on the sample. The detailed analysis of the different chemical compounds present on the surfaces is complex due to the large variety of possible compounds and is beyond the scope of this study. However, the binding energies of the contamination elements is similar on all the three contaminated samples. In particular, the binding energies of K 2p (293.4 eV), P 2p (133.7 eV) and S 2p (168.7 eV) can be ascribed to the presence of copper sulphate $CuSO_4$ and tripotassium phosphate K_3PO_4 [120, 146]. The position of the O 1s line above 531.5 eV and of the Cu 2p one above 934 eV, as well as the presence of the characteristic Cu^{2+} satellite is compatible with the presence of the above-mentionned species, eventually in an hydrated form, and the presence of copper hydroxide and chemisorbed oxygen [132, 147].

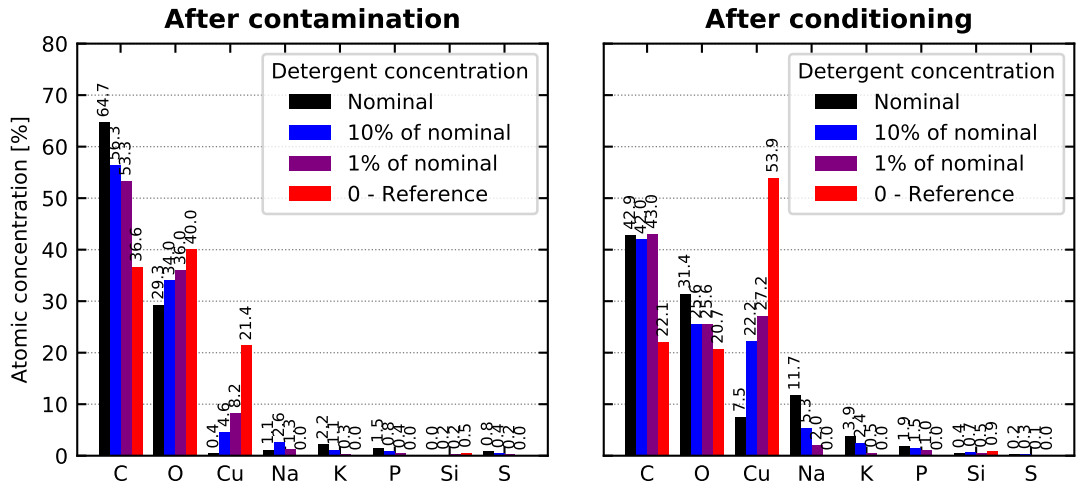

Figure 3.31: Surface atomic concentration of the different elements found on the 3 samples contaminated with detergent residues just after contamination (left) and after conditioning (right). A non-contaminated sample is shown as a reference.

The conditioning curves of the three contaminated samples are given in Fig. 3.32, together with a reference non-contaminated beam screen sample. The error bars correspond to the standard SEY deviation over 4 locations of the samples. The maximum SEY of the three prepared samples is strongly affected by the contamination (points at a dose of 10^{-7} C/mm^2). The more concentrated the detergent solution, the higher the maximum SEY after contamination.

The contamination of the surface by the most diluted detergent solution only seems to affect the maximum SEY before conditioning, the subsequent evolution of the SEY

during irradiation following the one of the reference sample. However, for the two most contaminated samples, i.e. detergent concentrations of 100% and 10%, the conditioning behaviour is radically different from a normal copper surface. Indeed, the maximum SEY decreases in the first steps of irradiation, but for an electron dose greater than 10^{-3} C/mm^2, the maximum SEY of both samples starts increasing and the samples get strongly inhomogeneous as seen by the increasing error bars. No charging effect was observed for these surfaces. When the conditioning was stopped, after an irradiation dose of 3-4 $\times$ 10^{-2} C/mm^2, the SEY increase did not yet saturate. The average maximum SEY were then 1.58 and 1.92 for the 10% and 100% of nominal concentration samples respectively.

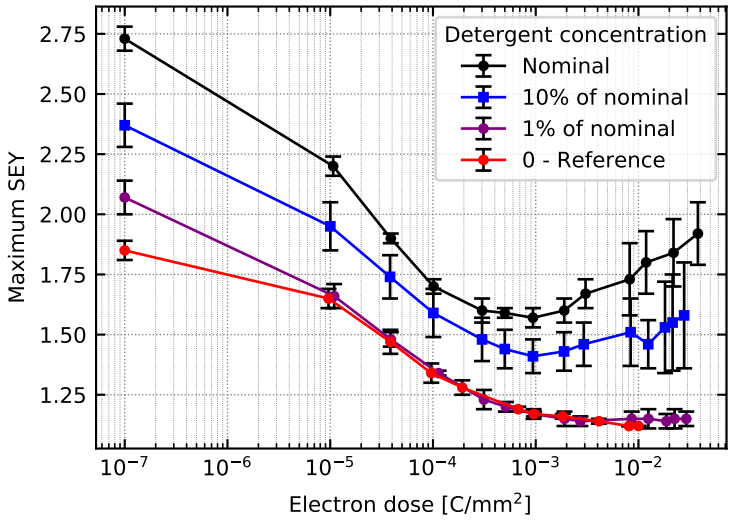

Figure 3.32: Conditioning curves of beam screen samples after contamination of their surface with residues of detergent solutions at different concentrations. The conditioning curve of a non-contaminated sample is given as a reference.

After their first conditioning, the detergent contaminated samples were wrapped in aluminium foil and stored for 10 to 15 days in a polyethylene bag in air. Their reconditioning was then performed, looking for any difference of behaviour with respect to the first irradiation. The reconditioning curves for the most (nominal detergent concentration) and the least (1% of nominal concentration) contaminated samples are given in Fig. 3.33, together with their respective first conditioning curve. For the most contaminated sample, the maximum SEY after storage is similar to the one measured at the end of its first conditioning. The second irradiation leads then to a non-monotonic evolution of the maximum SEY, i.e. sequence of decreases and increases, which finally stabilizes at about 1.65 for a dose of 10^{-2} C/mm^2. The dispersion of SEY over the surface remains significantly higher than for a non-contaminated sample. For the sample contaminated with a detergent solution at 1% of the nominal concentration, the reconditioning path is similar to the one for the first irradiation, and equivalent to a non-contaminated sample.

The atomic concentrations of the different elements present on the surfaces after the first conditioning are given in Fig. 3.31 (right). As expected from the conditioning study

presented in Section 3.2, surface cleaning occurred as visible from the decrease of carbon amount and increase of copper concentration with respect to the contaminated state. The contribution of $Cu(OH)_2$ on the Cu 2p line also disappeared. As a result, the amount of contaminant elements from the detergent, in particular Na and K, increased. The amounts of these elements for the different samples remain coherent with the respective detergent concentrations. Furthermore, line shifts are observed for these elements, but no coherence could be found between the detergent concentration, the SEY and the line shift of the different samples, neither for the conditioning nor the reconditioning. Therefore, the origin of the unusual conditioning behaviour of the most contaminated surfaces is not fully understood. In addition, the large inhomogeneity of the surfaces and the difficulty to perform XPS analysis in the exact same locations as SEY measurements with the experimental system used here make any correlation between surface chemical modification and SEY measurement not reliable. Accordingly, the most solid hypothesis which can be made concerning the origin of the unusual conditioning is the presence of alkali metals. Indeed, the presence of such elements, like potassium, is known to increase the secondary electron yield [103, 148].

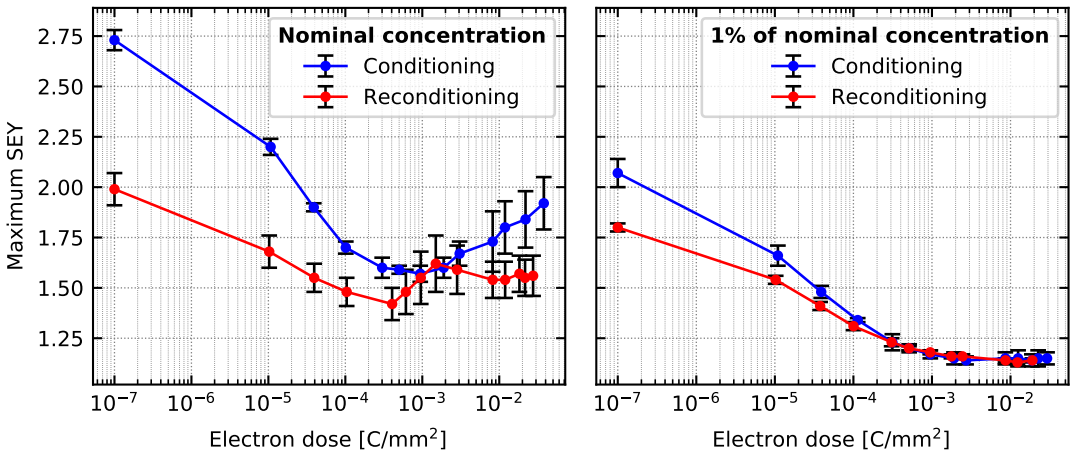

Figure 3.33: Conditioning and reconditioning curves of beam screen samples contaminated with detergent solutions at nominal (left) and 1% of nominal concentration (right). The samples were stored for 10-15 days between the two irradiations.

3.5.2.3 Contamination at installation / 2009 repair

Many of the considered contamination sources related to LS1 listed in Section 3.3 should also be considered to have possibly happened at machine installation or during the repair following the accident of 2008. Therefore, the reconditioning of the sample contaminated with pump oil and the one stored in humid atmosphere were performed. The corresponding reconditioning curves, acquired after 10 months in air and 9 months in saturated vapour pressure of water, respectively, are shown in Fig. 3.34. After 10 months in air, the maximum SEY of the pump oil sample remains below 1.60. This excellent preservation of the conditioning state is ascribed to the large amount of carbon present on the surface which was graphitized during the first conditioning and allows to keep a low

SEY thanks to a high chemical stability. Indeed, it is observed in Fig. 3.35 (left) that the low energy side of the C 1s line of the sample contaminated with pump oil is at the same position after storage as at the end of the first conditioning, while for the sample stored in humid atmosphere, carbon recontamination during storage led to a globally less graphitic carbon layer than at the end of conditioning (Fig. 3.35 (right)). During irradiation, the SEY decreases and the ultimate SEY and the dose required to reach it are similar to the values obtained during the first conditioning. After 9 months stored in saturated water vapor pressure, the maximum SEY of the corresponding sample is about 2, i.e. higher than before its first conditioning. The following reconditioning is identical to the one obtained in the first irradiation.

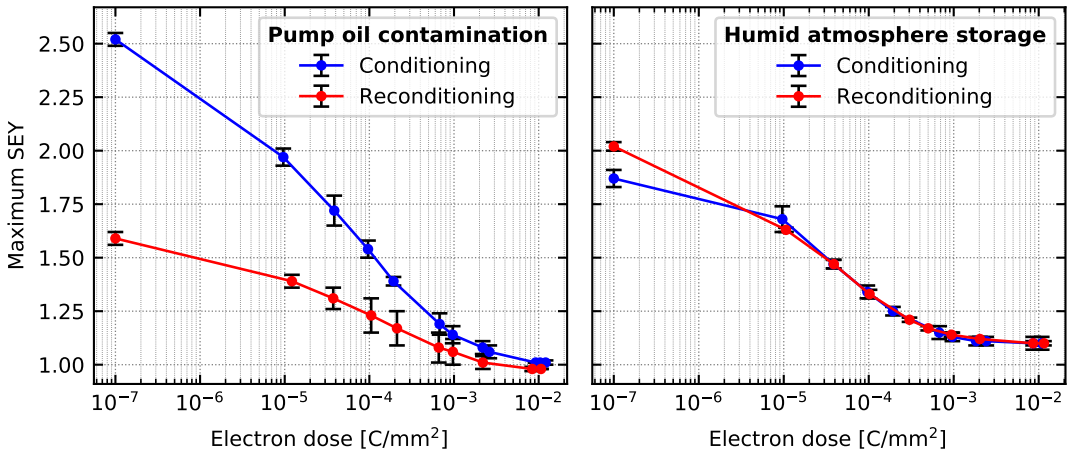

Figure 3.34: Conditioning and reconditioning curves of a beam screen sample contaminated with pump oil (left) and of a beam screen sample stored in saturated vapour pressure of water (right). The samples were stored for 10 and 9 months respectively between the two irradiations.

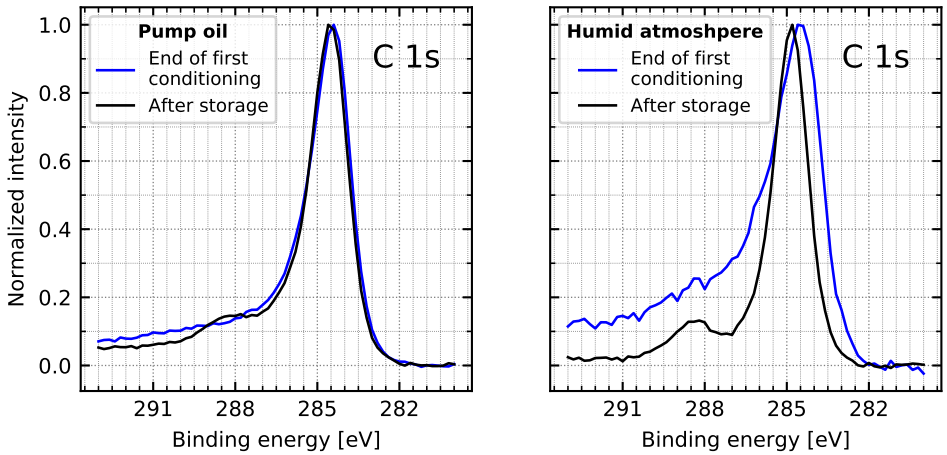

Figure 3.35: C 1s lines of the sample contaminated with pump oil (left) and of the one stored in humid atmosphere (right) at the end of the first conditioning and after the 9-10 months storage.

3.5.2.4 Inspection of spare beam screens

The hypothesis that beam screens with a non-conform copper surface could have been installed in the machine naturally led to perform visual inspections on spare beam screens from the stock, ready for insertion into LHC magnets. The first objective of these inspections was to prevent the installation of visually damaged or dirty beam screens during LS2, the second being to assess their conditioning behaviour.

Visual inspection consisted in carefully controlling the selected beam screens, either using an endoscope, or directly by eye, looking through the pumping slots. These inspections revealed the presence of dust, eventually in large amounts, which was, when judged to be necessary, removed by air circulation. Moreover, for two beam screens (assemblies HCVSSB_011-BU000096 and HCVSSB_012-BU000823), stains were visible on the copper surface, as shown in Fig. 3.36. From their aspect, the stains seem to result from the drying of a liquid. An endoscopic inspection performed inside one of the two abnormal beam screens revealed that the stains were only present at one extremity, over a length of 3.5 m. This observation could be related with the fact that, during the drying phase following the detergent cleaning and rinsing steps, the beam screens are slightly tilted, to help draining the liquid out of the pipes. The two incriminated beam screens were discarded from insertion, and samples were collected to investigate the origin and the impact of these stains in the laboratory. After cutting, a frontal visual observation as shown in Fig. 3.37 revealed that the stains observed in the two beam screen assemblies have actually different aspects.

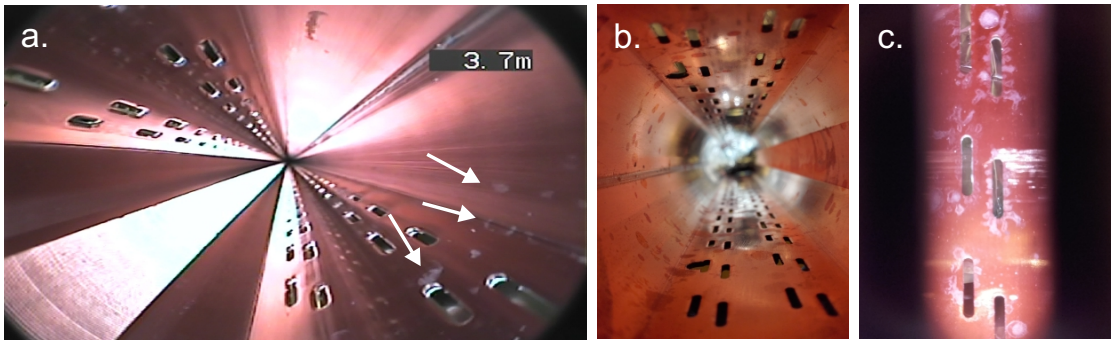

Figure 3.36: Visual inspection of spare beam screens revealing the presence of stains on the inner copper surface. (a) endoscopy of assembly 096, the presence of stains is indicated with white arrows, (b) and (c) direct observation of assembly 823.

Scanning electron microscope (SEM) observations were performed on both assemblies to determine the morphology of the stains, in particular to clarify whether they correspond to a deposit onto the copper surface. The SEM pictures of assembly 823 are presented in Fig. 3.38. Two different morphologies were observed. The low magnification picture (Fig 3.38 (a)), shows a circular feature, as observed by eye. A zoom at the border of the feature (Fig 3.38 (b)) clearly shows three different areas: the stain, where small agglomerates are visible, a smooth surface and a peripheral zone where flakes are visible. A further zoom in the stain area (Fig 3.38 (c)) allows to see that, in the stain, the copper surface is etched and is partially covered by some spheres of about 2 µm

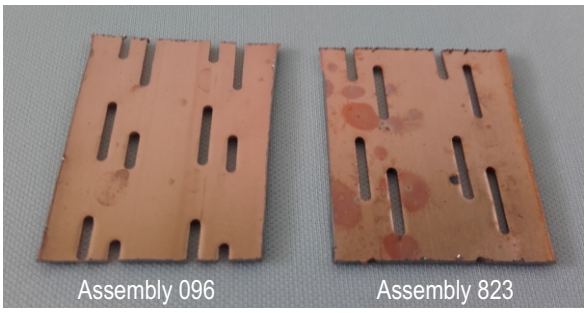

Figure 3.37: Samples cut from beam screen assemblies 096 and 823.

in diameter. Such a morphology was also observed on the assembly 096. On another location of the sample from assembly 823 (Fig 3.38 (d)), small crystals with a pyramidal shape are visible (Fig 3.38 (e) and (f)). Such features were not observed on the assembly 096. Energy dispersive X-ray spectroscopy (EDX) performed after SEM observation in the different locations revealed the presence of copper, carbon and oxygen on the surface. No trace of residues of detergent was found.

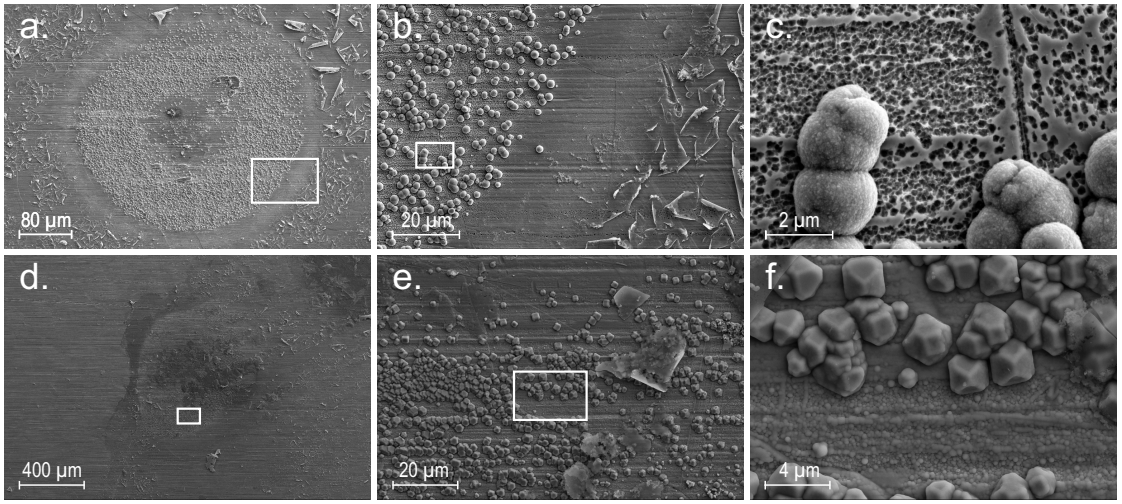

Figure 3.38: Scanning electron microscope observations of a stain present on the assembly 823 in different locations. (a) circular feature (b) zoom in the region delimited by the rectangle in (a), (c) zoom in the region delimited by the rectangle in (b), (d) observation at the limit of the stain: the healthy part is on the left side of the picture, (e) zoom in the region delimited by the rectangle in (d), (f) zoom in the region delimited by the rectangle in (e).

To investigate the eventual impact of such stains on the behaviour of the surface with respect to electron cloud, secondary electron yield measurements and conditioning experiments were performed on samples presenting the stains. XPS analyses were also carried out to gain understanding on the nature of the traces. The surface analysis was performed on the SPECS system, before SEM observations.

SEY curves acquired on the sample from both assemblies, in the exact regions which were later observed by SEM, are shown in Fig. 3.39. For measurements acquired inside the stain areas, a clear charging effect is observed, through the deformation of the SEY

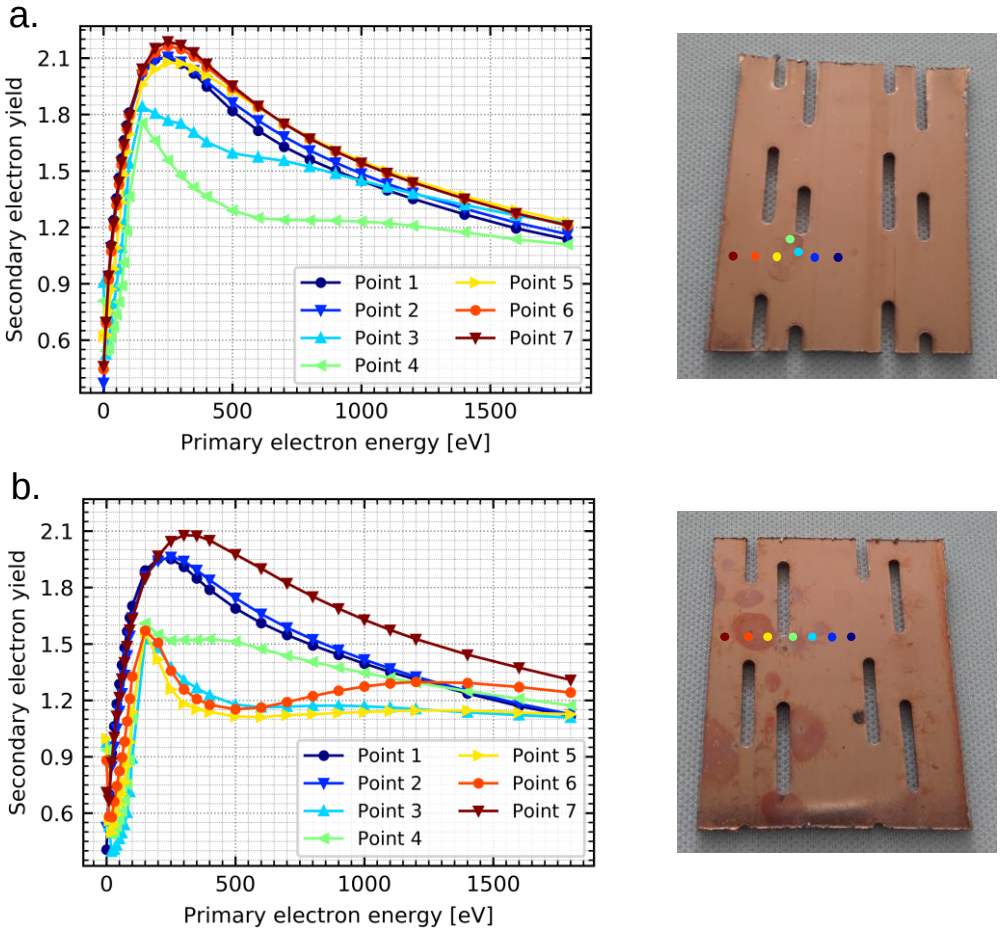

Figure 3.39: SEY curves and corresponding positions of the measurements for the assembly (a) 096 and (b) 823.

curve (broken shape at the expected position of the maximum, flat curve above). Outside of the affected zones, the SEY curve shape and values correspond to the expected one for normal copper.

XPS spectra aquired in the stains were affected by the surface charging, resulting in deformed and shifted peaks towards higher binding energies for all the elements. The example of the Cu 2p line, acquired on assembly 823, is given in Fig. 3.40. It should be mentioned that the persistence of a contribution at the expected binding energy of 932.7 eV demonstrates the presence, within the escape depth of the photoelectrons, of non-charging parts. This is compatible with the SEM observation of both assemblies showing small spheres/crystals on an etched copper surface. Outside of the visible stains, the XPS spectra are similar to the one of normal copper. Due to the close binding energies of the different possible compounds, in particular for copper, the access to the chemical state of the different elements was not possible. However, it was confirmed that the only elements present on the surface were the expected ones (Cu, O, C), in expected amounts and the presence of detergent residues was discarded here as well. Similar observations were performed on the sample from assembly 096.

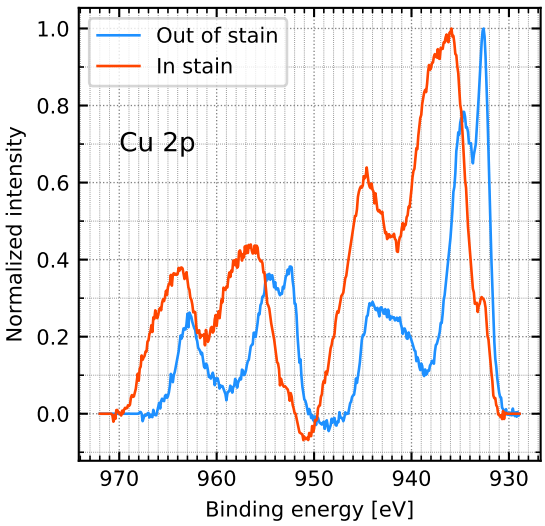

Figure 3.40: Cu 2p lines acquired in different positions of the sample from assembly 823. A clear charging effect is visible from the shape and the position of the different peaks in the affected area with respect to a non-affected one.

Since samples from both assemblies exhibit similar surfaces, only conditioning of sample from assembly 823 was carried out. The SEY curves corresponding to different doses are shown in Fig. 3.41 for measurements performed at position 3 (inside a stain, see Fig. 3.39). For electron bombardment up to 10^{-4} C/mm^2, charging of the surface is still present. However, it disappears for higher irradiation doses. A normal SEY curve shape is recovered and the maximum SEY is about 1.07 for a dose of 7.7 x 10^{-3} C/mm^2 as expected for normal copper. The subsequent irradiation of the other stains of the sample by a dose of 1.6 x 10^{-2} C/mm^2 (lower limit of the real dose, the actual one may be greater due to the small dose received by the neighbour parts during the irradiation of the previous stain) confirmed the low and conform ultimate SEY reached also in these areas.

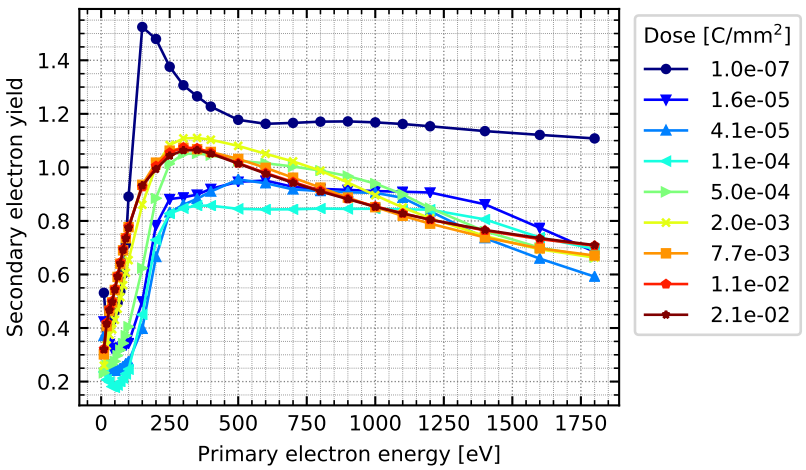

Figure 3.41: SEY curves acquired in a stain of assembly 823 during electron irradiation at 250 eV.

Thanks to the disappearing of the charging effect, XPS analysis allowed to clarify the chemistry of the surface after conditioning. The C 1s, O 1s and Cu 2p lines taken in affected (stain) and non-affected areas of the sample from assembly 823 after conditioning are given in Fig. 3.42. The position of the main C 1s peak at 284.6 eV is similar for the two lines and corresponds to the expected position for normal copper after conditioning. This proves that graphitization occured, even in the affected area of assembly 823. An additional contribution at 289.4 eV is found in the affected zone, which is ascribed to carbonate group (-CO_3^{2-}) [149]. Since only carbon, copper and oxygen were found on the surface, this suggests the presence of copper carbonate $CuCO_3$. The presence of a component at 531.4 eV on the O 1s line is also compatible with the presence of $CuCO_3$ [150]. The Cu 2p line exhibits a satellite structure above 940 eV typical of the presence of CuO [131], as confirmed by the shoulder at 933.6 eV [131] and the presence of a contribution below 530 eV on the O 1s line [131]. The observed Cu 2p line shape is significantly different from the one expected for $CuCO_3$ [149]. However, taking into account the amount of surface carbon in carbonate form (about 6.3 at.% as estimated from the area of the main and secondary C 1s peaks), the 1:1 ratio of copper to carbon in $CuCO_3$ and a surface copper concentration of 56.7 at.%, only 11% of the total amount of copper is found in $CuCO_3$ form, and is thus not expected to give the typical shape of pure $CuCO_3$ to the Cu 2p line. In the non-affected area, the Cu 2p and O 1s lines are, as expected from a regular copper surface after irradiation, compatible with the presence of Cu_2O.

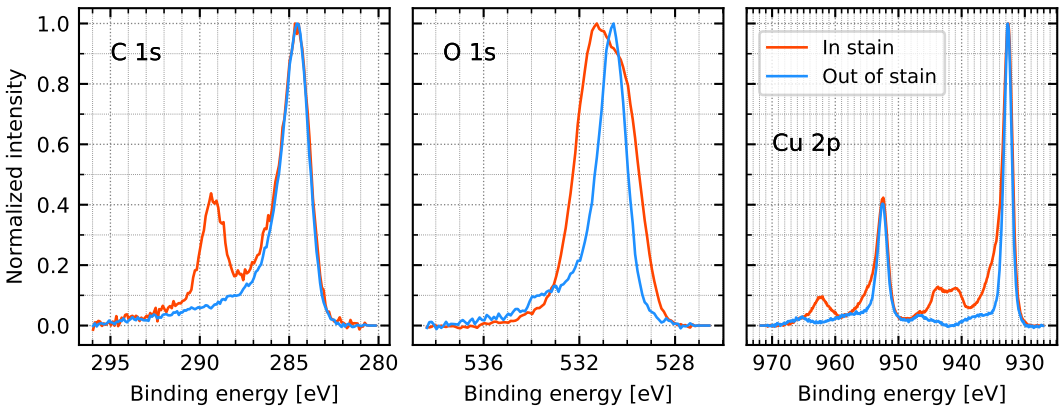

Figure 3.42: C 1s, O 1s and Cu 2p lines of the sample from assembly 823, after a conditioning dose of 2.1 x 10^{-2} C/mm^2.

3.5.3 Conclusions on the conditioning of modified surfaces

Among all the tested possible sources of contamination related to LS1 activities, several of them were found to have a significant impact on the chemistry of the surface, leading to an increase of the secondary electron yield of the samples. However, all these modified surfaces were found to properly condition under irradiation with 250 eV electrons at room temperature. Indeed, the maximum SEY of all the samples was found to decrease and the decrease saturates at a value and for a dose similar to the ones observed for a

reference (non-contaminated) sample. It is worth mentioning that for samples heavily contaminated with an insulating compound (pump oil, polycarbonate from RF ball), charging of the surface is observed during the conditioning, and disappears for greater doses. Such a charging effect could actually be more severe and persist for higher dose in the real machine environment, due to the cryogenic conditions. The reconditioning of some of the modified surfaces, in an attempt to reproduce the sequence 'surface modified at installation - nominal conditioning during Run 1 - reaction of the surface at LS1 venting - abnormal conditioning during Run 2', is also similar to the conditioning of a non-contaminated surface.

It is shown that a deficient rinsing of the beam screens after detergent cleaning, leading to detergent solution drying on their copper surface, can completely modify their conditioning. Indeed, for high enough detergent concentration, the maximum SEY was found to increase under irradiation. The reconditioning of these surfaces was also erratic and does not conform with the behaviour of a normal copper surface. A dedicated study would be required to fully understand the mechanisms behind this unusual conditioning behaviour. In particular, a monitoring of the surface chemistry and sample work function at each conditioning step and at the exact position of the SEY measurement could allow to explain the origin of this behaviour. In the frame of this study, the key point of these experiments lies in the fact that a beam screen, which dried with residues of detergent solution at a concentration below 1% of the nominal one on its copper surface behaves nominally with respect to conditioning. Thus, only a beam screen which dried with a detergent solution at a concentration above 1% of the nominal one could be problematic once installed in the machine. However, according to these experiments, such a beam screen would already have behaved erratically during its first conditioning in Run 1, but no heat load anomaly was detected before LS1. In addition, the UHV cleaning process of the beam screens involves two rinsing steps, the last one being performed by immersion of the pipes in a continuously purified ultra-pure water bath. Thus, the dilution factor associated with the rinsing of the detergent solution remaining on the beam screen after cleaning is expected to be more than a factor 100. The probability of having heavily detergent-contaminated beam screens in the machine is therefore judged to be very low.

Finally, visual inspections of spare beam screens from the stock revealed the presence of stains of different aspects in some pipes. In these stains, surface charging was observed upon electron and photon irradiation, and thus, no estimate of the real SEY value of the affected surface could be obtained with the used SEY set-ups. Due to charging, chemistry of the stains could not be elucidated by XPS for the 'as stored' state. For irradiation doses greater than 10^{-4} C/mm^2, charging of the surface is no longer observed. Electron bombardment of the affected surface finally results in a normal ultimate SEY obtained after the usual irradiation dose. After full conditioning, XPS revealed the presence of copper carbonate $CuCO_3$. This copper salt is not expected to form under electron irradiation since vacuum is a reducing atmosphere, but it most likely appeared during the drying phase as a results of reaction between copper, water and carbon dioxide CO_2 [151, 152]. Therefore, copper carbonate, eventually in a hydrated form [152] is assumed to be already present on the surface before irradiation. Furthermore, the presence of

this copper salt (insulator) which would be modified during conditioning (via creation of defects or transformation into a conductive compound) could explain the observed increase of sample conductivity. The presence of other compounds in the 'as stored' state which would be dissociated under electron bombardment and no longer exist after conditioning cannot be ruled out by XPS. In addition, the presence of CuO may result from the dissociation of $CuCO_3$ into CuO and CO_2 [152] under electron bombardment. Other analytical techniques such as Fourier Transformed Infrared Spectroscopy (FTIR) are being considered to clarify the surface chemistry of the 'as stored' state. As a consequence of these observations, systematic visual inspection of the beam screens is now performed before their insertion into magnets, to prevent the installation of abnormal beam screens inside the machine. In the particular case of the present study, a second conditioning of these surfaces with stains would be required, to assess if they could have a detrimental effect only after a first conditioning-venting cycle and therefore explain the observed LHC heat load.

In conclusion, based on these experiments at room temperature, none of the induced or already existing modifications of the beam screen copper surface could be held responsible for the observed LHC heat load. However, since this test campaign evidenced the potential presence of charging surfaces in the LHC, and taking into account that the behaviour of such surfaces under electron bombardment at cryogenic temperature and in a closed environment may be significantly different from the one observed in the laboratory, this work triggered a simulation-based study evidencing, in certain conditions, a non-negligible effect of surface charging on beam-induced heat loads [153].

Chapter 4

Conditioning of surfaces in the LHC arcs

The opportunity of analysing surfaces exposed to the proton beam during LHC operation occurred both during the EYETS 2016-2017 and during the LS2 (2019-2020). This chapter describes the results of secondary electron yield measurements and surface chemical analysis performed on vacuum components exposed to the electron cloud developing in the machine. In particular, the surfaces of beam screens extracted from a low and from a high heat load magnet are compared. The characteristics of such surfaces are also compared with those of surfaces conditioned in the laboratory, to gain understanding in the *in-situ* mechanisms of copper conditioning.

4.1 First surface analysis of LHC extracted vacuum components

4.1.1 Context

During the EYETS 2016-2017, a faulty LHC dipole located at the position A31L2 in the middle of the arc 1-2 of the LHC was exchanged. The opportunity was therefore taken to perform, for the first time, SEY measurements and XPS analyses on surfaces exposed to the proton beam during LHC operation, with the objective of investigating beam-induced effects on the surface properties. A schematic of the environment of the extracted magnet in the LHC is given in Fig. 4.1 (a). To proceed with the magnet extraction, the full arc 1-2 was warmed up to room temperature, and its two beam lines were vented from the arc extremity with pure nitrogen. Then, to check for any eventual beam pipe obstruction the so-called RF ball was pushed into the two beam lines by filtered air from the tunnel. The Plug-In Modules located at the extremities of the two vacuum pipes of the magnet in A31L2 were then cut, and the beam lines of the A31L2 and of the neighbouring magnets were closed with Viton-sealed caps. Finally, the magnet was removed from its position in the ring, brought to the tunnel access pit, where it was lifted to a surface facility. There, the beam screens were extracted from the cold bores: sections of 2-5 cm were cut with a clean saw, by hand and without

lubrication at different longitudinal positions (i.e. along the beam axis, see Fig. 4.1 (b)) in field and field-free regions. Some pumping slot shields (see Fig. 1.6) were selected for laboratory analysis. Finally, to fit the beam screen sections on the sample holder of the surface analysis system and to allow for analysis of their inner surface, the sections were cut in six pieces as shown in Fig. 4.2. After extraction from the magnet, the different components were wrapped in aluminium foil, and kept in a PE bag in air. From the moment of the RF ball passage to their laboratory analysis, the samples were therefore exposed to air for 1 to 4 months. In particular, the analysis of the beam screen sections from the vacuum line 2 (V2, where Beam 2 is circulating, see Fig. 4.1 (b)) was performed after the one of V1 components (hosting Beam 1). A schedule of the different steps from the beam lines venting to the analysis of the components is given in Table 4.1.

The cryogenic instrumentation of the A31L2 half-cell, i.e. the implementation of extra-thermometers on the beam screen helium cooling circuit at the interconnection between magnets, occurred only during the EYETS, in parallel with the magnet exchange. Therefore, the heat load associated with the extracted magnet is not known.

If not mentioned otherwise, the analyses presented in the following were performed on the SPECS system, which allows for precise (millimetre) positioning of the sample and for a precise matching of the area analysed by XPS with the spot where the SEY is measured.

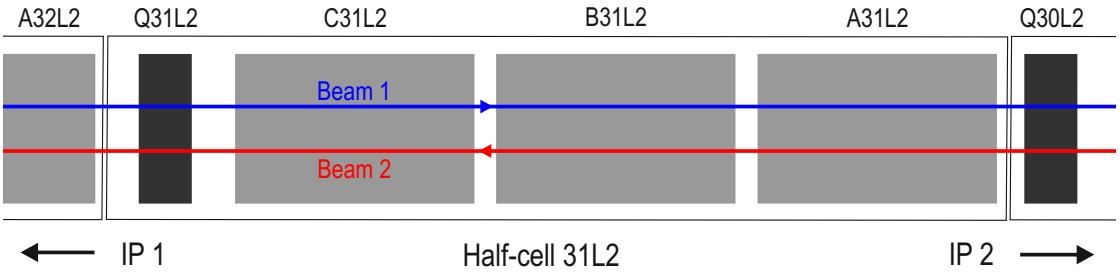

(a) 31L2 LHC half-cell

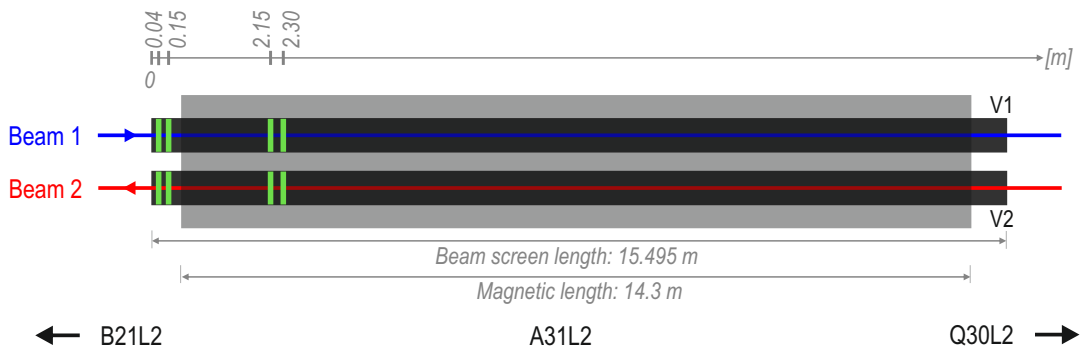

(b) A31L2 location

Figure 4.1: (a) Situation of the A31L2 location in the LHC, (b) A31L2 location: position of the beam screen sections cut for analysis (green stripes).

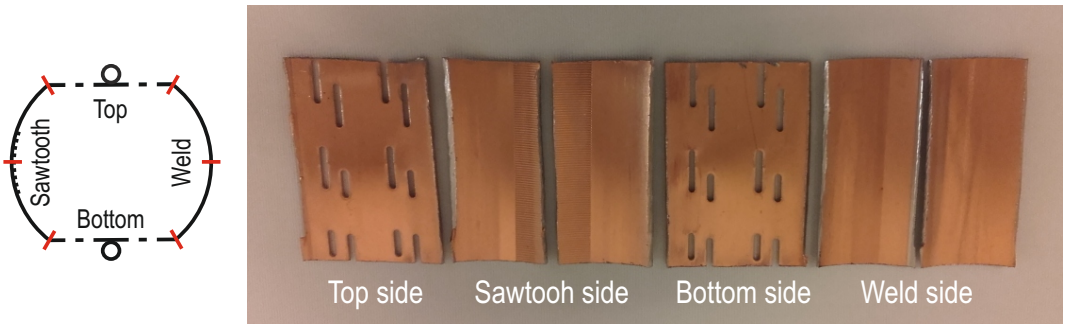

Figure 4.2: (left) Position of the cuts (in red) performed on beam screen sections to allow for their copper inner surface analysis. (right) Resulting samples.

Table 4.1: Schedule of the extraction and the analysis of vacuum components of the two beam lines of the dipole magnet located in A31L2.

	V1	V2
Beam lines venting with nitrogen	04.01.2017	
RF ball passage Filtered tunnel air	04.01.2017	
Vacuum component extraction Storage in Al foil + PE bag	07.02.2017	10.04.2017
Start of the analysis	10.02.2017	24.04.2017

4.1.2 Beam screens

Surface analyses were performed in different azimuthal positions of the beam screen sections, investigating possible differences of conditioning state induced by the confinement of the electron cloud by the field (see Fig. 1.12). The maximum SEY profiles for beam screen sections cut at different positions along the beam axis are given in Fig. 4.3. The maximum SEY range measured on beam screens from the stock (never installed in the LHC) is given for comparison.

For V1 beam screen, the maximum SEY of all the sections is globally between 1.6 and 1.85, i.e. the maximum SEY of the LHC extracted beam screen is significantly lower than the maximum SEY of beam screens from the stock. The observed scattering is above the error bars of the SEY measurement. For V2 beam screen, the maximum SEY globally ranges from 1.7 to 2.0, except for the sample at 2.13 m, which is rather between 1.9 and 2.2 and exhibits abrupt changes in SEY, such as when moving from top to sawtooth side (through a cut). In conclusion, V2 beam screen exhibits a higher maximum SEY than V1 beam screen on average, but remains globally below the SEY observed on beam screens from the stock.

In spite of the different spatial distributions of the electron cloud depending on the presence or not of a magnetic field (see Fig. 1.12), the sections collected in 'field-free' or

in 'in field' regions exhibit the same maximum SEY profiles beyond the scattering of the data. However, it should be noted that for the sections of V1 beam screen at 0.15 m and 2.3 m, the maximum SEY is lower at the position of the sawtooth profile. A geometric effect which would decrease the yield in the sawtooth profile is discarded since such a locally low SEY is not observed neither on V2 beam screen, nor on beam screens from the stock. In addition, the dimensions of the sawtooth pattern (40 µm height, 500 µm long) are not expected to influence the SEY [144]. Therefore, the observed minimum in the SEY profile could be a real effect, as induced by the impinging synchrotron radiation. Additional measurements would be required to obtain more statistics.

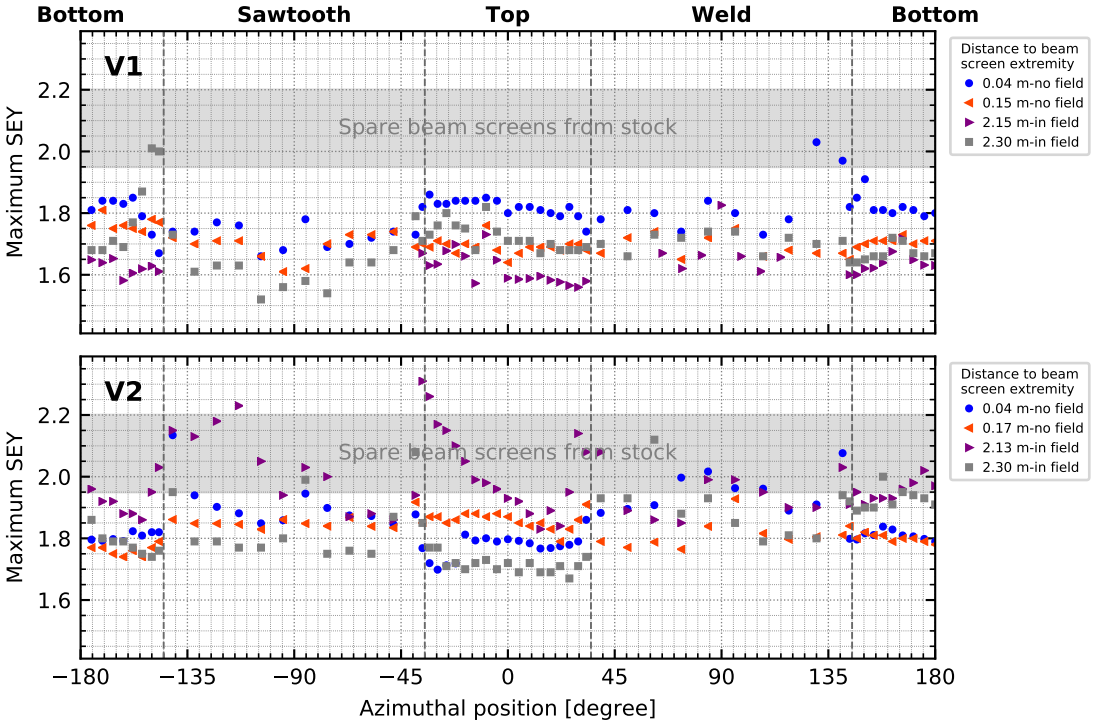

Figure 4.3: Maximum of the secondary electron yield as a function of the azimuthal position for different sections of the V1 (top) and V2 (bottom) beam screens extracted from the LHC dipole at location A31L2. The maximum SEY range measured on beam screens from the stock (never installed in the LHC) is given for comparison.

XPS spectra taken at different azimuthal positions reveal the presence of carbon, oxygen, and nitrogen on top of copper, as well as traces of usual contaminant (Si, Cl). The azimuthal profiles of carbon atomic concentrations are given in Fig. 4.4 for V1 and V2 beam screens. The amount of carbon ranges from 20 to 40 at.%, which is usual for air exposed surfaces. As for the SEY, the presence or not of a magnetic field does not seem to affect the profiles. In particular, in the field, the areas receiving the highest dose (top and bottom sides) do not exhibit a higher carbon amount, by opposition to observations in the SPS, where a dark trace identified as carbon, was observed on the stainless steel pipes at the position where the cloud is expected [118]. It should be mentioned that the points presenting a high carbon amount in the section located at 2.13 m from V2 beam screen extremity correspond to the points with a high SEY (see Fig. 4.3 (bottom)).

Such a high SEY could therefore be explained by carbon contamination. Even though the origin of the contamination cannot be ascribed with certainty, the discontinuity of the carbon content profile at the cut between the sawtooth and the top side suggests a contamination during the handling of the samples.

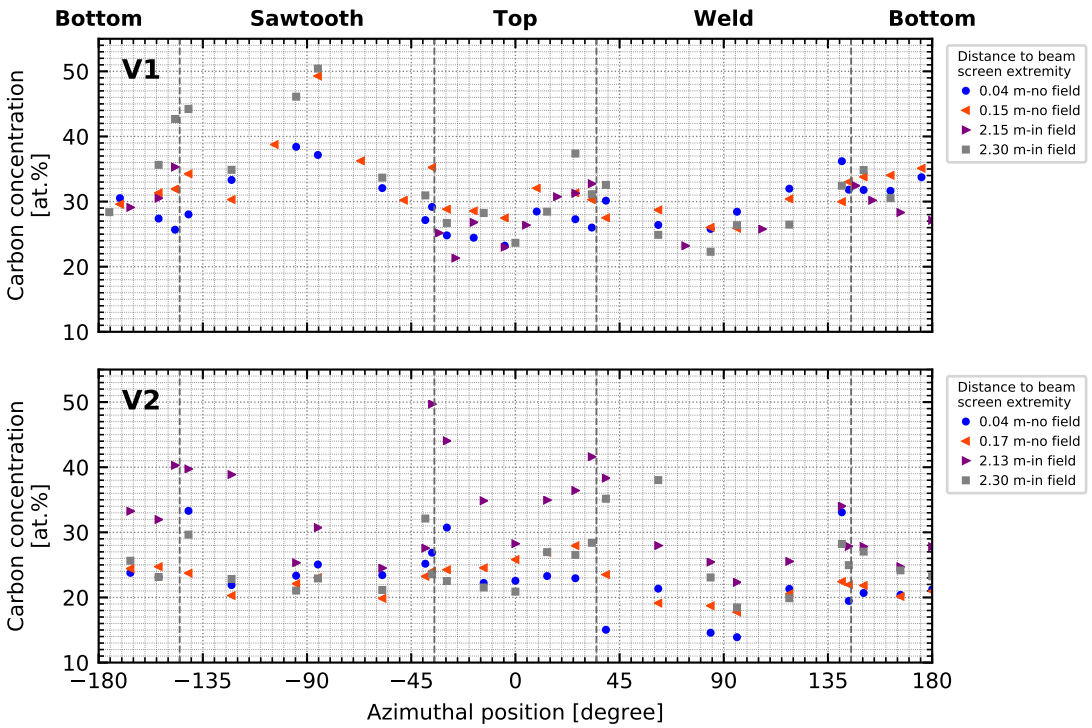

Figure 4.4: Atomic concentration of carbon measured by XPS for the V1 (top) and V2 (bottom) beam screens extracted from the LHC dipole at location A31L2.

The position of the maximum of the C 1s lines varies between 284.7 and 285.3 eV, therefore covering the range of values expected for both air exposed and conditioned surfaces. The energy of the C 1s line is randomly distributed all around the azimuth. However, it is worth mentioning that V2 beam screen presents, on average, a slightly higher binding energy for the C 1s line, as shown is Fig. 4.5.

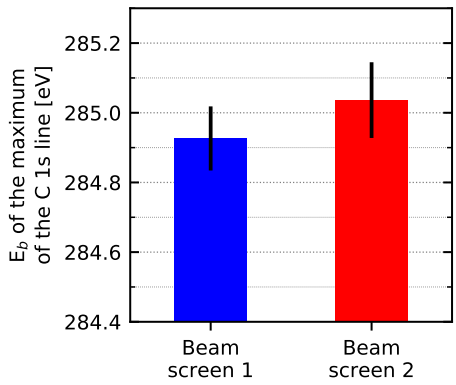

Figure 4.5: Average position of the maximum of the C 1s line for XPS spectra acquired in V1 and V2 beam screens. The error bars represent the standard deviation over ∼100 spectra.

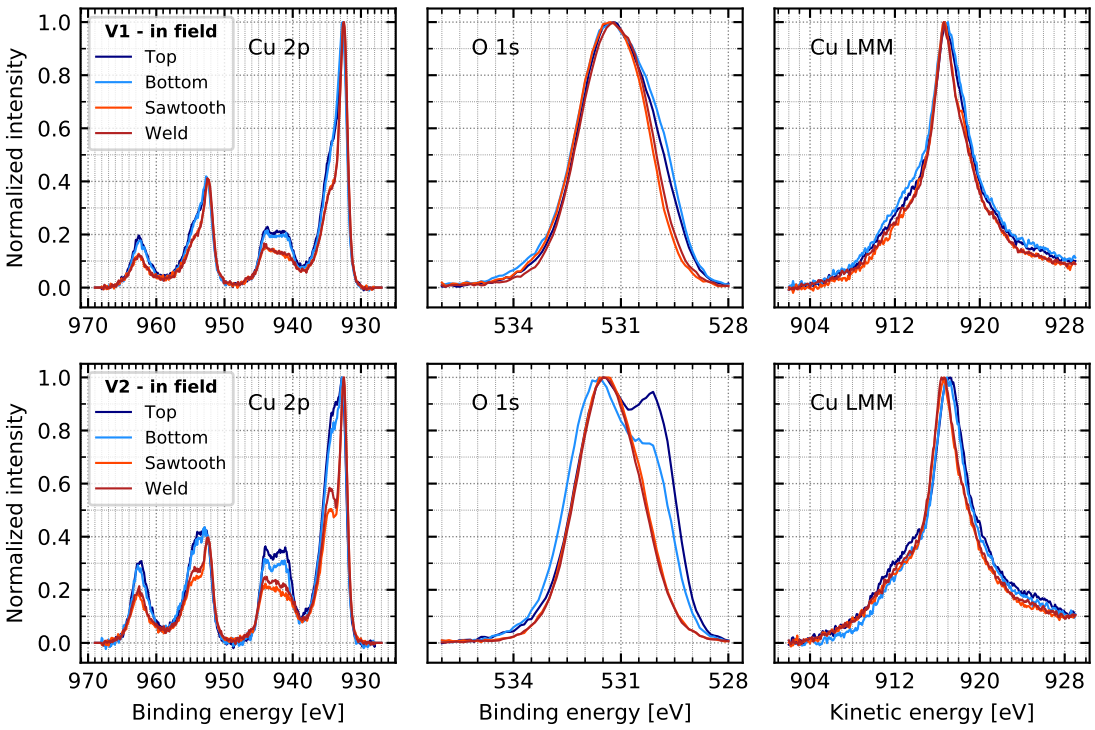

Figure 4.6: Cu 2p (left), O 1s (centre) and Cu LMM (right) lines for the samples at 2.30 m (in field) from the extremity of V1 (top) and V2 (bottom) beam screens, acquired in different azimuthal positions.

The Cu 2p, O 1s and Cu LMM lines for the sections located at 2.30 m of each beam screen extremity (i.e. in the dipole field) are shown in Fig. 4.6. For both beam screens, it clearly appears that the shape of the satellite of the Cu 2p line is different whether the spectrum was taken on a flat or on the lateral side. Indeed, for both beam screens, the satellite exhibits the characteristic shape associated with $Cu(OH)_2$ for the lateral sides [130], while it exhibits two bumps for the flat sides, showing the presence of cupric oxide CuO [130]. In addition, for the flat sides, the shoulder visible on the low energy side of the O 1s line of V1 beam screen and even more pronounced for V2 beam screen is compatible with the presence of CuO since the associated oxygen contribution is expected at 529.7 eV [131]. Furthermore, for these sides, the maximum of the Cu LMM line is shifted towards the higher kinetic energy, as expected for the presence of CuO [131]. Therefore, for these two beam screen sections, the faces receiving the highest electron dose and where the energy of the bombarding electrons is the highest exhibit different surface chemistry than the other faces. The intensity of the satellites and the shoulder at low energy on the O 1s line is higher for V2 than for V1 beam screen, suggesting a larger quantity of CuO on the flat sides of V2 beam screen. In addition, the bumps of the CuO satellites of V1 beam screen are less pronounced than for V2 beam screen. Therefore, the co-presence of CuO and $Cu(OH)_2$ on the flat sides of V1 beam screen cannot be discarded. Finally, from the intensity of the $Cu(OH)_2$ associated satellite, it is clear that the amount of $Cu(OH)_2$ is larger on V2 than on V1 beam screen.

The Cu 2p, O 1s and Cu LMM lines for sections located at 4 cm from the beam screen

extremities (i.e. in a field-free region) are shown in Fig. 4.7. For these two sections, no systematic difference is observed in the chemical state of copper between the flat and lateral sides of the beam screens. For both sections, the presence of Cu^{2+} is clear from the presence of the satellite on the Cu 2p line. The shape of this satellite, the O 1s line shape (maximum at 531.5 eV and shoulder at lower binding energy) and the position of the Cu LMM at 916.5 eV suggests the presence of both CuO and $Cu(OH)_2$. As for the sections in the field, V2 beam screen exhibits a higher satellite intensity.

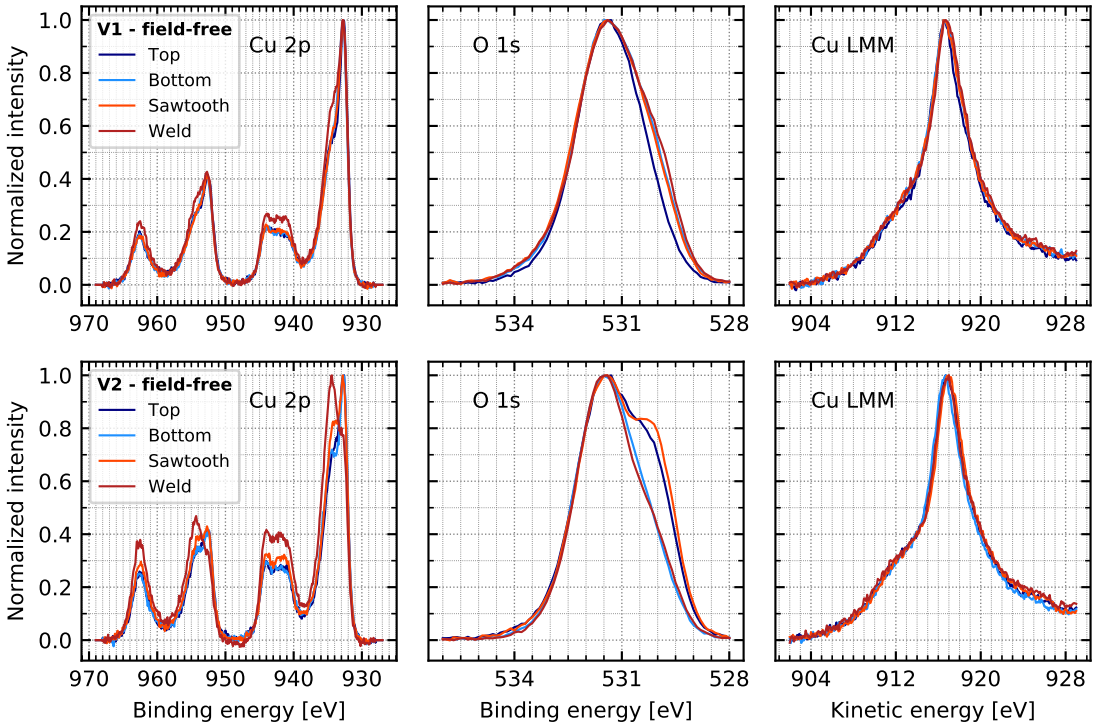

Figure 4.7: Cu 2p (left), O 1s (centre) and Cu LMM (right) lines for the samples at 0.04 m (field-free region) from the extremity of V1 (top) and V2 (bottom) beam screens, acquired in different azimuthal positions.

The conditioning of two samples (flat sides) in the dipole field of V1 beam screen was performed after 3 months of air exposure while a sample from V2 beam screen was conditioned after 1.5 year in air. The corresponding conditioning curves are given in Fig. 4.8, together with the conditioning curve of a reference beam screen sample, i.e. coming from a spare beam screen, never installed in the LHC. The conditioning experiments were carried out on the PHI system (SEY measured with a collector, non-monochromatic Mg Kα XPS source) after cutting the samples to 15 x 20 mm^2.

The two samples from V1 beam screen exhibit similar conditioning curves. In particular, as already clear from Fig. 4.3, the SEY before conditioning (dose = 10^{-7} C/mm^2) is lower than for the reference sample, and the ultimate SEY and the dose at saturation of the SEY decrease is similar to the reference sample ones. However, the relevant characteristic for the machine is rather the dose required to reach the electron cloud build-up SEY threshold (SEY = 1.25), which appears to be slightly lower for these two LHC extracted samples than for the reference. This would translate into a faster reconditioning

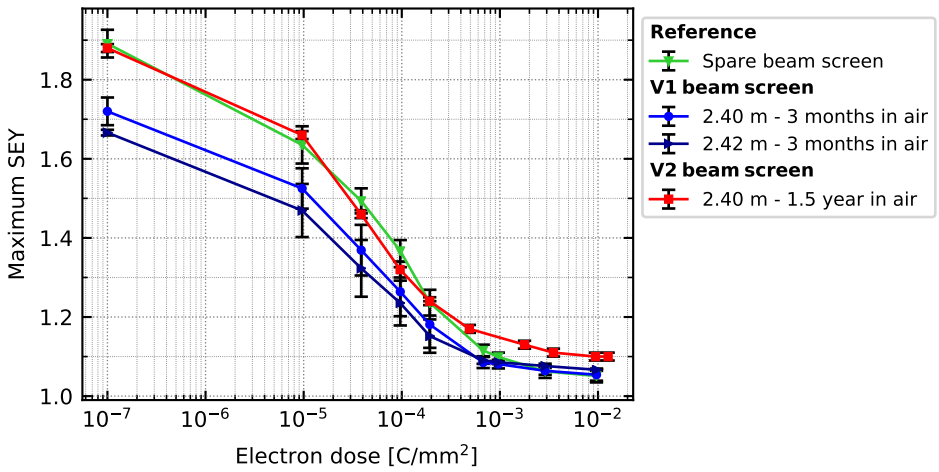

Figure 4.8: Conditioning curves of two neighbour samples located at 2.4 m from V1 beam screen after 3 months of air exposure and of a sample at 2.4 m from V2 beam screen, after 1.5 year of air exposure. The conditioning curve of a sample from a spare (never installed) beam screen is given as a reference. The error bars represent the standard SEY deviation over 3 different locations of the samples.

of the machine after the EYETS venting than for the first machine commissioning. For the sample from V2 beam screen, the 1.5 year of air exposure seems to have reset the conditioning state, since the maximum SEY before conditioning is the same as for the reference sample. The conditioning path is similar to the one of the reference sample up to 5×10^{-4} C/mm^2. For a higher dose, the decrease of the SEY of V2 beam screen slows down, ending up in an ultimate SEY of 1.1 for a saturation dose similar to the one observed for the reference. The ultimate SEY of the V2 sample remains thus slightly higher than the one of V1 and of the reference. However, the reached SEY value is significantly lower than the SEY threshold for electron cloud build-up, and therefore is considered to be sufficient to allow for a complete machine scrubbing.

The C 1s, O 1s and Cu 2p lines of these different samples are given in Fig. 4.9. The XPS lines were found to be identical for the two samples from V1 beam screen, therefore, only the lines for the sample at 2.40 m are shown. The sample from V1 beam screen clearly shows a usual chemical transformation during conditioning: the $Cu(OH)_2$ contribution (visible by the Cu 2p satellite shape and the position of the O 1s line at 531.5 eV) disappears, the C 1s line shifts to lower binding energies (i.e. carbon gets graphitized) and the bump around 288.5 eV disappears. The fully conditioned state of this sample is therefore similar to the one of the reference sample. Before conditioning, the sample from V2 beam screen is different from the one of V1 beam screen: the shoulder at low energy present on the O 1s line could result from the presence of CuO, as expected from the spectra presented in Fig. 4.6. The shape of the Cu 2p satellite suggests however that the top most surface is dominated by the $Cu(OH)_2$ copper product. After full conditioning of this surface, the O 1s line presents a higher intensity at 530 eV than the O 1s line of the reference, still compatible with the presence of CuO. Furthermore, the structure at 944 eV on the Cu 2p line is more pronounced on the LHC extracted sample

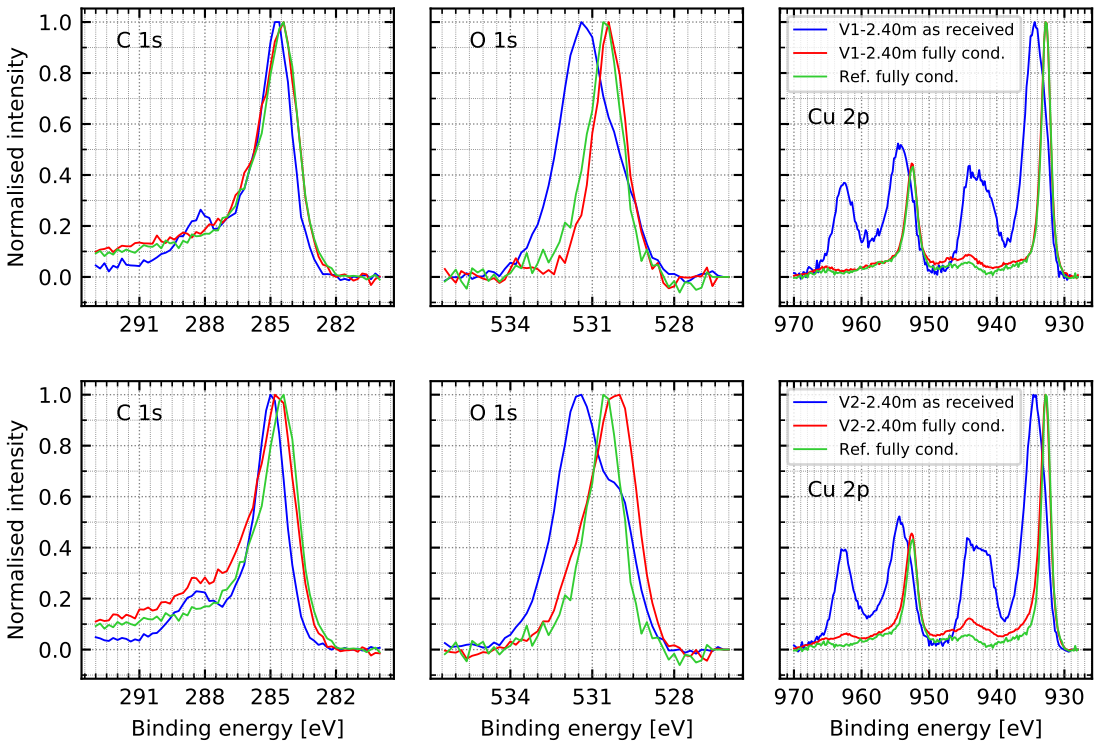

Figure 4.9: C 1s (left), O 1s (centre) and Cu 2p (right) lines of the samples at 2.40 m from V1 (top) and V2 (bottom) beam screens, before and after full conditioning. The fully conditioned state of a reference sample is given for comparison.

and could also result from the presence of CuO. Finally, even though the graphitization of this sample occured, as visible by the shift of the C 1s line, the high energy tail of the V2 beam screen sample is higher than for V1 beam screen and the reference sample. As demonstrated in Section 3.2, carbon plays a crucial role in the conditioning of air exposed copper. Therefore, the difference of the C 1s line between V1 and V2 beam screens as well as the lower amount of carbon on V2 beam screen (26 at.% against $\sim$ 40 at.% for V1 beam screen) could be responsible for their different ultimate SEY after full conditioning.

4.1.3 Pumping slot shields

During the extraction of the vacuum components of the magnet located in A31L2, the pumping slots shields, made of copper beryllium alloy, were also collected for laboratory analysis. Before their installation in the LHC, the surface of the shields was degreased and passivated in a chromic acid solution. SEY curves and XPS spectra were acquired along the beam axis on a section of the shield to investigate possible differences of conditioning state between areas exposed to the beam through the pumping slots and areas being masked from the beam by the beam screen (see Fig. 1.6).

A visual inspection of the side of the shield facing the beam screen revealed the presence of dark areas, corresponding to the beam screen pumping slots. These traces were well visible in some locations, and invisible in some others. Their origin will be

discussed more in details in Section 4.1.4. A picture of two sections of pumping slot shields cut at 35 cm and 85 cm from V1 beam screen extremity, i.e. in a field-free region and inside the dipole field respectively, are shown in Fig. 4.10, after 26h of air baking at 120°C. After the bake, the traces appear even darker. In particular the difference of color between the 'inside the trace' and 'outside the trace' areas suggests that the surfaces exposed to the beam got oxidized faster during the air bake [137]. For the sample cut from the region in the field (Fig. 4.10 (b)), the contour of the traces is well defined and the traces have exactly the shape of the pumping slots (see Fig. 4.10 (c)). For the sample outside of the field, the contour is blurry and the change of colouration extends outside of the exact shape of the slot. Such a difference is due to the confinement by the dipole magnetic field of the electrons which can move only along the field lines. Therefore, in the presence of a field, the area where the electrons can impact the pumping slot shield is restricted to the projection of the pumping slot onto the pumping slot shield (see Fig. 1.6).

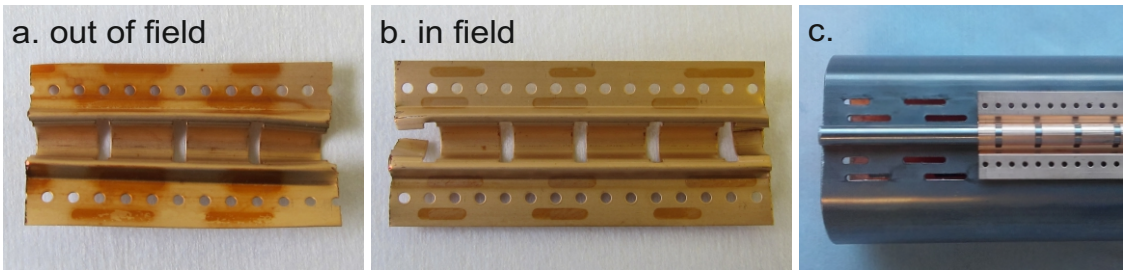

Figure 4.10: Samples of pumping slot shield from V1 beam screen, cut at (a) 35 cm (out of field) and (b) 85 cm (in field) from the beam screen extremity. To enhance the contrast of the dark areas visible after extraction of the shield from the magnet, an air bake of 26h at 120°C has been performed. (c) spare beam screen only half equipped with a pumping slot shield, to let the pumping slots visible.

SEY measurements were performed on a section of pumping slot shield located in the dipole field (as extracted, not baked). The resulting longitudinal maximum SEY profile is given in Fig. 4.11, where the grey stripes correspond to the dark traces observed on the sample.

From these measurements, it clearly appears that the maximum SEY is significantly and systematically lower in the dark areas, i.e. in the zones directly exposed to the beam, than in the areas which are sheltered by the beam screen. In addition, measurements were performed on a reference sample, namely on a pumping slot shield never installed in the machine. The maximum SEY of such a sample was found to be around 2 before conditioning and below 1.9 after conditioning in the laboratory followed by one week of air exposure. The SEY measured on the LHC extracted sample in its non-irradiated areas corresponds thus well to the SEY of a non-conditioned pumping slot shield, while in the irradiated areas, it matches with the SEY of a conditioned and air exposed pumping slot shield.

XPS analysis performed on the pumping slot shield evidenced the presence of chromi-

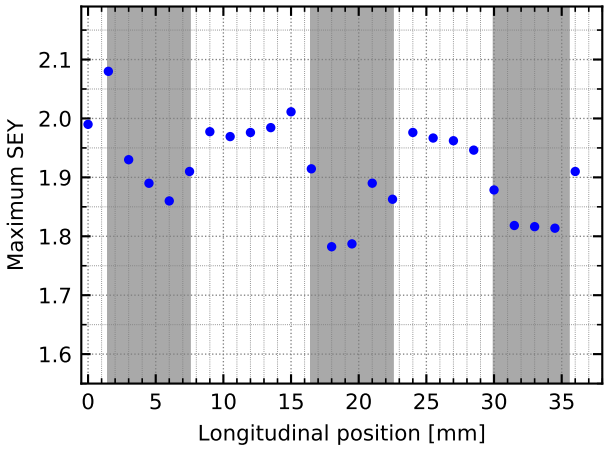

Figure 4.11: Maximum secondary electron yield as a function of the longitudinal position (arbitrary origin) for a pumping slot shield from V1 cut in the dipole field. The grey stripes correspond to the dark areas observed on the analysed sample.

um from the passivation up to 2.5 at.%, as well as about 20 at.% of beryllium, in addition to the usual elements. The amount of beryllium exhibits a wide dispersion between different shields. A dedicated study should be performed to evaluate the impact of the amount of beryllium found on the surface of the shields, since beryllium oxide is known to have a high SEY [154].

Cu 2p lines from XPS spectra acquired in different longitudinal positions are given in Fig. 4.12 (left). It is clear from the intensity of the satellite as well as from the height of the line around 934.8 eV that the irradiated area exhibits a lower amount of $Cu(OH)_2$ at its surface. This observation is systematic for all the points measured on this pumping slot shield: as shown in Fig. 4.12 (right), the ratio $I_{Cu(OH)_2}/I_{Cu,Cu_2O}$ is significantly lower in the beam exposed areas of the shield, as expected for a conditioned surface.

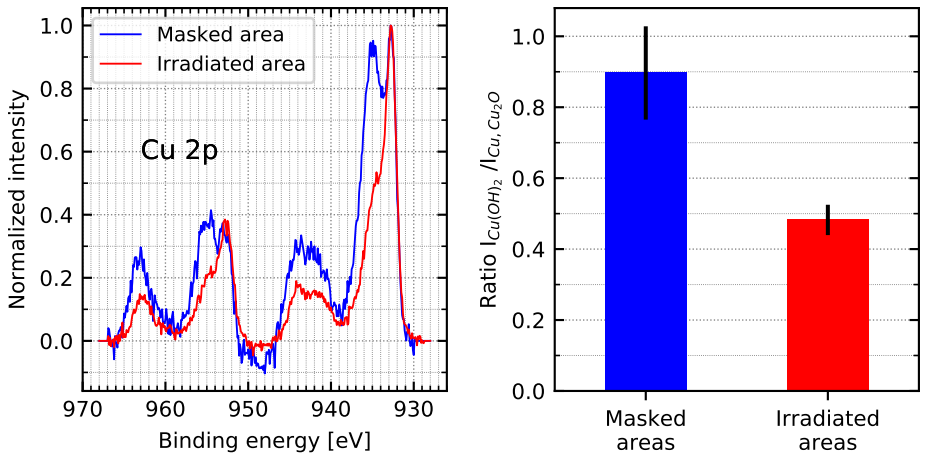

Figure 4.12: (left) Cu 2p lines acquired in masked and irradiated areas of a section of a pumping slot shield from V1. (right) Average ratio $I_{Cu(OH)_2}/I_{Cu,Cu_2O}$ for spectra acquired in and outside of the irradiated areas. The error bars represent the standard deviation over 5-6 spectra.

The C 1s lines acquired in and out of an irradiated area are displayed in Fig. 4.13 (left). Inside the irradiated areas, the C 1s line is found at a lower binding energy, i.e. the carbon is in a more graphitic form in the irradiated areas than in the masked ones. Furthermore, the amount of carbon in the two kinds of areas is equivalent, as seen from Fig. 4.13 (right).

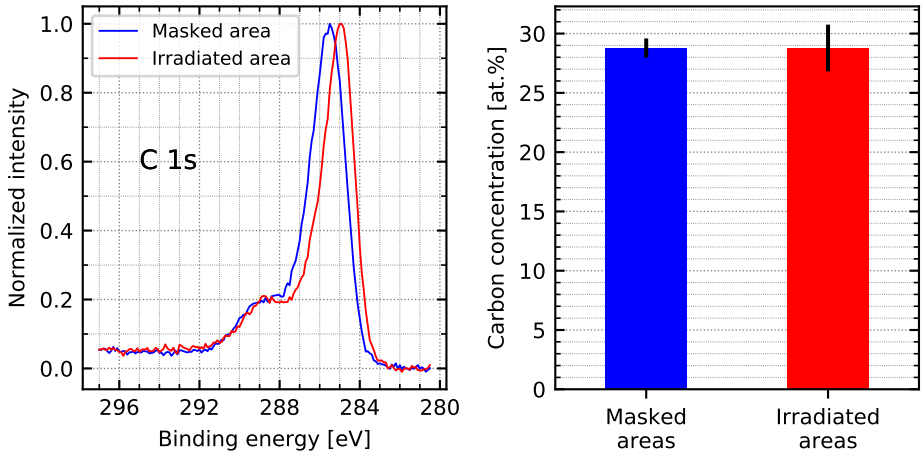

Figure 4.13: (left) C 1s lines acquired in masked and irradiated areas of a section of a pumping slot from V1. (right) Average carbon atomic concentration in masked and irradiated areas. The error bars represent the standard deviation over 5-6 spectra.

4.1.4 Observations after long air exposure

Beam screen samples were investigated again after 1.5 year of storage wrapped in aluminium foil, in a PE bag, in air. It was then observed that in some places, the copper faces of the top and bottom sides exhibit traces corresponding to the shape of the pumping slots. An air bake was performed to enhance the contrast and pictures of these surfaces after different times in the oven are given in Fig. 4.14. A reference sample, never installed in the LHC is also shown for comparison.

On the top side, the traces are lighter than the rest of the copper face after 3h15 at 120°C, but the contrast vanishes after 26h30. For the bottom side, the traces are clearly darker, i.e. more oxidized, than the rest of the material. Furthermore, they do not look complete: not the full slot, but only half of it is printed on the copper surface. Finally, for both top and bottom sides, a darker (more oxidized) stripe appeared in the center of the section, all along the beam axis, i.e. at the position of the helium capillary, but on the copper face. No specific feature was observed neither on the weld nor on the sawtooth side.

To understand whether the observed features result from the exposure of the surfaces to the beam and its related effects or are induced by the manufacturing processes of the beam screen (welding of the capillary for instance), the LHC extracted surfaces are compared with a spare beam screen. The flat side of the reference section also presents contrasts of oxidation (Fig. 4.14 (d)). However, no darker stripe in the central part, neither pumping slot pattern is observed on this sample. Therefore, the features observed

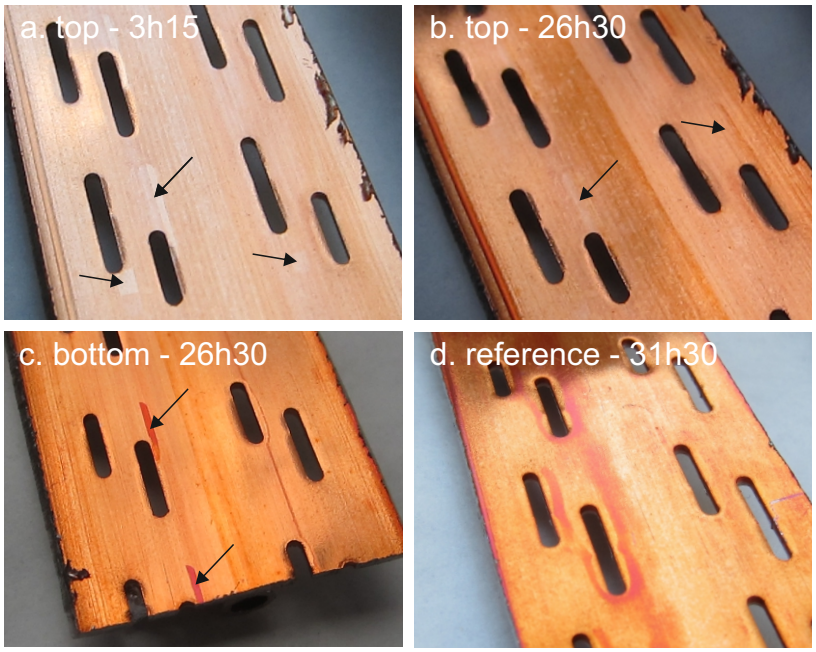

Figure 4.14: Air bake at 120°C of a section from V1 beam sceen, in the field, after 1.5 year of air exposure. (a) top side after 3h15, (b) after 26h30, (c) bottom side after 26h30, (d) spare beam screen never installed in the LHC after 31h30. The arrows indicate the position of the pumping slot-shape traces.

on the LHC extracted samples seem to be induced by the LHC machine operation, and may possibly result from different irradiation doses with respect to surrounding areas. Such an hypothesis is discussed in details below.

To understand how a pumping slot shape could get printed in such a way on the beam screen copper surface, the geometric configuration of the slots has to be considered. A schematic of the configuration is given in Fig. 4.15. The slots are punched into the colaminated stainless steel - copper flat sheet in such a way that when rolling the composite sheet into its final shape, the pumping slots of the two sides do not fully overlap, as shown in Fig. 4.15. It results in parts of the bottom beam screen surface facing the pumping slots, and therefore the pumping slot shield, of the top surface and vice versa. Taking into account this configuration, the pumping slot traces observed on the LHC extracted sample in Fig. 4.14 correspond to beam screen areas facing the pumping slot shield of the opposite side through its pumping slots.

Since a similar situation also occurs for the pumping slot shields, which are either facing the copper opposite beam screen side or the opposite shield through two pumping slots (see Fig. 4.15), more observations were also performed on these components. A picture of a pumping slot shield from V2, in the field, and after an air bake of 6 days at 120°C is given in Fig. 4.16 with its corresponding beam screen section. The pumping slots are there clearly visible all along the shown section. In addition, for some of them, two areas are clearly distinguishable within a single trace. These areas correspond to the case 'shield facing beam screen' and 'shield facing opposite shield'.

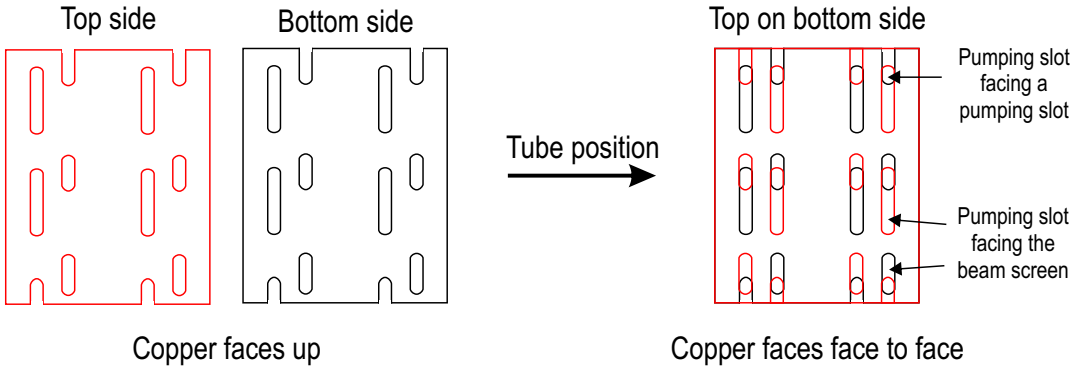

(a) Top view

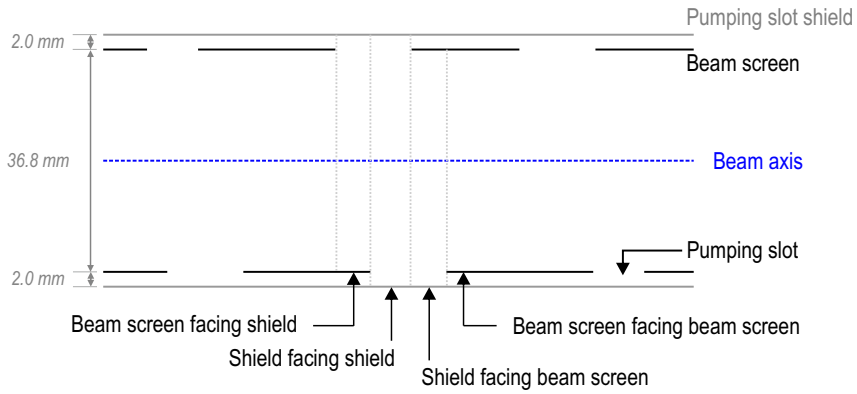

(b) Longitudinal view

Figure 4.15: Geometric configuration of the pumping slots: when the copper faces are upside, the top and corresponding bottom sides of a beam screen section exhibit the same pattern of the slots (see Fig. 4.2). This geometrical distribution results in only partially overlapping slots when the copper faces are face to face, i.e. in the 'tube' configuration. (a) top view, (b) longitudinal view.

4.1.5 Investigation of the origin of the discolouration in the laboratory

To investigate the origin of the traces observed on the pumping slot shield before the air bake (see Fig. 4.10), in particular to determine whether they were possibly already present *in-situ* or appeared at air exposure, and the difference of oxidation kinetics, samples were fully conditioned with a mask (dose = 10^{-2} C/mm^2), letting only part of their surface to be irradiated, while sheltering the rest of it from electron bombardment. A schematic of the configuration for this experiment is given in Fig. 4.17 (left).

The configuration takes profit from the possibility of inserting two sample holders on top of each other on the SPECS system manipulator. The sample was placed on the small sample holder, inserted in the lower position. Then, after XPS analysis of the as received state of the sample, a mask with a 3 mm-wide slot was inserted on the upper position with the transfer rod. After conditioning, the mask was retracted to the load lock without exposing the sample to air, and the entire sample surface was

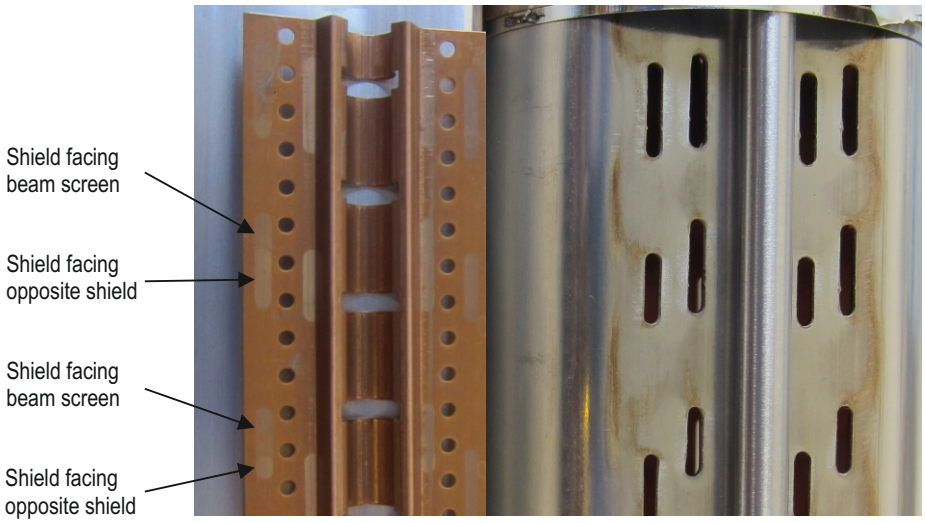

Figure 4.16: Pumping slot shield from V2 (in field) after 6 days at 120°C and its corresponding beam screen section. Before dismantling the pumping slot shield, the visible face of the beam screen and of the shield were facing each others in the machine.

again accessible for XPS and SEY analysis, as well as for visual inspection through the viewports of the system. An *in-situ* picture of a detergent-cleaned OFE copper sample after such a conditioning with the mask is shown in Fig. 4.17 (right). A dark stripe is visible in the middle of the sample, at the position of the irradiated area. A similar observation was performed on a chromium-passivated OFE copper sample conditioned with the mask. This *in-situ* change of colouration could be induced by the graphitization which makes carbon visible [155]. However, an impact of an increased oxide thickness under electron irradiation (see Section 3.2.1) cannot be excluded.

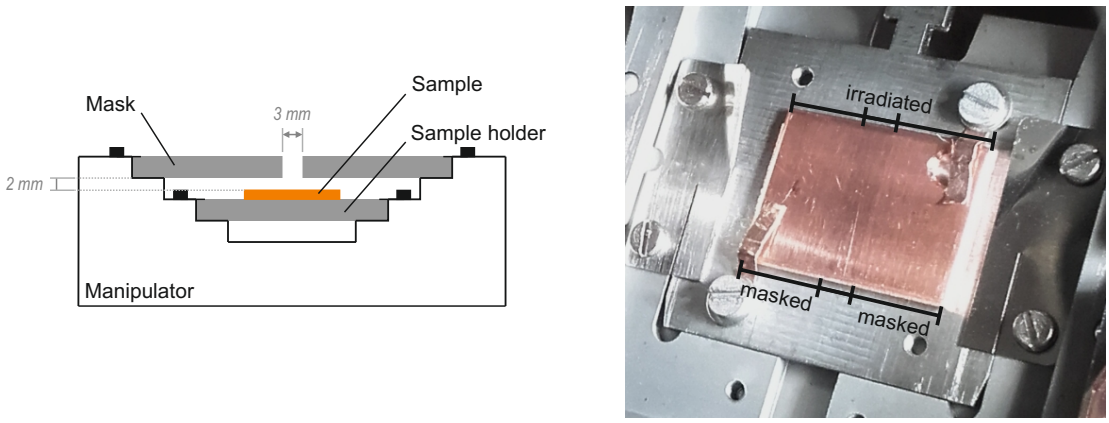

Figure 4.17: (left) Conditioning with a mask removable under vacuum: only part of the sample is irradiated through the 3 mm slot of the mask. (right) Degreased OFE copper sample after conditioning with the mask (D = 10^{-2} C/mm^2) and extraction of the mask under vacuum. The irradiated area corresponds to the dark stripe in the middle of the sample.

A detergent-cleaned and a passivated OFE copper sample conditioned with the mask were heated in air at 120°C and pictures taken after different times in the oven are shown in Fig. 4.18. After 1h at 120°C, the conditioned stripe is barely visible on the degreased

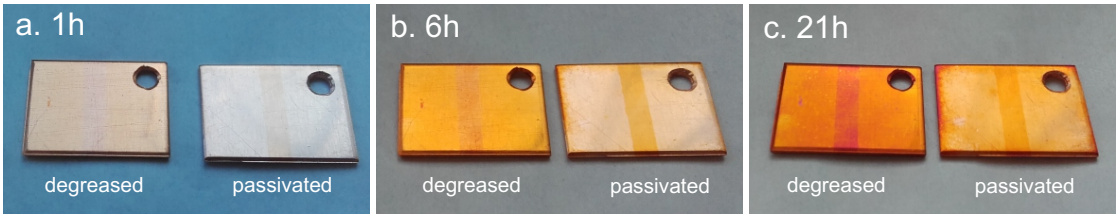

Figure 4.18: Detergent degreased and passivated samples conditioned with a mask after an air bake at 120°C of (a) 1h, (b) 6h, (c) 21h.

sample, while it is already well defined on the passivated one. For longer heating times, the contrast between the irradiated and non-irradiated areas is accentuated and for both samples, the stripe looks clearly darker, i.e. more oxidized than the non-irradiated area. A possible electron-induced degradation of the chromium passivation layer as the only mechanism for the observed difference of oxidation can therefore be excluded. It is known that graphene, a single layer of graphite, acts as an anti-corrosion barrier thanks to its high impermeability to gases [156,157]. On another hand, it has been demonstrated that the presence of graphene can enhance the corrosion of copper on longer time scales due to the cathodic character of graphite to copper [158, 159]. However, in the present case, graphitic carbon is not in direct contact with metallic copper but formed on the native oxide layer through the graphitization of the adventitious carbon layer. Nonetheless, the possibility of graphite easing the transport of charges towards the solid/gas interface (therefore easing the reduction of oxygen and the oxidation of copper) from the top of the thin oxide layer to the top of the growing one cannot be excluded. Accordingly, graphitic carbon remains a possible candidate to explain the different oxidability of the surface induced by electron irradiation.

In the case of LHC extracted beam screens (top and bottom sides), the presence of binary contrast 'fully conditioned' versus 'non-conditioned' surfaces as in the above laboratory experiment is excluded since a non-conditioned surface has a yield above the multipacting threshold and would thus immediately lead to electron multipacting and start conditioning. However, the ultimate SEY reached by conditioning at room temperature in the laboratory (PHI system) is higher for the pumping slot shield than for the beam screen as shown in Fig. 4.19, possibly due to their different surface treatment. Even though the ultimate SEY of the shield seems to be below the multipacting threshold, an error in the absolute value of the measured SEY and/or in the estimation of the threshold may change the situation. Furthermore, the effective beam pipe diameter difference depending on whether the shield/beam screen is facing the shield or the beam screen (see Fig. 4.15 (b)) also induces a difference of electron cloud density [160]. Therefore, having areas in the LHC beam screen where the accumulated scrubbing dose is significantly higher than in other areas is possible. Under this hypothesis, differences of graphitization degree of the carbon layer could arise, leading to different oxidation kinetics between the different zones of the LHC components.

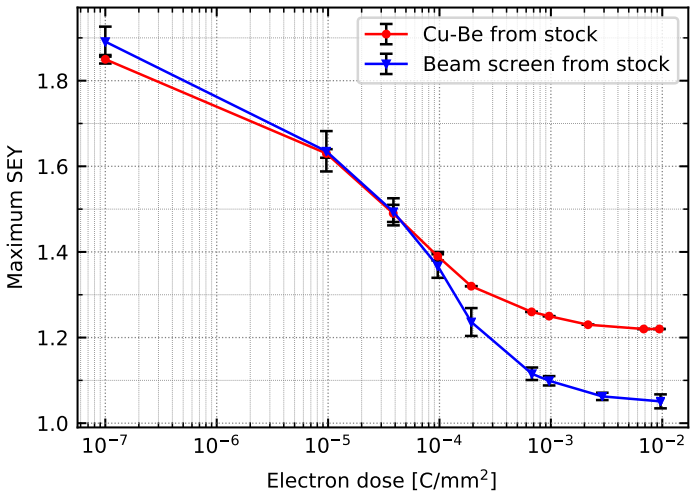

Figure 4.19: Conditioning curves of a pumping slot shield and of a beam screen sample from the stock. The error bars represent the standard SEY deviation over 3 different locations of the samples.

4.1.6 Conclusions on the analysis of the A31L2 vacuum components

For the first time, surfaces of beam screens and pumping slot shields exposed to the proton beam during LHC operation were analysed in the laboratory. For one beam screen sample, the SEY was found to exhibit strong non uniformities, which could later be related to the presence of a higher amount of carbon. The effect of sample handling (cutting and fixing for instance) could be responsible for such a contamination. However, the comparison between surfaces exposed to the beam in the LHC and reference surfaces conditioned in the laboratory evidenced common features: the SEY and the hydroxide component are lower for the surfaces exposed to the beam than for the reference one. In addition, on the pumping slot shield, the carbon is found to be in a more graphitic form in the irradiated areas facing the slots. The amount of carbon was found to be in the usual range for air exposed surface, by opposition to the CERN SPS case where a carbon layer growth was observed in the beam pipe area irradiated by the electron cloud [118]. Finally, the ultimate SEY and the dose needed to reach it by conditioning the LHC extracted samples in the laboratory was observed to be similar to the ones of a reference surface. It is worth mentioning that the dose needed to reach the SEY threshold for electron cloud build-up in a dipole (maximum SEY = 1.25) is slightly lower for the LHC extracted sample than for the reference. All these observations are compatible with the hypothesis that the LHC extracted surfaces were conditioned in the machine by the electron cloud. In addition, these analyses confirmed that copper exhibits a memory effect of the conditioning, even after 2 months of air exposure.

The deconditioning of the surfaces due to air exposure is however clearly visible. Indeed, the SEY as well as the hydroxide contribution on the Cu 2p line is globally higher for the V2 beam screen, which was measured later than the V1 beam screen. The fact that the C 1s line is at a higher binding energy for V2 than for V1 beam screen could also result from the deconditioning. Due to this phenomenon, it is impossible to

assess the *in-situ* conditioning state of the machine, by the analysis of these air exposed surfaces. In particular, the maximum SEY reached by the accumulated scrubbing of the surfaces in the machine cannot be known, and the question remains whether the scattering of SEY observed between different beam screen samples results from *in-situ* SEY differences or appeared during air exposure. Therefore, in view of new analyses of LHC extracted surfaces, the study of the deconditioning mechanisms presented in Section 3.3 was launched with the objectives of determining a procedure for limiting at most the deconditioning, even though the air exposure of the surfaces is unavoidable to extract the components, and to define the limit of accessible information while analysing these accelerator extracted surfaces.

In parallel, it is observed that the exposure of the surfaces to the beam modifies their oxidation properties. First, the presence of the cupric oxide CuO, which is not observed on the laboratory conditioned surfaces neither on the spare beam screens, shows that phenomena not foreseen by the laboratory experiment are occurring in the machine. The origin of this oxide is not known, but its azimuthal distribution is influenced by the presence or not of a magnet field and matches with the electron cloud distribution. However, according to the conditioning experiments performed on these LHC extracted beam screens sample, the presence of CuO on the A31L2 beam screens did not seem to affect the conditionability of the surfaces. This point will be discussed in details in Chapter 5. Second, it is observed that the LHC operation induces a difference of colouration between the different areas of the components. As extracted, the pumping slot traces observed on both the beam screens and the pumping slot shields can result from the graphitization of the surface carbon layer, and be induced by a higher irradiation dose with respect to the surrounding areas. While air-baking these components, the colour contrasts increases, translating a faster oxidation kinetics in the most irradiated zones. Such a phenomenon could also be due to the presence of graphitic carbon.

Finally, since the heat load of this particular magnet was not known, no correlation could be done between its performance and any characteristics of the surfaces.

4.2 Surface state comparison between high and low heat load dipole beam screens

The opportunity of comparing the surface of beam screens hosted in a low and in a high heat load magnet occurred in LS2 (2019-2020), when a series of 19 dipole magnets presenting operating deficiencies were exchanged in the LHC. Among the exchanged magnets, was the dipole D3 of the instrumented half-cell 31L2 (LHC location B31L2) whose heat load is presented in Fig. 1.8. According to its associated heat load value, this magnet was chosen as the high heat load one for the comparison. Since no low heat load magnet from any instrumented cells was taken out from the LHC during LS2, it was decided to chose among the 19 extracted dipoles the one located in the half cell exhibiting the lowest heat load. With this logic, the dipole from the location C21R6 (arc 6-7) was chosen since its half-cell exhibits one of the lowest heat load around the LHC (30 W for the full 21R6 half-cell for the same fill as for Fig. 1.8, against more than

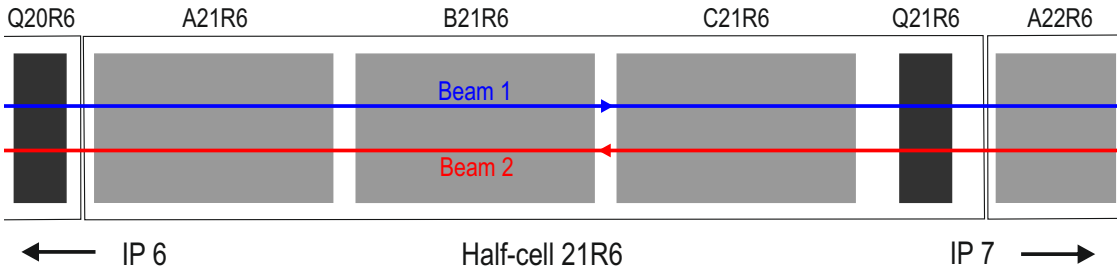

Figure 4.20: Situation of the C21R6 location in the LHC.

60 W for the B31L2 magnet alone). A schematic of the environment of the B31L2 and C21R6 locations is given in Fig. 4.1 and 4.20 respectively. The first outcomes of the analyses of the two pairs of beam screens extracted from these dipoles are presented in the following.

4.2.1 Extraction, sampling and storage procedure

Based on the laboratory study of the deconditioning mechanisms presented in Section 3.3 which evidenced the necessity of venting and storing electron irradiated surfaces in clean and dry atmosphere and to perform the analyses as soon as possible after their venting, a specific procedure was applied to preserve at most the *in-situ* conditioning state of the beam exposed surfaces by reducing their air exposure at most. In addition, a parallel schedule was followed for the two selected magnets, to allow for their beam screen comparison despite the fact that their extraction occurred with two months of interval, because of the overall LHC maintenance schedule and of the duration of the analysis.

Table 4.2: Schedule for the extraction and the analysis of beam screens extracted from dipoles in B31L2 and C21R6 LHC locations.

	B31L2	C21R6
Beam lines venting N_2/O_2 (80%/20%)	16-17.04.2019	24-25.06.2019
Plug-In Modules cut	23-24.04.2019	01-02.07.2019
Vacuum component extraction Storage in static vacuum	06.05.2019	12.07.2019
Start of the analysis	23.05.2019	22.07.2019

The first exposure of the proton beam exposed surfaces to a reactive gas was controlled by venting the LHC arcs with a mixture of N_2/O_2 (80%/20%) as validated in Section 3.4. The RF ball was not passed before the extraction of the magnets, to limit the sources of contamination. A week after venting, the Plug-In Modules at each magnet extremity were cut. The beam lines were thus shortly exposed to tunnel air, and

immediately closed with Viton-sealed caps. The extraction of the vacuum components from the magnets was performed 10 days later in a surface facility. 5 cm-long beam screen sections were cut (by hand, with a clean saw) at the selected positions shown in Fig. 4.21, in field and field-free regions, for laboratory analysis and the remaining parts were cut in sections of 1 to 2 m. All the inner beam screen surfaces were visually inspected and no singularity (stain, discolouration,...) was detected for none of the beam screens. All beam screen sections and pumping slot shields were stored under vacuum at the end of the extraction to stop their deconditioning, based on the results presented in Section 3.3. To fit into the experimental system, the selected 5 cm-long beam screen sections were again cut in 6 pieces as described in Fig. 4.2. The schedule for the full sequence of events is given in Table 4.2 for these two dipoles. The analyses typically spread over 2 months per magnet and were performed in the SPECS system.

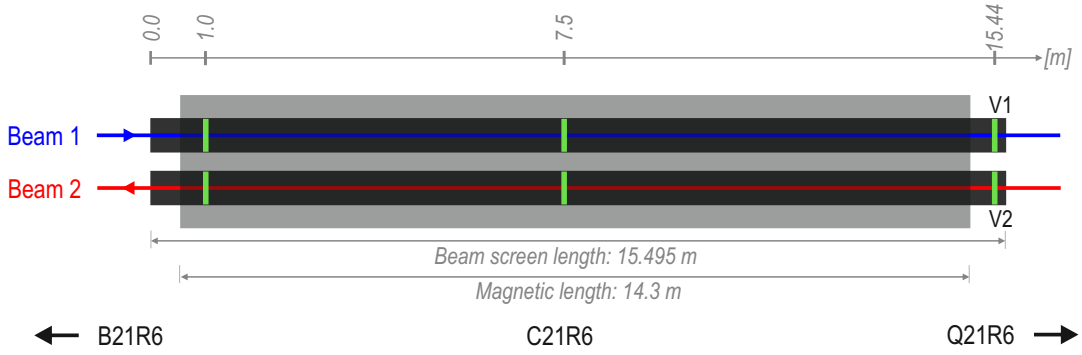

(a) C21R6 location

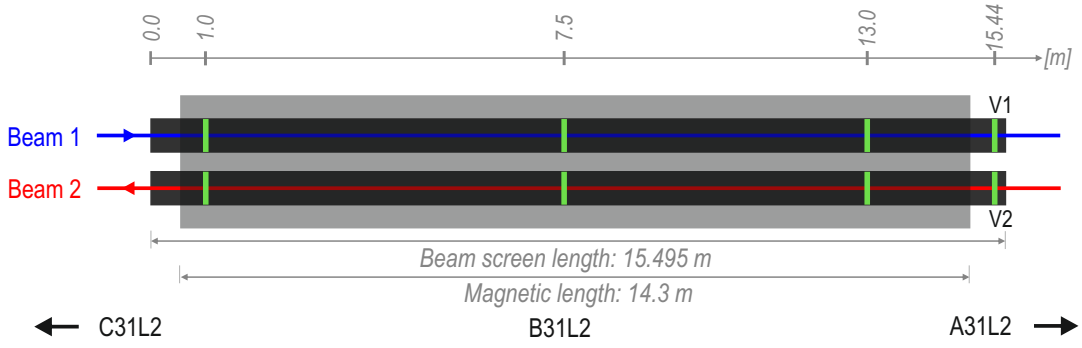

(b) B31L2 location

Figure 4.21: LHC locations C21R6 (a) and B31L2 (b): position of the beam screen sections cut for analysis (green stripes).

4.2.2 Surface characterisation of beam screens from a low heat load dipole

Both XPS and SEY measurements were performed at different azimuthal positions of all sections to look for any impact of the field on the surface state, since the spatial distribution of the cloud electrons impinging on the surface is a function of the field.

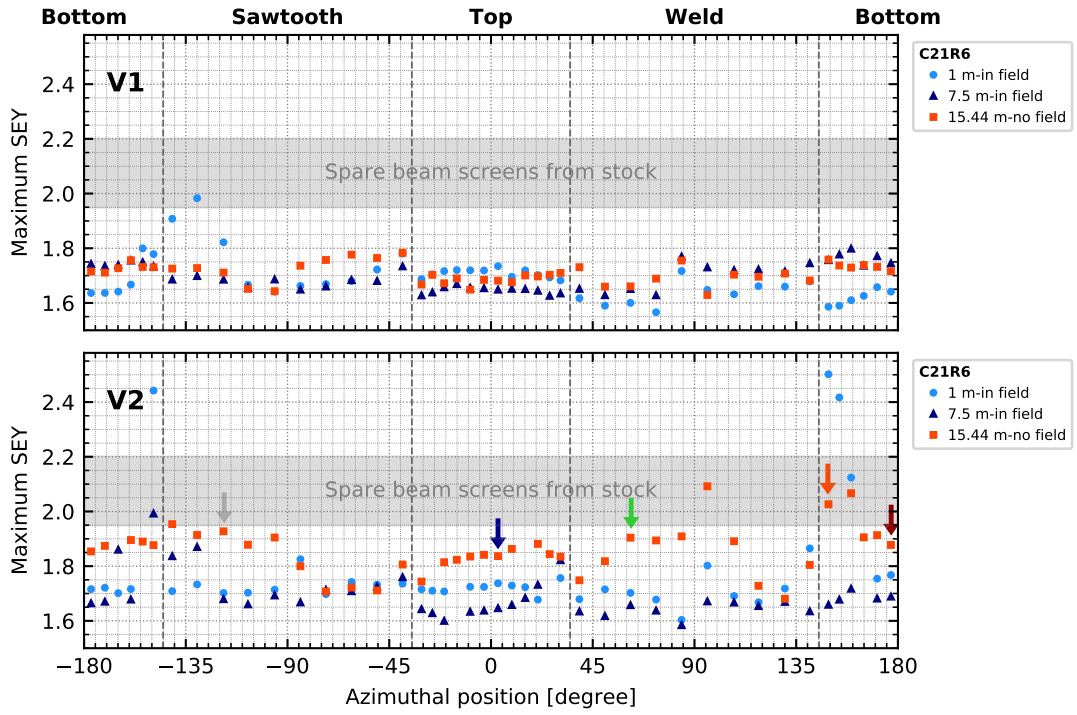

Figure 4.22: Maximum SEY as a function of the azimuthal position for different sections of V1 (top) and V2 (bottom) beam screens extracted from the LHC dipole at location C21R6. The distances are given from the beam screen extremity. The maximum SEY range measured on beam screens from the stock is given for comparison. The arrows correspond to the position where the XPS spectra of Fig. 4.24 were acquired.

- **Secondary electron yield**

Maximum SEY profiles acquired all around the azimuth for the different beam screens sections, in field and field-free regions, are given in Fig. 4.22. For V1 beam screen, all the three profiles are flat and exhibit a very small scattering. The maximum SEY is globally between 1.6 and 1.8, i.e. significantly lower than for a spare beam screen. For V2 beam screen, the scattering is larger. The two sections in the field region again exhibit a flat profile, with few higher SEY points (e.g. around 155° for the section at 1 m) which are also found to be close to the sample edge (see Fig. 4.2) and more carbon contaminated. As for V1, the maximum SEY of these sections ranges from 1.6 to 1.8. For the section cut in a field-free region, the SEY profile presents some variations which are not correlated with the different beam screen sides but occur within a single side, as for instance within the sawtooth lateral side. The maximum SEY of this section is globally higher compared to the other V2 sections, between 1.8 and 2.0. In contrast to some V1 beam screen sections of the magnet from the A31L2 location (see Fig. 4.3), no low SEY feature is observed on the sawtooth profile.

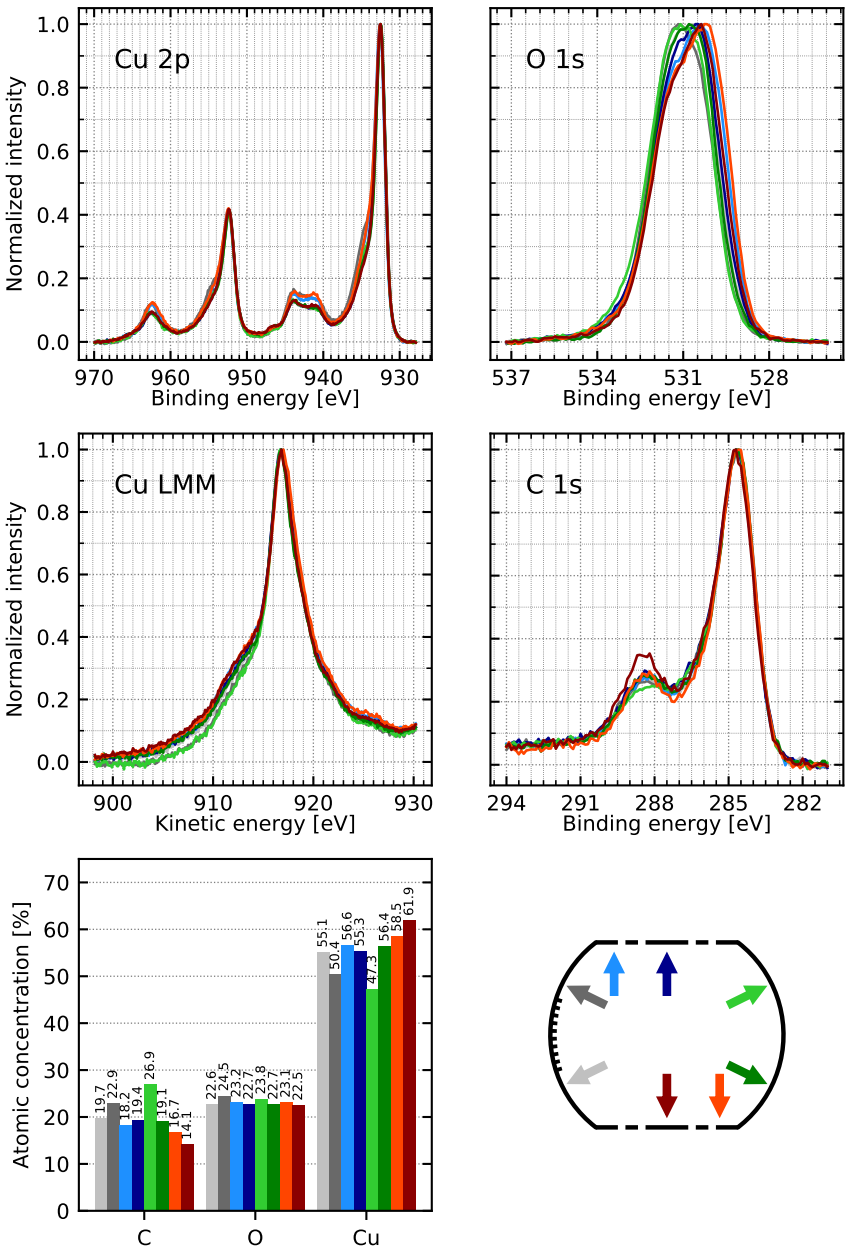

Figure 4.23: Cu 2p (top left), O 1s (top right), Cu LMM (centre left) and C 1s (centre right) lines and corresponding atomic concentrations (bottom left) for different azimuthal positions (bottom right) of the V2 beam screen section located at 7.5 m (field region) from the C21R6 dipole.

- **Surface chemistry**

XPS analysis revealed the presence of carbon, oxygen and copper as well as nitrogen and traces of sulphur and silicon from the detergent below 1 at.%, i.e. in usual amounts for detergent-cleaned surface. The Cu 2p, O 1s, Cu LMM and C 1s lines acquired in different azimuthal positions of the V2 beam screen section located at 7.5 m (field region) are given in Fig. 4.23, together with the corresponding atomic concentrations of carbon, oxygen and copper. The satellite at 939-946 eV on the Cu 2p line witnesses

the presence of Cu^{2+}. The shape of this satellite suggests the presence of CuO (orange line) and $Cu(OH)_2$ (brown line), without any correlation to the azimuthal position. The intensity of the satellite remains however low (in particular lower than for an air exposed surface, see Fig. 3.3 and 3.9), and the position of the Cu 2p line at 932.6 eV and of the Cu LMM line at 916.7 eV indicates that the dominant copper oxidation product is Cu_2O, i.e. the native copper oxide. The C 1s line shape is usual for an air exposed surface. Its maximum is located at 284.6 eV, independently from the azimuthal position, which is a lower binding energy than expected for an air exposed surface. The *in-situ* graphitization of these surfaces is therefore plausible. Finally, the amount of surface carbon is between 14 and 25 at.% corresponding to the lower end of the expected values for air exposed surfaces. It is furthermore independent from the azimuthal position. Similar observations were performed on all the beam screen sections in a field region of this magnet as well as on the field-free section of the V1 beam screen. However, the field-free section of V2 beam screen, whose XPS lines and atomic concentrations are given in Fig. 4.24, was found to be different.

The satellite of the Cu 2p lines clearly exhibits the characteristic shape for $Cu(OH)_2$ [130, 131]. From its intensity, two families of points can be distinguished. The satellite intensity of the dark grey, green and light blue curves is only slightly higher than the one of the lines for the other beam screen sections (see Fig. 4.23). However, the other curves show a much stronger satellite as well as a higher intensity of the high-energy shoulder on the Cu $2p_{3/2}$ line, compatible with a higher $Cu(OH)_2$ amount. When comparing the maximum SEY profile in Fig. 4.22 (bottom) and the corresponding XPS analysis, it clearly appears that the high $Cu(OH)_2$ points (indicated on the SEY profile of Fig. 4.22 with arrows of the corresponding XPS line color) exhibit a higher SEY than the rest of the beam screen. This higher SEY is thus a consequence of the stronger presence of $Cu(OH)_2$. In parallel, it is observed that the low $Cu(OH)_2$ positions exhibit a higher carbon content (Fig. 4.24 (bottom left)) as well as a different C 1s line shape around 288.5 eV (Fig. 4.24 (middle right)). The energy of the maximum of the lines is 284.6 eV for all azimuthal positions. This binding energy is compatible with graphitic carbon. Thus, the higher carbon content observed in some azimuthal positions of this beam screen section was already present *in-situ* and does not result from accidental contamination during extraction. During the air exposure of the beam screen, hydrocarbon reasdorption occurred at all azimuths. In particular, species containing O-C=O groups reappeared on the surface. Due to the higher carbon amount present in some locations, the contribution related to O-C=O groups appears lower, in normalized intensity, in these locations, thus explaining the different C 1s line shape. The presence, in some azimuthal positions, of a thicker graphitic carbon layer (short-term protective layer) could better protect the surface from copper hydroxide grow-up and therefore explain the observed discrepancies in hydroxide amount. However, the reason for this hydroxide build-up on this particular beam screen section is not explained.

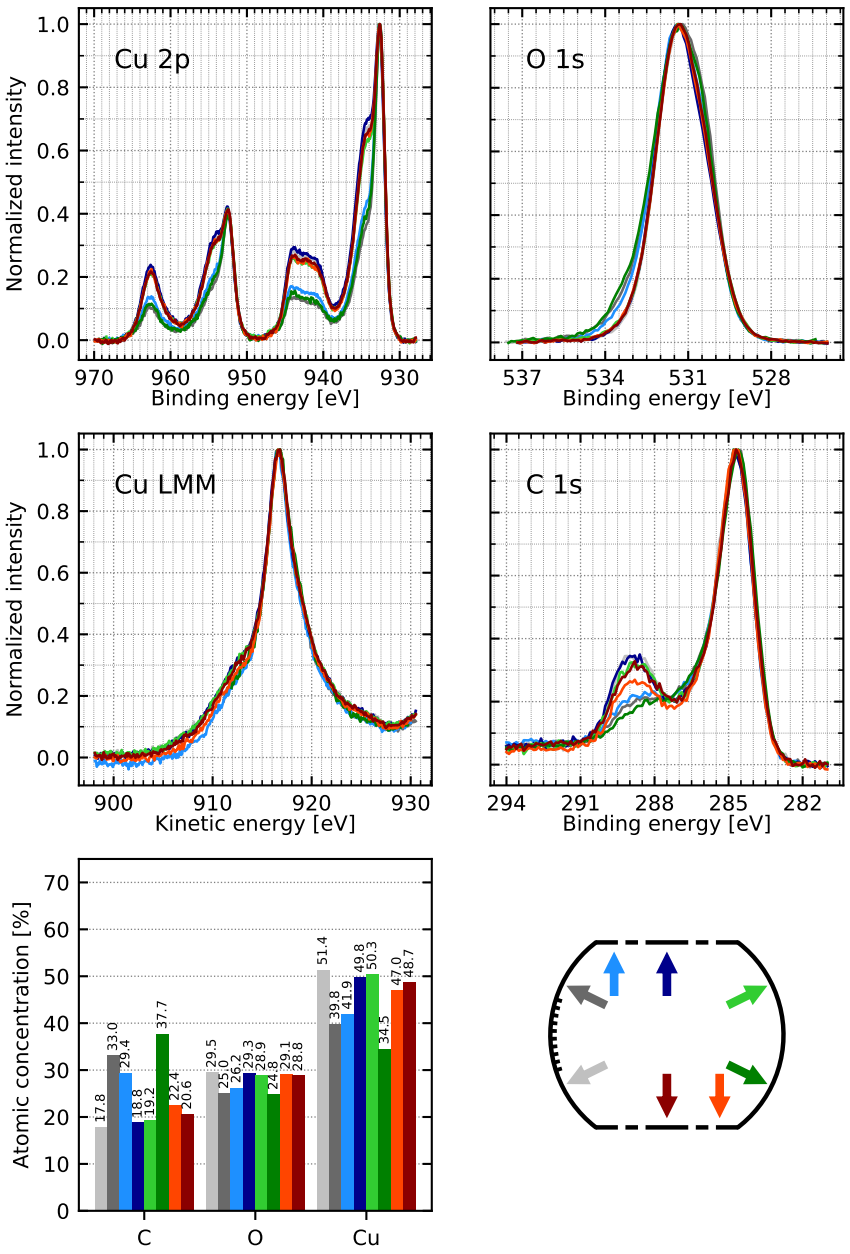

Figure 4.24: Cu 2p (top left), O 1s (top right), Cu LMM (centre left) and C 1s (centre right) lines and corresponding atomic concentrations (bottom left) for different azimuthal positions (bottom right) of the V2 beam screen section located at 15.44 m (field-free region) from the C21R6 dipole.

- **Conditioning**

The top sides of the sections at 7.5 m (in field region) from both V1 and V2 beam screens were conditioned in the laboratory set-up. The corresponding conditioning curves are shown in Fig. 4.25, together with the conditioning curve of a spare, never installed beam screen, as a reference. The ultimate SEY and the dose required to reach it are similar for all the three samples (ultimate δ_{max} difference of 0.03). In particular, a δ_{max} well below the calculated electron cloud build-up threshold is obtained for all of them.

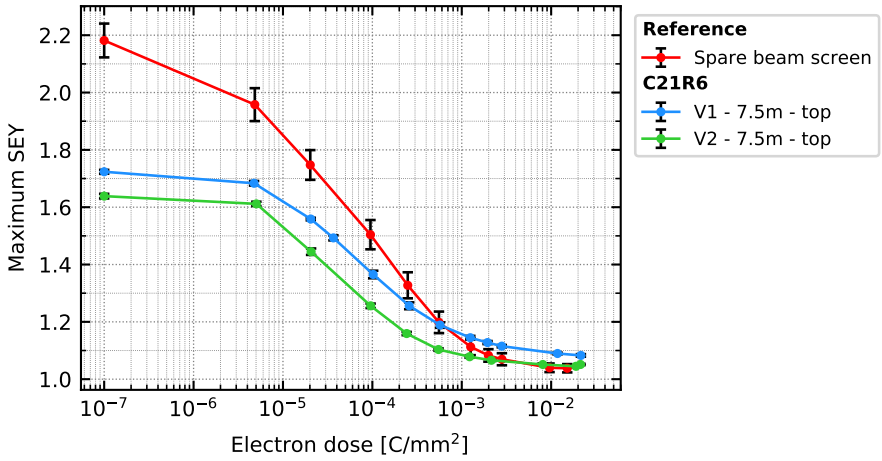

Figure 4.25: Conditioning curves of the top sides of the beam screen sections located at 7.5 m (in field region) from V1 and V2 C21R6 beam screens. The conditioning curve of a beam screen from the stock (never installed in the LHC) is given as a reference. The error bars represent the standard SEY deviation over 3 different locations of the samples.

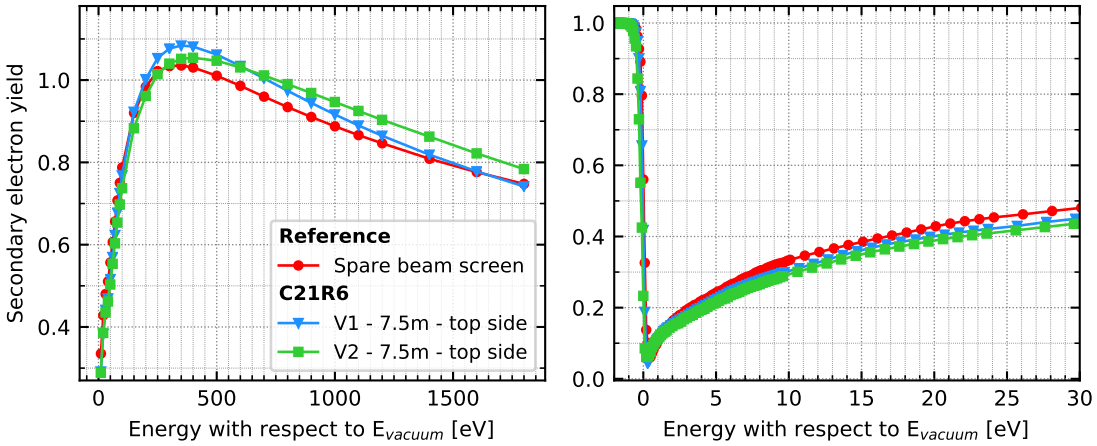

Figure 4.26: (left) SEY curves from 10 to 1800 eV of the two top sides of the beam screen sections at 7.5 m from V1 and V2 of the C21R6 magnet and of a never installed beam screen, all after full conditioning, (right) low energy SEY curves. The energy is referenced to the vacuum level.

The SEY curves after full conditioning of these three samples are shown in Fig. 4.26. All the three SEY curves exhibit a similar shape, and no anomaly is detected for the LHC extracted samples.

The C 1s, Cu 2p and O 1s lines of the conditioned V2 sample are presented in Fig. 4.27, before and after full conditioning. The fully conditioned state of the reference sample is also given for comparison. During conditioning, the Cu 2p satellite, whose shape suggests the presence of both $Cu(OH)_2$ and CuO, the high energy Cu $2p_{3/2}$ shoulder and the contribution around 531.5 eV on the O 1s line vanish, as a result of the reduction of the Cu^{2+} product. In the fully conditioned state, the Cu 2p lines are similar for both the LHC extracted and the reference sample. However, the O 1s line is narrower, and at a lower binding energy for the beam screens from the LHC. The

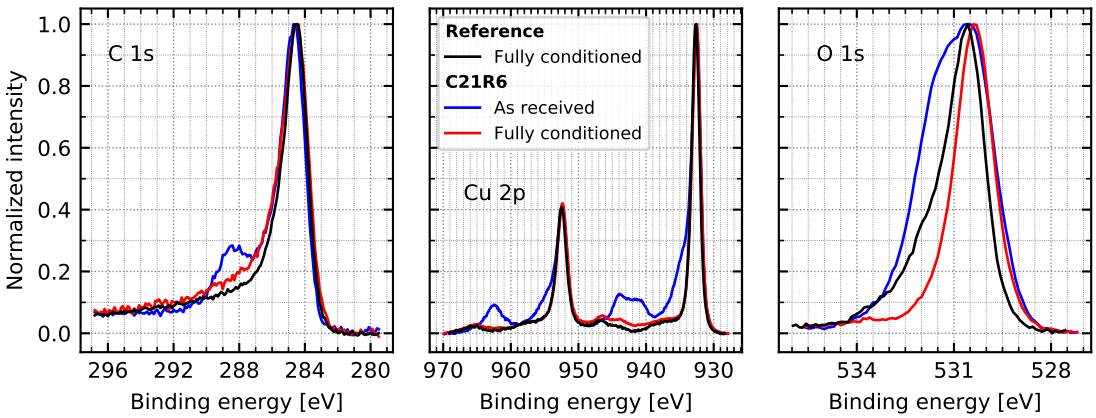

Figure 4.27: C 1s (left), Cu 2p (centre) and O 1s (right) lines of the V2 beam screen sample at 7.5 m (top side) before and after full conditioning. The fully conditioned state of a reference sample (never installed beam screen) is given as a reference.

persistence of CuO at a depth where the electrons from Cu 2p (kinetic energy ∼550 eV) can no longer escape from the material but the one of O 1s (kinetic energy ∼955 eV) still can is thus possible. A small shift of the C 1s line of the LHC extracted sample, which was already at a lower binding energy than a usual air exposed surface, is observed. The C 1s line after full conditioning is at 284.5 eV for both samples, but its high energy tail is slightly more intense for the LHC extracted one. Similar observations were performed on the V1 sample.

- **Conclusions on the beam screens of the low heat load dipole**

After their extraction from the machine, the beam screens from a low heat load dipole were found to exhibit a globally lower SEY than a reference, never installed beam screen. Their surface exhibits the characteristics of an irradiated surface shortly exposed to air, expected from the laboratory studies presented in Chapter 3: lower copper hydroxide amount and more graphitic carbon than a spare beam screen. Even though their analysis spread over several weeks, the SEY and chemical state of the surfaces did not show any difference of deconditioning state between the earliest and latest analysed ones. This confirms the successful strategy of storing the extracted components under vacuum. In addition, a very small amount of CuO was observed on the surface of these beam screens. However, its azimuthal distribution did not show a correlation with the distribution of the cloud electrons and no systematic difference was observed between flat (top and bottom) and lateral sides, in contrast to the A31L2 case. Furthermore, one section located in a field-free region presented large amounts of $Cu(OH)_2$ whose origin could not be identified. Finally, it is shown that the conditioning kinetics of the C21R6 samples is similar to a reference surface, even though the persistence of CuO after conditioning could not be discarded.

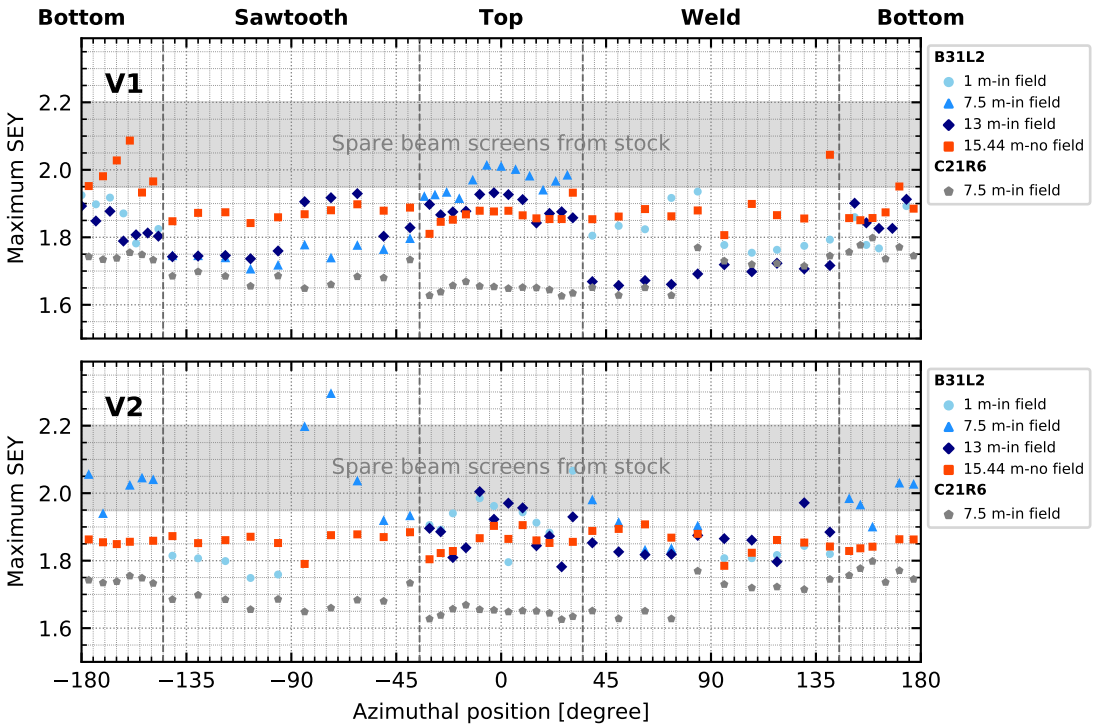

Figure 4.28: Maximum SEY as a function of the azimuthal position for different sections of V1 (top) and V2 (bottom) beam screens extracted from the LHC dipole at location B31L2. The SEY profile of a C21R6 beam screen section (V1, 7.5 m) and the maximum SEY range measured on beam screens from the stock are given for comparison.

4.2.3 Comparison with beam screens from a high heat load dipole

Similar analysis were performed for the high heat load B31L2 dipole and the surface of the beam screens from the two dipoles were compared.

- **Secondary electron yield**

Maximum SEY profiles acquired all around the azimuth of different beam screen sections are given in Fig. 4.28, where a profile from the C21R6 magnet (representative of its two beam screens, apart from the section exhibiting $Cu(OH)_2$) is also shown, for comparison. For the sections in the field region of the V1 beam screen, it is possible to distinguish a global trend beyond the large scattering of the data. The SEY of the flat (top and bottom) sides yields between 1.8 and 2.0, i.e. it is significantly higher than observed on the C21R6 beam screens. On the lateral (sawtooth and weld) sides, the SEY tends to be lower, between 1.6 and 1.8, i.e. in the range of SEY measured on the C21R6. For the V2 beam screen, this effect is less visible, possibly hidden by the larger data scattering. For both beam screens, the section in the field-free region exhibits a flat SEY profile between 1.8 and 2.0, i.e. at the level of the flat sides of the sections in the dipole field. Therefore, for the first time, the azimuthal variation of the SEY could be correlated with the electron cloud distribution: the SEY is observed to be globally higher in the areas the most irradiated by the electron cloud (flat sides in the dipole field, all azimuths in the field-free region) than in the least irradiated ones. Furthermore,

the SEY in the most irradiated areas of the B31L2 beam screens is higher than the one measured in the same zones of the C21R6 magnet, in spite of a similar extraction and storage procedure for all samples. Such difference could therefore not be due to different deconditionings of the samples.

The SEY curves of the central point (azimuthal position $\sim 0°$) of two sections in the field region of V1 beam screens of both C21R6 and B31L2 magnets are shown in Fig. 4.29. The C21R6 exhibits both a lower δ_{max} and E_{max}. The low energy SEY curve is slightly higher for the B31L2 section, but the global shape is similar for both magnets: the SEY just above the vacuum level is about 0.15, it then steeply increases to reach a plateau where $\delta = 0.55$ and increases again for an energy above 10 eV. These low-energy SEY curves are similar to the one observed for air exposed copper (see Fig. 3.1). Indeed at such low energies, the SEY is strongly influenced by the adsorbates and even a short air exposure might cancel the history of the surface.

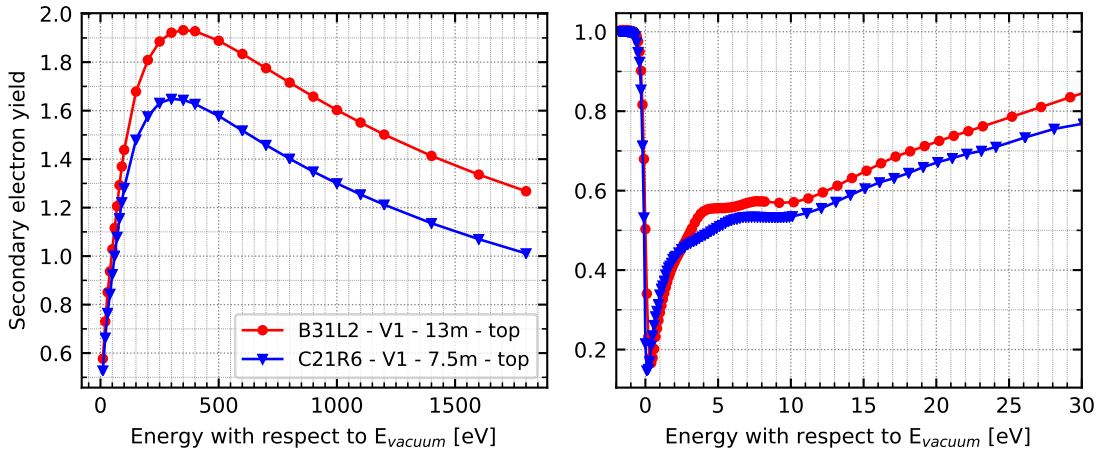

Figure 4.29: (left) SEY curves from 10 to 1800 eV of the top side of the beam screen sections in the field region of V1 beam screens of B31L2 and C21R6 magnets, (right) low energy SEY curves. The energy is referenced to the vacuum level.

A zoom on the flat (top and bottom) sides of different beam screen sections are shown in Fig. 4.30, where the horizontal axis is the transverse position in millimetres with respect to the beam position (centre of the side). In spite of the data scattering, for the sections in the field region of V1 beam screen from B31L2 (graphs (a), (b) and (c)), δ_{max} appears slightly higher in the central part of the sample, around x = 0 mm. For the section in a field-free region (graph (d)) and on V2 beam screen (graph (e)), this pattern is not visible, possibly hidden by the larger scattering. For the C21R6 magnet (graph (f)), the profiles are completely flat: any specific pattern is absent. Once again, for the B31L2 beam screens, in the field region, the SEY profile could be correlated with the electron cloud properties: in the centre of the flat regions, both the energy and the cloud density are different from the most external parts of these regions, due to the presence of the field (see Fig. 1.12).

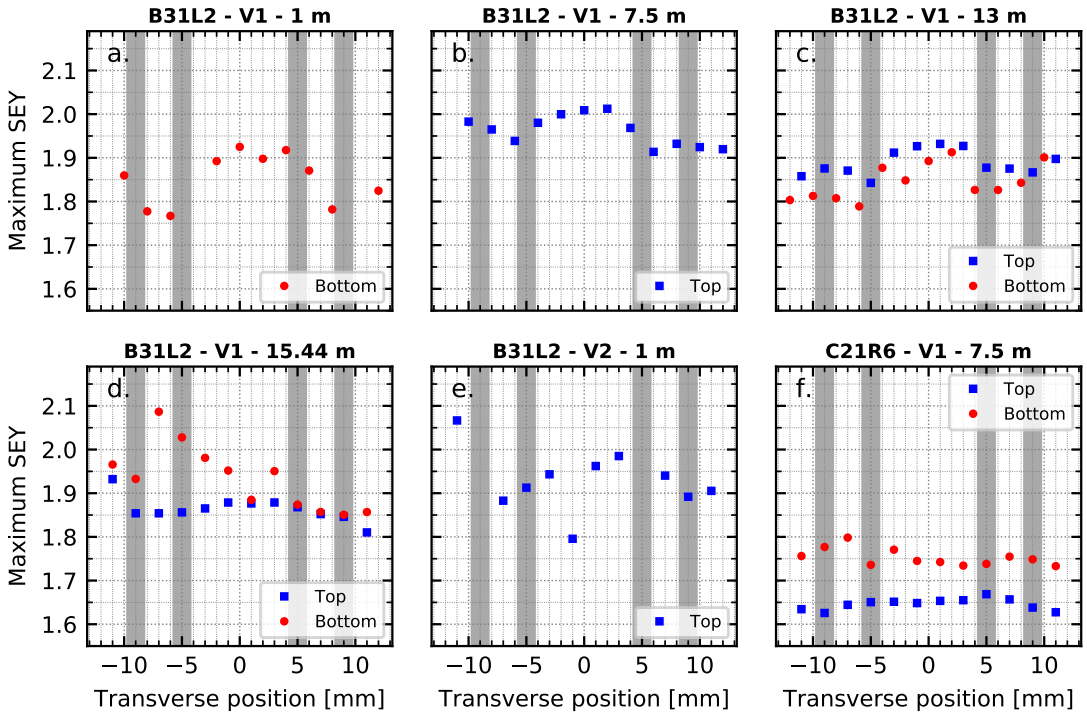

Figure 4.30: Transverse SEY profiles for the flat sides of beam screens from B31L2 V1 (a), (b), (c), (d), B31L2 V2 (e), and C21R6 V1 (f). The position is indicated from the center of the side (beam position) and the grey stripes correspond to the position of the pumping slots.

- **Surface chemistry**

XPS analysis performed on the B31L2 beam screens evidenced the presence of carbon, oxygen and copper, as well as traces of nitrogen, silicon and sulphur as for the C21R6 beam screens.

The XPS lines of a top side in the field of the V1 beam screen of the B31L2 and C21R6 magnets are shown in Fig. 4.31. The satellite shape of the B31L2 sample unambiguously witnesses the presence of CuO [130,131]. The position of the Cu $2p_{3/2}$ peak at 933.4 eV, of the Cu LMM line at 917.7 eV and of the O 1s line at 529.7 eV indicates that CuO is the dominant copper oxide [130–132]. Accordingly, the B31L2 sample dramatically differs from the C21R6 sample: even though a small amount of CuO may be present on the beam screens from the low heat magnet, this oxide is significantly more abundant on the high heat load one. Furthermore, the amount of carbon is extremely low on the B31L2 sample. Indeed, carbon amount as low as 4.1 at.% is unachievable with the CERN wet cleaning procedure for UHV parts, and therefore unexpected for an air exposed coper surface, even after conditioning. Finally, the C 1s line is different from the C21R6 one: the base of the main peak is narrower and the component at 288.5 eV slightly higher. It is worth mentioning that in spite of the presence of large amount of CuO on the B31L2 sample, the ratio of the oxygen to copper concentration is larger for the C21R6 sample than for the B31L2 one. Two main reasons could be responsible for this. First, oxygen from the airborne contamination is more present on the C21R6 where the hydrocarbon carbon contamination is significantly higher. Second, due to the higher carbon amount,

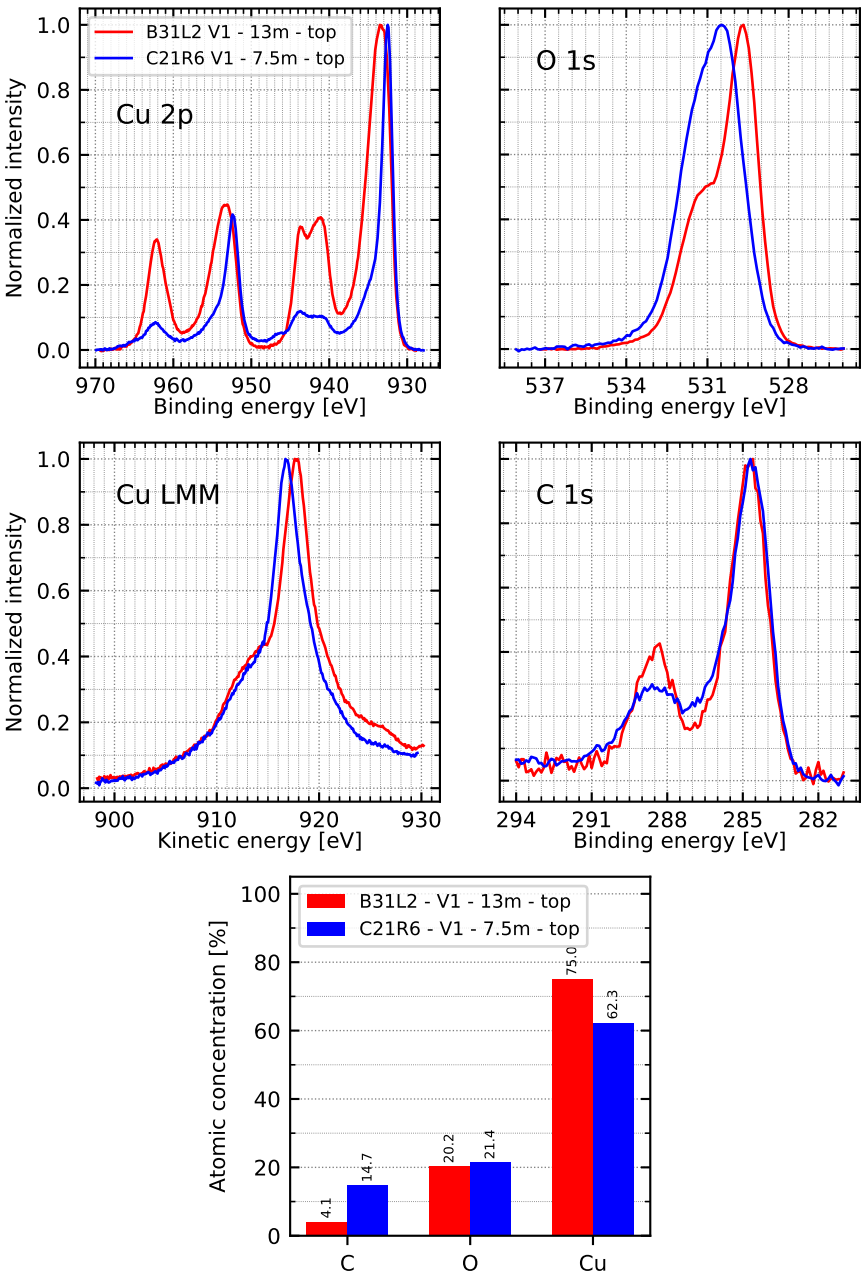

Figure 4.31: Cu 2p (top left), O 1s (top right), Cu LMM (centre left) and C 1s (centre right) lines and corresponding atomic concentrations (bottom) for the top sides of V1 beam screen sections in the field region of B31L2 and C21R6 magnets.

the higher attenuation of the signal originating from copper ($E_k \sim 550$ eV) with respect to the one from oxygen ($E_k \sim 955$ eV) is more pronounced on the C21R6 sample.

XPS lines for different azimuthal positions of the section at 13 m of V1 beam screen from B31L2 magnet are shown in Fig. 4.32. From the intensity of the Cu 2p satellite, two families of spectra can be distinguished. The spectra corresponding to the flat (top and bottom) sides exhibit a high intensity satellite whose shape is for all of them clearly ascribed to CuO. The spectra acquired on the lateral sides present a much lower satellite intensity, comparable with the one observed on the C21R6 beam screens, and probably

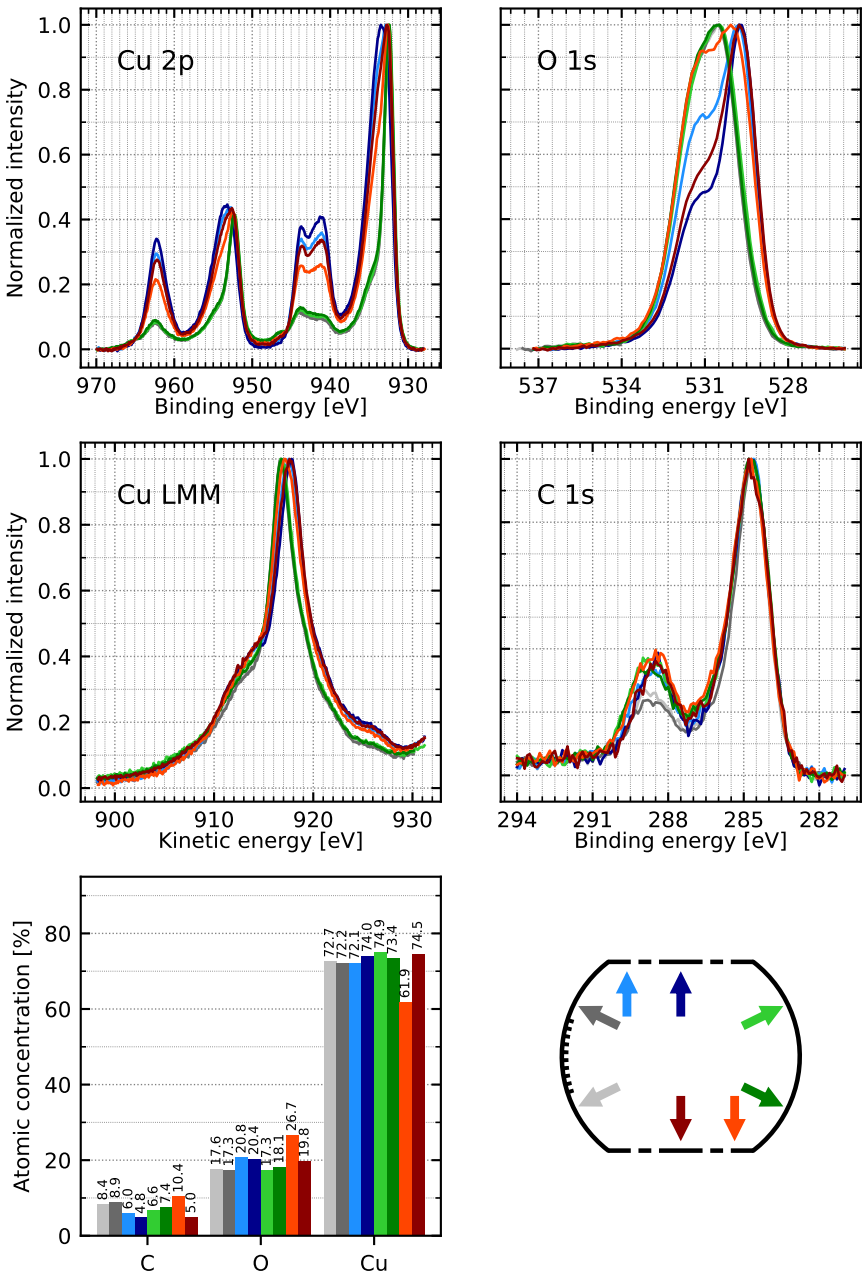

Figure 4.32: Cu 2p (top left), O 1s (top right), Cu LMM (centre left) and C 1s (centre right) lines and corresponding atomic concentrations (bottom left) for different azimuthal positions (bottom right) of the V1 beam screen section located at 13 m (field region) from the B31L2 dipole.

resulting from the presence of $Cu(OH)_2$ and CuO. These differences of copper oxidation product are coherently also observed on the Cu LMM and O 1s lines, whose position (917.8 eV and 529.7 eV respectively) confirms the dominance of CuO on the flat sides and Cu_2O on the lateral ones. Therefore, once again, the beam screen presents an azimuthal pattern which can be correlated with the electron cloud distribution and/or energy. However, neither the C 1s lines nor the carbon atomic concentration show systematic differences between flat and lateral sides. Carbon amount is indeed low at all azimuths.

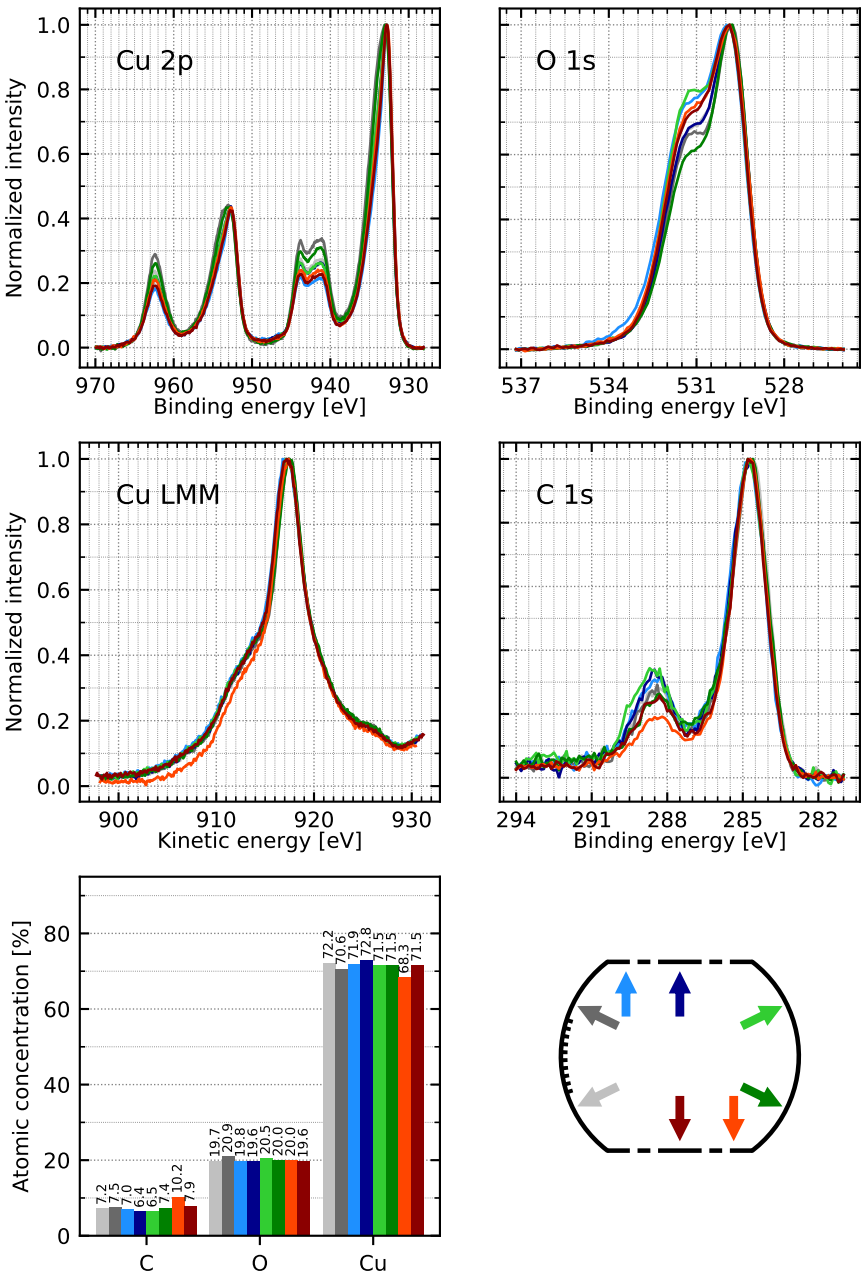

Figure 4.33: Cu 2p (top left), O 1s (top right), Cu LMM (centre left) and C 1s (centre right) lines and corresponding atomic concentrations (bottom left) for different azimuthal positions (bottom right) of the V1 beam screen section located at 15.44 m (field-free region) from the B31L2 dipole.

The azimuthal distribution of CuO is different for a beam screen section out of the field of the B31L2 dipole, as shown in Fig. 4.33. Indeed, from the Cu 2p satellite intensity, CuO is now also present on the lateral sides. From the Cu LMM and O 1s position, CuO becomes the dominant oxide for all azimuths. This observation is again coherent with the cloud distribution, which is no longer confined by the magnetic field. The C 1s line are once more similar at all azimuths and the carbon atomic concentration is perfectly homogeneous and there as well, very low.

The presence of CuO and the dependence of its azimuthal distribution on the field were also observed on the other sections of the two B31L2 beam screens. A full picture of the chemical state and of its dependence on azimuthal position and field can be obtained for both magnets thanks to a Wagner plot [120]. In this graphical representation, the kinetic energy of the Cu LMM line is displayed as a function of the binding energy of the corresponding Cu $2p_{3/2}$ line, and thus allows to distinguish between different copper compounds, in particular between CuO, Cu_2O and $Cu(OH)_2$ which are here of interest [131]. Wagner plots are typically used for pure compounds, having sharp chemical shifts of Auger and XPS lines. In the present case, most of the time, the surfaces exhibit several copper oxidation products whose presence does not result in a full chemical shift but rather to an additional shoulder on the lines. A Wagner-like plot is therefore computed by using the centre of gravity of the area below the Cu $2p_{3/2}$ line, between 927 and 938.5 eV, as described in Fig. 4.34, instead of using the energy of its maximum intensity. This takes into account the presence of several components at different energies. For the Auger line, the energy of the maximum of the Cu LMM line intensity was used. The resulting plot, which includes all the spectra taken for both the C21R6 and B31L2 dipoles, is shown in Fig. 4.35. Data points measured with the same XPS spectrometer on pure CuO and Cu_2O samples are shown for reference. Also including $Cu(OH)_2$ would have required a much wider horizontal scale, which would have in turn blurred the main message of the figure. Consequently, only the direction of its expected position is indicated with an arrow, as a guide.

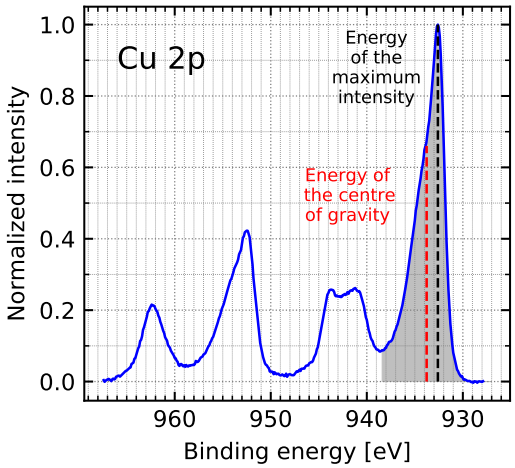

Figure 4.34: Cu 2p energy used for the Wagner-like plot: energy of the maximum line intensity versus energy of the centre of gravity of the area below the Cu 2p line, between 927 and 938.5 eV.

From the distribution of the data points in the upper graphs of Fig. 4.35, it appears that all the sections of C21R6 beam screens, except the field-free section of V2 beam screen, are similar and exhibit mainly Cu_2O oxide, slightly covered by copper hydroxide. As previously mentioned, the section in the field-free region of V2 beam screen exhibits more hydroxide. The data points corresponding to XPS spectra acquired on the lateral beam screen sides (crosses) are found in the same plot regions as the data points corresponding to flat sides (circles). These beam screens are thus homogeneous in azimuth.

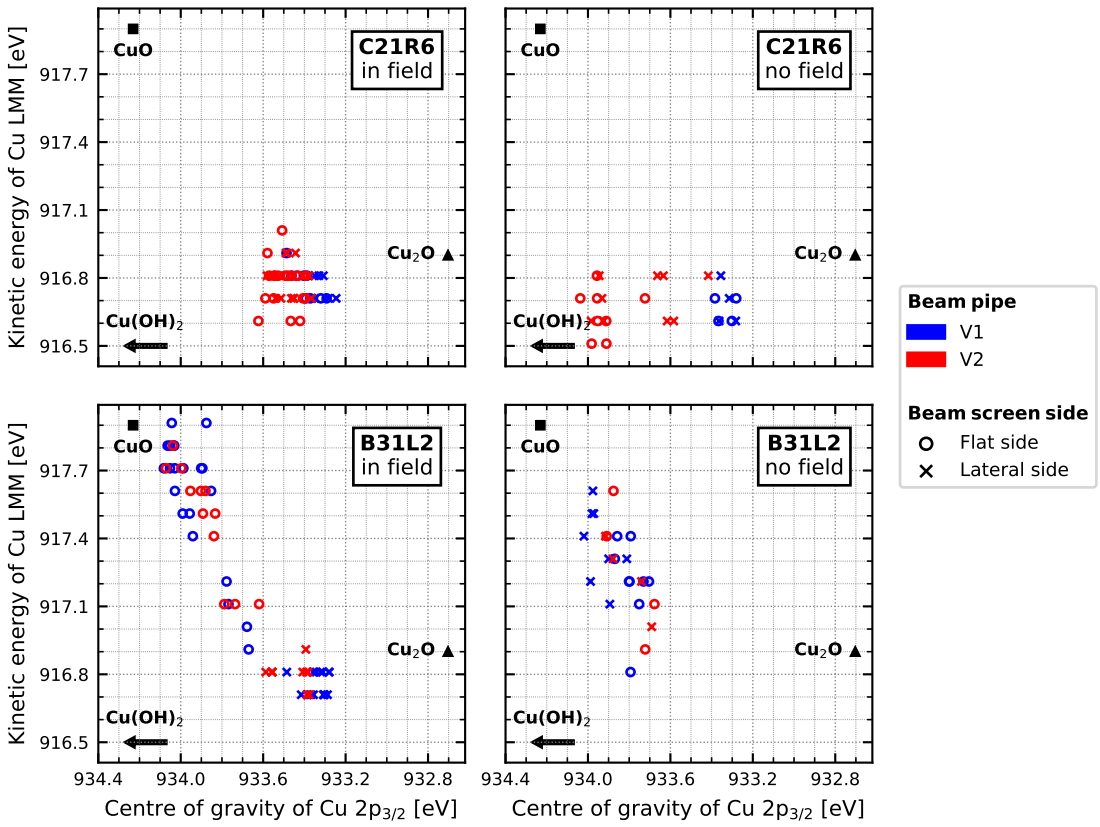

Figure 4.35: Wagner-like plot for all the XPS spectra acquired on the beam screens from the C21R6 (top) and B31L2 (bottom) locations, in field (left) and field-free regions (right). The data points corresponding to spectra acquired on the flat (top and bottom) sides of the beam screens are represented with empty circles, while crosses correspond to spectra acquired on the lateral (sawtooth and weld) sides.

Concerning the beam screens from B31L2 location, in the field region (Fig. 4.35 (bottom left)), two families of data points appear, which correspond to the two families of beam screen sides. The data points corresponding to lateral beam screen sides (crosses) are found in the same region of the plot as for the C21R6 beam screens. They also exhibit mainly Cu_2O with a small amount of hydroxide. Instead, the data points acquired on the flat sides of the beam screens (circles) are mainly found close to the plot region corresponding to CuO. Therefore, for most of the points in the flat beam screen sides, CuO is the dominant oxide. It is worth mentioning that for the plot corresponding to the field region of the B31L2 beam screens, the CuO amount is the same all along the magnet for the measured samples. In the field-free region of the B31L2 beam screens (Fig. 4.35 (bottom right)), such a distinction between flat and lateral beam screen sides is no longer observed: all the data points are found in the same plot region indicating that CuO is clearly present all around the azimuth. The same trend is observed for both B31L2 beam screens. In summary, while for the low heat load magnet, no systematic correlation is observed between the characteristics (density and energy distribution) of the electron cloud and the surface properties of the beam screens, a clear link is observed for the beam screen surfaces of the high heat load dipole: both in field and field-free

regions, CuO is systematically found where the electron cloud density and the electron energy are the highest.

From the Wagner-like plot, it appears that some B31L2 flat sides from the field region are very close to the position of the CuO reference sample. The Cu 2p line for the B31L2 spectra exhibiting the most of CuO is shown in Fig. 4.36, together with the line of the reference CuO sample. Even though a component at low energy, certainly Cu_2O at 932.5 eV, is still probably present for the B31L2 case, both lines are very similar. In the analysed depth, copper of the B31L2 sample is therefore almost only in the form of CuO. The intensity I emitted from the surface corresponding to the photoelectron current I_0 generated at a depth x below the surface is given by:

$$I = I_0.e^{\frac{-x}{\lambda}} \tag{4.1}$$

where λ is the energy-dependent attenuation length. Consequently, 63% of the XPS signal originates from a depth equal to λ. Neglecting the elastic effects in the attenuation length, λ becomes equal to the inelastic mean free path. In the case of CuO, the inelastic mean free path of the Cu 2p photoelectrons ($E_k \sim 550$ eV), is about 1.2 nm [161] giving an estimated CuO thickness of at least 1.5-2 nm for this B31L2 sample.

Among the flat sides of B31L2 beam screens, no systematic difference of surface chemistry was observed which could explain the SEY pattern reported in Fig. 4.30.

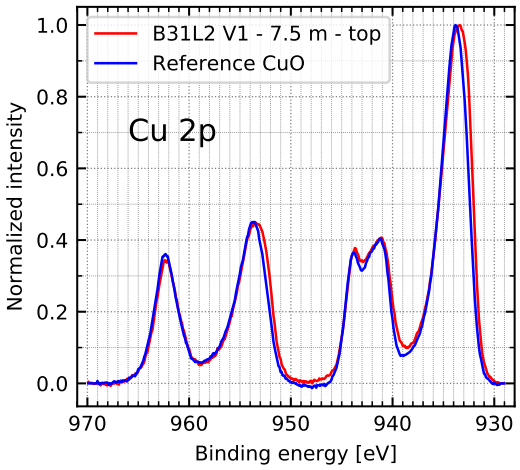

Figure 4.36: Cu 2p lines for the B31L2 spectrum exhibiting the most of CuO and for a reference CuO sample.

- **Conditioning**

Since a different chemical composition was observed between lateral and flat beam screen sides for the sections in the field region of the B31L2 dipole, the two types of surfaces were conditioned in the laboratory, for comparison. The conditioning curves of both the bottom and weld sides of the slice at 13 m (in field region) of the V1 beam screen from B31L2 are shown in Fig. 4.37, where the curves for a beam screen from the C21R6 magnet and from the stock (never installed in the LHC) are shown for comparison.

The bottom side (exhibiting CuO) from the B31L2 beam screen clearly shows a conditioning curve different from both the reference and the C21R6 sample. A δ_{max} decrease is actually observed during conditioning. However, no saturation of the decrease is observed, even after a dose of 3×10^{-2} C/mm^2, i.e. three times higher than the usually required one. Furthermore, after such a dose, the maximum SEY is still at 1.2, which is significantly higher than the ultimate SEY observed for the reference and C21R6 samples. Such a behaviour was consistently observed for three flat sides of sections at different locations in the field region of the B31L2 magnet. In contrast, the conditioning curve of the lateral weld side (showing much less CuO) is more similar to the reference and C21R6 ones. A saturation of the δ_{max} decrease is observed at 10^{-2} C/mm^2. The ultimate SEY, equal to 1.12, remains slightly higher than the one of the C21R6 and reference samples, but is well below the electron cloud build-up threshold.

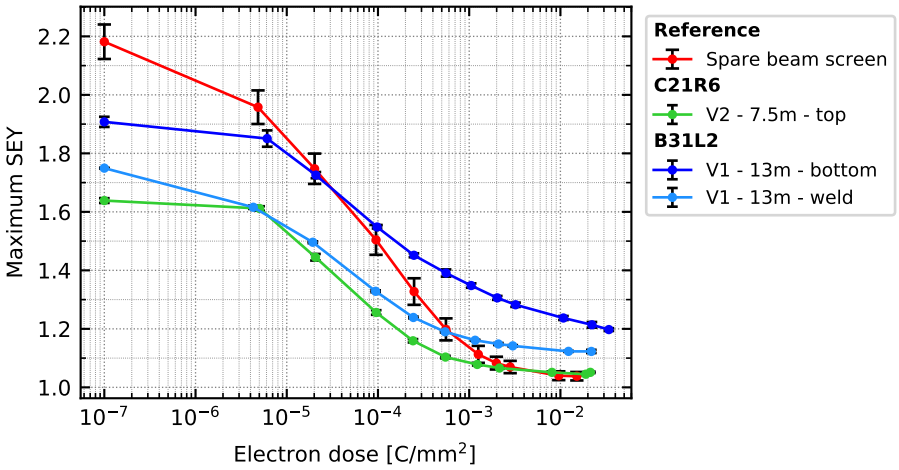

Figure 4.37: Conditioning curves of the bottom and weld sides of the V1 beam screen sections located at 13 m (in field region) of B31L2 dipole. The conditioning curve of a spare beam screen (never installed in the LHC) and of a C21R6 beam screen are given for comparison. The error bars represent the standard SEY deviation over 3 different locations of the samples.

The SEY curves after full conditioning of the two B31L2, the C21R6 and the reference samples are shown in Fig. 4.38. Apart from a different maximum SEY, the SEY curves of the B31L2 samples exhibit a similar shape to the C21R6 and reference ones. It is also observed that the low energy part of the SEY curve is identical for all samples.

The Cu 2p, O 1s and C 1s lines for the bottom and weld sides of the section at 13 m of V1 beam screen of B31L2 are shown in Fig. 4.39 at different irradiation doses. For the bottom side, the intensity of the satellite and of the high energy shoulder of the Cu $2p_{3/2}$ peak decrease during irradiation, witnessing a strong decrease of the CuO amount. This observation is coherent with the small shift of the O 1s line towards higher binding energy. However, the satellite is still visible after a dose of 3×10^{-2} C/mm^2 and the O 1s line position remains lower than expected for pure Cu_2O (530.5 eV). It is thus concluded that the reduction of the CuO oxide is not completed at this dose and under these experimental conditions. In parallel, a shift of the C 1s line is observed, confirming the graphitization of the present carbon. Nevertheless, the contribution at

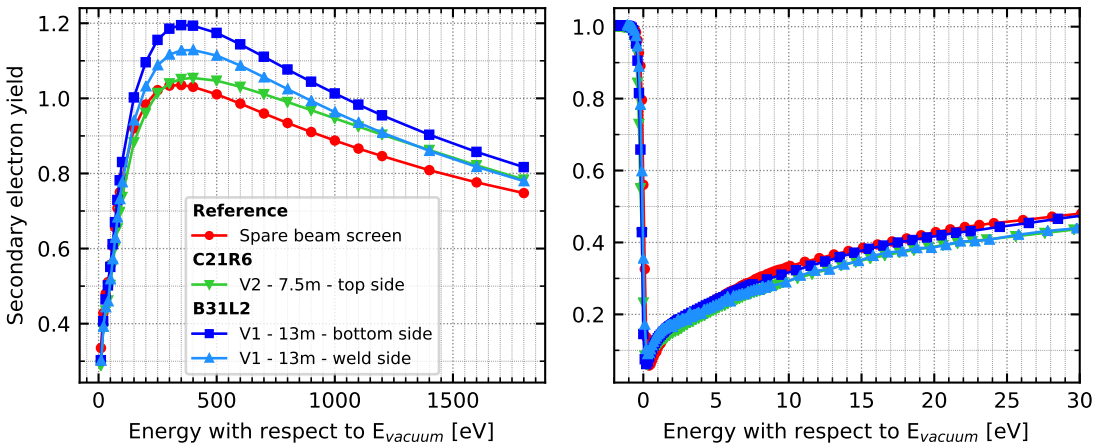

Figure 4.38: (left) SEY curves from 10 to 1800 eV of the two sides (bottom and weld) of the V1 beam screen section at 13 m from the B31L2 magnet, of the section at 7.5 m from V2 beam screen of C21R6 and of a never installed beam screen, all after full conditioning, (right) low energy SEY curves. The energy is referenced to the vacuum level.

288.5 eV, which disappears during the irradiation of 'normal' air exposed copper, is still visible. For the weld side, the irradiation leads to a complete reduction of CuO as proved by the disappearing of the Cu 2p satellite and the position of the O 1s line at 530.5 eV. A shift of the C 1s line is also observed. Furthermore, as for the bottom side, the bump at 288.5 eV is still present after full conditioning.

4.2.4 Conclusions on the analyses of low and high heat load dipole beam screens

The characterisation of beam screens extracted from both a high and a low heat load dipole revealed significant differences of surface properties between the two magnets, in particular concerning the copper oxidation product, as summarized in Fig. 4.40. The beam screens extracted from the low heat load magnet clearly show the memory of conditioning: lower copper hydroxide component, lower binding energy of the C 1s line and lower SEY than expected for a beam screen never exposed to an LHC beam. A small amount of CuO is also present on the surfaces. For both beam screens of the C21R6 magnet, in their field region, the surface chemistry and SEY seem independent from the azimuthal position, even though the density and energy distributions of the electron cloud are strongly different between the flat and lateral sides. Such an homogeneity could be due to the large integrated dose (from the electron cloud and the synchrotron radiation) seen by the surfaces over the LHC Run 2. The conditioning of these C21R6 beam screens is similar to the one of a spare beam screen in terms of ultimate SEY and dose required to reach it. Furthermore, it is observed that apart from one section in the field-free region, the beam screens from each beam aperture exhibit similar surface characteristics, even though their analysis spread over several weeks. This confirms the efficiency of storing the components to be analysed under vacuum to stop their deconditioning. It also allows to conclude that no large difference (i.e. which could

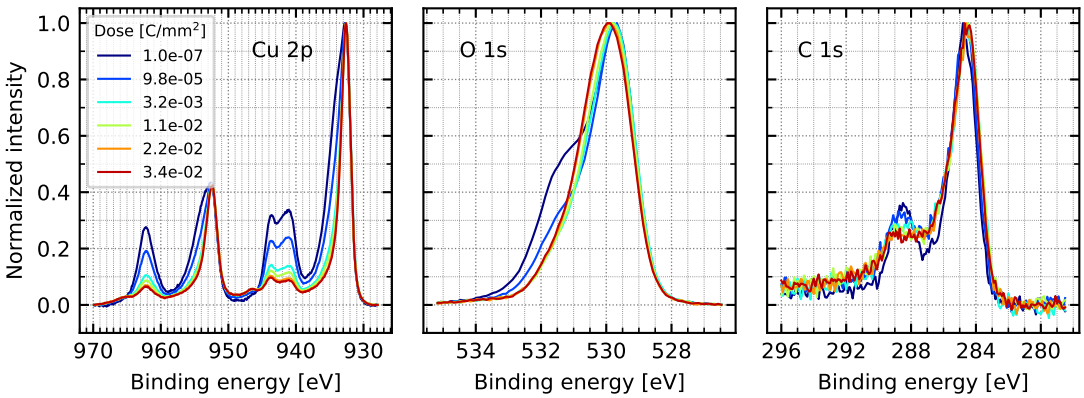

(a) Bottom side

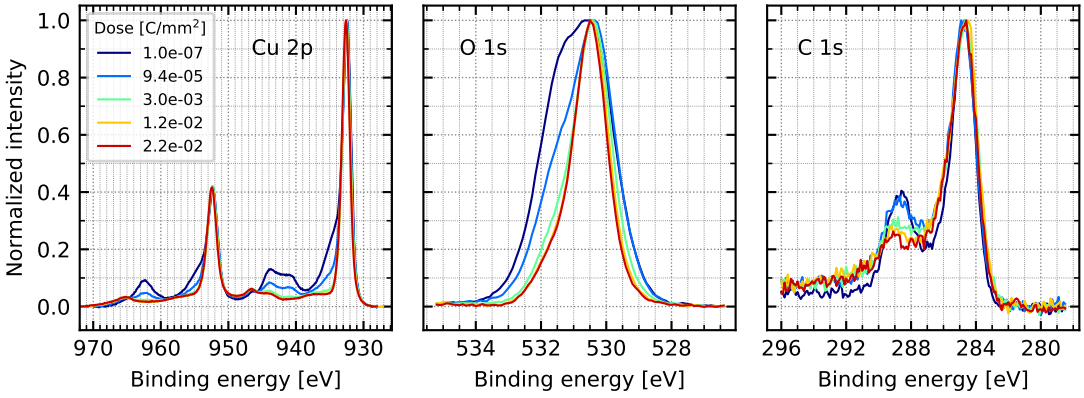

(b) Weld side

Figure 4.39: Cu 2p (left), O 1s (centre) and C 1s (right) lines during conditioning of the (a) bottom and (b) weld sides of the section at 13 m from V1 beam screen of B31L2 magnet.

persist after venting) were present along the beam screen length, yet with small sampling rate along the magnet length. It is however observed that hydroxide is more present for the section cut in the field-free region of the V2 beam screen. Copper hydroxide gets easily removed under electron irradiation at room temperature (see Section 3.2). Its quasi-absence in the other sections of these beam screens suggests that its removal is also effective at cryogenic temperature. Therefore, its presence after air exposure on the LHC beam exposed surface most probably results from a hydroxide build-up at air exposure rather than from its persistence over LHC operation. However, the reason of its presence in this particular field-free section is unclear. The fact that the field-free sections are close to the magnet interconnections and therefore are more prone to a possible contamination when opening the beam lines and to differences in the handling during extraction should be considered.

The beam screens from the high heat load magnet show a completely different picture, as shown in Fig. 4.40. In the field region, CuO is widely observed on the flat sides of the beam screens, while on the lateral side, its presence is negligible, even though it cannot be fully discarded. In the field-free region, CuO is observed all around the azimuth. Such a variation of the azimuthal distribution of CuO correlates well with the electron cloud

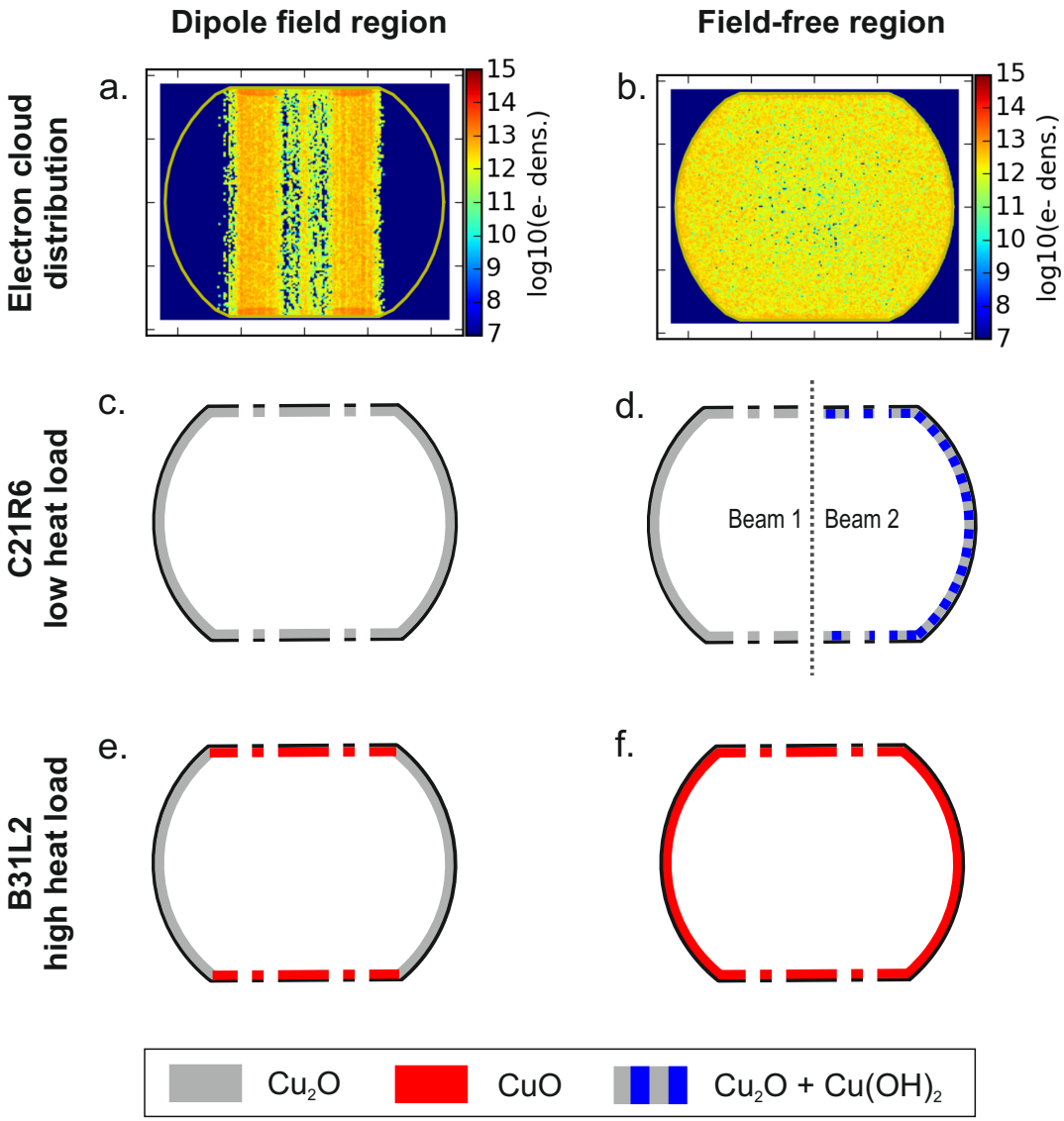

Figure 4.40: Summary of the electron cloud distribution (a, b) [79], of the main copper oxidation products found on the beam screens of the low (c, d) and the high (e, f) heat load LHC dipoles and their dependence on the magnetic field.

density distribution, both for field and field-free regions. The CuO distribution also matches with the regions where the electron energy is the highest. Such a correlation unambiguously ascribes the presence of CuO to the machine operation. Furthermore, the amount of carbon is found to be low at all azimuths, both in and outside the field regions. Such a low amount of carbon cannot be achieved by a careful chemical cleaning with the procedure applied for the UHV components at CERN. Therefore, the low carbon amount seems also to be a consequence of machine operation. In spite of a significant dispersion, which can partly be related to contamination of the samples during their preparation, a trend emerges from the SEY profiles, in particular for the V1 beam screen. For the sections collected in the field regions, the SEY of the flat sides is between 1.8 and 2.0 which is higher than observed for the C21R6 magnet and close to the range of SEY value of never installed beam screens. On the lateral sides, the SEY value seems lower for some

sections, between 1.6 and 1.8, i.e. closer to the value observed for the C21R6 magnet. In the field-free regions, the SEY is uniform in azimuth and is found between 1.8 and 2.0 as for the flat sides in the field region. It thus appears that the high SEY regions are the ones where CuO is found, and therefore, the SEY profiles also matches with the electron cloud density and energy distributions. Furthermore, the SEY measured in the flat sides in the field regions and all around the azimuth in the field-free regions is unexpectedly high for such clean surface (low carbon amount and no or very few hydroxide). No other anomaly was detected on the B31L2 beam screen surface, in particular, no trace of potassium or sodium from the detergent nor visible stains. Therefore, CuO could be responsible for the higher yield observed in these regions. A measurement of the SEY of pure (carbon-free) and smooth CuO surface would be required to confirm this hypothesis. Such a surface should be produced *in-situ*, i.e. directly in the characterisation set-up, since a transfer through air would modify the SEY of the pure material, and operation such as sputtering to remove carbon contamination should be avoided on CuO [136]. Furthermore, the grown CuO layer should be smooth, in order to exclude any influence of the surface morphology on the SEY. The possibility of producing such a CuO layer in the surface characterisation set-up is thus currently being studied.

These differences of surface chemistry result in different conditioning paths. In the presence of CuO, the conditioning kinetics is significantly slower and the decrease of the maximum SEY does not saturate for doses up to 3×10^{-2} C/mm^2. The conditioning involves the reduction of CuO into Cu_2O, which is known to have an intrinsic maximum SEY around 1.25. This situation is different from the air exposed and C21R6 beam screen surfaces, where the SEY decrease during conditioning relies on surface cleaning and carbon graphitization. This graphitization was also observed in the B31L2 case, however, the contribution of O-C=O groups on the C 1s lines is not fully removed by irradiation as expected for a 'normal' copper surface. The persistence of this contribution is also observed for the conditioning of a lateral side (without CuO) of the B31L2 beam screen, but in this case, the conditioning proceeds with a usual kinetics and allows for a decrease of the SEY below the electron cloud build-up threshold. The unusual conditioning characteristics of the flat B31L2 beam screen sides is therefore ascribed to the large presence of CuO.

Chapter 5

Discussion

5.1 Mechanisms of copper conditioning and deconditioning in the laboratory

As a first mandatory step, a laboratory study of the mechanisms governing copper conditioning at room temperature in well defined conditions was performed (Section 3.2). It is shown that this conditioning, i.e. the reduction of the SEY down to value close to unity under electron bombardment at 250 eV relies on:

- surface cleaning by ESD and conversion of $Cu(OH)_2$ into Cu_2O
- carbon graphitization, which allows to decrease the maximum SEY of air exposed copper below the one of pure Cu and Cu_2O

In parallel, this study provided full energy range copper SEY curves for different conditioning doses as inputs for electron cloud simulations. It allowed to compare and evidence differences between simulations based on analytical SEY models or on experimental data, in particular for high SEY [123]. Additional laboratory data sets such as energy spectra of the secondary electrons for different materials and different conditioning states would help to improve the accuracy of the electron cloud simulations tools.

A second study (Section 3.3), triggered by the evidence that the information accessible by analysing the surface of LHC extracted vacuum components would be spoiled by deconditioning if the surfaces were not properly stored and handled, demonstrated that deconditioning involves the reverse mechanisms of conditioning. Indeed, a conditioned surface exposed to air will quickly get hydrocarbon recontaminated and covered with copper hydroxide, leading to SEY increase. For the analysis of beam screens extracted from the LHC during LS2, the air exposure time of the surfaces between the machine venting and the start of the surface analysis was therefore reduced at most, by optimizing the magnet and beam screens extraction planning and by storing the components under vacuum as soon as possible. Such a strategy, i.e. limiting the deconditioning of the beam screens by reducing their air exposure time, can also be applied to the LHC arcs, to save reconditioning time of the machine at the resuming of operation at the end of technical stops.

5.2 Consequence of the beam screen surface state on the LHC operation

The analyses of beam screens extracted from a low (C21R6) and a high (B31L2) heat load LHC dipole revealed the presence of different copper oxidation products in the two families of beam screens. While the surface state of the beam screens from the low heat load C21R6 dipole is similar to the one expected for a conditioned copper surface after short air exposure, cupric oxide CuO is the dominant oxide in the area of the B31L2 beam screens where the density and electron energy of the electron cloud are the highest. Furthermore, an extremely low amount of carbon is observed on the B31L2 beam screens, which cannot be achieved by the standard UHV cleaning procedure. Such observations unambiguously link these two major differences of surface chemistry between B31L2 and C21R6 beam screens to the LHC machine operation. The impact of such chemical differences on the heat load of the respective dipoles is discussed in the following.

During conditioning of the CuO-rich surfaces at room temperature in the laboratory, a slower kinetics is observed with respect to the nominal (CuO-free) copper surface. However, a maximum SEY below the electron cloud build-up threshold is obtained for doses of about 3×10^{-2} C/mm^2 in spite of the presence of CuO. This conditioning involves the partial reduction of CuO into Cu_2O and this different mechanism is held responsible for the slower conditioning kinetics of the CuO-rich surfaces. The reduction of this oxide under electron bombardment has already been observed at room temperature [162, 163]. This process was shown to be eased in the presence of carbonaceous species and is limited by the diffusion of oxygen or copper to and from the surface, respectively [162]. Indeed, it has been reported that the transformation of CuO into Cu_2O is significantly hindered at 180 K [162] which is coherent with the reduced diffusion coefficient at such temperature. Therefore, in contrast to the laboratory experiment, the reduction of CuO oxide at the beam screen surface under electron bombardment could be partly or even completely hindered in the LHC operation conditions, due to the low temperature (5-20 K) and low surface carbon amount. Such an hypothesis is compatible with the fact that CuO is still present on the B31L2 beam screen surface after several years of accumulated scrubbing. Conditioning and monitoring of the surface chemistry of a clean (low carbon concentration) CuO surface at cryogenic temperature would be required to validate this hypothesis. In addition, since carbon graphitization has been demonstrated to be a key phenomenon in the decrease of the SEY of air exposed copper, the extremely low carbon amount found on the B31L2 beam screens is certainly an additional obstacle to their proper conditioning. Indeed, presence of CuO was also found on the beam screens of the A31L2 dipole, while no anomaly of conditioning was observed for these beam screens. Such a different behaviour under electron bombardment in the laboratory between A31L2 and B31L2 beam screens could thus be explained by the usual amount of carbon (20-40 at.%) present on the surface of the A31L2 beam screens.

According to the analyses performed on the beam screens of the B31L2 and C21R6 LHC dipoles, and to the above considerations, the following hypothesis is proposed to explain the abnormal *in-situ* beam screen conditioning and thus, the high heat load

observed in parts of the LHC: very low amount of graphitic carbon and presence of CuO which either i) is not *in-situ* reduced during Run 2 because of the low carbon amount and/or the cryogenic temperature or ii) is continuously reduced and built up (dynamic equilibrium). The possible mechanisms for the formation of CuO in the LHC are discussed in the following.

5.3 Hypotheses for the formation of CuO in the LHC

CuO oxide build-up is not observed in the laboratory, neither during the conditioning of normal air exposed copper nor during sample venting and air exposure after conditioning. As discussed in Section 3.1, the laboratory and LHC environments are significantly different. Therefore, two hypotheses can be made concerning the CuO growth in the LHC:

- the LHC beam screen surface was not similar to the laboratory samples, i.e. contaminated or subjected to non-nominal maintenance or operational conditions and this led to CuO build-up,

or

- CuO results from a difference in conditioning mechanisms induced by the different laboratory and LHC environments.

In the following, mechanisms for CuO build-up are proposed and discussed.

Cuprous oxide Cu_2O is the native copper oxide at room temperature, i.e. it spontaneously grows on a copper surface exposed to air [106]. Instead, CuO can be formed in air above 300°C [164] or at lower temperature in a higher partial pressure of oxygen [165]. These two possibilities are discarded in the present case since the LHC machine is thermally cycled between room temperature and 1.9 K and the beam pipe atmosphere varies between ambient air and UHV. CuO has also been observed to form while exposing copper to ozone [166]. This was confirmed in the laboratory, at room temperature, where CuO built up on an air exposed copper surface while exposed to ozone produced by UV light in air. In the machine, the presence of ozone is plausible, since this reactive gas can be formed for instance by electron irradiation of condensed oxygen [167] or by oxygen absorption of UV light [168]. In addition, copper exposure to ozone could also explain the low carbon amount observed on the B31L2 beam screen surface. Indeed, ozone is commonly used for surface cleaning [168–170] as the combination of carbon with reactive ozone molecules leads to the creation of molecules such as CO and CO_2 [168] which could easily be desorbed from the beam screen by ESD. Furthermore, ozone was observed to increase the amount of O-C=O groups on the exposed surfaces [129,171,172], i.e. of the same functional groups which are unusually observed to persist, in spite of the low carbon amount, on the surface of the B31L2 beam screens after conditioning in the laboratory. Finally, CuO was also formed at 80 K under O_2^+ bombardment at 500 eV [173]. In this case, the proportion of Cu_2O to CuO obtained during bombardment was shifted to the

latter oxide by decreasing the temperature. Here again, the presence of such ions in the machine resulting from the ionization of the residual and condensed gas is possible [174]. Furthermore, at 8.3 T, the Larmor radius of a 200 eV O_2^+ ion is below one millimetre, i.e. such ions would also be confined by the magnetic field. An azimuthal distribution of CuO as the one observed in the B31L2 beam screens would thus be expected. Even though some of the proposed mechanisms leading to CuO build-up seem to be conceivable for the LHC case, all of them require a source of oxygen, which is not obvious in a UHV system such as the LHC beam pipe as discussed in the following.

The analyses of the LHC extracted components were all performed after air exposure. Therefore, it is not possible to exclude rigorously the possibility that CuO only builds up at venting, when oxygen is available (in the present case, it would have built up during LS1 venting). In such a case, the difference of CuO amount observed in the B31L2 beam screens between the areas where the electron dose and electron energy are the highest and the others should result from different surface reactivity at the venting, induced by the electron cloud. However, CuO oxide build-up is not observed in the laboratory during the venting and air exposure of a conditioned surface, even though at venting, the environmental conditions, in particular temperature, are similar for the laboratory and LHC cases. Therefore, the possibility of having a significant difference between laboratory and LHC cases at venting, leading to CuO build-up only in the LHC configuration is estimated to be very unlikely.

Then, apart from the presence of CuO and the low carbon amount which both result from machine operation, no particular feature such as contamination with an unexpected element or presence of stains, was observed on the B31L2 beam screens. This may arise from two scenarii: either the CuO-covered beam screens indeed presented initially some anomalies such as the presence of carbonates (see Section 3.5.2.4), which got converted into CuO and are no longer visible after the Run, or the beam screens were nominal and only exposed to nominal conditions and it is the effect of these nominal conditions themselves which is not reproduced in the laboratory, at room temperature. Even though the poor conditioning and high heat load of some half-cells have often been tentatively ascribed to hypothetical contamination and non-conformities (see Section 3.5), the results of Chapter 4 do not indicate that the beam screens were affected by such accidents before Run 2 leading to the formation of CuO. Furthermore, in the case of a contamination such as the ones considered in Section 3.5, the damages are expected to be longitudinally localised and randomly distributed in azimuth, and thus, the affected beam screens are not expected to be as longitudinally homogeneous as the ones of B31L2, and contaminants should still be present on the lateral beam screen sides, where no CuO is observed. Consequently, the oxygen necessary for CuO build-up is most probably not coming from a contamination of the beam screens by accidental event. The hypothesis that the differences between laboratory and LHC environments are responsible for different conditioning mechanisms of a given air exposed copper surface becomes thus evident, and the most striking difference is the temperature.

The presence of water in the beam pipe could provide the necessary oxygen atoms for CuO build-up. Indeed, while in the laboratory, at room temperature, water would

be desorbed from the sample either thermally or by ESD and would no longer readsorb effectively, the situation at cold in the LHC is different due to a sticking coefficient of one. In an unbaked system such as the LHC arcs vacuum system, the main residual gas at room temperature is water. Considering a pressure of 10^{-4} mbar of water in the arcs before the cool-down and the worst (but unrealistic) cool-down scenario, i.e. the beam screen is colder than the cold bore and all gases condensate on its copper surface during the cool-down, the amount of available water molecules allows to cover the beam screen surface with roughly a hundredth of a monolayer. Such a low quantity of water is not enough to explain the amount of CuO observed on the B31L2 beam screens, which corresponds to at least several molecular layers. Furthermore, in such a scenario, one expects to see a higher heat load and more CuO on the coldest machine parts during the cool-down phase, i.e. on the magnets which are the closest to the helium flux inlet in the cells. Such a heat load pattern is actually not observed. Indeed, the B31L2 magnet is actually located close to the 'warm' side, i.e. the helium outlet side of the cell. According to these different arguments, the presence of water on the copper beam screen surface at the beginning of Run 2 is therefore not the source of oxygen for CuO build-up.

The gas density required in the beam pipe to build up CuO by ion bombardment was estimated, and the details are given in Appendix B. Considering that the beam vacuum contains only molecules which, if ionized, will produce CuO by ion bombardment, a production rate of one CuO monolayer per year would require a two orders of magnitude higher gas density than the required one for 100 h beam lifetime. Such a gas density is not compatible with machine observations [175]. CuO build-up by ion bombardment is thus very unlikely.

Another source of oxygen could be copper hydroxide itself. Indeed, this copper compound contains already two atoms of oxygen per copper one and grows spontaneously on an air exposed copper surface, even in a rather dry atmosphere (see Fig. 3.17). In addition, the beam screens were not only exposed to air for several months, but tunnel air was circulated in the beam lines for the RF ball passage. The presence of copper hydroxide on the beam screen surface at the repump-down of the machine at the end of LS1 is therefore very likely. In the laboratory, copper hydroxide is observed to degrade under electron bombardment and to be, at least partly, converted into Cu_2O. It is reported that bulk $Cu(OH)_2$ was degraded into CuO at room temperature under electron bombardment [176]. Such a conversion is not observed in the laboratory for $Cu(OH)_2$ on a copper substrate, possibly due to the rapid further reduction of CuO into Cu_2O or because of the influence of the underlying substrate. However, if the reduction of CuO to Cu_2O is hindered at cryogenic temperature [162], the electron bombardment of $Cu(OH)_2$ could lead to the build-up of CuO on the beam screen copper surface in the LHC. Under this hypothesis, the presence of CuO only on the beam screen areas where the electron cloud current density and electron energy are the highest could for instance result from an energy threshold for the conversion of $Cu(OH)_2$ into CuO which is higher than the energy of the electrons impinging on the lateral beam screen sides, in the dipole field. One could also suggest that hydroxide itself built up with the azimuthal distribution observed for CuO in the B31L2 beam screens, because the lateral and flat

sides had different surface reactivity at venting, as a result of the different electron cloud bombardment during Run 1. Such a scenario will be assessed by monitoring $Cu(OH)_2$ growth in air on the different sides of the C21R6 beam screens.

All these hypotheses would require to be assessed in the laboratory to validate the mechanisms of CuO production in the LHC. Additional efforts are thus being currently targeted towards understanding the differences of conditioning between room temperature laboratory set-up and cold LHC environments. Indeed, understanding the mechanisms behind CuO build-up would allow to more efficiently prevent its further growth in the healthy parts of the machine. A dedicated set-up where both electron irradiation and surface characterisation by XPS could be performed on a cold sample would help in these tasks, namely to confirm or infirm the difficulty to convert CuO into Cu_2O and the possibility to form CuO from $Cu(OH)_2$ by electron irradiation at low temperature.

Finally, the above mentioned hypotheses alone do not explain the distribution of low and high heat load magnets and half-cells along the machine which appeared in Run 2. Indeed, nothing in the proposed mechanisms can explain the presence of a low heat load next to a high heat load dipole as shown in Fig. 1.8, neither the splitting of the LHC into a globally high load half (arcs 1-2, 2-3, 7-8 and 8-1) and low load half (arcs 3-4, 4-5, 5-6 and 6-7) (see Fig. 1.7). Under the assumption of CuO built from $Cu(OH)_2$, the hypothesis that some magnets were still below dew point when exposing their beam screens to air in LS1, leading to water condensation which could in turn favour $Cu(OH)_2$ growth and later lead to more CuO on these beam screen surfaces, arose. However, the monitoring of the magnet temperature and tunnel air characteristics allowed to discard this hypothesis. Furthermore, once again, the position of the low and high heat load magnets should correlate with the thermal gradient present during the warm-up of the arcs and induced by the circulation of the 'warm' helium flux, but it is not the case. An other possibility would be that the arc beam screens were slightly different at machine installation. Indeed, the laboratory study showed that 'as received' or 'air exposed' is not a well defined surface state and quantities such as carbon and hydroxide amounts may vary significantly from one beam screen to another, while still staying within the acceptable values for UHV compatibility. These differences can be found right after cleaning and are also influenced by the beam screen storage time and conditions before their insertion into the machine. The distribution of 'clean' and 'cleaner' beam screens is thus expected to be random in the machine. If, for instance, the amount of graphitic carbon on the beam screen surface at their venting at the beginning of LS1 impacts the reactivity of the surface and the products which build up on it, which would in turn determine the production or not of CuO, differences of beam screen surface at installation may explain the random character of the LHC heat load pattern. While a laboratory study will help validating or discarding the hypothesis that the deconditioning and reconditioning of a surface depends on its initial (before first conditioning) state, it would not be possible to correlate the initial LHC beam screen state with their current one.

5.4 Preventing further degradation of the LHC

In short-term perspectives (the pump-down and cool-down of the LHC before its restart for Run 3 are planned for mid-2020), the priority is to prevent further degradation of the beam screen surface in the low heat load parts of the machine. According to the present level of knowledge of the mechanisms for CuO build-up and on the previous studies on conditioning and deconditioning, several steps have been implemented, all aiming at limiting at most the air exposure of the beam screens during LS2:

- arc beam lines venting with N_2/O_2 mixture to ensure a controlled and reproducible first exposure of the beam screens to a reactive gas
- closing of the beam lines with covers after PIMs opening
- repump-down of the beam lines as soon as possible, i.e. when all interconnections between magnets of an arc are closed and intervention on the beam vacuum system is no longer needed

Such actions, by limiting the deconditioning of the beam screens, could also help saving reconditioning time of the machine at the resuming of operation after LS2.

Furthermore, the possibility of performing a mild warm-up (up to 80°C) of the arc beam screens while pumping down the machine has been proposed, to minimize the presence of water during cool-down. Indeed, the heating system used for pre-loading the cryogenic system before injection of the beams [72] could be used for this purpose. However, such an operation could present some risks for the machine and is being currently evaluated. In particular, it must be ensured that such a warm-up, even though it remains well below the temperature of a proper bake-out, does not have any detrimental impact on delicate mechanical parts such as bellows.

Additional proposals could be done if further understanding of the CuO build-up mechanisms in the LHC is gained, in particular concerning the pump-down, cool-down and scrubbing schemes of the machine.

5.5 Towards a curative solution for the LHC heat load problematic

On a longer term, curative solutions against the presence of CuO must be proposed, taking into account the particular LHC environment and the dimensions of its vacuum system.

The stability diagram of CuO shows that this oxide can be reduced under vacuum at temperatures above 300°C [177]. While such a temperature is not achievable with the present machine configuration, the presence of a reducing gas (such as H_2, or a non-flammable mixture containing H_2) could lower this temperature down to more acceptable ones [178, 179]. However, as mentioned above, warming up the arc vacuum system is a delicate operation and a risk assessment should be done. A dedicated laboratory study would be furthermore required to confirm the efficiency of such an operation and tune the

parameters for optimization of the process. CuO reduction by UV light should also be considered [180]. A removal of this oxide could also be obtained by plasma etching. CuO is indeed known to be easily converted into Cu_2O under ion bombardment [136]. Both options of UV irradiation and ion sputtering imply the insertion of a device travelling along the beam screen. Such a treatment could be implemented taking profit from the designed set-up for *in-situ* amorphous carbon coatings to be implemented in some specific LHC sections during LS2 and LS3 [181]. However, this solution is far from being ready for implementation, since the length of beam screens to treat is large (one half on the LHC corresponds roughly to 2 x 10.5 km of arc beam screens) and with the present set-up such an operation would require to open all magnet interconnections for inserting the sputtering device inside each single beam screen to treat (cutting and removing the four PIMs of a single dipole takes about 1.5 day). According to the work amount that such an operation would represent, this option is not currently considered as feasible.

An other approach would consist in masking the CuO with a low SEY material rather than removing this oxide. Carbon coatings are the most natural idea arising when thinking of low SEY thin film coatings, according to CERN experience in this field [43, 57, 118, 122, 181–183]. However, for the same reasons as mentioned for the CuO plasma etching option, implementing carbon coatings over such a long vacuum system is a highly challenging and time consuming work and therefore currently not a viable option. Nevertheless, an innovative solution would be to rebuild a carbon layer onto the CuO surface, which could later be graphitized during LHC operation, by injecting carbon species in gas phase into the LHC beam pipes at room temperature. Here again, such an option would require a dedicated development study for the gas selection, process parameters, risks for the machine and time scale for such a work.

Conclusion and perspectives

The study of air exposed copper conditioning mechanisms under electron bombardment at 250 eV and at room temperature in the laboratory evidenced two processes: surface cleaning by electron stimulated desorption as well as graphitization of the adventitious carbon layer. Both processes lead to the decrease of the secondary electron yield of copper, but graphitization was demonstrated to be the mechanism allowing for maximum SEY reduction down to value close to unity. It was in addition proved that no carbon growth is required on the air exposed copper surface to reach low SEY value during conditioning. Later, the study of copper deconditioning showed that the reverse processes, i.e. carbon recontamination and hydroxide growth occur when a bombarded surface is exposed to air. It therefore indicates the necessity of storing vacuum components extracted from the LHC in dry and clean atmosphere to prevent at most their deconditioning if investigation of their *in-situ* conditioning state has to be performed in the laboratory.

The comparative surface analysis of beam screens extracted from a low and a high heat load LHC dipole during LS2, evidenced significant differences between the two families of beam screens. While the ones extracted from the low heat load dipole showed surface features characteristic from a conditioned and shortly air exposed copper surface (low SEY, more graphitic carbon and lower amount of copper hydroxide than a never beam exposed surface) and comparable to the ones observed on a surface conditioned in the laboratory, the beam screens of the high heat load dipole exhibit cupric oxide CuO and a very low carbon amount. These features result from the machine operation itself, as the azimuthal distribution of CuO in the beam screens correlates perfectly with the properties of the electron cloud: CuO is found where the electron density and energy are the highest. The presence of CuO tends to increase the SEY of the beam screen surface and was found to slow down the conditioning kinetics (in the laboratory) with respect to a CuO-free surface. This conditioning at room temperature involves the reduction of CuO into Cu_2O, phenomenon which may be inhibited at cryogenic temperature, in the LHC arcs. Under this assumption, the presence of CuO and of a very low amount of carbon in some of the LHC beam screens is the most probable hypothesis explaining the high heat load observed in some sections of the LHC.

Since CuO is not observed in the laboratory, its presence on some LHC beam screens must result from conditioning mechanisms discrepancy induced by the different laboratory and LHC environments. Among all the considered mechanisms for CuO build-up, its formation from $Cu(OH)_2$ is currently considered as one of the most likely process.

This assumption should be tested in the laboratory at cryogenic temperature. If CuO is obtained, it would evidence the limits of the room temperature laboratory experiments in mimicking and studying the conditioning processes with an application to cryogenic vacuum system.

Short-term protective steps have been implemented to limit at most the exposure of the beam screens to air during LS2 and reduce the risk of further degradation of the LHC heat load for Run 3. On longer term, methods for removing or masking CuO should be developed, taking into account the particular LHC environment and the dimensions of its vacuum systems.

Extended French summary

Le nuage d'électrons se développant dans les chambres à vide du LHC lors de l'opération des faisceaux de protons engendre une charge thermique sur le système cryogénique de ses aimants supraconducteurs. La valeur de cette charge thermique présente une forte dispersion entre les différents arcs du LHC, pourtant identiques par design, dont certains sont actuellement proches de la limite de la capacité cryogénique. Sous l'effet du nuage d'électrons, le conditionnement de la surface de cuivre des chambres à vide du LHC a lieu, réduisant son rendement d'électrons secondaires et diminuant ainsi en retour l'intensité du nuage. Un tel processus est supposé décroître la charge thermique associée au nuage vers un niveau acceptable pour l'opération du LHC et semble donc actuellement mis en défaut dans certaines zones de l'accélérateur.

Ce travail étudie les phénomènes de conditionnement du cuivre ayant lieu dans le LHC afin d'expliquer les différences d'activité du nuage électronique observées le long de l'anneau.

Une étude en laboratoire, où le bombardement électronique de surfaces de cuivre à température ambiante est obtenu par l'usage d'un canon à électrons, sera réalisée afin d'expliquer le rôle des différents composants chimiques d'une surface de cuivre exposée à l'air dans son conditionnement. Les mécanismes du déconditionnement ayant lieu à la remise à l'air d'une surface irradiée (étape nécessaire à l'extraction de tubes faisceau du LHC) seront investigués. Il en découlera une procédure spécifique visant à limiter l'effacement de l'état de conditionnement *in-situ* des composants extraits du LHC en vue de l'analyse de leur surface au laboratoire.

Dans un second temps, des mesures de rendement d'électrons secondaires et de composition chimique de surface seront réalisées sur des tubes faisceau extraits d'un dipôle du LHC à faible et d'un dipôle à forte charge thermique. Une interprétation des ces analyses sera donnée dans l'optique d'expliquer l'origine des différences de charges thermiques observées le long de l'accélérateur.

Cette partie est un résumé en français de la thèse intitulée *Conditioning of surfaces in particle accelerators*. Les résultats majeurs y sont décrits et discutés et les principales conclusions et perspectives de cette étude y sont données. Pour plus de détails, le lecteur est invité à se reporter aux chapitres correspondants de la partie principale du manuscrit.

1 Contexte de l'étude

1.1 Le nuage d'électrons dans les accélérateurs de particules

1.1.1 Mécanismes de production, impact et contre-mesures

Au cours de l'opération des accélérateurs de particules à faisceaux intenses et positivement chargés tels que le *Large Hadron Collider* (LHC) au CERN, l'interaction du faisceau avec le gaz résiduel ainsi que le rayonnement synchrotron qu'il émet conduisent à l'émission d'électrons primaires dans la chambre à vide. Il s'en suit un phénomène en cascade décrit en Fig. 1, résultant de l'accélération des électrons primaires par le potentiel du faisceau, leur collision avec les parois de la chambre et l'émission d'électrons secondaires [15, 22, 23, 25, 26].

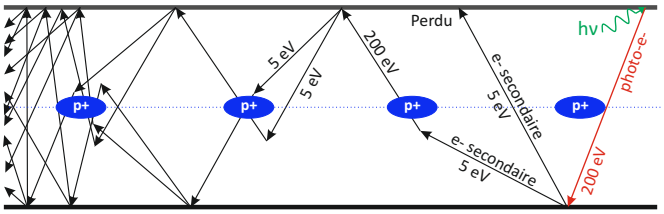

Figure 1: Mécanismes de développement du nuage d'électrons dans la chambre à vide d'un accélérateur. Le rayonnement synchrotron (vert) excite un photo-électron (rouge) qui est accéléré par le faisceau (bleu). A son impact avec la paroi de la chambre à vide, des électrons secondaires (noirs) sont émis. Schéma adapté d'après [22].

L'apparition de ce phénomène, connu sous le nom de nuage d'électrons, dépend notamment de la structure et de l'intensité du faisceau ainsi que du rendement d'électrons secondaires de la paroi interne de la chambre à vide [36–38]. Ce coefficient, défini comme le nombre d'électrons émis par électron incident, représente la capacité de la surface de la chambre à multiplier les électrons primaires et joue donc un rôle majeur dans le développement du nuage d'électrons.

Les conséquences de la présence d'un tel nuage dans le tube à vide du faisceau incluent le développement d'instabilités néfastes à la qualité du faisceau [22, 23, 39, 40], la dégradation du niveau de vide résiduel [18, 38, 41], ainsi que le dépôt d'une charge thermique sur le système à vide [22, 75].

Diverses techniques ont été développées afin d'atténuer ou stopper l'apparition du nuage d'électrons, par exemple en recouvrant la paroi des chambres à vide d'une couche mince à faible rendement électronique [42–46].

En outre, il est observé que l'intensité du nuage d'électrons décroît au cours de l'opération de l'accélérateur [41, 67, 117]. Le LHC profite de ce phénomène, nommé conditionnement, pour permettre la stabilité des opérations vis-à-vis du nuage d'électrons [9].

1.1.2 Conséquences pour le LHC

Dans les arcs du LHC, représentant environ 85% des 26.7 km de circonférence de l'accélérateur, le système à vide de chaque faisceau est immergé dans le bain d'hélium

liquide à 1.9 K des aimants supraconducteurs. Dès lors, toute charge thermique induite sur le système à vide lors de l'opération, notamment celle liée au nuage d'électrons, doit être dissipée par le système cryogénique, dont la capacité est limitée. Le système à vide du LHC, montré en Fig. 2, a donc été conçu dans l'optique de limiter la charge thermique déposée sur la zone à 1.9 K. Ainsi, un écran de faisceau possédant son propre système de refroidissement et opérant entre 5 et 20 K a été inséré dans le tube froid à 1.9 K. La face interne de cet écran est recouverte de cuivre OFE (*Oxygen Free Electronic grade*), pour accroître sa conductivité. Des trous de pompage situés sur les cotés haut et bas de l'écran permettent l'évacuation des gaz désorbés durant l'opération vers le tube froid où ils sont condensés. De plus, un profil en dents de scie a été imprimé sur la face latérale située vers l'extérieur de l'anneau du LHC afin d'absorber le rayonnement synchrotron. La présence d'un champ magnétique dipolaire confine les électrons du nuage dans une zone proche du faisceau, résultant en un bombardement électronique de l'écran de faisceau majoritairement localisé sur ses faces plates (haut et bas) [36]. Un écran électronique en cuivre béryllium a donc été fixé en haut et bas de l'écran de faisceau protégeant ainsi le tube froid des électrons du nuage s'échappant par les trous de pompage.

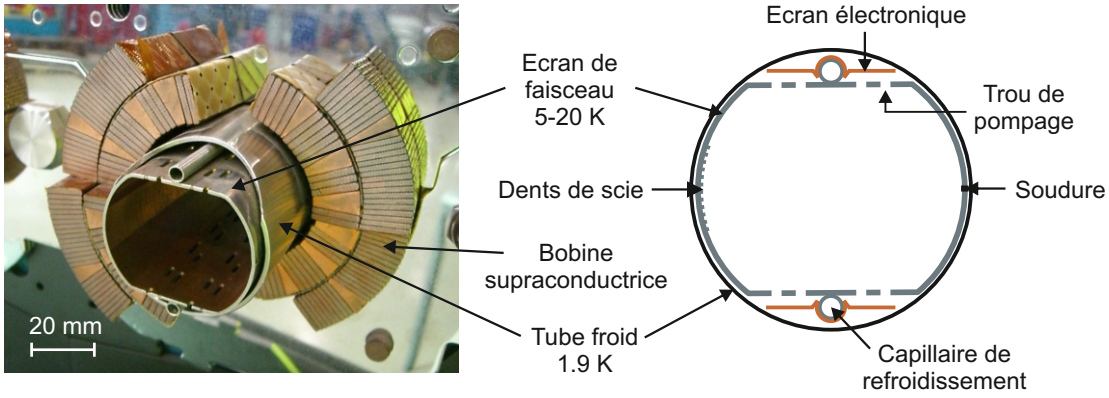

Figure 2: Système à vide d'un faisceau dans les arcs du LHC : image d'un tube faisceau dans un dipôle (gauche) et schéma associé (droite).

La charge thermique actuellement observée dans le LHC présente plusieurs caractéristiques [70, 73, 75, 184] :

- **distribution spatiale inhomogène** : en dépit d'un design identique des 8 arcs de la machine, leur charge thermique moyenne présente une large dispersion (voir Fig. 3). Une large dispersion est également observée entre les aimants au sein des arcs les plus critiques.

- **historique** : cette dispersion n'est observée que depuis la phase d'opération dite *Run 2* (2015-2018) suivant le long arrêt technique 1 (*Long shutdown 1, LS1*, 2013-2014) durant lequel toutes les chambres à vide ont été mises à l'air pour effectuer la maintenance de l'accélérateur.

- **effet de conditionnement** : la charge thermique décroît clairement au cours

du *Run 2* confirmant un effet de conditionnement des écrans de faisceaux. La dispersion entre les différents arcs reste, elle, constante (voir Fig. 3).

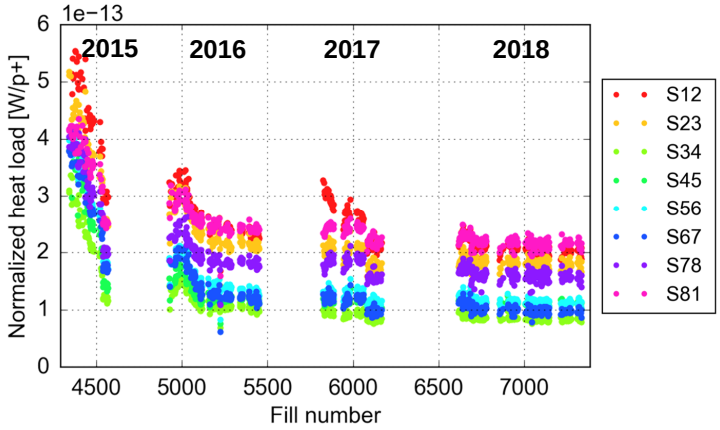

Figure 3: Evolution de la charge thermique moyenne par proton pour les 8 arcs du LHC (S12 à S81) au cours du *Run 2* [70].

En 2026, le LHC entrera dans sa phase de Haute-Luminosité et opérera avec des faisceaux encore plus intenses [7]. Les arcs les plus critiques présentent actuellement une charge thermique déjà proche de la limite de la capacité du système cryogénique. Il sont donc considérés comme facteur limitant des performances futures de l'accélérateur [70, 80].

1.2 Emission électronique secondaire et conditionnement

L'interaction d'électrons incidents avec un matériau résulte en l'excitation et l'émission d'électrons dits secondaires [99–103]. La profondeur d'échappement de ces derniers étant de l'ordre de quelques nanomètres, les propriétés d'émission secondaire d'un matériau sont étroitement liées à son état de surface [27, 29, 99, 105]. Pour les matériaux typiques des systèmes à vide des accélérateurs, le maximum du rendement d'électrons secondaires à l'installation de la machine est supérieur à 2 [28, 34, 35, 111]. De telles surfaces multiplient donc efficacement les électrons primaires.

Cependant, sous bombardement électronique, un effet de conditionnement de ces surfaces a lieu, se manifestant notamment par la diminution du rendement d'électrons secondaires vers des valeurs proches de 1 pour des doses de 10^{-2} C/mm^2 (cas du cuivre) [31, 49, 89]. Ainsi, sous l'effet du nuage d'électrons lui-même, le rendement d'électrons secondaires des chambres à vide des accélérateurs diminue, atténuant en retour l'intensité du nuage. Dans le cas du LHC, un tel processus est supposé décroître l'activité du nuage à un niveau compatible avec l'opération et semble donc actuellement partiellement mis en défaut.

L'étude des modifications chimiques des surfaces irradiées par des électrons à faible énergie (50 - 500 eV) a mis en évidence un effet de nettoyage de surface ainsi que la graphitisation de la couche de carbone surfacique (contamination liée à l'exposition à

l'air) [31, 33, 89, 94, 95, 109]. Certains auteurs rapportent également la croissance d'une couche de carbone en surface du cuivre au cours de l'irradiation, dont l'origine est encore ambigüe [33, 89, 90, 95]. Le rôle du carbone dans le processus de conditionnement n'est ainsi pas encore parfaitement compris.

1.3 Objectif et déroulement de l'étude

Dans ce contexte, l'objectif de l'étude est d'améliorer la compréhension des phénomènes liés au conditionnement par nuage d'électrons ayant lieu dans une machine telle que le LHC. Ce travail se compose de deux parties :

- **Etude des phénomènes de conditionnement et déconditionnement du cuivre en laboratoire**

Etant donné qu'aucun système de caractérisation de surfaces *in-situ* n'existe dans le LHC, les mécanismes de conditionnement du cuivre seront étudiés en laboratoire où le bombardement électronique est réalisé par un canon à électrons. Le suivi de l'évolution du rendement d'électrons secondaires et de la chimie de surface au cours de l'irradiation permettra de dissocier le rôle des différents composants chimiques de la surface dans le processus de conditionnement. L'analyse de surfaces exposées au nuage d'électrons dans le LHC ne pouvant être réalisée qu'après extraction et exposition à l'air des composants concernés, une étude du déconditionnement, i.e. de l'influence de la mise à l'air et de la durée de stockage sur l'état de conditionnement des surfaces irradiées, sera réalisée. L'hypothèse d'une modification de la surface des écrans de faisceaux du LHC menant à leur conditionnement anormal durant le *Run 2* sera également évaluée.

- **Analyse de composants exposés au nuage d'électrons dans le LHC**

Les surfaces de composants des systèmes à vide de cryo-dipoles extraits du LHC durant le long arrêt technique 2 (LS2, 2019-2020) et provenant d'un aimant à forte et d'un aimant à faible charge thermique seront analysées. Une comparaison de ces surfaces du point de vue de la composition chimique et du rendement d'électrons secondaires sera établie dans le but d'expliquer la dispersion de charge thermique observée le long du LHC.

2 Dispositif expérimental

Au laboratoire, deux systèmes expérimentaux sous ultra-vide et opérant à température ambiante permettent le suivi de l'évolution du rendement d'électrons secondaires et de la chimie des surfaces de cuivre au cours du conditionnement.

La composition chimique des surfaces est évaluée par spectroscopie photoélectronique à rayons X (XPS). Cette technique, basée sur la mesure de l'énergie de liaison des électrons arrachés à la surface par un rayonnement X, permet de déterminer les éléments présents dans les premières couches atomiques du matériau ainsi que leur environnement chimique. Une source monochromatique Al Kα (hν = 1486.6 eV) et une source non-monochromatique Mg Kα (hν = 1253.6 eV) sont utilisées dans cette étude.

Le rendement d'électrons secondaires $\delta = I_{secondaires} / I_{primaires}$ est mesuré à l'aide d'un canon à électrons dédié. La Fig. 4 représente les différents courants impliqués dans la mesure de δ. Sous l'effet du courant primaire (volontairement restreint à quelques nano-ampères pour limiter le conditionnement de l'échantillon durant la mesure), un courant d'électrons secondaires est émis, compensé par le courant d'échantillon $I_{echantillon}$. La somme de ces trois courants étant nulle, la mesure de seulement deux d'entre eux est nécessaire à la détermination de δ. Un des systèmes mesure $I_{echantillon}$ et utilise un collecteur pour mesurer simultanément $I_{secondaires}$, le second mesure d'abord $I_{primaires}$ en appliquant une tension positive sur l'échantillon, puis $I_{echantillon}$ après inversion de la polarité de cette tension. Ce système étant équipé d'une chambre μ-métal, il permet de mesurer le rendement d'électrons secondaires à partir d'une énergie incidente de 0 eV, permettant ainsi la mesure du travail de sortie de l'échantillon [124].

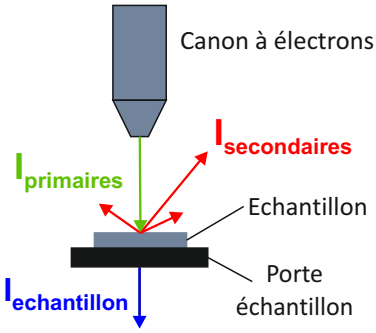

Figure 4: Schéma des différents courants impliqués dans la mesure du rendement d'électrons secondaires.

Les conditionnements sont réalisés grâce à un second canon à électrons et à 250 eV, soit une énergie équivalente aux électrons impliqués dans le conditionnement du LHC [78].

3 Etude des phénomènes de conditionnement et déconditionnement du cuivre en laboratoire

Ce chapitre décrit les mécanismes de conditionnement du cuivre sous irradiation d'électrons à 250 eV, à température ambiante et ceux du déconditionnement ayant lieu lors de la remise à l'air d'une surface irradiée. En outre, la possibilité qu'une modification de la surface des écrans de faisceau du LHC, empêchant par la suite leur conditionnement et conduisant à une forte intensité du nuage d'électrons, soit à l'origine de la charge thermique observée dans le LHC, est évaluée.

3.1 Conditionnement

3.1.1 Cinétique du conditionnement et modifications de surface associées

Les courbes de rendement d'électrons secondaires mesurées au cours du conditionnement d'un échantillon d'écran de faisceau du LHC précédemment exposé à l'air sont données en Fig. 5.

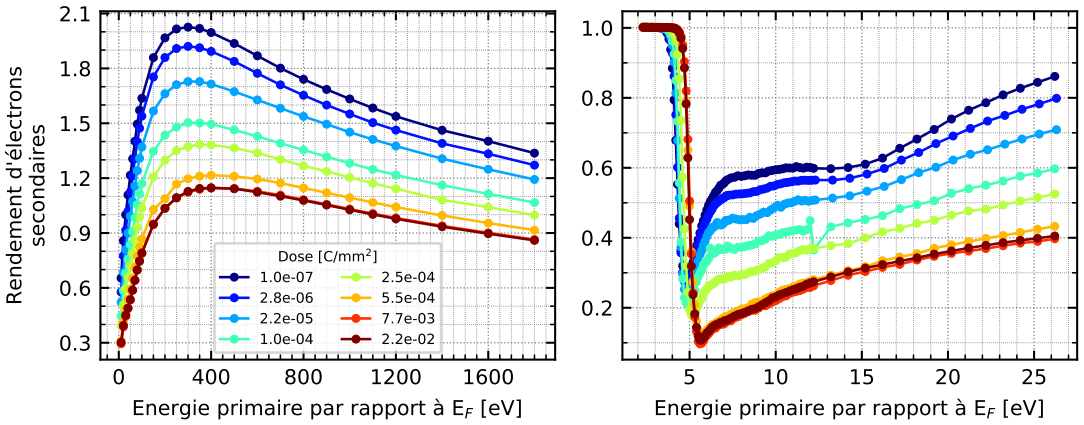

Figure 5: Rendement d'électrons secondaires d'un échantillon d'écran de faisceau du LHC après différentes doses d'irradiation pour une énergie primaire entre 10 et 1800 eV (gauche) et entre 0 et 26 eV (droite).

Au cours du conditionnement, une diminution du rendement d'électrons secondaires est observée sur toute la gamme d'énergie primaire considérée. Cette diminution sature pour des doses supérieures à 5×10^{-3} C/mm^2 (conditionnement complet). Le maximum du rendement, initialement égal à 2 pour une énergie incidente de 300 eV, décroît pour atteindre une valeur seuil d'environ 1.15 à 400 eV. En parallèle, une augmentation du travail de sortie est observée par le décalage du point d'inflexion des courbes en Fig. 5 (droite), passant ainsi de 4.3 à 5.0 eV.

Les principales lignes XPS du cuivre, de l'oxygène et du carbone pour les différentes doses sont données en Fig. 6.

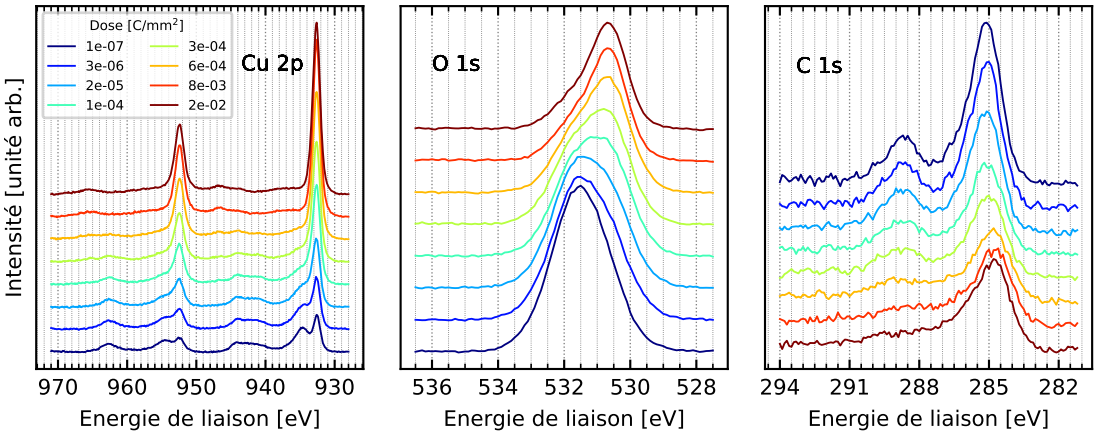

Figure 6: Lignes principales du cuivre Cu 2p (gauche), de l'oxygène O 1s (centre) et du carbone C 1s (droite) d'un échantillon d'écran de faisceau du LHC après différentes doses d'irradiation.

Dès le début de l'irradiation, un effet de nettoyage de la surface est observé via :

- la disparition de la contribution associée à l'hydroxyde de cuivre (à 934.6 eV sur la ligne Cu 2p) et du satellite associé (à 939 - 945 eV) [131]. Le décalage en parallèle de la ligne O 1s de 531.5 eV à 530.6 eV confirme une transition de $Cu(OH)_2$ vers

Cu_2O [131].

- la disparition de la composante à 288.5 eV sur la ligne C 1s associée aux groupes carboxyles [120]
- une diminution de l'aire sous les courbes C 1s et O 1s et une augmentation de celle sous la ligne Cu 2p

Pour des doses supérieures à 10^{-4} C/mm^2, la graphitisation du carbone surfacique s'amorce, comme le démontre le décalage du pic principal du carbone de 285.1 eV à 284.7 eV (Fig. 6 (droite)) [31].

3.1.2 Rôle des différents composants chimiques de la surface

Afin de séparer le rôle de chaque constituant chimique d'une surface de cuivre exposée à l'air (cuivre pur, Cu_2O, hydroxyde, espèces carbonées adsorbées) et notamment d'évaluer l'impact d'une éventuelle modification de la couche d'oxyde dans le processus de conditionnement du cuivre, une surface de cuivre pur (obtenue par décapage ionique), de Cu_2O pur (produite par exposition d'une surface décapée à un mélange N_2/O_2) et de cuivre exposé à l'air ont été conditionnées. Les courbes de rendement d'électrons secondaires associées sont données en Fig. 7.

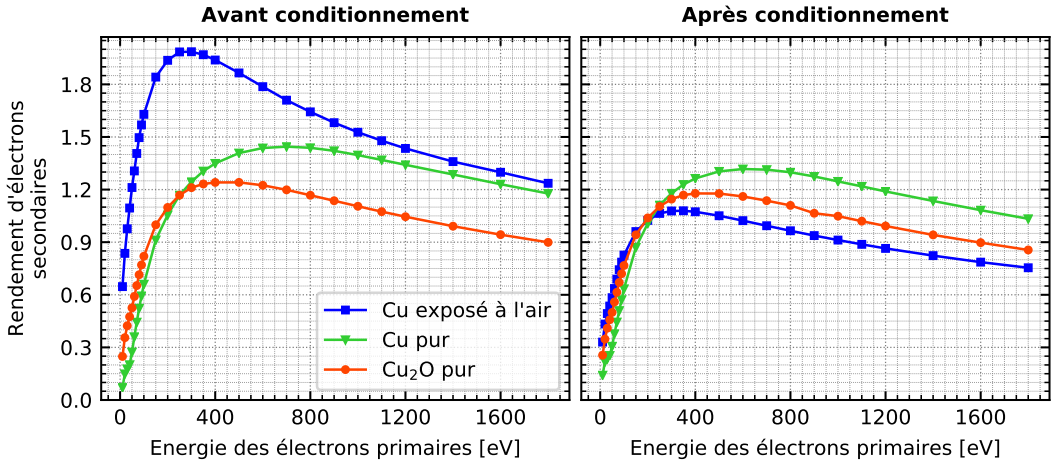

Figure 7: Rendement d'électrons secondaires du cuivre exposé à l'air, du cuivre métallique pur et du Cu_2O pur avant (gauche) et après irradiation (droite) (dose = 1×10^{-2} C/mm^2).

La surface exposée à l'air présente le rendement le plus élevé avant conditionnement et le plus faible après. Il est également observée que les rendements du cuivre et du Cu_2O purs (surfaces sans carbone) ne varient que très peu durant le conditionnement et restent significativement supérieurs à celui observé après conditionnement d'une surface exposée à l'air. L'apparition de carbone graphitique (concentration inférieure à 2 % at.) en surface de ces deux derniers échantillons est observée et résulte de l'utilisation du canon à électrons. Aucune autre modification de ces deux surfaces n'est observée par XPS durant l'irradiation.
De ces observations et de celles décrites en Section 3.1.1, il est conclu que :

- conformément à de précédentes observations [27,29,105] la présence d'hydroxyde et d'adsorbats augmente le rendement d'électrons secondaires du cuivre. Leur disparition partielle au cours du conditionnement permet donc de réduire le rendement de la surface.

- le Cu_2O a un rôle passif dans le conditionnement du cuivre : son rendement intrinsèque est plus faible que celui du cuivre pur. Cependant, son irradiation ne permet pas de décroître son rendement à une valeur aussi basse qu'observée après conditionnement du cuivre exposé à l'air.

- la graphitisation du carbone surfacique est responsable de la réduction du rendement d'électrons secondaires du cuivre exposé à l'air jusqu'à des valeurs proches de 1. En revanche, l'augmentation de la quantité de carbone en surface du cuivre exposé à l'air au cours de l'irradiation n'est pas nécessaire à son conditionnement.

3.2 Déconditionnement

3.2.1 Cinétique et mécanismes du déconditionnement

En vue de l'analyse de surfaces de composants extraits du LHC, la cinétique et les mécanismes du déconditionnement ayant lieu lors de la remise à l'air d'une surface conditionnée ont été étudiés. Un échantillon de cuivre OFE a été complètement conditionné puis stocké à l'air dans un dessiccateur. L'évolution de son rendement d'électrons secondaires, de sa quantité de carbone surfacique ainsi que de l'intensité relative de sa composante d'hydroxyde $I_{Cu(OH)_2}(934.4\ eV)/I_{Cu,Cu_2O}(932.6\ eV)$ extraite de la ligne Cu 2p ont été suivies au cours du stockage et sont présentées en Fig. 8.

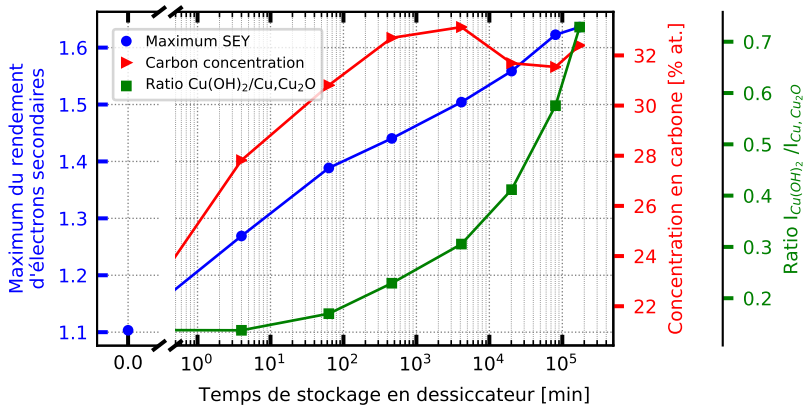

Figure 8: Evolution du maximum du rendement d'électrons secondaires, de la concentration en carbone surfacique et de la composante d'hydroxyde de cuivre d'un échantillon de cuivre OFE stocké dans un dessiccateur après conditionnement complet. Le temps t=0 représente la fin du conditionnement, i.e. l'instant juste avant la mise à l'air.

Immédiatement lors de la remise à l'air, la surface se recontamine en carbone, induisant une augmentation du rendement d'électrons secondaires. La composante d'hydroxyde reste, elle, inchangée. Pour des temps de stockage entre 4 minutes et 8 heures, l'augmentation du rendement d'électrons secondaires résulte à la fois de l'augmentation

de la concentration en carbone ainsi que de la croissance d'une couche d'hydroxyde de cuivre en surface de l'échantillon. Au delà de 8 heures de stockage, l'augmentation de la quantité de carbone sature, l'augmentation du rendement n'est donc plus que reliée à la croissance d'hydroxyde.

3.2.2 Impact sur les différences d'états de conditionnement

Afin d'évaluer si des différences de rendement d'électrons secondaires présentes après conditionnement partiel disparaissent au cours du stockage, des échantillons de cuivre OFE ont été conditionnés à différentes doses (résultant en différents rendements d'électrons secondaires) puis stockés en dessiccateur. Leur rendement a ensuite été mesuré après 2 semaines, 8 semaines et 4 mois de stockage. Les résultats sont présentés en Fig. 9.

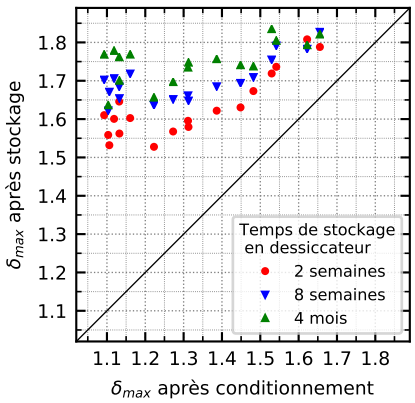

Figure 9: Maximum du rendement d'électrons secondaires δ_{max} d'échantillons de cuivre OFE conditionnés à différents niveaux puis stockés dans un dessiccateur.

Après deux semaines de stockage, une claire tendance se distingue pour les échantillons dont le maximum du rendement après conditionnement était compris entre 1.45 et 1.7 : plus le rendement est faible après conditionnement, plus il est faible après stockage. Les contrastes présents entre les échantillons après conditionnement persistent donc. En revanche, tous les échantillons conditionnés à des valeurs de rendement inférieures à 1.45 deviennent équivalents : leur rendement après stockage se situe aux environs de 1.6. Plus le temps de stockage est long, plus les contrastes présents après conditionnement entre les différents échantillons s'amenuisent : après 4 mois de stockage en dessiccateur, tous les échantillons ont un rendement compris entre 1.65 et 1.85 et il n'est plus possible de distinguer une tendance entre ces échantillons. Les analyses de surfaces exposées au nuage d'électrons doivent donc être réalisées le plus rapidement possible après leur mise à l'air sous peine d'effacement des différences de rendement présentes avant mise à l'air.

3.2.3 Conditions de stockage

D'après les résultats présentés en Sections 3.2.1 et 3.2.2 il est notamment conclu que la préservation de l'état de conditionnement *in-situ* de surfaces à analyser après leur extraction du LHC nécessite de stocker les échantillons en atmosphère sèche et propre

pour limiter la recontamination en carbone et la croissance d'hydroxyde. Les résultats présentés en Fig. 10, où l'évolution du maximum du rendement d'électrons secondaires est suivie pour des échantillons complètement conditionnés puis stockés en différentes atmosphères, montrent qu'un stockage sous vide est particulièrement efficace. Lors d'un stockage à l'air dans un tube inox fermé, représentant la situation où les lignes faisceau d'un aimant du LHC sont fermées après leur mise à l'air (étape nécessaire en vue de l'extraction de l'aimant de l'accélérateur), l'état de conditionnement est modérément dégradé.

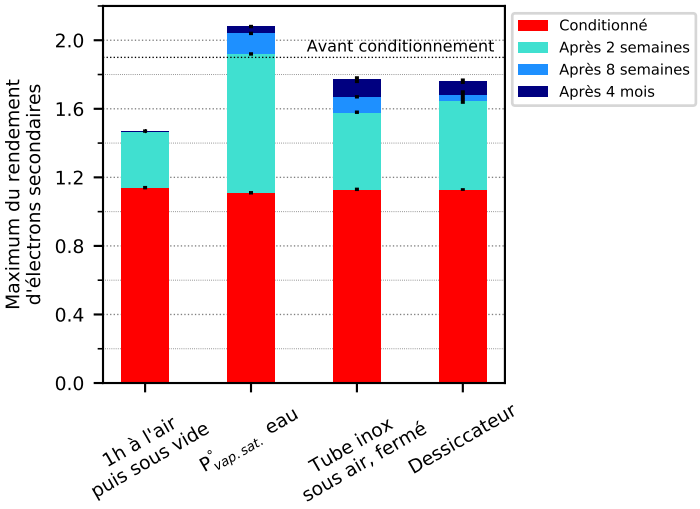

Figure 10: Maximum du rendement d'électrons secondaires d'échantillons de cuivre OFE complètement conditionnés puis stockés en différentes atmosphères.

3.3 Recherche de l'origine des différences de charge thermique dans le LHC

3.3.1 Hypothèse d'une modification de surface durant le LS1

Différents événements liés aux activités du LS1 qui auraient pu conduire à une modification de la surface des écrans de faisceau ont été envisagés. Une contamination par des outils d'inspection des lignes faisceaux (endoscope, balle radio-fréquence), par le dispositif de pompage (huile de pompe primaire, lubrifiant des roulements de pompes Roots) ou un impact des conditions de mise à l'air des lignes (mise à l'air avant réchauffement complet de l'aimant induisant de la condensation, longue exposition à une atmosphère humide) ont été considérées. Des échantillons d'écran de faisceau ont été préparés en conséquence afin d'évaluer l'impact de telles modifications de leur surface sur leur capacité de conditionnement. Les courbes de conditionnement des différents échantillons et d'un échantillon de référence sont données en Fig. 11.

Certaines modifications ont pour conséquence une augmentation importante du maximum du rendement d'électrons secondaires avant conditionnement (D = 10^{-7} C/mm^{-2}). En revanche, pour tous les échantillons, le rendement diminue au cours de l'irradiation et atteint une valeur de saturation entre 1 et 1.15 pour une dose d'environ 3×10^{-3}

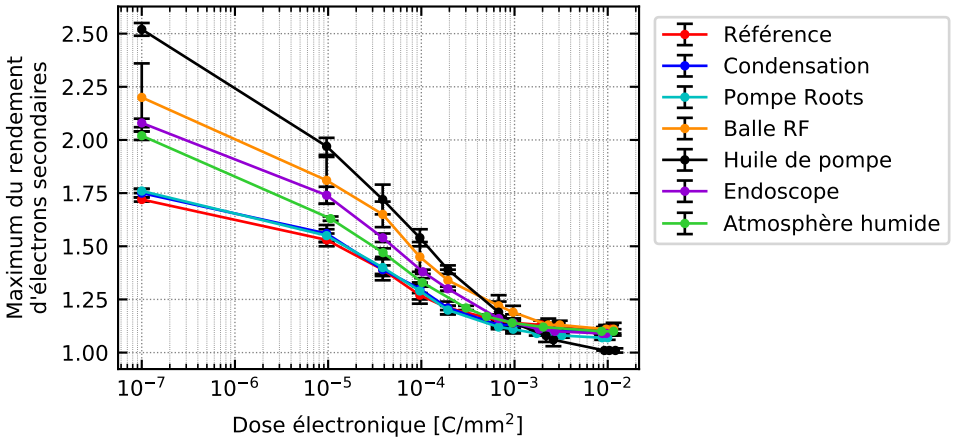

Figure 11: Impact de différentes modifications de la surface d'échantillons d'écran de faisceau : courbes de conditionnement à 250 eV. La dose D = 10^{-7} C/mm^2 correspond à la mesure juste avant le début du conditionnement.

C/mm^{-2}. Ces valeurs étant comparables à celles relevées pour l'échantillon de référence, il n'est donc pas possible de conclure que les contaminations envisagées sont néfastes au conditionnement des écrans de faisceau en se basant sur ces conditionnements réalisés à température ambiante par des électrons à 250 eV.

3.3.2 Hypothèse d'une surface modifiée à l'installation

L'hypothèse d'une surface du tube faisceau déjà modifiée à l'installation de la machine, dont le premier conditionnement durant le *Run 1* serait possible, mais qui réagirait à la mise à l'air lors du LS1 pour donner une surface non conditonnable durant le *Run 2*, est étudiée. En particulier, l'impact de la présence de résidus du détergent utilisé pour le nettoyage de certains composants du système à vide du LHC (éventuel défaut de rinçage) a été évalué. Des échantillons d'écran de faisceau ont été recouverts de solutions de détergent à différentes concentrations puis laissés évaporer à l'air. Leurs courbes de conditionnement et reconditionnement après 15 jours d'exposition à l'air sont présentées en Fig. 12.

La présence de résidus de détergent (contenant notamment du silicium, du potassium, du sodium, du phosphore et du soufre) résultant du séchage d'une solution de nettoyage à concentration nominale sur la surface de cuivre altère son conditionnement : le rendement, très élevé après contamination, ne diminue que partiellement puis réaugmente significativement avec l'irradiation. Le reconditionnement d'une telle surface est lui aussi différent de celui attendu pour une surface de cuivre non contaminée. La présence de résidus laissés par une solution diluée 100 fois ne semble en revanche pas affecter le conditionnement de la surface. Ainsi, un défaut de rinçage des écrans de faisceaux pourrait avoir un impact sur la charge thermique des aimants les hébergeant, via un défaut de conditionnement de leur surface. Cependant, la persistance d'une solution de détergent fortement concentrée au moment du séchage des écrans de faisceau du LHC est jugée peu probable, les écrans étant rincés dans deux bains d'eau successifs après celui de détergent.

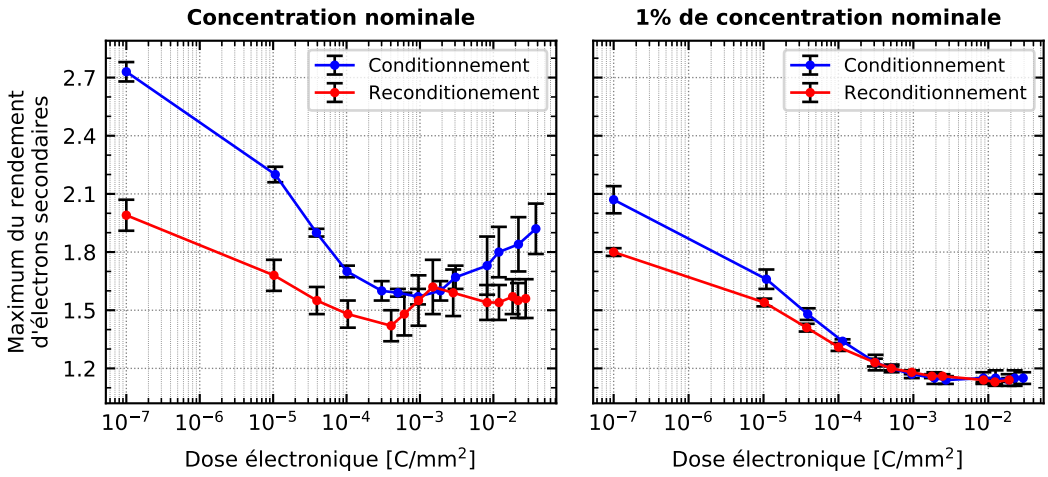

Figure 12: Courbes de conditionnement et reconditionnement d'échantillons d'écran de faisceau contaminés par des solutions de détergent en concentration nominale (gauche) et diluée 100 fois (droite).

De plus, pour la surface la plus contaminée, l'effet sur la charge thermique aurait dû être visible dès le premier conditionnement des écrans, i.e. durant le *Run 1*, mais aucune anomalie n'a été détectée pour cette période. Ainsi, l'hypothèse d'une charge thermique expliquée par la persistance de détergent sur la surface des écrans de faisceau est jugée peu probable.

4 Conditionnement des surfaces dans les arcs du LHC

4.1 Première analyse de surface de composants extraits du LHC

Durant l'arrêt de fin d'année 2016-2017, un dipôle défectueux d'un arc du LHC (emplacement A31L2) a été échangé. Après réchauffement et mise à l'air de l'arc concerné, les deux lignes faisceaux du dipôle ont été coupées puis fermées à chaque extrémité de l'aimant pour permettre son extraction de l'anneau et sa remontée vers la surface. Les écrans de faisceaux ont ensuite été extraits et des sections ont été prélevées à différentes positions longitudinales (le long de l'axe du faisceau). Pour chaque section, le rendement d'électrons secondaires a été mesuré et des spectres XPS ont été acquis sur la surface interne en différentes positions azimutales. L'écran électronique, où des contrastes d'état de conditionnement sont attendus entre les zones exposées au nuage d'électrons au travers des trous de pompage et celles étant masquées (voir Fig. 2), a également été analysé. Le temps d'exposition à l'air de ces composants avant l'analyse de leur surface est d'un à deux mois durant lesquels ils ont été stockés dans le tube froid fermé (à température ambiante), puis dans une feuille d'aluminium.

4.1.1 Ecran de faisceau

Le maximum du rendement d'électrons secondaires en fonction de la position azimutale pour quatre sections de l'écran du faisceau 1 est donné en Fig. 13.

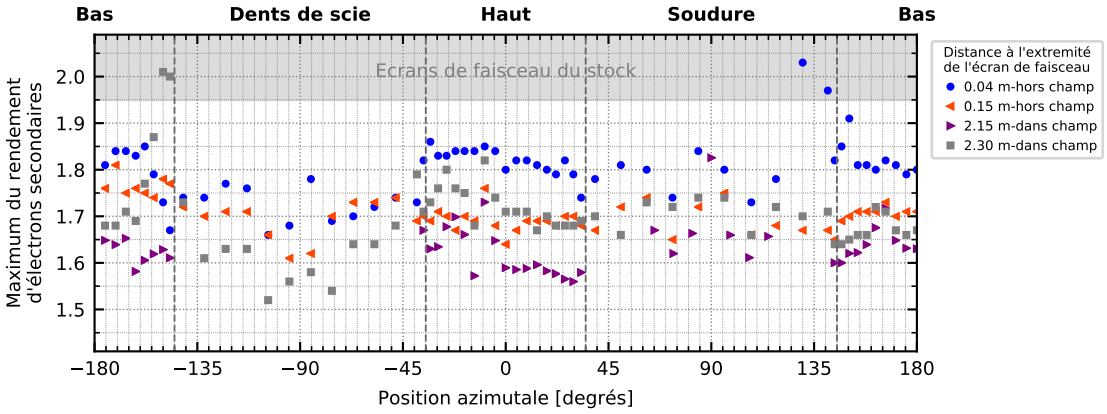

Figure 13: Maximum du rendement d'électrons secondaires en fonction de la position azimutale pour des échantillons d'écran de faisceau extraits du LHC (emplacement A31L2, faisceau 1). La gamme de rendements mesurés sur des écrans provenant du stock (jamais installés dans le LHC) est indiquée en gris.

En dépit de la présence d'un champ magnétique confinant les électrons, aucune différence significative de rendement d'électrons secondaires n'est observée entre les faces plates (haut et bas) et le coté de la soudure, des sections se trouvant à 2.15 et 2.3 m de l'extremité de l'écran. Cependant, le rendement d'électron secondaires des quatres échantillons est significativement plus faible que celui des écrans de faisceau n'ayant jamais été insérés dans le LHC. Des observations similaires ont été faites sur les écrans du faisceau 2.

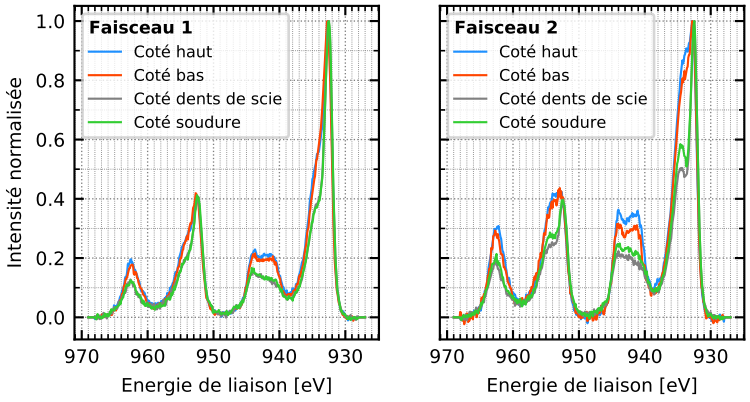

Figure 14: Lignes Cu 2p d'échantillons d'écrans de faisceaux pour la ligne du faisceau 1 (gauche) et du faisceau 2 (droite) situés dans le champ du dipôle, à 2.3 m de l'extrémité des écrans.

Les lignes Cu 2p des échantillons situés à 2.3 m (dans le champ magnétique) de chacun des deux écrans de faisceau sont montrées en Fig. 14 pour plusieurs positions azimutales. Pour les deux faisceaux, la présence d'hydroxyde sur les faces latérales est déduite de la forme du satellite [130]. Pour les faces plates, le satellite présente deux bosses et indique donc la présence de CuO [130]. Ces deux bosses étant moins prononcées pour le faisceau 1 que pour le faisceau 2, la co-présence d'hydroxyde et de CuO sur les faces plates de l'écran 1 ne peut pas être exclue. En outre, l'échantillon du faisceau 2 présente plus

d'hydroxyde que celui du faisceau 1, probablement en raison d'un temps d'exposition à l'air plus long avant sa mesure (déconditionnement). Aucun contraste systématique entre les faces plates et latérales de l'écran n'est visible pour les sections en dehors du champ magnétique. Pour toutes les sections, la quantité de carbone se situe globalement entre 20 et 35 % at. comme attendu pour des surfaces exposées à l'air.

Enfin, le rendement après conditionnement de ces échantillons et la dose nécessaire pour l'atteindre sont similaires à ceux observés pour des échantillons de référence, non installés dans le LHC.

4.1.2 Ecran électronique

La face de l'écran électronique en regard de l'écran de faisceau présente des zones sombres (Fig. 15, gauche), correspondant aux zones irradiées par le nuage d'électron au travers des trous de pompage de l'écran de faisceau. L'origine de ces traces n'est pas encore expliquée.

Le maximum du rendement d'électrons secondaires le long de l'axe longitudinal de l'écran électronique est montré en Fig. 15, où les bandes grises correspondent aux zones sombres observées sur l'échantillon. Systématiquement, le rendement dans les zones irradiées est significativement plus faible que celui mesuré dans les zones non-irradiées.

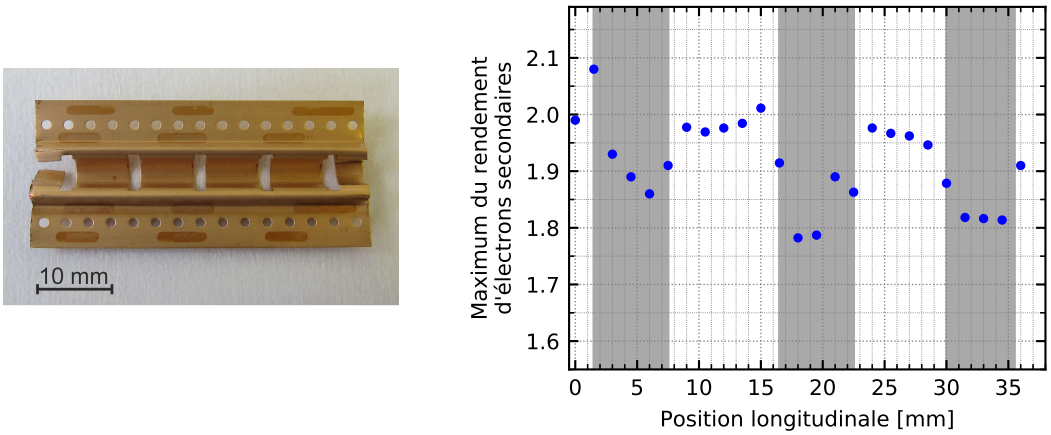

Figure 15: (gauche) Face d'un écran électronique en regard de l'écran de faisceau. Les zones sombres, (contraste accentué par 26 h de recuit à 120°C à l'air), correspondent aux zones irradiées par le nuage d'électrons au travers des trous de pompage de l'écran de faisceau. (droite) Maximum du rendement d'électrons secondaires le long de l'axe longitudinal pour un écran électronique extrait du LHC. Les bandes grises correspondent aux zones sombres observées sur l'échantillon.

La partie gauche de la Fig. 16 montre que la contribution en hydroxyde de cuivre (934.8 eV) présente sur la ligne Cu 2p dans une zone irradiée est fortement réduite par rapport à celle présente dans une zone non irradiée. De plus, il apparait (Fig. 16, droite) que la ligne C 1s d'une zone irradiée est décalée vers la droite du spectre ; le carbone est donc sous forme plus graphitique dans les zones irradiées que dans les zones masquées.

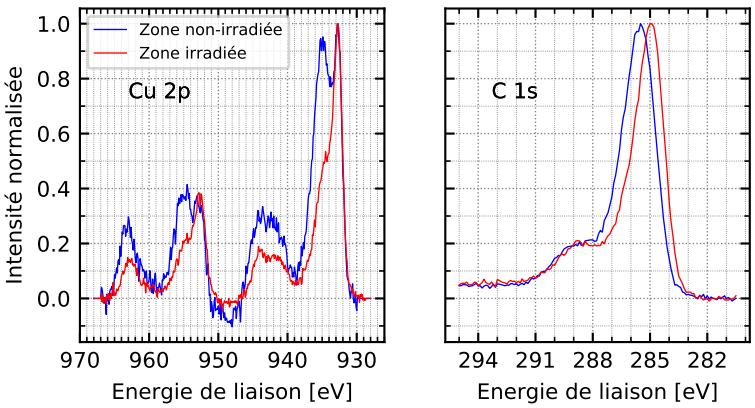

Figure 16: Lignes Cu 2p (gauche) et C 1s (droite) mesurées dans des zones irradiées et non-irradiées d'un écran électronique extrait du LHC.

4.1.3 Conclusion

L'analyse de surfaces de composants exposés au nuage d'électrons dans le LHC a mis en évidence des caractéristiques communes entre ces surfaces et celles conditionnées en laboratoire (réduction du rendement d'électrons secondaires et de la composante d'hydroxyde de cuivre...) ainsi que la présence de CuO, qui n'est pas observé au laboratoire. Ces résultats prouvent que le conditionnement au moins partiel de ces composants a bien eu lieu dans l'accélérateur, bien que les mécanismes associés semblent partiellement différents dans les deux environnements. La charge thermique de ce dipôle en particulier n'étant pas connue, ces analyses ne permettent pas d'éclaircir l'origine de la dispersion de charge thermique dans le LHC. En revanche, elles ont mis en évidence l'effet du déconditionnement et la nécessité d'en comprendre les mécanismes afin de le limiter au maximum.

4.2 Comparaison d'écrans de faisceaux de dipôles à faible et forte charge thermique

Lors du LS2 (2019-2020), deux dipôles localisés aux emplacements C21R6 et B31L2 des arcs du LHC et clairement identifiés comme présentant une faible et forte charge thermique respectivement, ont été extraits du LHC. Afin de préserver au maximum l'état de conditionnement *in-situ* des écrans de faisceaux (voir Section 3.2.3) et de permettre la comparaison entre les composants des deux dipôles, le temps d'exposition à l'air des surfaces a été réduit au maximum (environ 20 jours, identique pour les deux dipôles) en optimisant le planning d'extraction et en les stockant sous vide dès que possible.

4.2.1 Rendement d'électrons secondaires

Le maximum du rendement d'électrons secondaires en fonction de la position azimutale est présenté en Fig. 17, pour des sections du faisceau 2 du dipôle en C21R6 et du faisceau 1 du dipôle en B31L2. En dépit de la présence d'un champ magnétique, le rendement d'électrons secondaires des échantillons prélevés en C21R6 à 1 et 7.5 m ne présente

pas de différence systématique entre les faces plates (haut et bas) et les faces latérales (dents de scie et soudure) et se situe entre 1.6 et 1.8. Pour l'échantillon en dehors du champ magnétique (15.44 m), le rendement est globalement plus élevé et présente une plus forte dispersion, sans qu'elle ne soit systématiquement liée à la position azimutale. Pour les échantillons prélevés en B31L2, dans le champ magnétique, les faces latérales présentent un rendement similaire à celui mesuré en C21R6, alors que les faces plates ont un rendement plus élevé, entre 1.8 et 1.95. Pour la section en dehors du champ magnétique, le rendement est uniforme en azimut et se situe au niveau de celui des faces plates des sections dans le champ.

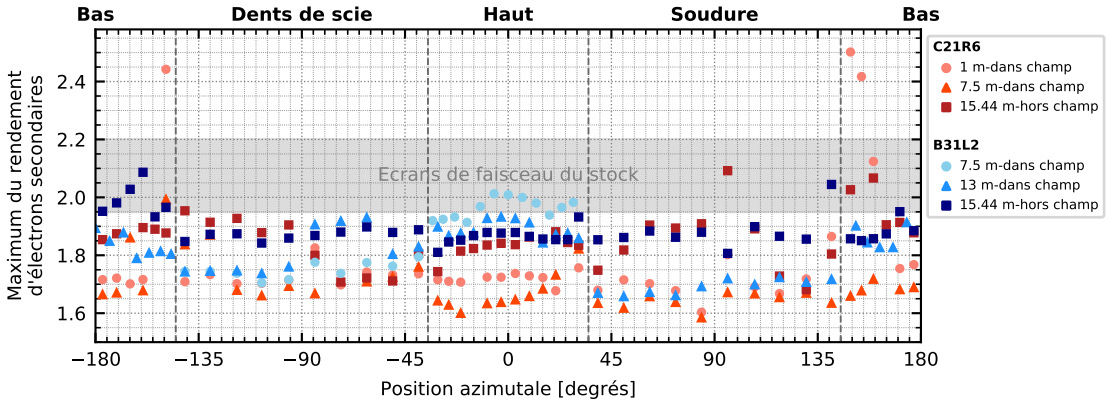

Figure 17: Maximum du rendement d'électrons secondaires en fonction de la position azimutale pour des sections d'écrans de faisceaux extraits des dipôles C21R6 (faisceau 2) et B31L2 (faisceau 1). Les échantillons ont été prélevés à différentes positions longitudinales (distance indiquée depuis l'extrémité des écrans de faisceaux), dans et en dehors du champ magnétique des dipôles.

4.2.2 Analyse chimique des surfaces

Les lignes Cu 2p pour différentes positions azimutales de sections d'écran de faisceaux prélevées dans le champ magnétique des deux dipôles sont données en Fig. 18.

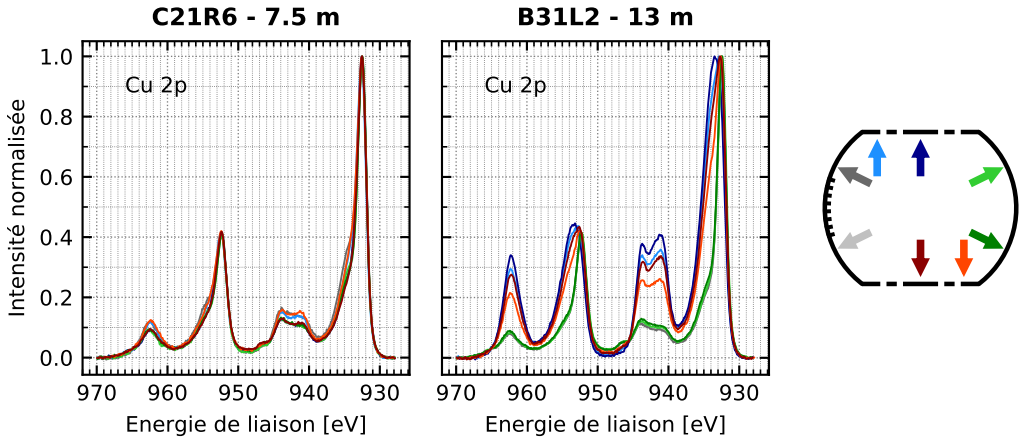

Figure 18: Lignes Cu 2p de sections d'écrans de faisceaux des emplacements C21R6, faisceau 2 (gauche) et B31L2, faisceau 1 (centre), pour différentes positions azimutales (droite).

Pour la section prélevée en C21R6, la présence d'un épaulement du côté des hautes énergies de liaison du pic Cu $2p_{3/2}$ ainsi que la présence d'un satellite entre 939 et 945 eV indiquent la présence de Cu^{2+}. La forme du satellite, en particulier celui de la ligne orange (coté bas) suggère la présence du CuO [130]. En revanche, la faible intensité du satellite et la position du pic Cu $2p_{3/2}$ à 932.6 eV indiquent que le Cu_2O reste l'oxyde dominant. Le taux de carbone se situe autour de 20 % at., ce qui est usuel pour une surface exposée à l'air. La composition chimique de la surface est uniforme en azimut. La ligne Cu 2p de la section provenant du B31L2 présente, elle, des différences systématiques entre les faces plates et latérales. Pour les cotés haut et bas, la forme du satellite et le décalage de la ligne Cu $2p_{3/2}$ vers les énergies de liaison plus élevées indique clairement la présence de CuO. L'intensité du satellite ainsi que la position de la ligne O 1s (voir Fig. 21) à 529.8 eV indiquent que le CuO est l'oxyde dominant. Les faces latérales présentent un satellite d'une intensité moindre et de forme différente. Elles semblent donc couvertes d'une faible quantité de $Cu(OH)_2$. Le taux de carbone est, lui, uniforme en azimut et se situe aux environs de 7%, ce qui est extrêmement faible pour une surface exposée à l'air.

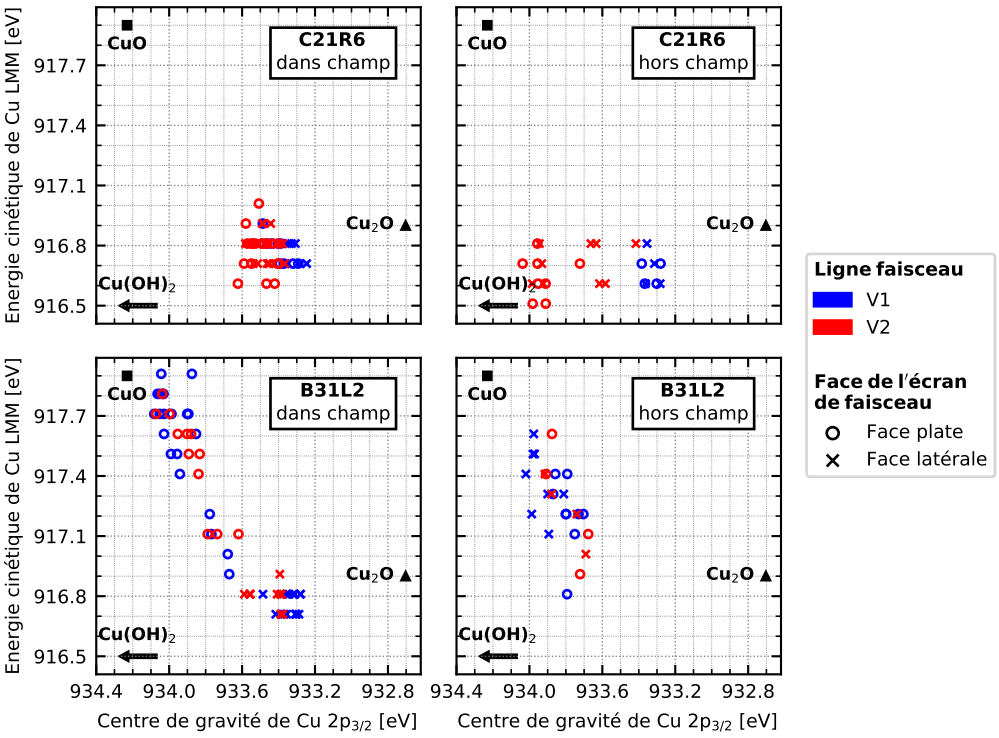

Figure 19: Energie cinétique du maximum de la ligne Cu LMM en fonction de la position du centre de gravité de l'aire sous la ligne Cu $2p_{3/2}$ entre 927 et 938.5 eV (intensité normalisée) pour l'ensemble des spectres XPS des échantillons des écrans de faisceaux extraits en C21R6 et B31L2.

L'énergie cinétique du maximum de la ligne Cu LMM en fonction de la position du centre de gravité de l'aire sous la ligne Cu $2p_{3/2}$ entre 927 et 938.5 eV est présentée en Fig. 19 pour tous les spectres XPS acquis sur les écrans de faisceaux des emplacements C21R6 et B31L2. La position des points dans ce diagramme permet de déterminer la forme chimique du cuivre des écrans [131]. Ainsi, il apparait de manière systématique

que :

- dans le champ magnétique, les écrans du C21R6 sont homogènes en azimut et Cu_2O est l'oxyde dominant. En dehors du champ, certains spectres présentent du $Cu(OH)_2$, résultant probablement du déconditionnement.
- pour le B31L2, dans le champ magnétique, les faces plates présentent de fortes quantités de CuO, les faces latérales étant elles dominées par le Cu_2O. En dehors du champ, les faces latérales se couvrent elles aussi de CuO, et l'écran de faisceau devient homogène en azimut.

4.2.3 Conditionnement

Les courbes de conditionnement d'un échantillon d'écran de faisceau de référence (jamais installé dans le LHC), d'un échantillon provenant du C21R6 (coté haut) et du B31L2 (coté bas et coté soudure) (voir Fig. 18 pour les ligne Cu 2p associées) sont présentées en Fig. 20. Comme la référence, l'échantillon du C21R6 atteint un rendement de 1.05 après une dose de 10^{-2} C/mm^2. Sa composition chimique à la fin du conditionnement est similaire à celle de la référence. En revanche, pour l'échantillon du B31L2, coté bas (présentant le CuO), la diminution du rendement ne sature pas, et atteint 1.20 pour une dose de 3×10^{-2} C/mm^2. Le coté de la soudure (très peu de CuO) présente un conditionnement proche de celui de l'échantillon du C21R6, bien que le rendement après conditionnement complet reste légèrement supérieur.

Les lignes Cu 2p, O 1s et C 1s de l'échantillon du B31L2, coté bas sont montrées en Fig. 21, pour différentes doses. La décroissance de l'intensité du satellite de la ligne Cu 2p et le décalage de la ligne O 1s vers les énergies de liaison plus élevées indiquent une réduction partielle du CuO. Le décalage du pic principal de la ligne C 1s prouve la graphitisation du carbone. En revanche, la composante à 288.5 eV ne disparait pas complètement au cours du conditionnement, contrairement à un échantillon de référence (voir Section 3.1.1) et aux échantillons du C21R6.

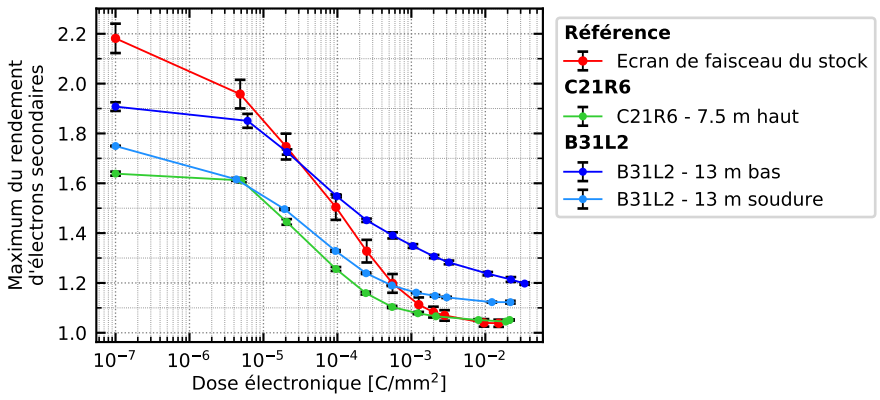

Figure 20: Courbes de conditionnement d'échantillons d'écrans de faisceau extraits de dipôles du LHC, emplacements C21R6 et B31L2. La courbe de conditionnement d'un écran de faisceau n'ayant jamais été installé dans le LHC est montrée pour référence.

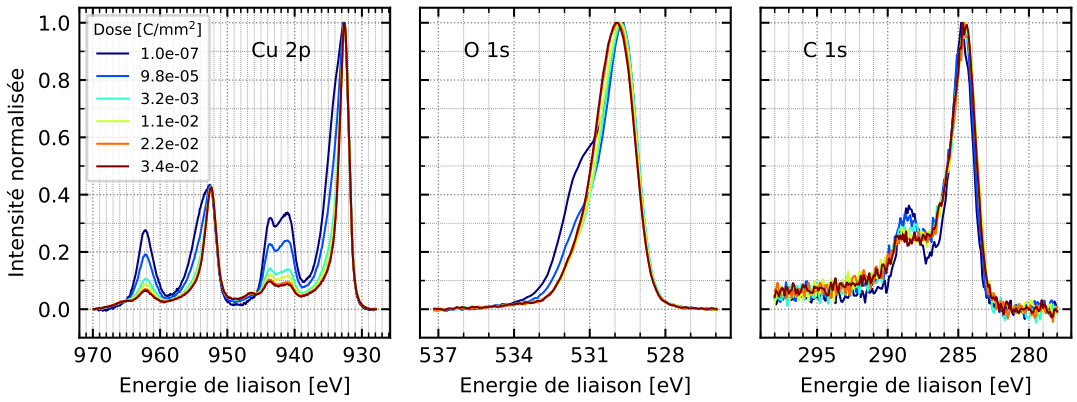

Figure 21: Lignes Cu 2p (gauche), O 1s (centre) et C 1s (droite) de l'échantillon prélevé sur l'écran de faisceau de l'emplacement B31L2 (faisceau 1, 13 m, coté bas) pour différentes doses.

4.2.4 Conclusion

Les écrans de faisceaux du dipôle B31L2 (forte charge thermique) présentent une forte quantité de CuO dans les zones où la densité du nuage d'électrons est la plus forte : faces plates des sections dans le champ magnétique, et sur toutes les faces en dehors du champ. Cet oxyde n'est présent ni sur les écrans avant installation dans le LHC ni sur des échantillons conditionnés au laboratoire. Ces résultats prouvent que la présence de CuO est induite par l'opération du LHC elle-même. Les écrans du dipôle C21R6 (faible charge thermique) présentent des caractéristiques similaires à une surface conditionnée en laboratoire. En outre, le rendement d'électrons secondaires est plus élevé et le conditionnement à température ambiante est significativement plus lent pour les échantillons présentant du CuO que pour ceux en étant exempts. Le CuO pourrait donc favoriser l'activité du nuage électronique.

5 Discussion et conclusion

Une étude des mécanismes de conditionnement du cuivre sous bombardement électronique à température ambiante a mis en évidence le rôle crucial du carbone dans la réduction du rendement d'électrons secondaires du cuivre exposé à l'air. Par la suite, une étude du déconditionnement ayant lieu à la remise à l'air d'une surface irradiée a montré la nécessité de stocker les surfaces à analyser en atmosphère sèche et propre après leur extraction du LHC, sous peine d'effacer les informations relatives à leur état de conditionnement *in-situ*. Une procédure spécifique a donc été mise en place lors de l'extraction de deux dipôles du LHC (emplacements B31L2 et C21R6), présentant une forte et une faible charge thermique respectivement, pour l'analyse de la surface de leurs écrans de faisceau.

L'analyse de ces surfaces montre la présence de quantités importantes de CuO dans les écrans du B31L2, résultant de l'opération du LHC. De plus, ces écrans présentent de très faibles quantités de carbone sur toute leur surface interne. La surface des écrans du C21R6 est, elle, similaire à une surface conditionnée en laboratoire : très peu ou pas

de CuO et taux de carbone usuel. En parallèle, le rendement d'électrons secondaires est plus élevé sur les surfaces présentant le CuO. En outre, le conditionnement est normal pour les échantillons ne présentant pas de CuO alors que la cinétique est beaucoup plus lente lorsqu'il est présent et met en jeu la réduction de cet oxyde. Il n'est pas démontré qu'une telle réduction puisse avoir lieu en milieu cryogénique, où la diffusion de l'oxygène dans le matériau est fortement limitée [162]. De ce fait, l'apparition de cet oxyde, l'éventuelle impossibilité de le réduire *in-situ* ainsi que le très faible taux de carbone surfacique, obstacle supplémentaire au conditionnement comme démontré dans cette étude, forment actuellement l'hypothèse la plus probable pour expliquer la forte charge thermique observée dans certaines zones du LHC. Des expériences de conditionnement à froid d'échantillons extraits du LHC et présentant le CuO permettront de confirmer ces hypothèses.

A court terme (LS2), il est nécessaire de comprendre les mécanismes de formation du CuO dans le LHC, afin d'éviter sa formation dans ses zones encore saines. La présence d'une atmosphère oxydante résultant par exemple de la production d'ozone ou d'ions d'oxygène par le faisceau, le rayonnement synchrotron ou le nuage d'électrons pourrait conduire à la réduction du taux de carbone (via sa transformation en espèces volatiles), ainsi qu'à l'oxydation du cuivre sous forme de CuO [173]. L'oxygène nécessaire pourrait venir de la présence d'hydroxyde ou d'eau adsorbée en surface du cuivre au démarrage de la machine. Ces hypothèses sont actuellement testées en laboratoire. A plus long terme, des solutions tenant compte de l'environnement particulier du LHC et des dimensions de son système à vide devront être proposées pour supprimer le CuO des écrans de faisceau ou pour le masquer : décapage, réduction chimique ou recouvrement par un matériau à faible rendement d'électrons secondaires par exemple.

Appendix A

Error calculation for the SEY measurements

This appendix details the error calculation associated with the SEY measurements. The following base formula is used for computing the error associated with $z = f(x, y)$:

$$\Delta z = \sqrt{\left(\Delta x \times \frac{\partial f}{\partial x}\right)^2 + \left(\Delta y \times \frac{\partial f}{\partial y}\right)^2} \tag{A.1}$$

The following currents are considered, and are chosen as being positive when the electrons travel in the direction indicated by the arrows.

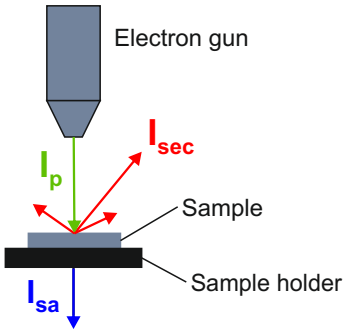

Figure A.1: Currents involved in the SEY measurements. The currents are chosen as being positive when electrons travel in the direction of the arrows.

A.1 Collector system

In a collector system, the SEY δ is given by:

$$\delta = \frac{I_{sec}}{I_{sec} + I_{sa}} \tag{A.2}$$

where I_{sec} is the collector (secondary) current and I_{sa} is the sample current.
From Eq. A.1 it comes:

$$\Delta\delta = \sqrt{\left[\frac{I_{sa}}{(I_{sec}+I_{sa})^2}\times\Delta I_{sec}\right]^2 + \left[\frac{I_{sec}}{(I_{sec}+I_{sa})^2}\times\Delta I_{sa}\right]^2} \tag{A.3}$$

A.2 Sample bias method

When performing a measurement with the sample bias method, the SEY δ is given by:

$$\delta = 1 - \frac{I_{sa}}{I_p} \tag{A.4}$$

where I_p is the primary current and I_{sa} is the sample current.
From Eq. A.1 it comes:

$$\Delta\delta = \sqrt{\left(\frac{I_{sa}}{{I_p}^2}\times\Delta I_p\right)^2 + \left(\frac{1}{I_p}\times\Delta I_{sa}\right)^2} \tag{A.5}$$

Considering now only the error induced by the measurement method, i.e. the underestimate of I_p due to its measurement with a positively biased sample:

$$\Delta\delta = \frac{I_{sa}}{{I_p}^2}\times\Delta I_p \tag{A.6}$$

which is equivalent to:

$$\Delta\delta = (1-\delta)\times\frac{\Delta I_p}{I_p} \tag{A.7}$$

Since $\Delta I_p = I_p^{real} - I_p^{measured}$ is positive in all cases (the elastically reflected electrons are not collected), and I_p is chosen as being positive, two cases should be distinguished:

- δ is above unity
  Thus:
  $$\Delta\delta < 0$$
  The SEY is overestimated.

- δ is below unity
  Thus:
  $$\Delta\delta > 0$$
  The SEY is underestimated.

Appendix B

Estimate of the ion density necessary for CuO build-up

This appendix qualitatively discusses the possibility of having oxygen-containing ions in sufficient amount for building up the CuO layer observed in the B31L2 dipole beam screens by ion bombardment such as in Ref. [173]. Two ionization processes are considered: ionization by the proton beam and by the electrons from the cloud, as represented in Fig. B.1. Then, the gas density required in the beam pipe for producing an ion flux responsible for the CuO build-up is evaluated. In the following, it is assumed that all the gas in the beam pipe is made of oxygen-containing molecules, which, if ionized, will produce CuO by ion bombardment. Furthermore, the following values are used for the estimates:

- ionization cross-section by the electrons from the cloud [185]: $\sigma_{e^-} = 10^{-20}$ m^2
- ionization cross-section by the protons of the beam [186]: $\sigma_{p^+} = 10^{-22}$ m^2
- electron cloud current impinging on the surface in a meter of beam screen in dipoles [78]: $I_{e^-} = 2 \times 10^{14}$ e$^-$/sec
- proton beam current at nominal parameters [9]: $I_{p^+} = 3 \times 10^{18}$ p$^+$/sec
- surface effectively covered by CuO per meter of beam screen: 0.1 m^2
- beam screen volume per meter of beam screen: 0.1 m^3

B.1 Ionization process

We first evaluate the dominant contribution between ionization by the proton beam and by the electron cloud. Considering a beam pipe section of 1 m length, with a pressure P at 5 K corresponding to a gas density n, the ionization rate induced by the circulating particles x (protons or electrons) is given by:

$$\frac{dN}{dt}\,[\text{ion m}^{-1}\,\text{sec}^{-1}] = I_x \,.\, \sigma_x \,.\, n \tag{B.1}$$

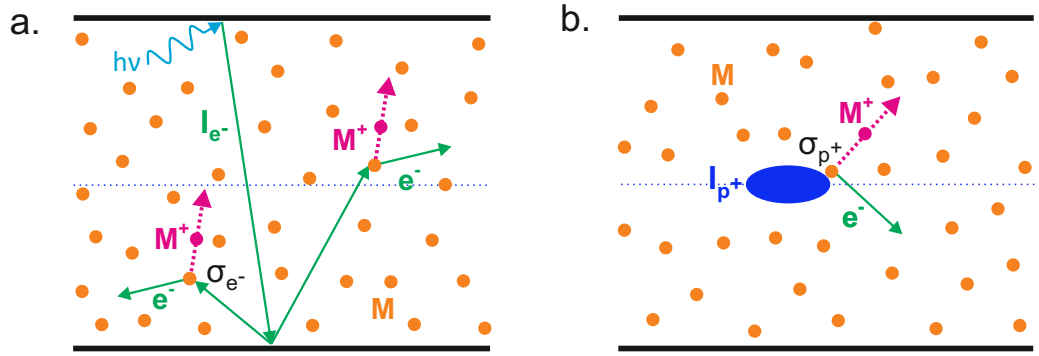

Figure B.1: Considered ionization processes: (a) ionization by the electrons from the cloud: at the interaction (cross-section σ_{e^-}) between the electron and a molecule M from the residual gas, an ion M^+ and an other electron are generated, (b) ionization by the proton beam (blue): the cross-section is now σ_{p^+}.

Comparing the ionization rate induced by the beam and the one induced by the electron cloud is thus equivalent to comparing the product of the particle current times the corresponding ionization cross-section:

$$I_{p^+} \,.\, \sigma_{p^+} \quad \text{compared to} \quad I_{e^-} \,.\, \sigma_{e^-}$$

From the values given above for I_{p^+}, I_{e^-}, σ_{p^+} and σ_{e^-}, it comes:

$$\frac{I_{p^+} \,.\, \sigma_{p^+}}{I_{e^-} \,.\, \sigma_{e^-}} \sim 100$$

It is thus concluded that the dominant ionization process is the one induced by the circulating proton beam.

B.2 Estimate of the gas density required for CuO build-up by ion bombardment

The gas density required in the beam pipe is estimated, considering that a monolayer of CuO (i.e. 10^{15} molecules cm^{-2}) built up on the beam screen surface as a result of a full year of continuous oxygen-containing ion bombardment.

Bombarding a surface with an accumulated flux of 10^{15} molecules cm^{-2} in a year corresponds to a ion flux of $\sim 10^{12}$ ions m^{-2} sec^{-1}. This requires in turn an ionization rate of 10^{12} ions m^{-3} sec^{-1} in the beam pipe, according to the considered geometry. It is verified that, the production of such an ion density does not significantly add more electrons to the cloud and therefore, the ionization process remains dominated by beam-gas interactions. The required gas density to obtain such an ion production rate by proton beam ionization is deduced from Eq. B.1 with x corresponding to protons. The computed gas density is:

$$n \sim 3 \times 10^{17} \text{ molecules m}^{-3}$$

which corresponds to a pressure at 5 K:

$$P \sim 10^{-7}\,\text{mbar}$$

Such a gas density is two orders of magnitude higher than the nominal one as derived from the beam vacuum lifetime requirements [9] and is not compatible with machine observations [175].

Bibliography

[1] J. Ellis, "Beyond the standard model with the LHC," *Nature*, vol. 448, no. 7151, pp. 297–301, 2007.

[2] O. Brüning and P. Collier, "Building a behemoth," *Nature*, vol. 448, no. 7151, pp. 285–289, 2007.

[3] M. Esma, "The CERN accelerator complex." http://cds.cern.ch/record/2197559/files/CCC-v2017.png?version=2, 2016.

[4] S. Myers, "The Large Hadron Collider 2008–2013," *International Journal of Modern Physics A*, vol. 28, no. 25, p. 1330035, 2013.

[5] L. Evans, ed., *The Large Hadron Collider: a marvel of technology*. EPFL Press, Lausanne, 2nd ed., 2018.

[6] V. Baglin, B. Henrist, B. Jenning, J. M. Jimenez, E. Mahner, G. Schneider, A. Sinturel, and A. Vidal, "Reconvering about 5 km of LHC beam vacuum system after sector 3-4 incident," in *Proceedings of the 10th International Particle Conference IPAC'10*, (Kyoto, Japan), pp. 3870–3872, 2010.

[7] G. Apollinari, I. Béjar Alonso, O. Brüning, P. Fessia, M. Lamont, L. Rossi, and L. Tavian, *High-Luminosity Large Hadron Collider (HL-LHC): Technical Design Report V. 0.1*. CERN Yellow Reports: Monographs, Geneva: CERN, 2017.

[8] Wiedemann, *Particle Accelerator Physics*. Graduate Texts in Physics, Berlin: Springer, 4th ed., 2015.

[9] O. Brüning, P. Collier, P. Lebrun, S. Myers, R. Ostojic, J. Poole, and P. Proudlock, *LHC Design Report*. CERN Yellow Reports: Monographs, CERN, Geneva: CERN, Geneva, 2004.

[10] S. Y. Lee, *Accelerator physics*. Singapore: World Scientific, 3rd ed., 2012.

[11] P. Willmott, *An introduction to synchrotron radiation: techniques and applications*. Chichester: John Wiley & Sons, 2nd ed., 2019.

[12] J. R. M. Vaughan, "Multipactor," *IEEE Transactions on electron devices*, vol. 35, no. 7, 1988.

[13] J. Hillairet, M. Goniche, N. Fil, M. Belhaj, and J. Puech, "Multipactor in High Power Radio-Frequency Systems for Nuclear Fusion," in *Presented at the International Workshop on Multipactir, Corona and Passive Intermodulation 2017*, (Noordwijk, The Netherlands), 2017.

[14] D. González-Iglesias, A. M. Pérez, O. Monerris, S. Anza, J. Vague, B. Gimeno, V. E. Boria, Gomez, A. Vegas, E. Díaz, D. Raboso, and A. Coves, "Recent advances of the multipactor RF breakdown in RF satellite microwave passive devices," in *Proceedings of 2016 Progress In Electromagnetics Research Symposium, PIERS*, (Shangai, China), pp. 4401–4405, 2016.

[15] F. Zimmermann, "A simulation study of electron-cloud instability and beam-induced multipacting in the LHC," Tech. Rep. LHC-Project-Report-95. SLAC-PUB-7425, CERN, Geneva, Switzerland, 1997.

[16] G. I. Budker, G. I. Dimov, and V. Dudnikov, "Experiments on production of intense proton beams by charge exchange injection method," *Soviet Atomic Energy*, vol. 22, no. 3, pp. 348–356, 1967.

[17] O. Gröbner, "Bunch induced multipactoring," in *Proceedings of the 10th International Conference on High-Energy Accelerators*, (Protvino, Russia), pp. 277–282, Inst. High Energy Phys., Serpukhov, 1977.

[18] W. Fischer, M. Blaskiewicz, J. M. Brennan, H. Huang, H. C. Hseuh, V. Ptitsyn, T. Roser, P. Thieberger, D. Trbojevic, J. Wei, S. Y. Zhang, and U. Iriso, "Electron cloud observations and cures in the Relativistic Heavy Ion Collider," *Physical Review Special Topics - Accelerators and Beams*, vol. 11, no. 4, p. 0410002, 2008.

[19] H. Fukuma, "Electron Cloud Effects in KEKB," in *Proc. of Mini Workshop on Electron Cloud Simulations for Proton and Positron Beams - ECLOUD'02*, (Geneva, Switzerland), pp. 1–9, CERN, Geneva, 2002.

[20] H. Fukuma, K. Ohmi, Y. Suetsugu, and M. Tobiyama, "Electron Cloud at SuperKEKB," in *Proc. of ICFA Advanced Beam Dynamics Workshop on High Luminosity Circular e^+e^- Colliders (eeFACT'16), Daresbury, UK, October 24-27, 2016*, no. 58 in ICFA Advanced Beam Dynamics Workshop on High Luminosity Circular e^+e^- Colliders, (Geneva, Switzerland), pp. 125–129, JACoW, jul 2017.

[21] G. Rumolo, H. Bartosik, E. Belli, P. Dijkstal, G. Iadarola, K. Li, L. Mether, A. Romano, M. Schenk, and F. Zimmermann, "Electron cloud effects at the LHC and LHC injectors," in *Proceedings of the 8th International Particle Accelerator Conference: IPAC 2017*, no. MOZA1, (Copenhagen, Denmark), pp. 30–36, JACoW, Geneva, 2017.

[22] G. Rumolo, F. Ruggiero, and F. Zimmermann, "Simulation of the electron-cloud build up and its consequences on heat load, beam stability, and diagnostics," *Physical Review Special Topics - Accelerators and Beams*, vol. 4, no. 1, p. 012801, 2001.

[23] R. Cimino and T. Demma, "Electron cloud in accelerators," *International Journal of Modern Physics A*, vol. 29, no. 17, p. 1430023, 2014.

[24] H. Kawano, "Effective work functions for ionic and electronic emissions from mono- and polycrystalline surfaces," *Progress in Surface Science*, vol. 83, no. 1-2, pp. 1–165, 2008.

[25] A. Chao, M. Tigner, K. Mess, and F. Zimmermann, eds., *Handbook of Accelerator Physics and Engineering*. Singapore: World Scientific, 2nd ed., 2013.

[26] J. S. Berg, "Energy Gain in an Electron Cloud During the Passage of a Bunch," Tech. Rep. LHC Project Note 97, CERN, Geneva, 1997.

[27] N. Hilleret, C. Scheuerlein, and M. Taborelli, "The secondary-electron yield of air-exposed metal surfaces," *Applied Physics A: Materials Science and Processing*, vol. 76, no. 7, pp. 1085–1091, 2003.

[28] L. A. Gonzalez, M. Angelucci, R. Larciprete, and R. Cimino, "The secondary electron yield of noble metal surfaces," *AIP Advances*, vol. 7, no. 11, p. 115203, 2017.

[29] I. Bojko, N. Hilleret, and C. Scheuerlein, "Influence of air exposures and thermal treatments on the secondary electron yield of copper," *Journal of Vacuum Science & Technology A: Vacuum, Surfaces, and Films*, vol. 18, no. 3, pp. 972–979, 2000.

[30] R. Larciprete, D. R. Grosso, A. Di Trolio, and R. Cimino, "Evolution of the secondary electron emission during the graphitization of thin C films," *Applied Surface Science*, vol. 328, pp. 356–360, 2015.

[31] R. Cimino, M. Commisso, D. R. Grosso, T. Demma, V. Baglin, R. Flammini, and R. Larciprete, "Nature of the decrease of the secondary-electron yield by electron bombardment and its energy dependence," *Physical Review Letters*, vol. 109, no. 6, p. 064801, 2012.

[32] T. Gineste, M. Belhaj, G. Teyssedre, and J. Puech, "Investigation of the electron emission properties of silver: From exposed to ambient atmosphere Ag surface to ion-cleaned Ag surface," *Applied Surface Science*, vol. 359, pp. 398–404, 2015.

[33] R. Larciprete, D. R. Grosso, M. Commisso, R. Flammini, and R. Cimino, "Secondary electron yield of Cu technical surfaces: Dependence on electron irradiation," *Physical Review Special Topics - Accelerators and Beams*, vol. 16, no. 1, p. 011002, 2013.

[34] V. Baglin, J. Bojko, O. Gröbner, B. Henrist, N. Hilleret, C. Scheuerlein, and M. Taborelli, "The secondary electron yield of technical materials and its variations with surface treatment," in *Proceedings of the 7th European Particle Accelerator Conference, EPAC 2000*, (Vienna, Austria), pp. 217–221, 2000.

[35] F. Le Pimpec, R. E. Kirby, F. K. King, and M. Pivi, "Electron conditioning of technical aluminium surfaces: Effect on the secondary electron yield," *Journal of Vacuum Science & Technology A: Vacuum, Surfaces, and Films*, vol. 23, no. 6, pp. 1610–1618, 2005.

[36] G. Iadarola, *Electron cloud studies for CERN particle accelerators and simulation code development*. PhD thesis, University of Naples Federico II, 2014.

[37] G. Arduini, P. Collier, B. Dehning, G. Ferioli, B. Henrist, L. Jensen, J. M. Jimenez, J. M. Laurent, G. Rumolo, K. Weiss, and F. Zimmermann, "Measurement of the electron cloud properties by means of a multi-strip detector in the CERN SPS," in *Proceedings of the 8th European Particle Accelerator Conference*, (Paris, France), pp. 1437–1439, 2002.

[38] J. M. Jimenez, G. Arduini, P. Collier, G. Ferioli, B. Henrist, N. Hilleret, L. Jensen, K. Weiss, and F. Zimmermann, "Electron Cloud with LHC-type beams in the SPS : a review of three years of measurements," in *Proceedings of the Mini Workshop on electron cloud simulations for proton and positron beams, ECLOUD'02*, (Geneva, Switzerland), pp. 17–28, 2002.

[39] K. Ohmi and F. Zimmermann, "Head-tail instability caused by electron clouds in positron storage rings," *Physical Review Letters*, vol. 85, no. 18, pp. 3821–3824, 2000.

[40] K. Ohmi, "Beam-photoelectron interactions in positron storage rings," *Physical Review Letters*, vol. 75, no. 8, pp. 1526–1529, 1995.

[41] C. Yin Vallgren, G. Bregliozzi, and P. Chiggiato, "LHC beam vacuum evolution during 2015 machine operation," in *Proceedings of the 7th International Particle Accelerator Conference: IPAC 2016*, (Busan, Korea), pp. 3673–3675, JACoW, Geneva, 2016.

[42] Y. Suetsugu, H. Fukuma, L. Wang, M. Pivi, A. Morishige, Y. Suzuki, M. Tsukamoto, and M. Tsuchiya, "Demonstration of electron clearing effect by means of a clearing electrode in high-intensity positron ring," *Nuclear Instruments and Methods in Physics Research, Section A: Accelerators, Spectrometers, Detectors and Associated Equipment*, vol. 598, no. 2, pp. 372–378, 2009.

[43] C. Yin Vallgren, G. Arduini, J. Bauche, S. Calatroni, P. Chiggiato, K. Cornelis, P. Costa Pinto, B. Henrist, E. Métral, H. Neupert, G. Rumolo, E. Shaposhnikova, and M. Taborelli, "Amorphous carbon coatings for the mitigation of electron cloud in the CERN Super Proton Synchrotron," *Physical Review Special Topics - Accelerators and Beams*, vol. 14, no. 7, p. 071001, 2011.

[44] P. Chiggiato and P. Costa Pinto, "Ti-Zr-V non-evaporable getter films: From development to large scale production for the Large Hadron Collider," *Thin Solid Films*, vol. 515, no. 2, pp. 382–388, 2006.

[45] S. Calatroni, E. Garcia-Tabares Valdivieso, H. Neupert, V. Nistor, A. T. Perez Fontenla, M. Taborelli, P. Chiggiato, O. Malyshev, R. Valizadeh, S. Wackerow, S. A. Zolotovskaya, W. A. Gillespie, and A. Abdolvand, "First accelerator test of vacuum components with laser-engineered surfaces for electron-cloud mitigation," *Physical Review Accelerators and Beams*, vol. 20, no. 11, p. 113201, 2017.

[46] H. Fukuma, J. Flanagan, K. Hosoyama, T. Ieiri, T. Kawamoto, T. Kubo, M. Suetake, S. Uno, S. Win, and M. Yoshioka, "Status of Solenoid System to Suppress the Electron Cloud Effects at the KEKB," *AIP Conference Proceedings*, vol. 642, no. 1, pp. 357–359, 2002.

[47] V. Baglin, "The LHC vacuum system: Commissioning up to nominal luminosity," *Vacuum*, vol. 138, pp. 112–119, 2017.

[48] B. Henrist, N. Hilleret, C. Scheuerlein, and M. Taborelli, "Secondary electron yield of TiZr and TiZrV non-evaporable getter thin film coatings," *Applied Surface Science*, vol. 172, no. 1-2, pp. 95–102, 2001.

[49] V. Baglin, I. Collins, B. Henrist, N. Hilleret, and G. Vorlaufer, "A Summary of Main Experimental Results Concerning the Secondary Electron Emission of Copper," Tech. Rep. LHC Project Report 472, CERN, Geneva, Switzerland, 2002.

[50] R. Cimino and I. R. Collins, "Vacuum chamber surface electronic properties influencing electron cloud phenomena," *Applied Surface Science*, vol. 235, no. 1-2, pp. 231–235, 2004.

[51] G. Iadarola and G. Rumolo, "Electron cloud in the CERN accelerators (PS, SPS, LHC)," in *Proceedings of the INFN-CERN-EuCARD-AccNet Workshop on Electron-Cloud Effects: ECLOUD'12*, (La Biodola, Italy), 2012.

[52] R. Cappi, M. Giovannozzi, E. Métral, G. Rumolo, and F. Zimmermann, "Electron cloud buildup and related instability in the CERN Proton Synchrotron," *Physical Review Special Topics - Accelerators and Beams*, vol. 5, no. 9, pp. 45–54, 2002.

[53] W. Hofle, K. Cornelis, G. Rumolo, G. Arduini, and F. Zimmermann, "Transverse behaviour of the LHC proton beam in the SPS: an update," in *Proceedings of the 19th Particle Accelerator Conference*, (Chicago, USA), pp. 1883–1885, 2001.

[54] G. Arduini, J. M. Jimenez, and K. Weiss, "The SPS as a vacuum test bench for the electron cloud studies with LHC type beams," in *Proceedings of the 19th Particle Accelerator Conference*, (Chicago, USA), pp. 685–687, 2001.

[55] H. Bartosik, T. Bohl, B. Goddard, G. Iadarola, G. Kotzian, K. Li, L. Mether, G. Rumolo, E. Shaposhnikova, M. Schenk, and M. Taborelli, "Detailed studies of beam induced scrubbing in the CERN-SPS," in *Proceedings of the 6th International Particle Accelerator Conference, IPAC 2015*, (Richmond, USA), pp. 3908–3910, 2015.

[56] W. Fischer, Y. Suetsugu, K. Cornelis, J. M. Jimenez, M. Meddahi, and F. Zimmermann, "LIU-SPS scrubbing review 8-9th September 2015: Conclusions and recommendations," Tech. Rep. EDMS LIU-PM-RPT-0023, CERN, Geneva, Switzerland, 2015.

[57] M. Van Gompel, P. Chiggiato, P. Costa Pinto, P. Cruikshank, C. Pasquino, J. Perez Espinos, A. Sapountzis, M. Taborelli, and W. Vollenberg, "Amorphous carbon thin film coating of the SPS beamline: evaluation of the first coating implementation," in *Proceedings of the 8th International Particle Accelerator Conference, IPAC 2017*, no. MOOCA3, (Copenhagen, Denmark), pp. 44–47, 2017.

[58] V. Baglin and B. Jenninger, "SPS electron cloud heat load measurements with WAMPAC and simulations," in *Proceedings of the Mini Workshop on electron cloud simulations for proton and positron beams, ECLOUD'02*, (Geneva, Switzerland), pp. 79–85, 2002.

[59] R. Salemme, V. Baglin, F. Bellorini, G. Bregliozzi, K. Brodzinski, P. Chiggiato, P. Costa Pinto, P. Gomes, A. Gutierrez, V. Inglese, B. Jenninger, E. Michel, M. Pezzetti, B. Rio, A. Sapountzis, and R. Kersevan, "Recommissioning of the COLDEX experiment at CERN," in *Proceedings of the 6th International Particle Accelerator Conference, IPAC 2015*, (Richmond, USA), pp. 7–9, 2015.

[60] R. Salemme, V. Baglin, G. Bregliozzi, P. Chiggiato, and R. Kersevan, "Amorphous carbon coatings at cryogenic temperatures with LHC type beams: First results with the COLDEX experiment," in *Proceedings of the 6th International Particle Accelerator Conference, IPAC 2015*, (Richmond, USA), pp. 3112–3114, 2015.

[61] R. Salemme, V. Baglin, G. Bregliozzi, and P. Chiggiato, "Vacuum performance of Amorphous carbon coating at cryogenic temperature with presence of proton beams," in *Proceedings of the 7th International Particle Accelerator Conference, IPAC 2016*, (Busan, Korea), pp. 3663–3666, 2016.

[62] O. Gröbner, "Technological problems related to the cold vacuum system of the LHC," *Vacuum*, vol. 47, no. 6-8, pp. 591–595, 1996.

[63] O. Gröbner, "Overview of the LHC vacuum system," *Vacuum*, vol. 60, no. 1-2, pp. 25–34, 2001.

[64] O. Grobner, "Beam induced multipacting," in *Proceedings of the 17th Particle Accelerator Conference*, (Vancouver, Canada), pp. 3589–3591, IEEE, 1998, 1997.

[65] F. Zimmermann, "Electron-cloud effects in past & future machines - walk through 50 years of electron-cloud studies," in *Joint INFN-CERN-EuCARD-AccNet Workshop on Electron-Cloud Effects*, (La Biodola, Italy), pp. 9–17, 2012.

[66] G. Rumolo, G. Arduini, V. Baglin, H. Bartosik, N. Biancacci, P. Baudrenghien, G. Bregliozzi, P. Chiggiato, S. Claudet, R. D. Maria, M. Favier, C. Hansen, J. M.

Jimenez, V. Kain, G. Lanza, K. Li, H. M. Cuna, G. Papotti, T. Pieloni, F. Roncarolo, B. Salvant, E. Shaposhnikova, R. Steinhagen, L. Tavian, D. Valuch, W. Venturini, F. Zimmermann, U. I. Cells, and O. Dom, "Electron Cloud Observation in LHC," in *Proceedings of the 2nd International Particle Accelertor Conference*, (San Sebastian, Spain), p. THOBA01, 2011.

[67] G. Rumolo, G. Iadarola, O. Dominguez, G. Arduini, H. Bartosik, S. Claudet, J. Esteban-Müller, F. Roncarolo, E. Shaposhnikova, and L. Tavian, "Electron cloud effects in the LHC in 2011," in *Proceedings of the 3rd Evian workshop on LHC beam operation*, (Evian-les-Bains, France), pp. 165–175, CERN, Geneva, 2011.

[68] G. Iadarola, G. Arduini, and H. Bartosik, "Electron cloud and scrubbing in 2012 in the LHC," in *Proceedings of the 4th Evian workshop on LHC beam operation*, (Evian-les-Bains, France), pp. 119–128, CERN, Geneva, 2012.

[69] G. Iadarola, H. Bartosik, K. Li, L. Mether, A. Romano, G. Rumolo, and M. Schenk, "Performance limitations from electron cloud in 2015," in *Proceedings of the 6th Evian workshop on LHC beam operation*, (Evian-les-Bains, France), pp. 101–110, CERN, Geneva, 2015.

[70] G. Iadarola, B. Bradu, P. Dijkstal, L. Mether, G. Rumolo, A. Romano, G. Skripka, and L. Tavian, "Electron cloud and heat loads in Run 2," in *Proceedings of the 9th Evian workshop on LHC operations*, (Evian-les-Bains, France), CERN, Geneva, 2019.

[71] C. Yin Vallgren, P. R. Metidieri, and G. Bregliozzi, "Beam induced dynamic pressure during Run 2 (2015 - 2018) machine operation in the LHC," 6th electron cloud workshop, ECLOUD'18, 4th June 2018, La Biodola, Italy, https://agenda.infn.it/event/13351/.

[72] B. Bradu, E. Rogez, E. Blanco-Viñuela, G. Ferlin, and A. Tovar-Gonzalez, "Beam screen cryogenic control improvements for the LHC run 2," *IOP Conference Series: Materials Science and Engineering*, vol. 171, p. 012128, feb 2017.

[73] L. Mether, P. Dijkstal, G. Iadarola, and G. Rumolo, "Electron cloud in 2016: cloudy or clear?," in *Proceedings of the 7th Evian workshop on LHC beam operation*, (Evian-les-Bains, France), pp. 147–152, CERN, Geneva, 2016.

[74] L. Mether, D. Amorim, G. Arduini, X. Buffat, G. Iadarola, A. Lechner, E. Métral, D. Mirarchi, G. Rumolo, and B. Salvant, "16L2: Operation, observations and physics aspects," in *Proceedings of the 8th Evian workshop on LHC beam operation*, (Evian-les-Bains, France), pp. 99–105, CERN, Geneva, 2017.

[75] G. Iadarola, G. Rumolo, P. Dijkstal, and L. Mether, "Analysis of the beam induced heat loads on the LHC arc beam screen during Run 2," Tech. Rep. CERN-ACC-NOTE-2017-0066, CERN, Geneva, Switzerland, 2017.

[76] G. Iadarola, "Overview on heat loads in the LHC," 6th electron cloud workshop, ECLOUD'18, 4th June 2018, La Biodola, Italy, https://agenda.infn.it/event/13351/.

[77] G. Iadarola and G. Rumolo, "PyECLOUD and build-up simulations at CERN," in *Proceedings of the Joint INFN-CERN-EuCARD-ACCNET Workshop on electron-cloud effects ECLOUD'12* (R. Cimino, G. Rumolo, and F. Zimmermann, eds.), (La Biodola, Italy), pp. 189–194, CERN, Geneva, 2013.

[78] G. Skripka and G. Iadarola, "Beam-induced heat loads on the beam screens of the HL-LHC arcs," Tech. Rep. CERN-ACC-NOTE-2019-0041, CERN, Geneva, Switzerland, 2019.

[79] P. Dijkstal, G. Iadarola, L. Mether, and G. Rumolo, "Simulation studies on the electron cloud build-up in the elements of the LHC Arcs at 6.5 TeV," Tech. Rep. CERN-ACC-NOTE-2017-0057, CERN, Geneva, Switzerland, 2017.

[80] G. Rumolo, "Beam Dynamics Challenges for the LHC and Injector Upgrades," in *Proceedings of the 61st ICFA ABDW on High-Intensity and High-Brightness Hadron Beams*, (Daejeon, Korea), pp. 8–13, JACoW, Geneva, 2018.

[81] J. M. Jimenez, G. Arduini, and L. Tavian, "Task Force on LHC Beam-induced heat loads: Mandate of the Task Force," Presentation at the 325th LHC Machine Committee, 25th October 2017, CERN, Geneva, https://indico.cern.ch/event/675827/.

[82] L. Tavian, "Report from the task force on beam induced heat loads," (Chamonix, France), Presented at the LHC performance workshop 2018, Chamonix'18, 29th January 2018, Chamonix, https://indico.cern.ch/event/676124/contributions/2767828/.

[83] S. Federmann, F. Caspers, E. Mahner, P. Costa Pinto, M. Taborelli, B. Salvant, and C. Yin Vallgren, "Electron Cloud Measurements of Coated and Uncoated Vacuum Chambers in the Cern SPS By Means of the Microwave Transmission Method," in *Proceedings of the 1st International Particle Accelerator Conference, IPAC'10*, (Kyoto, Japan), pp. 1497–1499, JACoW, Geneva, 2010.

[84] S. De Santis, J. M. Byrd, F. Caspers, A. Krasnykh, T. Kroyer, M. T. Pivi, and K. G. Sonnad, "Measurement of electron clouds in large accelerators by microwave dispersion," *Physical Review Letters*, vol. 100, no. 9, pp. 3–6, 2008.

[85] M. T. F. Pivi, A. K. Krasnykh, J. Byrd, S. De Santis, and K. G. Sonnad, "Microwave Transmission Measurement of the Electron Cloud Density in the Positron Ring of Pep-II," in *Proceedings of the 11th European Particle Accelerator Conference, EPAC'08*, (Genoa, Italy), pp. 694–696, JACoW, Geneva, 2008.

[86] Y. Suetsugu, K.-i. Kanazawa, K. Shibata, T. Ishibashi, H. Hisamatsu, M. Shirai, and S. Terui, "Design and construction of the SuperKEKB vacuum system," *Journal of Vacuum Science & Technology A: Vacuum, Surfaces, and Films*, vol. 30, no. 3, p. 031602, 2012.

[87] Y. Suetsugu, K. Shibata, T. Ishibashi, H. Fukuma, M. Tobiyama, J. Flanagan, E. Mulyani, M. Shirai, S. Terui, K.-i. Kanazawa, and H. Hisamatsu, "Achievements and problems in the first commissioning of superKEKB vacuum system," *Journal of Vacuum Science & Technology A: Vacuum, Surfaces, and Films*, vol. 35, no. 3, p. 03E103, 2017.

[88] T. Abe, T. Kageyama, H. Sakai, Y. Takeuchi, and K. Yoshino, "Breakdown study based on direct in situ observation of inner surfaces of an rf accelerating cavity during a high-gradient test," *Physical Review Accelerators and Beams*, vol. 19, no. 10, p. 102001, 2016.

[89] C. Scheuerlein, M. Taborelli, N. Hilleret, A. Brown, and M. A. Baker, "An AES study of the room temperature conditioning of technological metal surfaces by electron irradiation," *Applied Surface Science*, vol. 202, no. 1-2, pp. 57–67, 2002.

[90] C. Scheuerlein and M. Taborelli, "Electron stimulated carbon adsorption in ultrahigh vacuum monitored by Auger electron spectroscopy," *Journal Of Vacuum Science & Technology A-Vacuum Surfaces And Films*, vol. 20, no. 1, pp. 93–101, 2002.

[91] W. Hartung, J. Conway, C. Dennett, S. Greenwald, J.-S. Kim, Y. Li, T. Moore, and V. Omanovic, "Measurements of secondary electron yield of metal surfaces and films with exposure to a realistic accelerator environment," in *Proceedings of the 4th International Particle Accelerator Conference IPAC 2013*, (Shangai, China), pp. 3493–3495, JACoW, Geneva, 2013.

[92] M. T. Pivi, G. Collet, F. King, R. E. Kirby, T. Markiewicz, T. O. Raubenheimer, J. Seeman, and F. Le Pimpec, "Experimental observations of in situ secondary electron yield reduction in the PEP-II particle accelerator beam line," *Nuclear Instruments and Methods in Physics Research, Section A: Accelerators, Spectrometers, Detectors and Associated Equipment*, vol. 621, no. 1-3, pp. 47–56, 2010.

[93] S. Kato and M. Nishiwaki, "In-situ SEY measurements at KEKB positron ring and comparison with laboratory experiments," in *Proceedings of the International workshop on electron-cloud effects, ECLOUD'07* (H. Fukuma, E. Kim, and K. Ohmi, eds.), (Daegu, Korea), pp. 72–75, High Energy Accelerator Research Organization (KEK), 2007.

[94] B. Henrist, N. Hilleret, C. Scheuerlein, M. Taborelli, and G. Vorlaufer, "The variation of the secondary electron yield and of the desorption yield of copper under electron bombardment: Origin and impact on the conditioning of the LHC," in *Proceedings of the 8th European Particle Conference: EPAC 2002*, (Paris, France), p. 2553, European Physical Society, Geneva, 2002.

[95] M. Nishiwaki and S. Kato, "Graphitization of inner surface of copper beam duct of KEKB positron ring," *Vacuum*, vol. 84, pp. 743–746, dec 2009.

[96] M. Nishiwaki and S. Kato, "Influence of electron irradiation and heating on secondary electron yields from non-evaporable getter films observed with in situ x-ray photoelectron spectroscopy," *Journal of Vacuum Science & Technology A: Vacuum, Surfaces, and Films*, vol. 25, no. 4, pp. 675–679, 2007.

[97] E. Rudberg, "Inelastic scattering of electrons from solids," *Physical Review*, vol. 50, no. 2, pp. 138–150, 1936.

[98] J. Roupie, O. Jbara, T. Tondu, M. Belhaj, and J. Puech, "The study of electron emission from aluminum in the very low primary energy range using Monte Carlo simulations," *Journal of Physics D: Applied Physics*, vol. 46, no. 12, 2013.

[99] H. Bruining, *Physics and applications of secondary electron emission.* Pergamon Science series, Electronics and waves, London: Pergamon Press, 1954.

[100] R. G. Lye and A. Dekker, "Theory of secondary emission," *Physical Review*, vol. 107, no. 4, pp. 977–981, 1957.

[101] G. F. Dionne, "Effects of secondary electron scattering on secondary emission yield curves," *Journal of Applied Physics*, vol. 44, no. 12, pp. 5361–5364, 1973.

[102] G. F. Dionne, "Origin of secondary-electron-emission yield-curve parameters," *Journal of Applied Physics*, vol. 46, no. 8, pp. 3347–3351, 1975.

[103] A. Dekker, "Secondary Electron Emission," *Solid State Physics*, vol. 6, pp. 251–311, 1958.

[104] H. Seiler, "Secondary electron emission in the scanning electron microscope," *Journal of Applied Physics*, vol. 54, no. 11, pp. R1–R18, 1983.

[105] J. Halbritter, "On changes of secondary emission by resonant tunneling via adsorbates," *Journal de Physique Colloques*, vol. 45(C2), pp. 315–317, 1984.

[106] S. Chawla, B. Rickett, N. Sankarraman, and J. Payer, "An X-Ray Photoelectron Spectroscopic Investigation of the Air-formed Film on Copper," *Corrosion Science*, vol. 33, no. 10, pp. 1617–1631, 1992.

[107] T. L. Barr, "An ESCA study of the termination of the passivation of elemental metals," *Journal of Physical Chemistry*, vol. 82, no. 16, pp. 1801–1810, 1978.

[108] M. Taborelli, "Cleaning and surface properties," in *Proceedings of the CERN accelerator school - Vacuum in accelerators* (D. Brandt, ed.), (Platja d'Aro, Spain), pp. 321–340, CERN, Geneva, 2006.

[109] M. Nishiwaki and S. Kato, "Electron stimulated gas desorption from copper material and its surface analysis," *Applied Surface Science*, vol. 169-170, pp. 700–705, 2001.

[110] R. E. Kirby and F. K. King, "Secondary electron emission yields from PEP-II accelerator materials," *Nuclear Instruments and Methods in Physics Research, Section A: Accelerators, Spectrometers, Detectors and Associated Equipment*, vol. 469, no. 1, pp. 1–12, 2001.

[111] R. Valizadeh, O. B. Malyshev, S. Wang, S. A. Zolotovskaya, W. A. Gillespie, and A. Abdolvand, "Low secondary electron yield engineered surface for electron cloud mitigation," *Applied Physics Letters*, vol. 105, no. 23, p. 231605, 2014.

[112] K. Kennedy, B. Harteneck, G. Millos, M. Benapfl, F. King, and R. Kirby, "TiN coating of the PEP-II low-energy ring aluminum arc vacuum chambers," in *Proceedings of the 1997 Particle Accelerator Conference*, (Vancouver, Canada), pp. 3568–3570, IEEE, 1998.

[113] S. Wang, O. Malyshev, R. Valizadeh, E. Seddon, and M. Cropper, "The secondary electron yield from transition metals," in *Proceedings of the 5th International Particle Accelerator Conference, IPAC 2014*, (Dresden, Germany), pp. 2403–2405, JACoW, Geneva, 2014.

[114] A. Kuzucan, H. Neupert, M. Taborelli, and H. Störi, "Secondary electron yield on cryogenic surfaces as a function of physisorbed gases," in *Proceedings of the 2nd International Particle Accelerator Conference, IPAC2011*, (San Sebastian, Spain), pp. 1575–1577, JACoW, Geneva, 2011.

[115] H. Bruining and J. de Boer, "Secondary electron emission Part V. The mechanism of secondary electron emission," *Physica*, vol. 6, no. 7-12, pp. 834–839, 1939.

[116] V. Baglin, I. R. Collins, O. Gröbner, C. Grünhagel, B. Henrist, N. Hilleret, and B. Jenninger, "Measurements At EPA of Vacuum and Electron-Cloud Related Effects," in *Proceedings of the 11th Workshop of the LHC, Chamonix XI*, (Chamonix, France), pp. 141–143, CERN, Geneva, 2001.

[117] J. M. Jimenez, G. Arduini, P. Collier, G. Ferioli, B. Henrist, N. Hilleret, L. Jensen, J.-m. Laurent, K. Weiss, and F. Zimmermann, "Electron cloud studies and beam scrubbing effect in the SPS," Tech. Rep. LHC Project Report 634, CERN, Geneva, Switzerland, 2003.

[118] C. Yin Vallgren, *Low secondary electron yield carbon coatings for electron cloud mitigation in modern particle accelerators*. PhD thesis, Chalmers University of Technology, Goteborg, Sweden, 2010.

[119] S. Hofmann, *Auger- and X-Ray Photoelectron Spectroscopy in Materials Science, A User-Oriented Guide*. Springer Series in Surface Science, Heidelberg: Springer, 2013.

[120] J. F. Moulder, W. F. Stickle, P. E. Sobol, and K. D. Bomben, *Handbook of X-ray Photoelectron Spectroscopy: A Reference Book of Standard Spectra for Identification and Interpretation of XPS Data*. Eden Prairie: Physical Electronics Division, Perkin-Elmer Corporation, 1995.

[121] N. Stojilovic, "Why can't we see hydrogen in X-ray photoelectron spectroscopy?," *Journal of Chemical Education*, vol. 89, no. 10, pp. 1331–1332, 2012.

[122] C. Yin Vallgren, S. Calatroni, P. Costa Pinto, A. Kuzucan, H. Neupert, and M. Taborelli, "Characterization of carbon coatings with low secondary electron yield," in *Proceedings of the 2nd International Particle Accelertor Conference IPAC11*, (San Sebastian, Spain), pp. 1587–1589, JACoW, Geneva, 2011.

[123] L. Bitsikokos, G. Iadarola, L. Sabato, and P. Dijkstal, "Secondary emission models in e-cloud buildup simualtions: from the lab to the code," 6th electron cloud workshop, ECLOUD'18, 6th June 2018, La Biodola, Italy, https://agenda.infn.it/event/13351/.

[124] R. Cimino, L. A. Gonzalez, R. Larciprete, A. Di Gaspare, G. Iadarola, and G. Rumolo, "Detailed investigation of the low energy secondary electron yield of technical Cu and its relevance for the LHC," *Physical Review Special Topics - Accelerators and Beams*, vol. 18, no. 5, pp. 1–10, 2015.

[125] "Fiche de donnees de securite - NGL 17.40 SP ALU III," tech. rep., NGL Cleaning technology SA, Nyon, Switzerland, 2013.

[126] C. Kittel, *Introduction to Solid State Physics*. Hoboken, NJ: Wiley, 8th ed., 2004.

[127] V. Baglin, "Cold/sticky systems," in *Proceedings of the CERN accelerator school - Vacuum in accelerators* (D. Brandt, ed.), (Platja d'Aro, Spain), pp. 351–367, CERN, Geneva, 2006.

[128] P. Cruikshank, K. Artoos, F. Bertinelli, J. C. Brunet, R. Calder, C. Campedel, I. Collins, J. M. Dalin, B. Feral, O. Grobner, N. Kos, A. Mathewson, L. Nikitina, I. Nikitine, and A. Poncet, "Mechanical design aspects of the LHC beam screen," in *Proceedings of the 1997 Particle Accelerator Conference*, (Vancouver, Canada), pp. 3586–3588, IEEE, 1998.

[129] R. O. Verkuijlen, M. H. Van Dongen, A. A. Stevens, J. Van Geldrop, and J. P. Bernards, "Surface modification of polycarbonate and polyethylene naphtalate foils by UV-ozone treatment and μplasma printing," *Applied Surface Science*, vol. 290, pp. 381–387, 2014.

[130] N. S. Mclntyre and M. G. Cook, "X-Ray Photoelectron Studies on Some Oxides and Hydroxides of Cobalt, Nickel, and Copper," *Analytical Chemistry*, vol. 47, no. 13, pp. 2208–2213, 1975.

[131] M. C. Biesinger, "Advanced analysis of copper X-ray photoelectron spectra," *Surface and Interface Analysis*, vol. 49, no. 13, pp. 1325–1334, 2017.

[132] T. Robert, M. Bartel, and G. Offergeld, "Characterization of oxygen species adsorbed on copper and nickel oxides by X-ray photoelectron spectroscopy," *Surface Science*, vol. 33, no. 1, pp. 123–130, 1972.

[133] S. Poulston, P. M. Parlett, P. Stone, and M. Bowker, "Surface oxidation and reduction of CuO and Cu2O studied using XPS and XAES," *Surface and Interface Analysis*, vol. 24, no. 12, pp. 811–820, 1996.

[134] J. Díaz, G. Paolicelli, S. Ferrer, and F. Comin, "Separation of the sp3 and sp2 components in the C1s photoemission spectra of amorphous carbon films," *Physical Review B*, vol. 54, no. 11, pp. 8064–8069, 1996.

[135] V. Petit, M. Taborelli, H. Neupert, P. Chiggiato, and M. Belhaj, "Role of the different chemical components in the conditioning process of air exposed copper surfaces," *Physical Review Accelerators and Beams*, vol. 22, no. 8, p. 83101, 2019.

[136] G. Panzner, B. Egert, and H. P. Schmidt, "The stability of CuO and Cu2O surfaces during argon sputtering studied by XPS and AES," *Surface Science*, vol. 151, no. 2-3, pp. 400–408, 1985.

[137] U. Evans and H. Miley, "Measurements of oxide films on copper and iron," *Nature*, vol. 139, p. 283, 1937.

[138] T. N. Rhodin, "Low Temperature Oxidation of Copper. I. Physical Mechanism," *Journal of the American Chemical Society*, vol. 72, no. 11, pp. 5102–5106, 1950.

[139] M. R. Pinnel, H. G. Tompkins, and D. E. Heath, "Oxidation of copper in controlled clean air and standard laboratory air at 50C to 150C," *Application of Surface Science*, vol. 2, no. 4, pp. 558–577, 1979.

[140] C. Scheuerlein and M. Taborelli, "The assessment of metal surface cleanliness by XPS," *Applied Surface Science*, vol. 252, no. 12, pp. 4279–4288, 2006.

[141] H. Eckardt, L. Fritsche, and J. Noffke, "Self-consistent relativistic band structure of the noble metals," *Journal of Physics F: Metal Physics*, vol. 14, no. 1, pp. 97–112, 1984.

[142] A. Siokou, F. Ravani, S. Karakalos, O. Frank, M. Kalbac, and C. Galiotis, "Surface refinement and electronic properties of graphene layers grown on copper substrate: An XPS, UPS and EELS study," *Applied Surface Science*, vol. 257, no. 23, pp. 9785–9790, 2011.

[143] L. Wagner and W. Spicer, "Photemission study of the oxidation of copper films," *Surface science*, vol. 46, no. 1, pp. 301–307, 1974.

[144] M. Pivi, F. K. King, R. E. Kirby, T. O. Raubenheimer, G. Stupakov, and F. Le Pimpec, "Sharp reduction of the secondary electron emission yield from grooved surfaces," *Journal of Applied Physics*, vol. 104, no. 10, p. 104904, 2008.

[145] J. Cazaux, "Some considerations on the secondary electron emission, δ, from e-irradiated insulators," *Journal of Applied Physics*, vol. 85, no. 2, pp. 1137–1147, 1999.

[146] R. P. Vasquez, "CuSO4 by XPS," *Surface Science Spectra*, vol. 5, no. 4, pp. 279–284, 2002.

[147] V. Nefedov, Y. V. Salyn, P. M. Solozhenkin, and G. Y. Pulatov, "X-ray photoelectron study of surface compounds formed during flotation of minerals," *Surface and Interface analysis*, vol. 2, no. 5, pp. 170–172, 1980.

[148] G. E. Hill, "Secondary Electron Emission and Compositional Studies on Channel Plate Glass Surfaces," in *Photo-Electronic Image Devices* (B. L. Morgan, R. W. Airway, and D. McMullan, eds.), vol. 40 of *Advances in Electronics and Electron Physics*, pp. 153–165, Academic Press, 1976.

[149] R. P. Vasquez, "CuCO3 by XPS," *Surface Science Spectra*, vol. 5, no. 4, pp. 273–278, 1998.

[150] C. D. Wagner, D. A. Zatko, and R. H. Raymond, "Use of the Oxygen KLL Auger Lines in Identification of Surface Chemical States by Electron Spectroscopy for Chemical Analysis," *Analytical Chemistry*, vol. 52, no. 9, pp. 1445–1451, 1980.

[151] X. Deng, A. Verdaguer, T. Herranz, C. Weis, H. Bluhm, and M. Salmeron, "Surface chemistry of Cu in the presence of CO2 and H2O," *Langmuir*, vol. 24, pp. 9474–9478, 2008.

[152] F. Reiterer, W. Johannes, and H. Gamsjäger, "Semimicro determination of solubility constants: Copper(II) carbonate and iron(II) carbonate," *Mikrochimica Acta*, vol. 75, no. 1-2, pp. 63–72, 1981.

[153] G. Iadarola and M. Taborelli, "Modelling of a thin insulating layer in PyECLOUD," Presented at the 66th electron cloud meeting, 5th April 2019, CERN, Geneva, https://indico.cern.ch/event/790354/.

[154] B. Wang, E. Wu, Y. Wang, L. Xiong, and S. Liu, "Activation treatment effects on characteristics of BeO layer and secondary electron emission properties of an activated Cu-Be alloy," *Applied Surface Science*, vol. 355, pp. 19–25, 2015.

[155] J. Kim, F. Kim, and J. Huang, "Seeing graphene-based sheets," *Materials Today*, vol. 13, no. 3, pp. 28–38, 2010.

[156] S. S. Roy and M. S. Arnold, "Improving graphene diffusion barriers via stacking multiple layers and grain size engineering," *Advanced Functional Materials*, vol. 23, no. 29, pp. 3638–3644, 2013.

[157] J. S. Bunch, S. S. Verbridge, J. S. Alden, A. M. Van Der Zande, J. M. Parpia, H. G. Craighead, and P. L. McEuen, "Impermeable atomic membranes from graphene sheets," *Nano Letters*, vol. 8, no. 8, pp. 2458–2462, 2008.

[158] M. Schriver, W. Regan, W. J. Gannett, A. M. Zaniewski, M. F. Crommie, and A. Zettl, "Graphene as a long-term metal oxidation barrier: Worse than nothing," *ACS Nano*, vol. 7, no. 7, pp. 5763–5768, 2013.

[159] F. Zhou, Z. Li, G. J. Shenoy, L. Li, and H. Liu, "Enhanced room-temperature corrosion of copper in the presence of graphene," *ACS Nano*, vol. 7, no. 8, pp. 6939–6947, 2013.

[160] A. Romano, G. Iadarola, and G. Rumolo, "Effect of the LHC beam screen baffles on the electron cloud build-up," Presented at the 23rd electron cloud meeting, 18th September 2015, CERN, Geneva, https://indico.cern.ch/event/446452/.

[161] B. Lesiak, A. Jablonski, J. Zemek, and P. Jiricek, "Determination of the inelastic mean free paths of electrons in copper and copper oxides by Elastic Peak Electron Spectroscopy (EPES)," *Surface and Interface Analysis*, vol. 26, no. 5, pp. 400–411, 1998.

[162] A. Losev, K. Kostov, and G. Tyuliev, "Electron beam induced reduction of CuO in the prensence of a surface carbonaceous layer: an XPS/HREELS study," *Surface Science*, vol. 213, pp. 564–579, 1989.

[163] N. J. Long and A. K. Petford-Long, "In-situ electron-beam-induced reduction of CuO: A study of phase transformations in cupric oxide," *Ultramicroscopy*, vol. 20, no. 1-2, pp. 151–160, 1986.

[164] S. Choudhary, J. V. Sarma, S. Pande, S. Ababou-Girard, P. Turban, B. Lepine, and S. Gangopadhyay, "Oxidation mechanism of thin Cu films: A gateway towards the formation of single oxide phase," *AIP Advances*, vol. 8, no. 5, 2018.

[165] D. L. Cocke, G. K. Chuah, N. Kruse, and J. H. Block, "Copper oxidation and surface copper oxide stability investigated by pulsed field desorption mass spectrometry," *Applied Surface Science*, vol. 84, no. 2, pp. 153–161, 1995.

[166] S. Bok, G.-H. Lim, and B. Lim, "UV/Ozone treatment for adhesion improvement of copper/epoxy," *Journal of Industrial and Engineering Chemistry*, vol. 46, pp. 199–202, 2017.

[167] S. Lacombe, F. Cemic, K. Jacobi, M. N. Hedhili, Y. Le Coat, R. Azria, and M. Tronc, "Electron-induced synthesis of ozone in a dioxygen matrix," *Physical Review Letters*, vol. 79, no. 6, pp. 1146–1149, 1997.

[168] J. R. Vig, "UV / Ozone cleaning of surfaces," *Journal Of Vacuum Science & Technology A-Vacuum Surfaces And Films*, vol. 3, no. 3, pp. 1027–1034, 1985.

[169] R. R. Sowell, R. E. Cuthrell, D. M. Mattox, and R. D. Bland, "Surface Cleaning By Ultraviolet Radiation.," *Journal of Vacuum Science and Technology*, vol. 11, no. 1, pp. 474–475, 1974.

[170] Z. Li, Y. Wang, A. Kozbial, G. Shenoy, F. Zhou, R. McGinley, P. Ireland, B. Morganstein, A. Kunkel, S. P. Surwade, L. Li, and H. Liu, "Effect of airborne contaminants on the wettability of supported graphene and graphite," *Nature Materials*, vol. 12, no. 10, pp. 925–931, 2013.

[171] M. L. Sham and J. K. Kim, "Surface functionalities of multi-wall carbon nanotubes after UV/Ozone and TETA treatments," *Carbon*, vol. 44, no. 4, pp. 768–777, 2006.

[172] I. Sutherland, E. Sheng, R. H. Bradley, and P. K. Freakley, "Effects of ozone oxidation on carbon black surfaces," *Journal of Materials Science*, vol. 31, no. 21, pp. 5651–5655, 1996.

[173] N. Usuki, "Photoelectron spectroscopic study of copper surfaces changed by oxygen ion bombardment," *Vacuum*, vol. 41, no. 7-9, pp. 1683–1685, 1990.

[174] L. Mether, "Investigation of the e-/ion dynamics for very high gas densities (16L2 regime)," Presented at the 67th Electron Cloud meeting, 10th May 2019, CERN, Geneva, https://indico.cern.ch/event/811014/.

[175] R. Garcia Alia, G. Lerner, and S. O., "R2E Run 2 radiation level overview," Presented at the 375th LHC Machine Committee, 20th March 2019, CERN, Geneva, https://indico.cern.ch/event/807556/.

[176] J. R. Günter and H. R. Oswald, "Topotactic Electron Induced and Thermal Decomposition of Copper (Ii) Hydroxide," *Journal of Applied Crystallography*, vol. 3, pp. 21–26, 1970.

[177] A. E. Rakhshani, "Preparation, characteristics and photovoltaic properties of cuprous oxide-a review," *Solid State Electronics*, vol. 29, no. 1, pp. 7–17, 1986.

[178] J. A. Rodriguez, J. Y. Kim, J. C. Hanson, M. Pérez, and A. I. Frenkel, "Reduction of CuO in H2: In situ time-resolved XRD studies," *Catalysis Letters*, vol. 85, no. 3-4, pp. 247–254, 2003.

[179] J. Y. Kim, J. A. Rodriguez, J. C. Hanson, A. I. Frenkel, and P. L. Lee, "Reduction of CuO and Cu2O with H2: H embedding and kinetic effects in the formation of suboxides," *Journal of the American Chemical Society*, vol. 125, no. 35, pp. 10684–10692, 2003.

[180] T. H. Fleisch, G. W. Zajac, J. O. Schreiner, and G. J. Mains, "An XPS study of the UV photoreduction of transition and noble metal oxides," *Applied Surface Science*, vol. 26, no. 4, pp. 488–497, 1986.

[181] P. Costa Pinto, "SEY lowering with a-C coating in SPS and LHC," Presented at the 6th electron cloud workshop, ECLOUD'18, 6th June 2018, La Biodola, Italy, https://agenda.infn.it/event/13351/.

[182] P. Costa Pinto, S. Calatroni, P. Chiggiato, P. Edwards, M. Mensi, H. Neupert, M. Taborelli, and C. Yin Vallgren, "Carbon Coating of the SPS Dipole Chambers," in *Proceedings of ECLOUD'12*, (La Biodola, Italy), pp. 141–148, CERN, Geneva, 2012.

[183] M. Taborelli, P. Chiggiato, P. Costa Pinto, and P. Cruikshank, "Nine years of carbon coating development for the SPS upgrade: achievements and heritage," Tech. Rep. CERN-ACC-2016-0010, CERN, Geneva, Switzerland, 2016.

[184] G. Iadarola, L. Mether, and G. Rumolo, "Filling schemes and e-cloud constraints for 2017," in *Proceedings of the 7th Evian workshop on LHC beam operation*, (Evian-les-Bains, France), pp. 239–244, CERN, Geneva, 2016.

[185] L. Mether, "Implementation of cross-species ionization in PyECLOUD," Presented at the 69th electron cloud meeting, 14th August 2019, CERN, Geneva, https://indico.cern.ch/event/835473/.

[186] A. G. Mathewson and S. Zhang, "Beam-Gas Ionisation Cross Sections at 7.0 TeV," Tech. Rep. Vacuum-Technical-Note-96-01, CERN, Geneva, Switzerland, 1996.